5-2011

Methods Development and Force Field Evaluation for Molecular Simulations of Iinteractions Between Structured Peptides and Functionalized Material Surfaces

Galen Collier
Clemson University, galen@clemson.edu

METHODS DEVELOPMENT AND FORCE FIELD EVALUATION FOR MOLECULAR SIMULATIONS OF INTERACTIONS BETWEEN STRUCTURED PEPTIDES AND FUNCTIONALIZED MATERIAL SURFACES

A Dissertation
Presented to
the Graduate School of
Clemson University

In Partial Fulfillment
of the Requirements for the Degree
Doctor of Philosophy
Bioengineering

---

by
Galen Collier
May 2011

Accepted by:
Prof. Robert A. Latour, Committee Chair
Prof. Steven J. Stuart
Dr. David A. Bruce
Dr. Alexey Vertegel

ABSTRACT

The process of protein adsorption to material surfaces is highly complex and it is one of the most fundamental concepts upon which progress in the field of bioengineering is based. The strategic design of material surfaces for optimal utility in specific biological environments is absolutely dependent upon a thorough understanding of the mechanisms underlying protein adsorption, yet there is still a very limited understanding of these mechanisms. The primary reason for this lack of understanding is that protein adsorption is a dynamic process which occurs at the atomic and macromolecular scale, where experimental analyses provide a view that is static and too coarse to elucidate the stepwise processes behind this critical biochemical phenomenon. In recent years, continual improvements in speed and efficiency of computational hardware and simulation techniques have enabled the use of molecular simulation for studying systems of the size necessary for examining the mechanistic details of protein adsorption (tens to hundreds of thousands of atoms). Of the various forms of molecular simulation, all-atom empirical force field molecular dynamics (MD) simulation has shown the greatest potential for exploring the nature of protein adsorption because it offers a dynamic view of nanosecond-scale processes with atomistic detail. However, a shortcoming of the application of MD in studying protein adsorption is that the most widely used MD force fields (i.e., equations and parameter sets used for calculating structural and energetic properties) have been designed and validated for simulations of solvated molecular systems in the absence of solid surfaces. To address this shortcoming of an otherwise extremely powerful research tool, an initial evaluation of the applicability of existing MD

force fields to model systems of structured peptides interacting with functionalized material surfaces is warranted. The work presented here encompasses that initial evaluation of force fields. Numerous detailed analyses of water, ions, and peptides were completed in order to provide the most accurate and comprehensive examination of simulated peptide adsorption available. As a result of this work, simulation methods for these unique systems were tested and determined to be appropriate for accurately representing experimental results. Also, a comparative evaluation of force field performance identified the force field that most consistently reflects experimental findings.

TABLE OF CONTENTS

Page

LIST OF TABLES

Table Page

LIST OF FIGURES

List of Figures (Continued)

Figure Page

List of Figures (Continued)

Figure Page

List of Figures (Continued)

Figure Page

List of Figures (Continued)

Figure Page

List of Figures (Continued)

Figure Page

List of Figures (Continued)

Figure Page

List of Figures (Continued)

Figure Page

List of Figures (Continued)

Figure Page

CHAPTER ONE

INTRODUCTION

Protein adsorption to material surfaces is a highly complex phenomenon and it is one of the most fundamental concepts upon which progress in the field of bioengineering is based. The strategic design of material surfaces for sufficient biocompatibility or targeted biological response is absolutely dependent upon a thorough understanding of the mechanisms underlying protein adsorption. However, despite decades of experimental studies and recent simulation work, there is still a very limited understanding of these mechanisms. The primary reason for this lack of understanding is that protein adsorption is a dynamic process which occurs at the atomic and macromolecular scale, where experimental analyses provide a view that is static and too coarse to elucidate the stepwise processes behind this critical biochemical phenomenon. Also, protein adsorption typically takes place at the interface between a solid material and solution, resulting in a thin, delicate structural network that is difficult to examine using most experimental approaches. Recent improvements in the speed and efficiency of computational hardware and simulation techniques have enabled the use of molecular simulation for studying systems of the size necessary for examining the mechanistic details of protein adsorption (usually more than 100,000 atoms). Of the various forms of molecular simulation currently in use, all-atom empirical force field (FF) molecular dynamics (MD) simulation has shown the greatest potential for exploring the nature of protein adsorption. Unlike the faster coarse-grain techniques, MD simulation addresses all of the atoms of a molecular system. MD simulation is based on classical Newtonian

dynamics with atoms treated as point charges, so the variables used for the dynamics calculations govern the accuracy of the simulation. Also, protein adsorption occurs primarily through non-bonded electrostatic interactions, which makes FF selection critically important. For these reasons, a potential shortcoming of the application of MD in studying protein adsorption is that the most widely used MD FFs (i.e., equations and parameter sets used for calculating structural and energetic properties) have been designed and validated for simulations of solvated molecular systems in the absence of solid surfaces. With a solid surface present, the parameters intended for solvated molecules may misrepresent some atom-atom interactions proximal to the surface where water populations may be depleted or counter-ion populations may be very high. Other phenomena not specifically addressed by individual atomic parameters, such as the effect of mutual water exclusion between nonpolar molecules and a hydrophobic surface, may also fail to be represented accurately if certain combinations of atomic parameters do not cooperate as needed.

An appropriate set of model systems for this study includes peptides with defined secondary structures and functionalized material surfaces to enable the analysis of specific secondary structure forms interacting with defined surface chemistries. Water and ions play important roles in the adsorption process, so analyses of the solvent surrounding the adsorbing peptides serve as an important supplement to the peptide structural studies. The simulation methods (mathematical approach and optimizations) must match, as closely as possible, those for which the selected FFs have been successfully used in simulations of peptides and proteins. This requirement is

complicated by the addition of a solid surface to the simulation since the presence of a solid surface can create problems when using periodic boundary conditions for system imaging or when using particle-mesh Ewald summation for calculating long-range electrostatics. These concerns make an evaluation of the performance of the simulation methods necessary before proceeding with production simulations. The approaches used to address these issues, and many more, are presented within this document in the background section and in the chapters detailing the research work. Overall, the work presented here includes the development of the model systems, establishment of the appropriate simulation methods, detailed structural analyses of simulated peptides and solvent, and the comparison of selected FFs based on peptide structural characteristics.

The presentation of this work begins with an overview of the significance and preceding research background, followed by a discussion of the objectives of this work. The completed research work is then presented in three chapters, and each chapter stands alone as it was prepared for publication with introduction, methods, results and discussion, and conclusions sections. Finally, some concluding remarks are provided to summarize the overall project, followed by appendices of additional data supporting the latter two chapters of research work.

CHAPTER TWO

BACKGROUND AND SIGNIFICANCE

Protein Adsorption to Material Surfaces

Immediately following the introduction of a synthetic material (e.g., a medical implant) to a biological environment (e.g., blood, interstitial fluid), soluble proteins begin adhering to the material surface, resulting in the formation of a protein coat that entirely covers the material surface.[1, 2] This phenomenon renders a biologically and chemically inert material surface bioactive. The structural and chemical characteristics of the resulting protein coat are wholly responsible for the cellular response that follows. It is this complex protein film that cells (platelets, neutrophils, monocytes, etc.) encounter when they interact with the material surface. The interaction of cell receptors with certain exposed peptide sequences of adsorbed proteins triggers a series of biochemical reactions within the cell. These cell-protein interactions can lead to the secretion of biological signaling agents within or outside the cell that activate the cell, recruit additional cells to the surface, or initiate other biochemical processes in the body.[3]

The Role of Water in Protein Adsorption

Water is a highly structured liquid, and solvation interactions arise as a result of the structuring of water molecules around solutes and near surfaces. In bulk water, individual water molecules are linked to each other through hydrogen bonds, resulting in the formation of differing degrees of a tetrahedral arrangement. Ice can be maximally tetrahedrally coordinated water with four hydrogen bonds per water molecule in a perfect ice crystal. However, ice typically has an average of 3.7

hydrogen bonds per water molecule. Liquid water has fewer hydrogen bonds per water with an average of 2.7 hydrogen bonds per water molecule.[4] Water's hydrogen bonding network is disrupted in the presence of a solid surface, and the orientation of water molecules near a solid surface plays a key role in protein adsorption due to surface chemistry. In the case of a hydrophilic surface, where the solvent-exposed functional groups of the surface are polar or charged, hydrogen bonding between water molecules and the surface functional groups results in an energetically favorable interaction. For protein adsorption to occur, polar or charged residues on the exterior surface of the protein must displace water molecules from the surface by breaking hydrogen bonds and forming new hydrogen bonds between the surface functional groups and the protein's charged residues, with the surface-bound water molecules being displaced to the bulk solution. Water molecules near hydrophobic (nonpolar, uncharged) surfaces do not form hydrogen bonds with the surface functional groups. Instead, they form a self-assembled structure with its own hydrogen-bonding network.[5] Water molecules near a hydrophobic surface therefore tend to be more ordered than they are in bulk, which results in these water molecules being in a higher free energy state than bulk water. This effect results in a decrease in system free energy when this interfacial water layer is displaced from the surface to the bulk water when a protein adsorbs and represents the fundamental driving force leading to the adsorption of proteins to a nonpolar surface. Therefore, a complete analysis of protein adsorption must include an examination of the orientation of water molecules at the surface-water interface.

Experimental Characterization of Surfaces and Protein Adsorption

The study of the relationship between material surface properties and protein adsorption is widely recognized as being fundamental to future progress in the fields of bioengineering and biomaterials engineering.[2, 6-11] Additionally, protein adsorption on surfaces is of fundamental importance to environmental science,[12] tissue engineering,[13] food processing,[14] biosensors,[15] and bioseparations.[16] Various aspects of protein adsorption have been under study through experimental research for several decades. Also, a very large variety of experimental techniques have been applied to study protein adsorption at solid-liquid interfaces, and several reviews have extensively discussed the applied techniques.[17-20] Unique to the study of protein adsorption on material surfaces is the small mass of the biologically complex protein film combined with its localization at the material surface. This structural arrangement limits the usefulness of most traditional biochemistry methods for characterizing protein films. However, there are different ways to achieve the sensitivity required to characterize the nanoscale structure of surface bound peptides and proteins. One approach is to use techniques that, due to their sampling depths or selection rules, only detect species present in the uppermost surface region. Techniques such as these include x-ray photoelectron spectroscopy (XPS), static time-of-flight secondary ion mass spectrometry (ToF-SIMS), near edge x-ray absorption spectroscopy (NEXAFS), atomic force microscopy (AFM), surface plasmon resonance (SPR), and sum frequency generation spectroscopy (SFG).[21] Each of these techniques presents various strengths and limitations, and together they

have the capability to provide a detailed picture of surface-bound peptides and proteins. However, what remains to be captured by experimental studies that offer only static views of adsorbed surfaces is a step-by-step view of the chemical and physical interactions involved in protein adsorption, presented in a time frame sufficiently small (on the order of the adsorption event, itself) to provide solid mechanistic clues that can serve as a guide to the design of surface chemistries that govern the composition of the adsorbed protein coat.

The Application of Molecular Modeling to Studying Protein Adsorption

In recent years, computer simulation methods have become a very powerful tool for enhancing studies in statistical physics, physical chemistry, biophysics, and engineering. Although the theoretical description of complex systems in the framework of statistical physics is well developed, and the experimental techniques for detailed microscopic information are rather sophisticated, it is often only possible to study specific aspects of those systems in sufficient detail for simulations to be of use. However, simulations need specific input parameters that characterize the system under study, and those input parameters come either from theoretical considerations or are provided by experimental data.[22] Having characterized a physical system in terms of model parameters, simulations are often used both to solve theoretical models beyond certain approximations and to provide a hint to experimentalists for the direction of future investigations. In the case of large experimental facilities it is even often required to prove the potential outcome of an experiment by computer simulations.[23] In that way, it can be said that the field of computer simulations has developed into a very important branch of science, which both

helps theorists and experimentalists to go beyond their inherent limitations and also serves as a scientific field on its own. The traditional simulation methods for chemical and biological systems can be divided into two general classes of stochastic and deterministic simulations. Those classes are largely covered by the Monte Carlo (MC) method and the molecular dynamics (MD) method, respectively.[24] MC simulations probe the configurational space by trial moves of the simulated particles. Within the so-called Metropolis algorithm,[25] the energy change from state n to state n+1 is used as a trigger to accept or reject the new configuration. Paths toward lower energy states are always accepted, whereas paths toward higher energy states are accepted with a probability governed by Boltzmann statistics. In that way, properties of the system can be calculated by averaging over all MC moves. In contrast to MC methods, MD methods are governed by the system's Hamiltonian and classical equations of motion, which are integrated over time to move particles to new positions and to obtain corresponding new velocities at those new positions. This is an advantage of MD simulations with respect to MC since not only is the configurational space probed but the whole phase space which gives additional information about the dynamics of the system is also explored.[23] Both methods are complementary in nature and lead to the same averages of static quantities, assuming that the system under consideration is ergodically sampled (i.e., all regions of a state space are visited with similar frequency and all regions will be revisited given enough time)[26] and that the same statistical ensemble is used for both analyses. Although there are different methods to obtain information about complex systems, particle

simulations always require a model for the interaction between system constituents. This model has to be tested against experimental results. It should reproduce or approximate experimental findings such as distribution functions or phase diagrams, as well as theoretical constraints, such as obeying certain fundamental or limiting laws like energy conservation.[27]

Advanced Conformational Sampling

A major shortcoming of the application of MD simulation to systems involving the behavior of complex molecular structures, such as a peptide or a protein adsorbing on a surface, is that these systems usually exhibit a very rugged potential energy surface.[28] Depending on the particular molecular components simulated, this potential energy surface often has numerous local low-energy wells (troughs on an energy plot) that are separated from one another by relatively high potential energy barriers. A conventional MD simulation of the system will likely become trapped in one of the many local low-energy wells for the entire simulation, thus providing a very limited representation of the correct ensemble-average structure/position of the molecular system. To overcome this limitation of conventional MD simulation, advanced sampling methods can be employed that introduce an artificial driving force into the simulation that enables the system to escape from designated low-energy positions and more fully explore the entire phase space of the system.

Replica exchange molecular dynamics (REMD), also known as parallel tempering, is an advanced sampling method that is being increasingly applied and known as a "conformational sampling tool." REMD commonly utilizes multiple simultaneous

simulations at different temperatures (i.e., temperature levels or replicas), although other governing system properties may be (and have been) used. Initially used in the context of MC sampling, it was extended to molecular dynamics by Sugita and Okamoto[29] as a means of scaling the momenta after a swap of configurations between two simulations at two different temperatures. The decision to swap configurations between two adjacent temperature levels is made by the application of an exchange algorithm that is similar to the Metropolis criterion[25] used in MC sampling.

In an REMD simulation, as configurations move from temperature level to temperature level (replica to replica) by the implementation of a Metropolis-like exchange process, conformational changes (i.e., crossing of potential energy barriers) that are easily possible at higher temperatures will lead to the sampling of new low-energy states that then migrate by exchange into the lower temperature levels, improving the sampling of states found in the low temperature levels. A large number of published studies have confirmed the sampling efficiency of the REMD method.[30] REMD can be used to sample systems whose simulation cost would normally place them completely outside the timescale of MD simulations at the target (low) temperature. REMD also generates a Boltzmann ensemble of conformations with the same potential energy distribution as would be achieved by a conventional MD simulation at the same target temperature given sufficient sampling time. The REMD method has been applied using most of the common macromolecular simulation packages (including AMBER[31] and CHARMM[32]), and it is often

coordinated through an external procedural scripting interface such as Multiscale Modeling Tools for Structural Biology (MMTSB[33]).

Force Fields Used for Molecular Dynamics Simulation

In recent decades, a great deal of research has been conducted to investigate protein folding[34-43] and lipid bilayer membrane behavior[44-48] using force fields and methods that have been specifically designed and validated for these applications.[49-51] Three of the most widely used force fields for molecular dynamics simulations of proteins are the AMBER,[52] CHARMM,[22, 49] and OPLS-AA[53] force fields. Additionally, several studies have been conducted to evaluate and compare their performance for protein simulations.[50, 54] Molecular dynamics simulation has proven to be a powerful tool for the study of proteins and protein-membrane interactions, therefore, it also has enormous potential to be developed for application to the study of protein adsorption to biomaterial surfaces. However, as with protein folding, simulation results with different FFs must be compared with experimental results in order to evaluate the validity of the simulated molecular behavior. This validation process permits an assessment of the strengths and limitations of each force field used.

Model Peptide Structures for Experiment and Simulation

In order to model peptide structures with predictable patterns of behavior, the use of specifically designed model systems is required to efficiently develop both experimental and molecular modeling techniques for characterizing the interactions of peptides and proteins with biomaterial surfaces. These model systems must have well-defined structures. Once the appropriate methodology has been developed with the model

systems, it can then be applied to increasingly complex systems. Examples of this kind of model are peptides composed of alternating patterns of leucine (designated as L) and lysine (designated as K) amino acids (collectively known as "LK peptides"). These peptides provide both a defined and molecularly uniform model system for developing surface analytical approaches to determine protein secondary structure and orientation on biomaterial surfaces. Degrado and Lear[55] have demonstrated that specific secondary structures could be observed in short peptides at the interface between air and water by varying the hydrophobic periodicity in the peptides to match the periodicity of the desired secondary structure. The periodicity of hydrophobic and hydrophilic residues can thus be more important than the helical propensity of a particular amino acid in determining peptide secondary structure at certain interfaces.[56] Thus, the LK peptides are an excellent choice for developing the appropriate molecular modeling methodology for characterizing nanoscale structure and interactions of surface-bound peptides and proteins.

The Use of SAM Surfaces for Studying Protein Adsorption

The well-defined packing and orientation of alkanethiols in self-assembled monolayers (SAMs), as well as the interchangeable functionality of their head groups, provide an excellent structural base for functionalized surface construction for use in MD simulations. In an MD simulation, the atoms of the alkanethiols can be held fixed to keep the packing and orientation of the SAM stable, while the functionalized head group can remain free to move and interact normally with the bulk solution and solutes above it. Basalyga and Latour successfully used this approach in simulations

of charged peptides interacting with a variety of SAM surfaces.[57] In this work, the SAM surface was created based on data from both an experimentally defined structure and previous molecular simulations.[58-65] Using this procedure and structure, the functionality and structure of the SAM surfaces was maintained, and differently functionalized SAMs were created by simply changing the top functional group of the SAM surface.

Previous Simulations of Proteins at Surfaces

Numerous rudimentary molecular simulations of peptide/protein adsorption behavior to synthetic surfaces (and SAM surfaces, in particular) have been conducted over the past two decades, gradually giving way to more advanced simulations.[57-59, 66-78] Generally, molecular simulations of proteins at interfaces have been carried-out at three levels of precision in the forms of colloid-bead, united-residue, and all-atom models. The simplest simulations were based on a colloid model, in which the protein was modeled as a charged sphere[79-81] or as a combination of multiple beads for a large nonspherical protein, such as an antibody.[70] Simulation studies of protein adsorption based on all-atom models were initially performed using Monte Carlo,[82] molecular dynamics,[66] and Brownian dynamics[83] simulation methods, all with solvent described as a continuous dielectric media. However, one simulation study[84] of a small peptide, enkephalin, interacting with a polyethylene surface was conducted in the presence of explicit water molecules. The majority of these colloid-bead studies demonstrated a need for more detailed models of simulated structures in order to describe the events of protein adsorption in a useful way. In the united-residue model, each amino acid residue is represented by one or a few interaction sites.[85-87] This model can be used to predict the native structures of proteins

on the basis of sequence information. Using this model, Dai and coworkers[88] developed an energy-based algorithm to determine the permissible alignments of a protein with respect to the lattice vectors of a surface. Jiang and coworkers[70] have conducted united-residue model MC simulations of antibodies, IgG1 and IgG2a, interacting with amino- and carboxyl-terminated SAMs. For these simulations, a modified version of the CHARMM22 force field was used in conjunction with a new residue-based protein-surface interaction potential model. Using these tools, the effects of surface charge density and solution ionic strength on the orientation of adsorbed antibodies was examined. The simulation results showed that both vdW and electrostatic interactions codetermine the orientation of adsorbed proteins.

All-atom models, though understood to be the superior approach, were not often attempted in a rigorous fashion due to the size of the molecules involved in protein adsorption. Even now, for simulation of all but the smallest functional proteins, it is prohibitive to perform molecular simulation of an all-atom system with explicit solvent molecules near a surface. Tobias and coworkers[66, 69] have conducted all-atom model MD simulations of the adsorption of cytochrome c (a small heme protein) to -CH_3 and -OH functionalized SAMs in vacuum and in the presence of explicit TIP3 water molecules[89] using the CHARMM22 force field (with some parameter modifications). In this work, the protein radius of gyration and eccentricity, the deviation of the protein backbone from the x-ray crystal structure, the orientation of the protein relative to the SAM surface, and the profile structures of the SAM, protein, and water were examined. Overall, these studies demonstrated that the all-

atom CHARMM22 force field provides an excellent representation of the SAM structure,[69, 71] with the resulting adsorbed protein behavior being in general agreement with available experimental data.

In 2005, Latour and coworkers[59, 78] reported results from 5 ns MD simulations of a 30 kDa fragment of fibrinogen interacting with -CH_3, -OH, -NH_2, -COOH, and oligoethylene glycol-functionalized SAM surfaces using the GROMACS[90] molecular dynamics simulation package. The protein's behavior was characterized in terms of RMSD, changes in solvent-accessible surface area, surface separation distance, planar and rotational motion. An important protein adsorption concept introduced by this work was that the orientation of proteins on a surface can be manipulated independently from protein conformational changes, which provides two time-separable mechanisms for controlling adsorbed protein bioactivity through manipulation of surface chemistry. Also in 2005, Latour and coworkers[59] reported results from 10 ns simulations of a variable residue peptide adsorption model for determination of individual residue contributions to adsorption free energy. These simulations identified limitations in transferability of this force field to systems with solid surfaces with its united-atom representation of the alkane chains of the SAM. This resulted in unrealistic chain separation and subsequent peptide adsorption behavior on hydroxyl-functionalized SAM surfaces, as compared to experimental work conducted by Vernekar and Latour.[91] Another investigation into simulation of protein adsorption completed by Latour and coworkers[92] established the importance of initial positioning of proteins or peptides near surfaces for simulation by calculating orientation-dependent adsorption free energies between proteins and

functionalized surfaces. However, all of these simulations have involved very limited conformational sampling of the adsorbed protein structure (due to the inherent limitations of MD), thus emphasizing the need for enhanced sampling methods for these types of simulations.

CHAPTER THREE

OBJECTIVES

The long-term, overall objective of this multidisciplinary project is to develop surface analytical techniques for characterizing the nanoscale structure, orientation, and dynamics of peptides and proteins as they adsorb to nanoparticle and other solid surfaces. To accomplish this, complementary experimental and computational approaches have been developed to determine protein secondary and tertiary structures, identify side-chain interactions with surfaces, and to characterize the role of water in mediating protein-surface interactions. The resulting coordinated bioanalytical and computational suite of nanoscience-based tools have the potential to provide the molecular information necessary for the design and characterization of bioactive nanomaterials, biofunctionalized nanoparticles, and nanostructured biomaterials. For example, the function of proteins such as antibodies on nanoparticles is dependent on having the recognition domain accessible after immobilization. The bioactivity of nanostructured surfaces will also depend on the orientation of adsorbed proteins. This critical molecular information has previously not available for the nanotechnology field, and this project will develop fundamental capabilities that can be exported widely. To serve as a starting point for this project, a model system of designed peptides that fold into defined secondary structures on surfaces functionalized with self-assembled alkanethiolates has been studied in order to begin developing the suite of analytical tools for nanoscale structure determination. The work presented here comprises the computational portion of this complementary experimental and computational approach. The experimental portion

of this project has been conducted by Prof. David Castner's research group at University of Washington.

The goal of the computational research presented here was to develop the appropriate simulation methods and to evaluate the applicability of existing empirical all-atom MD force fields (FFs) to simulated systems that include a solid surface. This was accomplished through a series of pilot studies and through a comparison of three widely used molecular dynamics force fields in simulating adsorption of structured peptides to both charged and hydrophobic self-assembled monolayer (SAM) surfaces. The assessment of the performance of the MD force fields used was based on a comparison of simulation results with experimental results, which included studies of peptide orientation, conformation, interactions with SAM surfaces, and water structure over those surfaces. The specific aims of this work were as follows.

Aim 1. Construction of molecular models for the same peptide-surface systems used for the experimental portion of this project. These systems include models of the structured peptides, models of the functionalized SAM surfaces, explicit water models, and ion concentrations sufficient for neutralization of the systems and emulation of a physiological saline environment.

Aim 2. Molecular dynamics simulations using the replica-exchange molecular dynamics (REMD) technique will be performed using each of the CHARMM, AMBER, and OPLS-AA force fields. These simulations were to be continued until the structural characteristics being examined have stabilized sufficiently to be interpreted as convergence of the REMD simulation.

Aim 3. The results from the REMD simulations conducted under Aim 2 were to be analyzed to characterize the predicted behavior of each peptide-surface system. Data analysis for the peptide structures should include Ramachandran plots generated from the trajectory data for each peptide-surface and solvated peptide system. Separation distances between the amino acid residues of each peptide and each surface should also be examined. Data analysis for the water structure proximal to the surfaces should be examined in terms of diffusion characteristics and population analysis of dipole orientations. These results must be compared to experimental results to assess the accuracy of the applied simulation methods and to allow visualization of the theoretical molecular behavior of these peptides at the solid-liquid interface.

CHAPTER FOUR

METHODS ASSESSMENT FOR THE CALCULATION OF ELECTROSTATIC EFFECTS

Published as Collier G, Vellore NA, Stuart SJ, Latour RA. Development of molecular simulation methods to accurately represent protein-surface interactions: Method assessment for the calculation of electrostatic effects. Biointerphases 2009;4(4):57-64.

Introduction

The surfaces of synthetic biomaterials placed in contact with fluids containing soluble proteins become coated with adsorbed proteins in a matter of seconds, and it is this protein layer that is largely responsible for the reaction that living cells have to the presence of such materials. Generally, cells do not contact the implanted biomaterials directly. Instead, various cell receptor-protein binding events allow cells to interrogate the molecular structure of the exposed portions of the adsorbed proteins, leading to intracellular signaling processes and subsequent cellular responses. The exposed portions of the adsorbed proteins may not necessarily be the same as those found on the exterior of their native conformations. In the process of adsorbing to a biomaterial surface, proteins may undergo significant structural changes[93] that can result in the presentation of exposed or otherwise buried bioactive sites to the cellular environment. Overall, it is the particular conformation and orientation of the adsorbed proteins that govern the way in which cells react to a protein-coated surface. Thus, in order to control the cellular response to a biomaterial, the type of bioactive sites presented by the adsorbed layer of proteins must be controlled through strategic materials design.

The importance of examining protein adsorption mechanisms in determining the biocompatibility of implanted materials has been well established, but a means of

studying these mechanisms at a resolution sufficient to guide materials design has yet to be developed. Numerous experimental techniques have been used to explore protein conformations on a surface, but these analyses are generally unable to capture the critical mechanistic details underlying protein adsorption processes at the level that is needed for surface chemistry design to control protein adsorption behavior. Atomic-scale molecular simulation (e.g., all-atom empirical force field methods), coupled with experimental techniques for validation, have the potential to overcome this limitation by providing the ability to predict protein adsorption processes at an atomistic level. However, before this potential can be realized, molecular simulation methods must be carefully evaluated and adapted for this specific type of application. The issues to be addressed are not only those regarding the parameterization of the atomic interactions between a protein, a surface, and the surrounding aqueous solution, but also those associated with the general mathematical treatment of these interactions as well.[28] In this chapter, I address the issue of whether using three-dimensional (3-D) periodicity and the conventional 3-D implementation of the particle-mesh Ewald (PME) summation method for long-range electrostatics results in nonphysical effects due to the image of the charged surface over the top of the primary simulation cell.

In a molecular simulation, nonbonded interactions involve an accounting for van der Waals (vdW) interactions, which are short-range interactions that diminish as r^{-6}, with the distance r between atoms, and electrostatic effects, which are long-range interactions that diminish as a function of r^{-1}. Because of their short-range nature, vdW interactions are effectively addressed using cutoff methods wherein the vdW attraction between

atoms separated by more than a defined distance is neglected without introducing substantial artifacts into the system. Cutoff methods, however, are generally not recommended for use for the calculation of long range electrostatic effects because of the risk of introducing substantial nonphysical effects[94-97] which result from both the abrupt termination of pairwise interactions in the vicinity of the cutoff and the neglect of longer-range electrostatic interactions. While calculation schemes that use smoothing functions have been shown to significantly reduce the presence of nonphysical effects due to the use of abrupt cutoffs,[98] the neglect of long-range interactions is still a serious concern.

Today, the standard method that is recommended to account for long-range electrostatic interactions for protein folding simulations using empirical force field methods is particle mesh Ewald (PME).[99] The PME method is one of several variants of Ewald summation, in which contributions to the total energy are decomposed into a short-ranged component that is evaluated in real-space, and a long-ranged component, including the interaction with the periodic images, which is summed in Fourier space. These two series converge more rapidly than would be the case if the electrostatic interactions were summed directly. This is the most thoroughly validated and widely used method for computing electrostatic interaction energies for 3-D periodic systems. The use of PME thus provides a means to overcome the generation of nonphysical effects resulting from the use of cutoffs with a relatively minor increase in computational cost. This characteristic makes PME an excellent candidate for the calculation of long-range electrostatic interactions for highly charged systems, such as those containing proteins, peptides, or DNA in explicit water.[100, 101]

While PME with 3-D periodic boundary conditions is the most commonly used method for the treatment of nonbonded interactions for protein folding simulations, it may not be appropriate for the simulation of protein adsorption to a surface. Although periodic replication of the surface is realistic in the plane of the surface, there are concerns that the periodic images of this surface represented above and below the primary unit cell system may introduce nonphysical effects on the adsorption behavior, particularly in cases where the surface is charged or dipolar. Molecular dynamics simulations of systems such as these with slab geometry (i.e., 3-D systems with 2-D periodicity) are widely accepted as a means of simulating interfacial systems. However, the use of Ewald summation for handling the electrostatics of a system with slab geometry often requires modifications to the mathematical approach underlying the Ewald method.[102-107] An alternative approach for handling 2-D periodicity for a 3-D Ewald system may also be implemented by the construction of the primary simulation cell with structural features that serve to effectively reduce problematic electrostatic interactions from the periodicity in the third dimension to a negligible level. An example of this type of construction is the use of a fixed layer of explicitly represented bulk solvent at the top of the simulation cell to serve as a barrier between the mobile solution phase and the imaged bottom layer of the solid surface phase of the system. This model design serves the dual purpose of providing a boundary at the top of the simulation cell that more closely approximates bulk solution conditions than the imaged bottom layer of the adsorbent surface and additional separation distance between the mobile molecules in the primary simulation cell and the periodic image of the charged surface that is

represented above the primary cell. Using this type of alternative approach, the objective of this work was to evaluate PME and alternative electrostatic methods (e.g., cutoffs) as implemented in the CHARMM suite of simulation tools[32] and parameter libraries[108] to determine if such nonphysical effects occur, and the extent to which they occur, using a relatively simple but sensitive model system involving the distribution of Na^+ and Cl^- ions in 150 mM NaCl aqueous solution over a negatively charged surface with a layer of fixed bulk saline solution at the top of the simulation cell.

Before conducting our molecular dynamics simulations, we first performed an analytical calculation to theoretically predict the ion concentration profile in a 150 mM monovalent salt solution placed between two negatively charged surfaces separated by a designated distance using the Poisson-Boltzmann equation (P-B). In this analytical model, one surface serves to represent the charged surface in the primary unit cell of a molecular dynamics simulation of saline solution over a charged interface and the opposite surface represents the first periodic image above the primary unit cell system that would be represented when 3-D periodic boundary conditions are used. These calculations serve as a basis to demonstrate the possible nonphysical effects that may occur when using the PME method to represent the behavior of charged solutes over a charged surface in a molecular simulation. The obvious limitations of the Poisson-Boltzmann approach,[109] such as the neglect of van der Waals interactions, the treatment of atoms as point charges, and the use of a solute dielectric that does not account for arrangements of polar and charged groups in an external electric field, prevent direct comparison between the analytical and simulation results. Thus it must be recognized

that these analytical results only serve to provide a means of graphically illustrating the type of nonphysical effects that may occur in a simulation of this type of system when using 3-D periodic boundary conditions. To determine if similar types of nonphysical effects resulted from the use of the PME method, and if the use of cutoffs instead of PME may prevent these effects from occurring, we then conducted molecular dynamics simulations of this same type of system using both PME and cutoff methods for the calculation of electrostatic effects.

Our model system for our molecular dynamics simulations comprised a 150 mM NaCl aqueous solution with explicitly represented water molecules and Na^+ and Cl^- ions over a 50% deprotonated COOH-SAM surface (pK_d = 7.4 [110]) neutralized by additional Na^+ counter-ions. Nanosecond-scale molecular dynamics simulations were conducted to investigate the effect of the electrostatic method used upon the resulting concentration profiles of the ions in solution over the charged surface using PME and a range of radial cutoff distances. Because the distributions of the ions in solution are strongly influenced by how the electrostatic interactions are calculated during the MD simulation, comparisons between the resulting ion concentration profiles achieved using each method enable conclusions to be drawn regarding the appropriateness of the use of these different methods for the simulation of solute adsorption to a charged surface.

Materials and Methods

Analytical Study of Ion Distribution Between Two Negatively Charged Surfaces

In this section we present the analytical approach used to theoretically calculate the ion distribution over a COOH-SAM surface based on the Poisson-Boltzmann equation.

The developed equations are then applied to predict this distribution, to simply demonstrate (rather than actually model) the types of nonphysical effects that may possibly result from the use of 3-D periodic boundary conditions for a 2-D periodic system, and to provide a basis for the assessment of subsequent molecular dynamics simulation results.

To calculate the ion distribution between a pair of negatively charged COOH-SAM surfaces (i.e., representing a charged surface in a simulation and the first periodic image above it), we first need an analytical expression for the ion concentration distribution of sodium and chloride ions over a charged surface as a function of the ion concentration in bulk solution and the electrostatic potential of the SAM surface. The expression for the molar concentration of each ion type *i* (C_i) as a function of the perpendicular distance from the surface plane, *x*, can be derived based on the thermodynamic principle that at equilibrium the chemical potential of each ion type must be independent of position.[111, 112] This is also true at large distances from the surface, where the concentration reaches a bulk value and the electrostatic potential approaches zero. This relationship can thus be expressed as:

$$\mu_i(x) = \mu_i^o + z_i e\Psi(x) + k_B T \ln\{a_i(x)\} = \mu_i^o + k_B T \ln\{a_i^b\}. \qquad (1)$$

where μ_i(x), μ_i^o, and $a_i(x)$ are the chemical potential, the standard state chemical potential, and the activity of ion species *i* at position *x*; z_i is the charge on ion *i*; *e* is the absolute value of the charge of an electron (1.602 x 10^{-19} C); $\Psi(x)$ is the electrostatic potential at position *x*; k_B is Boltzmann's constant; *T* is the absolute temperature; and a_i^b is the activity of ion species *i* in bulk solution where $\Psi = 0$. Writing the activity as $a_i(x)$ =

$\gamma_i(x)\ C_i(x)/C_i^o$, where $C_i(x)$, C_i^o, and γ_i are the solution concentration, the standard state solution concentration (1.0 M), and the activity coefficient, respectively, of ion species *i* at position *x*, and assuming ideal conditions with $\gamma_i(x) = 1.0$, allows us to write:

$$C_i(x) = C_i^b \exp\{-z_i e\Psi(x)/k_B T\} \qquad (2)$$

Accordingly, by equation 2, the concentration of an ion at a distance *x* from a charged surface is exponentially related to the electrostatic potential at that distance above the surface.

To calculate the electrostatic potential of a COOH-SAM surface, we refer to a previous set of experimental studies conducted by our group in which we measured the pK_a of this type of surface to be 7.4 using surface plasmon resonance spectroscopy.[110] Based on this value, at a physiological solution pH of 7.4 the COOH groups on the COOH-SAM surface will be 50% deprotonated. Given that an individual alkane chain in an alkanethiol SAM surface on a gold substrate occupies a surface area of 21.4 $Å^2$,[113] this provides a surface charge density of $\sigma = -0.2336\ e/Å^2$. The relationship between the electrostatic potential at the surface, $\Psi(0)$, and the surface charge density (σ) is expressed by the Grahame equation[110, 111] as:

$$\Psi(0) = \frac{2k_B T}{e} \sinh^{-1}\left\{\frac{\sigma}{8\varepsilon\varepsilon_o k_B T C_{salt}^b}\right\} \qquad (3)$$

where ε and ε_o are the relative permittivity of water (78.5 at 298 K) and the permittivity of free space ($8.854 \times 10^{-12}\ C^2/J/m$), respectively, and C^b_{salt} is the concentration of the salt in the bulk solution.

Based on the Grahame equation, the Poisson-Boltzmann equation can be solved[110, 111] to express $\Psi(x)$ as:

$$\Psi(x) = \frac{2k_B T}{e} \ln\left\{\frac{1+\varphi\cdot\exp(-\kappa x)}{1-\varphi\cdot\exp(-\kappa x)}\right\} \qquad (4)$$

where $\varphi = \tanh\left\{\frac{e\cdot\Psi(0)}{4k_B T}\right\}$ and $\kappa = \left(2C^b_{salt}\, e^2 / \varepsilon\varepsilon_o k_B T\right)^{1/2}$, with κ being the inverse Debye length.

The relationship for $\Psi(x)$ expressed in equation (4) can now be used in equation (2) to express the concentration profiles of the cations and anions in solution as a function of x:

$$C_i(x) = C_i^b \exp\{-z_i e\Psi(x)/k_B T\} = C_i^b \exp\left\{-2z_i \ln\left(\frac{1+\varphi\cdot\exp(-\kappa x)}{1-\varphi\cdot\exp(-\kappa x)}\right)\right\} \qquad (5)$$

$$= C_i^b\left(\frac{1+\varphi\cdot\exp(-\kappa x)}{1-\varphi\cdot\exp(-\kappa x)}\right)^{-2z}$$

Finally, the resulting concentration profiles from equation (5) can be integrated over a range of distances from the COOH-SAM surface to calculate the number of ions contained in designated layers of solvent, or bins, ($N_j(x)$), for comparison to the molecular simulation results by equation (6):

$$N_j(x) = \int_{x_j}^{x_j+1} C_i(x) A_s dx \qquad (6)$$

where A_s represents the area of the COOH-SAM surface in the model system, which was set to be 45 × 43 Å^2 (about 90 SAM chains) to match the conditions that were used in the molecular dynamics simulations. In these calculations, the distance between the pair of parallel charged surfaces was set to 100 Å, which is large enough that the ion

concentration in the mid-plane between the two charged surfaces is able to represent bulk solution conditions (i.e., 150 mM NaCl).

The resulting distributions for Na^+ and Cl^- ions in aqueous solution between the two charged surfaces, as expressed by equation 6, are presented in Figure 1.1. As shown, the presence of each of the charged surfaces results in the formation of an electrical double layer with substantially increased concentration of counter-ions and reduced concentration of the co-ions adjacent to each surface.

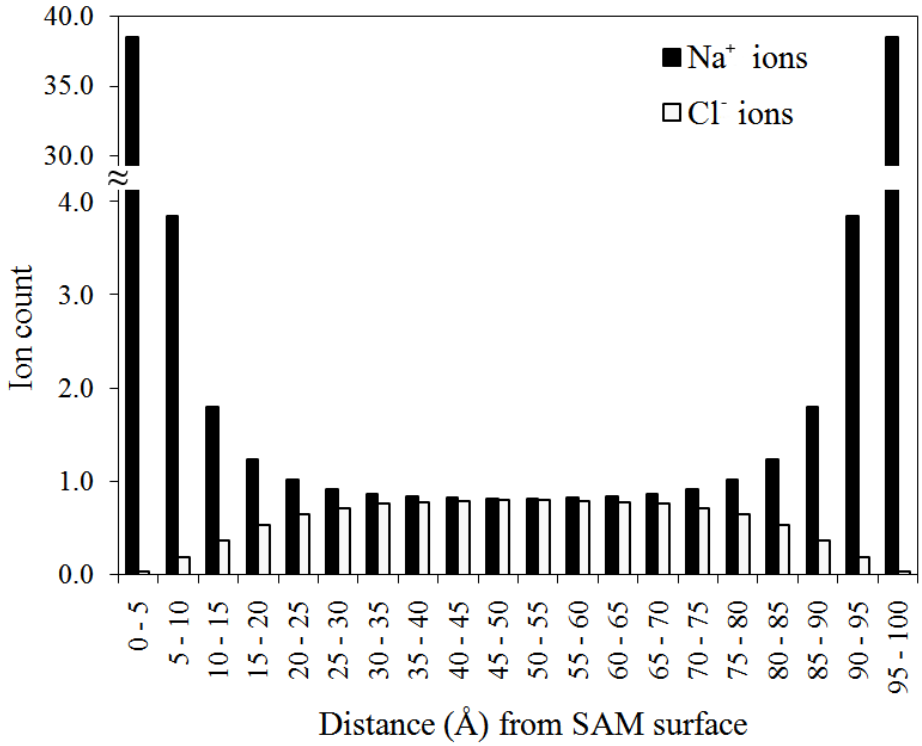

Figure 4.1: Plot of Na^+ and Cl^- ion distributions calculated based on the analytical model. The Na^+ ion population in both the 0-5 Å and 95-100 Å regions (the regions closest to the charged surfaces) were calculated to be 38.4 ions.

Among the significant features of this distribution is the population of Na^+ counter-ions in the first 5.0 Å layer over each of the negatively-charged surfaces, where the

number of Na^+ ions (38 of them) nearly completely neutralizes the surface charges (45 COO^- groups). In contrast to this, the Cl^- co-ions are almost absent in these first solvent layers adjacent to each surface. These ion concentrations steadily decay towards the bulk concentration with increasing distance from each surface, with ion concentrations effectively approaching bulk solution conditions within approximately 25 Å from each surface. These results thus theoretically indicate that surfaces with this charge density must be spaced at least 50 Å apart (whether as distinct surfaces or images under periodic boundary conditions) to approach bulk-like solution conditions in the mid-plane of the system.

Molecular Simulation to Determine the Ion Distribution Over a Charged Surface

The design of our simulated model system was guided by a variety of concerns related to the proper representation of long-range electrostatic interactions. As illustrated by the ion distribution generated from the analytical model, if we constructed the molecular model of an adsorbent surface as a single layer of charged groups with an overlying solution phase, we would expect periodic boundary conditions to cause nonphysical effects with a large counter-ion concentration gradient developing not only at the bottom of the solution phase (i.e, over the top of the charged surface), but also at the top of the solution phase due to the interactions of the counter-ions in solution with the periodic image of the charged surface that would be represented above the unit cell system. Additional nonphysical effects would then also be caused from the interactions between the two layers of counter-ions concentrated on either side of the charged surface,

thus not only resulting in nonphysical effects in the ion concentration distribution in the solution phase below the charged surface, but above it as well.

These effects could be prevented by constructing the molecular model of the system such that the top of the solution phase of the system was separated from the bottom of the charged surface in the periodic image above and then using a cutoff method for the calculation of electrostatic effects, with the electrostatics cutoff set to truncate interactions within this separation distance. However, it is not obvious whether or not this same strategy would prevent similar nonphysical effects from occurring when using PME, in which case the long-range range electrostatic effects from the surrounding periodic cells may still influence the system in some nonphysical manner. Based on these concerns, we proceeded with modeling this system, but with the model constructed to provide about 25 Å of distance separating the top of the mobile solution phase with the image of the charged surface that would be represented above the unit cell system when periodic boundary conditions were applied.

More specifically, our model system was comprised of an orthorhombic layer of mobile water molecules and ions (termed the "mobile core") bounded above and below in the *x* dimension (normal to the surface plane) by layers of fixed atoms. The mobile core of this model system was comprised of a 45 × 43 × 100 $Å^3$ volume containing 6,418 TIP3[114] water molecules with 17 Na^+ and 17 Cl^- ions, sufficient to provide a 150 mM NaCl aqueous solution. The adsorbent surface, which was modeled below the mobile core of the aqueous solution, was represented as a 10 Å thick, 50% deprotonated (pK_d = 7.4) COOH-functionalized alkanethiol self-assembled monolayer (SAM) surface with 45

negatively charged -COO^- terminal groups. 45 additional Na^+ counter-ions were included in the mobile core for neutralization of the surface charges. All atoms of the 90 alkyl chains were held fixed in position except for the terminal functional group atoms. The top COOH functional groups of each SAM chain thus remained free to move during the simulations. The basis for the specific design of this surface is a combination of experimentally defined structure and previous molecular simulations conducted by our group.[115]

As noted above, the ion distribution of the analytical model demonstrated the need for special handling of the mobile core water molecules and ions in proximity to the periodic image of the charged surface. In the analytical model, the effect of the charged surface on the ion distribution was attenuated to approximate bulk conditions within a distance of about 25 Å. Therefore, a similar separation distance between the top of the mobile core and the periodic image of the charged surface was deemed necessary. For this reason, in addition to the separation provided by the thickness of the SAM surface, we included a 15 Å thick fixed bulk water layer at the top of the mobile core. This fixed bulk water layer represented a 150 mM NaCl aqueous solution layer comprised of 2 Na^+ and 2 Cl^- ions within TIP3 water. All atoms of this layer were held fixed during the production simulations so that the free water molecules of the mobile core could interface with a bulk water-like surface instead of the periodic image of the hydrophobic bottom surface of the SAM's alkyl chains. Prior to being held fixed during the production simulations, the fixed upper water layer, like the mobile water core, was equilibrated at 298 K and 1.0 atm. The ions in the mobile core were then randomly distributed in the water, held fixed

for 100 ps of equilibration, and then all constraints were removed for an additional 500 ps of equilibration. During these procedures, the fixed bulk water layer and the charged SAM surface were moved into position above and below the mobile core, respectively, and the positions of these layers were adjusted through repeated 500 ps equilibration runs until the boundaries at the top and bottom of the mobile core moved by less than 0.1 Å in response to the presence of the inserted SAM and fixed bulk water layers. This procedure ensured that the simulated pressure inside the mobile core was maintained as closely as possible to its equilibrated pressure of 1.0 atm.

The completed model system, which is shown in Figure 1.2, was used as a starting structure for several different MD simulations, each of which employed a different method for calculating electrostatic interactions.

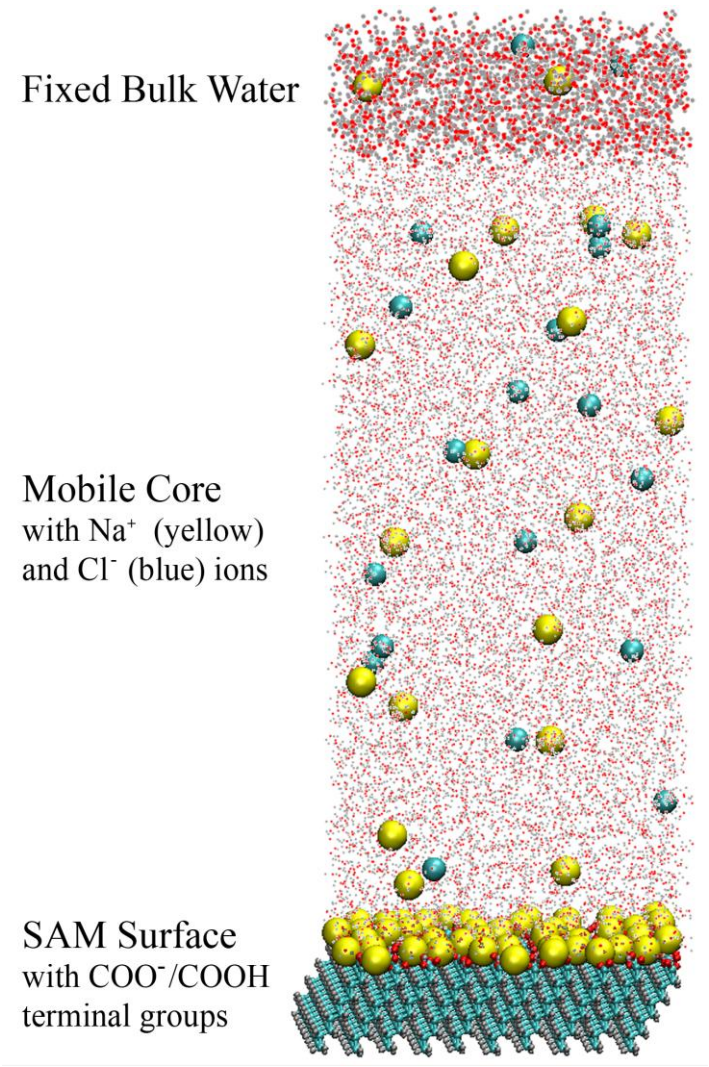

Figure 4.2: Diagram of the simulated system.

The CHARMM (version c32b2) suite of simulation tools[32] and parameter libraries (version 27),[108] compiled and run on Intel architecture CPUs using Intel compilers (version 9.1), was used for the construction of our model system and for performing molecular dynamics simulations. All systems were simulated under 3-D periodic boundary conditions using the explicit-image model. The methods used for handling nonbonded interactions included PME and radial cutoffs of 10, 14, and 16 Å.

Parameterization of the PME simulations[116] included truncation of the real-space summation at 12 Å, a value of 0.34 $Å^{-1}$ for the Ewald method's Gaussian distribution inverse width, and a distance cutoff of 14 Å for generating the pair list. The simulations using radial cutoffs were parameterized so that nonbonded interactions were truncated with a smoothing function set to begin at 2 Å inside of each radial cutoff, accompanied by a pair list cutoff 2 Å beyond each radial cutoff. The smoothing function used for all truncations was a force-based switching function.[117] Van der Waals interactions were also truncated using a force-based switching function. All simulations were conducted in the canonical (NVT) ensemble using the VV2 integrator (an implementation of the velocity Verlet algorithm[118]). The Nosé-Hoover method[119] was used for temperature control, with a target temperature of 298 K and a thermostat time constant of 0.1 ps. Bond lengths involving hydrogens were held fixed using the SHAKE algorithm,[120] which enabled a 2.0 fs time step to be taken during the MD simulations. Simulations were first conducted to enable the initially randomized ion distribution within the mobile core to fully re-equilibrate with respect to the charged surface, resulting in a higher concentration of Na^+ counter-ions near the SAM surface due to the presence of numerous carboxylate groups at this surface. For all seven systems, this final equilibration process required a dynamics period of approximately 6 ns before the ion concentration distributions finally stabilized, with minor differences in equilibration time amongst the various electrostatic methods (± 1 ns). Following this final equilibration stage, a production dynamics period of 4 ns was conducted and used for the analysis of the concentration profiles of the Na^+ and Cl^- ions over the surface, with the mobile solution phase binned into individual 5.0 Å

layers beginning at the interface between the mobile water and the top of the SAM surface.

Both Na^+ and Cl^- ion populations present in each 5.0 Å layer of the mobile water box were monitored as they fluctuated during the production molecular dynamics simulations. Population data were recorded every 2.0 ps during the simulations. The resulting ion population data were used to evaluate the performance of each of the electrostatics calculation methods. These results were compared to one another, and to the analytical solution of the ion distribution based on the Poisson-Boltzmann equation. Additionally, the resulting ion distributions were analyzed for indications of nonphysical effects resulting from the use of cutoffs or periodicity.

Results and Discussion

In order to evaluate possible nonphysical effects from the use of the PME method with 3-D periodic boundary for the simulation of solute-surface interactions, a set of molecular dynamics simulations were conducted using PME and a series of cutoff methods for the representation of electrostatic interactions, each resulting in the generation of 4 ns of production data following 6 ns of system equilibration. This enables comparison amongst the different electrostatic methods, as well as with the analytical distribution obtained from the Poisson-Boltzmann equation.

The production trajectories for each system were first analyzed by evaluating the time autocorrelation functions[121] of the ion populations in each 5.0 Å bin to determine the time required for the average ion population value within a given layer of the mobile solution phase to become sufficiently uncorrelated to serve as an independent sample. As shown

for the autocorrelation plots for PME (Figure 4.3), these correlation times are longer for the ion populations near the fixed segments of the molecular system (i.e., the 0–5 Å and 95–100 Å bins), indicating that the dynamics is slowed in the vicinity of the SAM surface and the fixed bulk water layer.

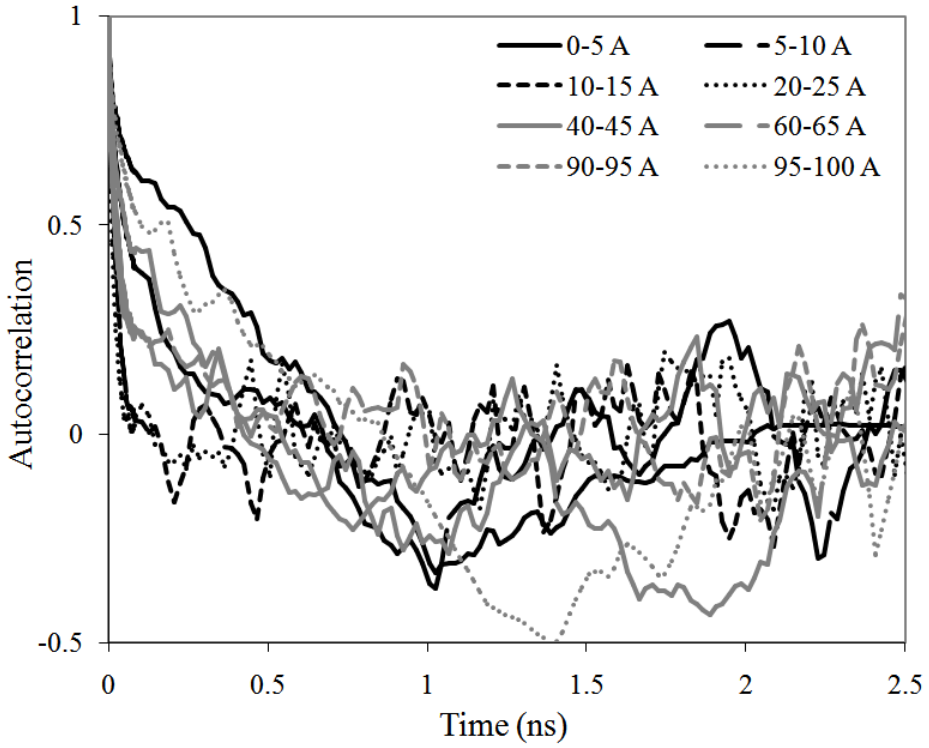

Figure 4.3: Plot of autocorrelation results for the Na^+ ion distribution calculated using the PME method.

The autocorrelation results for each electrostatic method indicated that 400 ps was sufficient time for the ion concentration in each bin to become substantially uncorrelated with the previous time period for even the slowest moving regions in each system. Accordingly, the trajectory data for each 4.0 ns production run was divided into 400 ps blocks, thus providing ten independent samples of the average ion population in each bin for each simulation. These block averages were then used to generate a mean and 95%

confidence interval for the ion count in each layer of solution above the SAM surface. The results of these analyses are plotted in Figure 4.4 (Na^+ ions) and Figure 4.5 (Cl^- ions) for each electrostatic method in comparison with the analytical solution results.

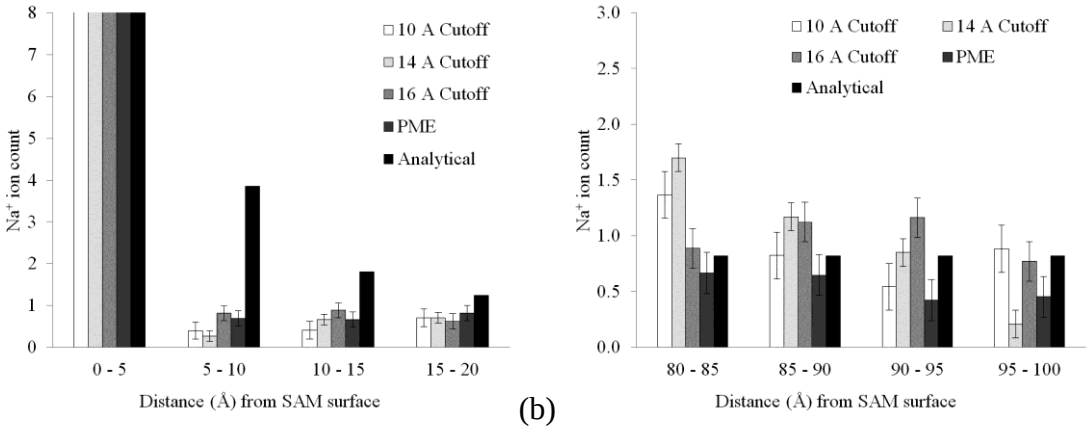

(a) (b)

Figure 4.4: Plots of Na^+ ion distributions for radial cutoffs, PME, and the analytical model for each of the 5 Å layers (a) within 20 Å of the charged surface or (b) within 20 Å of the fixed bulk water layer, 100 Å from the charged surface in the central unit cell. In plot (b), the analytical model values represent what the ion distribution would be if bulk-solution conditions were obtained.

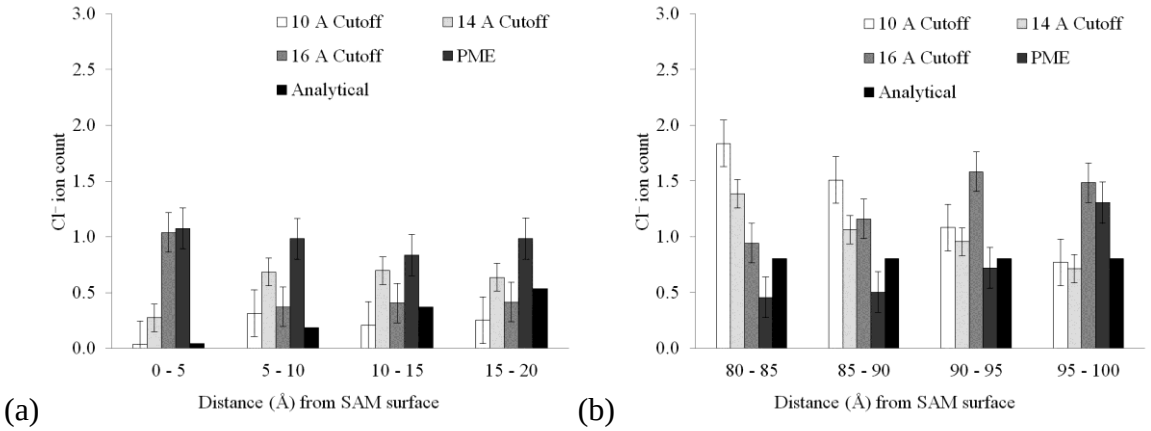

Figure 4.5: Plots of Cl^- ion distributions for radial cutoffs, PME, and the analytical model for each of the 5 Å layers (a) within 20 Å of the charged surface or (b) within 20 Å of the fixed bulk water layer, 100 Å from the charged surface in the central unit cell. In plot (b), the analytical model values represent what the ion distribution would be if bulk-solution conditions were obtained.

The ion distributions presented in Figure 4.4 show several important results. First of all, for each electrostatic method considered, the ion concentration profiles decayed to bulk solution conditions much more rapidly near the SAM surface than predicted by the analytical model. The simulation results show a substantially higher counter-ion concentrations in the first 5 Å from the surface compared to the analytical model, with these ion concentration profiles generally transitioning to bulk solution conditions within 10 Å from the surface. The co-ion concentrations are likewise higher than predicted, and decay more rapidly to bulk conditions. Similar trends have been reported in an early study comparing Monte Carlo simulations to Poisson-Boltzmann equation predictions of ion distributions between two charged surfaces.[111, 122] We attribute these differences to both the finite-size effects that are present in the molecular simulation and absent from the continuum analytical model, as well as the fact that the continuum model does not

take into account van der Waals interactions between the atoms in solution and the surface. It is also possible that these differences may reflect errors in the CHARMM force field for this type of system with the counter-ions being too strongly attracted to the carboxylate groups on the surface compared to the TIP3 water molecules. Similar types of imbalances in force field parameterization have been identified in other studies.[123] This is a major concern for the simulation of protein adsorption behavior over charged surfaces, which can be expected to be dominated by nonbonded electrostatic interactions, and may require force field adjustment for the accurate simulation of protein adsorption behavior on negatively charged surfaces. Further studies are needed to evaluate this possibility. The results shown in Figure 4.4 also show that while the PME method of accounting for electrostatic effects provides ion concentration profiles that differ significantly from each of the cutoff methods, particularly for the 5 Å of solution closest to the interface, PME typically agrees more closely with the populations obtained with longer cutoffs than those obtained with shorter cutoffs, in cases where the differences are statistically significant. Furthermore, the ion concentrations determined for each electrostatics method are generally comparable, with relatively minor differences in the predicted values between each method.

Most importantly for the purposes of this study, it is clear from the ion distributions presented in Figures 4.4 and 4.5 that the use of PME for treating long-range electrostatics in the presence of a charged surface in the manner implemented in our molecular dynamics simulations does not produce ion concentration effects at the top of the mobile core of the solution phase of the system due to the presence of a periodic image of the

charged surface represented above the primary simulation cell of the system. This is apparent from the fact that the Na^+ ion distributions obtained using PME method are not substantially different from the distributions provided by cutoff methods in the 5 Å layers of the mobile core of water closest to the rigid water layer. Because all of the cutoffs are shorter than the 25 Å thickness of the fixed water and SAM layers, these model systems include no direct interaction between mobile waters and the periodic image of the charged layer of carboxylate groups. Even for the PME system, however, it is apparent that the structure of the mobile ions was not affected by the images of the COOH surface. The adsorbed Na^+ layer effectively neutralizes the charge density at the interface. The presence of these adsorbed counter-ions, in addition to the 10 Å SAM and 15 Å of rigid water, screens the electrostatic interaction sufficiently to prevent the formation of a second double layer at distances far from the surface in the primary unit cell, and bulk solution conditions are thus maintained in this region of the system.

Conclusions

Overall, the comparison amongst the different ion distributions that result from varying treatments of the electrostatic interactions shows that PME does not result in the production of detectable nonphysical effects due to 3-D periodic boundary conditions for the case where there is sufficient distance between the imaged surface charges and the free ions in solution in the central unit cell. Based on the structure of the simulated system used here, a separation distance of 25 Å between the free ions in TIP3 water in the central unit cell and the image of the charged surface is sufficient to screen the electrostatic interactions between these components such that bulk solution conditions are

maintained at the top of the simulation cell. This finding is further supported by the fact that the ion distributions resulting from the use of radial cutoffs, which include no direct interactions with images of charged functional groups, are not substantially different from the distribution resulting from the use of PME, especially for longer cutoffs. However, the ion distributions resulting from both the PME and the radial cutoff methods do show much stronger attraction of the Na^+ counter-ions to the negatively charged surface than suggested by the analytical model, possibly indicating that the force field parameters governing these interactions may require adjustment so that the simulation of interfacial systems in aqueous solution containing these type of ions (e.g., the simulation of peptide and protein adsorption behavior in physiological saline), can be accurately modeled.

CHAPTER FIVE

MOLECULAR DYNAMICS SIMULATION OF STRUCTURED PEPTIDE ADSORPTION TO FUNCTIONALIZED SELF-ASSEMBLED MONOLAYER SURFACES

Introduction

Nearly all physiological environments consist of fluids containing soluble proteins. When synthetic materials are introduced into such environments, those materials very rapidly become coated with adsorbed proteins. The result of this rapid adsorption of soluble proteins is the formation of a highly complex protein layer, composed of proteins with a diverse range of non-native conformations and orientations[93] that are governed by the chemical and physical properties of the material surface.[124] Because of this phenomenon, cells do not actually come in contact with the material itself, but rather they contact only the adsorbed protein layer, with cellular response thus mediated by the bioactive sites presented by these proteins. For this reason, strategic material surface design is one of the most effective means of controlling cellular response to implanted materials. However, despite decades of experimental studies[11, 17-20, 125] and recent pioneering simulation work,[57-59, 66-78, 92, 126] the detailed chemical mechanisms of protein adsorption are still not well understood. This lack of understanding stems from the fact that protein adsorption is a complex, dynamic process that takes place at the atomic scale where experimental analyses are limited to a view that is essentially static compared to atomistic timescales and often too coarse for revealing the processes that control protein adsorption behavior. The limited mechanistic clarity of protein adsorption processes serves as an impediment to progress in material engineering and interfacial sciences for

applications involving contact between materials and biological environments. In order for these fields to move forward for the design of surfaces that are able to control protein adsorption behavior, new research tools necessary for studying the mechanistic details of protein adsorption to material surfaces must be developed. One of the most promising of these tools is empirical all-atom force field-based molecular simulation, with molecular dynamics (MD) simulation being the most informative type of simulation for systems of the scope needed for this area of research (i.e., systems of at least tens to hundreds of thousands of atoms) due to the ability of MD simulations to probe both the thermodynamic and the kinetic behavior of a molecular system.

Empirical force field MD simulation methods have been extensively used and continue to be developed for the study of peptide and protein adsorption behavior on functionalized surfaces.[58, 76-78, 126-130] The accuracy of these types of methods are largely dependent on the force field (FF) that is used to represent how atoms interact with one another in a given simulation. Because of their empirical nature, it is generally ill-advised to apply a force field that has been developed and validated for one specific application to another without further validation.

The successful parameterization of most empirical all-atom biomolecular FFs is based on the FF's ability to accurately represent the structural behavior of biomolecules (particularly nucleic acids, peptides, and proteins) in solution.[52, 131-134] That is, in the absence of a material surface. The presence of a material surface in a simulated system requires that the FF in use not only accurately simulate biomolecule-solvent, biomolecule-ion, and biomolecule-biomolecule interactions, but also requires that it

accurately represent biomolecule-surface and solvent-surface interactions as well. Recent studies published by our group using unstructured peptides have shown that the CHARMM22 force field tends to substantially under predict the strength of adsorption of the peptides on nonpolar surfaces while tending to slightly over predict the strength of adsorption on hydrophilic surfaces.[135] These results thus identify situations where the existing CHARMM22 parameterization is not adequately balanced to properly represent the interactions between amino acid residues and functional groups presented by a surface and provide direction for parameter adjustment to more accurately represent protein adsorption behavior.

Another difficulty of the application of MD simulation to systems involving the behavior of complex molecular structures, particularly for the case of a peptide or a protein adsorbing on a surface, is that these systems often have a complex, rugged potential energy surface.[28] Depending on the particular molecular components simulated, this potential energy surface can have numerous local low-energy wells (troughs on an energy plot) that are separated from one another by relatively high potential energy barriers. A conventional MD simulation of this type of system will likely become trapped in one of the many local low-energy wells for the entire simulation, thus providing a very limited representation of the correct ensemble-average conformation and orientation of the molecular system.

To overcome this limitation of conventional MD simulations, advanced sampling methods can be employed that introduce an artificial driving force into the simulation that enables the system to escape from designated low-energy positions and more fully

explore the entire phase space of the system. An advanced sampling algorithm known as parallel tempering is often used to address this problem.[29] In its most common implementation, parallel tempering utilizes multiple simultaneous simulations at different temperatures (i.e., temperature levels or replicas), with exchange attempts periodically attempted between neighboring temperature levels using a Metropolis-like exchange decision process, which generates a Boltzmann-weighted ensemble of sampled states at each temperature level. As configurations move from temperature level to temperature level, conformational changes (i.e., crossing of potential energy barriers) that readily occur at higher temperatures lead to the sampling of new low-energy states that then migrate by exchange into the lower temperature levels, thus improving sampling efficiency at the low temperatures. While this method was initially used with Monte Carlo (MC) sampling, a version of this algorithm known as replica exchange molecular dynamics (REMD) was subsequently developed that included the scaling the momenta after a swap of configurations between two different temperatures to provide rapid equilibration between replicas after exchange to a different temperature level. A large number of published studies have confirmed the sampling efficiency of the REMD method and its ability to enable molecular systems with rugged potential energy landscapes to be sampled, which would require sampling timeframes outside of practical limits using a conventional MD simulation.[30]

In the present studies, we sought to assess how well the CHARMM22 force field is able to accurately represent the structural behavior of peptides on functionalized surfaces. In order to provide a means to assess this type of molecular feature, we conducted MD

simulations of simple model systems of peptides that have been experimentally shown to form secondary structures at the interfaces between physiological solution and selected functionalized surfaces.[21, 55, 136-138] The model structured peptides that were selected for these simulations were composed of alternating patterns of leucine (L) and lysine (K) amino acids (collectively known as LK peptides[55]). Previous experimental studies have shown that LK peptides can be designed to form α-helix and β-sheet structures when adsorbed on hydrophobic and negatively charged surfaces, thus providing an excellent model system to determine whether or not simulations with the CHARMM22 FF will accurately predict the structural behavior of these peptides on these same types of surface chemistries. Because this type of molecular system can be expected to possess a very rugged energy landscape, the simulations were performed using the REMD method to efficiently overcome energy barriers and provide adequate sampling of the system so that the simulation results could be confidently compared with those obtained by experiment.

Materials and Methods

Model molecular structures for all simulated systems were constructed using the standard CHARMM (version c34b2) suite of simulation tools[32] and the CHARMM22 force field.[22] Generally, all model systems were comprised of an orthorhombic layer of mobile water molecules, ions, and peptides bounded above by a fixed bulk water layer and below by a fixed SAM surface with an unrestrained top layer of functional groups (Figure 5.1).

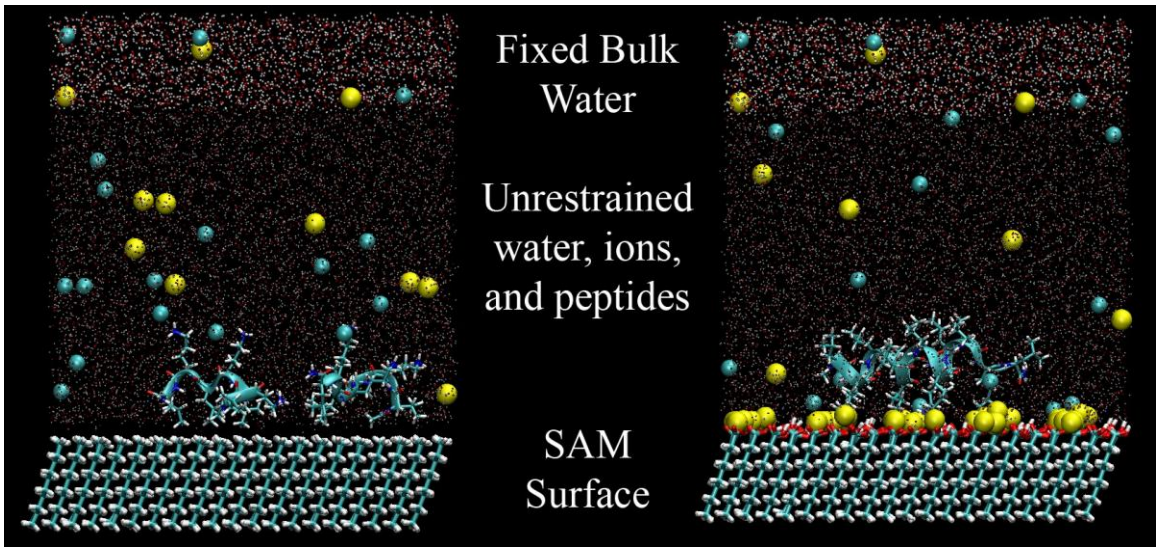

Figure 5.1: Diagram of two of the simulated systems. In these images, both taken from the production-phase of the REMD simulations, the pair of LKβ7 peptides (left) is shown adsorbed to the CH_3-SAM surface and the single LKα14 peptide (right) is shown adsorbed to the COOH-SAM surface, accompanied at the surface by Na^+ (yellow) ions attracted to the negatively-charged surface. Freely diffusing Na^+ and Cl^- (cyan) ions are also present in the solution above each SAM surface.

The central layer of mobile water molecules, ions, and peptides is referred to as the mobile core, and for spatial reference purposes, we consider the positive z-axis as the axis directed normal from the functionalized side of the SAM surface. All systems were simulated (setup and production) under 3-D periodic boundary conditions (PBCs) using the explicit-image model. Particle-mesh Ewald (PME) was used for calculation of long-range electrostatics. Parameterization of PME for all simulations included truncation of the real-space summation at 12 Å, a value of 0.34 $Å^{-1}$ for the Ewald method's Gaussian distribution inverse width, and an absolute distance cutoff of 14 Å for generating the interacting pair list.[116] Van der Waals interactions were truncated using a force-based switching function at cutoff distances matching those of the PME parameterization. All

simulations were conducted in the canonical (NVT) ensemble using the VV2 integrator (an implementation of the velocity Verlet algorithm[118]). The Nosé-Hoover method[119] with a thermostat time constant of 0.1 ps was used for temperature control of all replicas. Bond lengths involving heavy atoms and hydrogens (X-H bonds) were held fixed using the SHAKE algorithm,[120] which enabled a 2.0 fs time step to be used for all equilibration and production dynamics.

The mobile core of all simulated systems was constructed beginning with a $45 \times 43 \times 50$ Å^3 volume containing 3,641 TIP3 water molecules. 8 Na^+ and 8 Cl^- ions, sufficient to provide an approximately 140 mM NaCl aqueous solution, were added by replacement of a randomly-selected water molecule for each ion. The mobile core was equilibrated at 298 K and 1.0 atm with the ions held fixed for 100 ps of equilibration, and then all constraints were removed for 1 ns of additional equilibration. The 15 Å thick fixed bulk water layer at the top of the mobile core was comprised of 3 Na^+ and 3 Cl^- ions within TIP3 water. Prior to being held fixed during the production simulations, the fixed water layer, like the mobile core, was equilibrated at 298 K and 1.0 atm. All atoms of this layer were held fixed during the production simulations so that the free water molecules of the mobile core could interface with a bulk water-like surface instead of the periodic image of the hydrophobic bottom of the SAM's alkyl chains. The SAM surfaces were constructed using methods that Latour and coworkers[57-59, 76, 78, 110, 139] and others[64-66, 69, 71, 14064, 65, 140] have used in several previous studies involving SAMs. The hydrophobic methyl-terminated surface and the negatively charged -COOH surface were each represented as 10 Å thick SAMs. 50% of the carboxylic acid groups of the -COOH SAM

were deprotonated (approximating pK_d = 7.4) based on experimental findings.[110] To maintain neutrality of the systems with this SAM, 45 additional Na^+ counter-ions were included in the mobile core for neutralization of the 45 surface charges. For both SAMs, all atoms of the 90 alkyl chains were held fixed in position except for the top-most carbons and their attached functional group atoms, which were left unrestrained so that they were free to interact with the atoms in the solution phase of the system.

Each of the LK peptide models was constructed in a variety of backbone conformations (for variety in the pool of REMD starting structures), and each was terminated with an acetylated N-terminus and an amidated C-terminus (ACE and CT2, respectively, from the CHARMM22 force field topology library.[22]) The LKα14 structure consists of an α-helical 14-mer LK peptide with a sequence of CH_3-LKKLLKLLKKLLKL-NH_2, and the LKβ7structure consists of a β-strand 7-mer LK peptide (CH_3-LKLKLKL-NH_2). Both peptide designs provide a distinct "sidedness" where one side each folded peptide is dominated by the presence of nonpolar leucine side chains and the other side is dominated by the presence of positively charged lysine side chains. For the LKβ7 simulations, a pair of identical LKβ7 peptides was used in all cases. The peptides were added to their respective systems by replacement of water molecules within a 2.1 Å radius around the outermost atoms of each peptide. Additional Na^+ counter-ions for neutralization of the positively charged K side chains were added by replacing water molecules. Incremental equilibration stages were completed between discrete stages of the model system assembly process.

Three systems (one solo LKα14, one pair of LKα14s, and one pair of LKβ7s) were constructed and simulated as systems of peptides in solution with no SAM surface present (these systems were simulated with cubic geometry). Four systems were constructed and simulated with the inclusion of a SAM surface. For these four peptide-SAM systems, one solo LKα14 and the pair of LKβ7s were each simulated in the presence of each of the SAMs. Due to the observance of periodic boundary conditions, the sizes of the cubic or orthorhombic mobile cores were selected based on consideration of both the size of the peptides and the radial distance from the peptides within which nonbonded interacting atom lists would be generated. The final positions of the fixed bulk water layer and the SAM surface were adjusted with respect to the mobile core through repeated 500 ps equilibration runs until the boundaries at the top and bottom of the mobile core moved by less than 0.1 Å (during a complete 500 ps simulation) in response to the presence of the inserted SAM and fixed bulk water layers. This procedure ensured that the simulated pressure inside the mobile core was maintained as closely as possible to its equilibrated pressure of 1.0 atm.

The REMD simulations were coordinated using the MMTSB suite of simulation tools.[33] In order to maximize efficiency of the REMD simulations, the pool of starting configurations for each REMD simulation consisted of 3 different conformations of each peptide system (e.g., random, extended, and helical conformations) evenly distributed through the range of starting temperature replicas. Each REMD simulation was divided amongst 40 replicas spanning a temperature range of 298-520K with the "extra" replica of each system being addressed by assigning an extended (unfolded) starting

conformation to the 298 K replica to avoid an imbalance in the distribution of starting conformations. Each REMD simulation was conducted with 1 ps MD intervals between exchange attempts and multiple equilibration stages prior to initiating the production REMD simulation. It was determined that this simulation configuration resulted in exchange acceptance ratios between 0.16 and 0.25 after approximately 2 ns of REMD simulation time, and the same range of acceptance ratios was maintained through the duration of each simulation. Immediately before each exchange attempt, the coordinates of the atoms of the 298 K replica were saved as a contribution to the overall low temperature (298 K) ensemble of structures. These libraries of ensemble structures were combined in the form of MD trajectories for analysis.

Since an REMD simulation includes replicas at elevated temperatures, a unique simulation problem for interfacial systems exists where the interaction of interest is between a mobile molecular species in solution and a surface with a fixed position. The possibility of the molecular species (peptides, in this case) drifting away from the surface during the simulation, particularly for high-temperature replicas, must be addressed to maintain the simulated system in an arrangement that continually produces useful data (i.e., sampled states of the peptide interacting with the surface). Additionally, this modification must be done in a way that does not interfere with the interaction of interest. To accomplish this, we used a planar harmonic constraint potential that applied a relatively gentle force sufficient to slow and eventually stop the movement of peptides away from the SAM surface. This force was applied to the center of mass of each peptide to avoid disruption of conformational characteristics,

and it was only enabled if the center of mass of the peptide drifted beyond a distance of 10 Å from the top-most alkyl carbon atoms of each SAM surface. Monitoring of the activation of this potential force during initial parameter testing showed that it was enabled during less than 1% of all dynamics steps.

To provide a means of assessing the reproducibility of these complex simulations, each REMD simulation was conducted in duplicate, thus enabling a comparison between matching simulations with different overall trajectories (i.e., different due to selection of different random seeds used in assigning initial atomic velocities). To verify that the selected temperature range was sufficient to include sampling over all of the relevant conformational states of each system, high-temperature replica structures were examined for deterioration of the low-temperature ensemble's pattern of conformations (Figure B-2).

There are a large variety of approaches to evaluating the state of convergence of an REMD simulation,[141-148] and a consistent metric within all approaches is the convergence of specific system parameters of interest in the simulation. In these simulations, we were primarily concerned with structural features of the peptides and the surrounding solution as they interact with the surface chemistries presented to them. Based on energetic and structural analyses, all REMD simulations appear to have achieved convergence of all structural characteristics of interest within 3-5 ns of starting the simulations. Therefore, all simulations were continued through the completion of 12 ns in order to generate at least 6 ns of production data for analysis.

In addition to the adsorption behavior of the LK peptides on each SAM surface, we were also interested in characterizing how the presence of the SAM surface influenced the dynamical behavior of water compared to its behavior in bulk solution. Accordingly, conventional MD simulations of bulk solution (i.e., ions present, surface not present), neat water (i.e., no ions, no surface), and physiological saline with each of the SAM surfaces were conducted and used for the analysis of the water dipole orientation, rotational diffusion, and translational diffusion characteristics near each of the surfaces. System coordinates for these 1 ns MD simulations were saved every 20 fs to ensure sufficient resolution of water and ion translational diffusion characteristics.

Results and Discussion

Peptide amino acid secondary structure analysis of the 298 K ensemble of sampled states was conducted using the STRIDE[149] utility. Water and ion diffusion calculations at 298 K were completed using analysis features integral to the CHARMM (version c34b2) suite of simulation tools.[32] REMD simulation performance analysis was completed using analysis tools supplied with the MMTSB[33] package. Visualization software used during all stages of this work included Visual Molecular Dynamics (VMD)[150] and University of California San Francisco (UCSF) Chimera.[151]

Peptide Structure Analyses

Before analyzing the results of these simulations, it was necessary to check that the systems were adequately sampled, thus providing confidence that the resulting sampled ensemble of states represent properly equilibrated systems (i.e., Boltzmann-weight

ensemble of states). One approach to provide evidence of this is to compare the starting structures of the replicas to their final structures to see if replicas were able to unfold and refold (i.e., undergo the full relevant spectrum of structural rearrangements) over the course of the simulation. To assess this, the contribution of structured states in the final low temperature ensemble of structures and their associated replica number was compared to the initial distribution of starting conformations for this same set of replicas. The results of these analyses for a pair of LKβ7 peptides on the CH_3-SAM surface are shown in Figure B-1. These results clearly show that the replicas were able to change from one structure to another over the course of simulation. As a second assessment, the structures of the LKα14 peptide at the baseline temperature of 298 K, which was predominantly α-helix, was compared to those at the highest temperature level (520 K) to see if this temperature was sufficiently high to completely unfold the helical structure, thus sampling the unfolded as well as the folded states. Characteristic structures from each of these temperature levels are provided in Figure B-2, which clearly show that all α-helix structure was eliminated at the 520 K temperature level. These analyses provide evidence that the REMD simulations were able to readily cross the energy barriers separating the different structural states during the simulation and properly sample the full relevant conformational space of these molecular systems. Thus, we have evidence that the applied REMD methods provided the ability to access all relevant conformational states of our systems, which is a necessary condition to obtain a proper Boltzmann-weighted ensemble of states.

Generally, the peptide secondary structure and orientation analyses for each peptide-surface system showed that the simulations closely represent the experimentally-determined behavior,[21, 136-138] with notable changes in peptide conformations induced by the different surface chemistries. This general agreement between the simulation and experimental results thus indicates that the CHARMM22 force field is able to capture the general characteristics regarding realistic trends regarding the structural behavior of peptides on these types of surface chemistries. For all of the REMD simulations, the duplicate simulations produced closely matching results (see Appendix B for figures from duplicate simulations), indicating consistency of the results obtained for each simulation. Ramachandran plots of peptide phi/psi backbone dihedral angles for all systems showed consistent backbone conformations congruent with each peptide's design (i.e., intended secondary structure based on ordering of the L and K residue sequence). The LKβ7 pair of peptides adsorbed to the CH_3-SAM exhibited distinct β-strand character (Figure 5.2a), while the same peptides adsorbed to the COOH-SAM exhibited less distinct β-strand character with a pronounced introduction of α-helical character (Figure 5.2b). The LKα14 peptide adsorbed to the CH_3-SAM exhibited distinct α-helical character (Figure 5.2c), while maintaining the helical character less strictly when adsorbed to the COOH-SAM (Figure 5.2d).

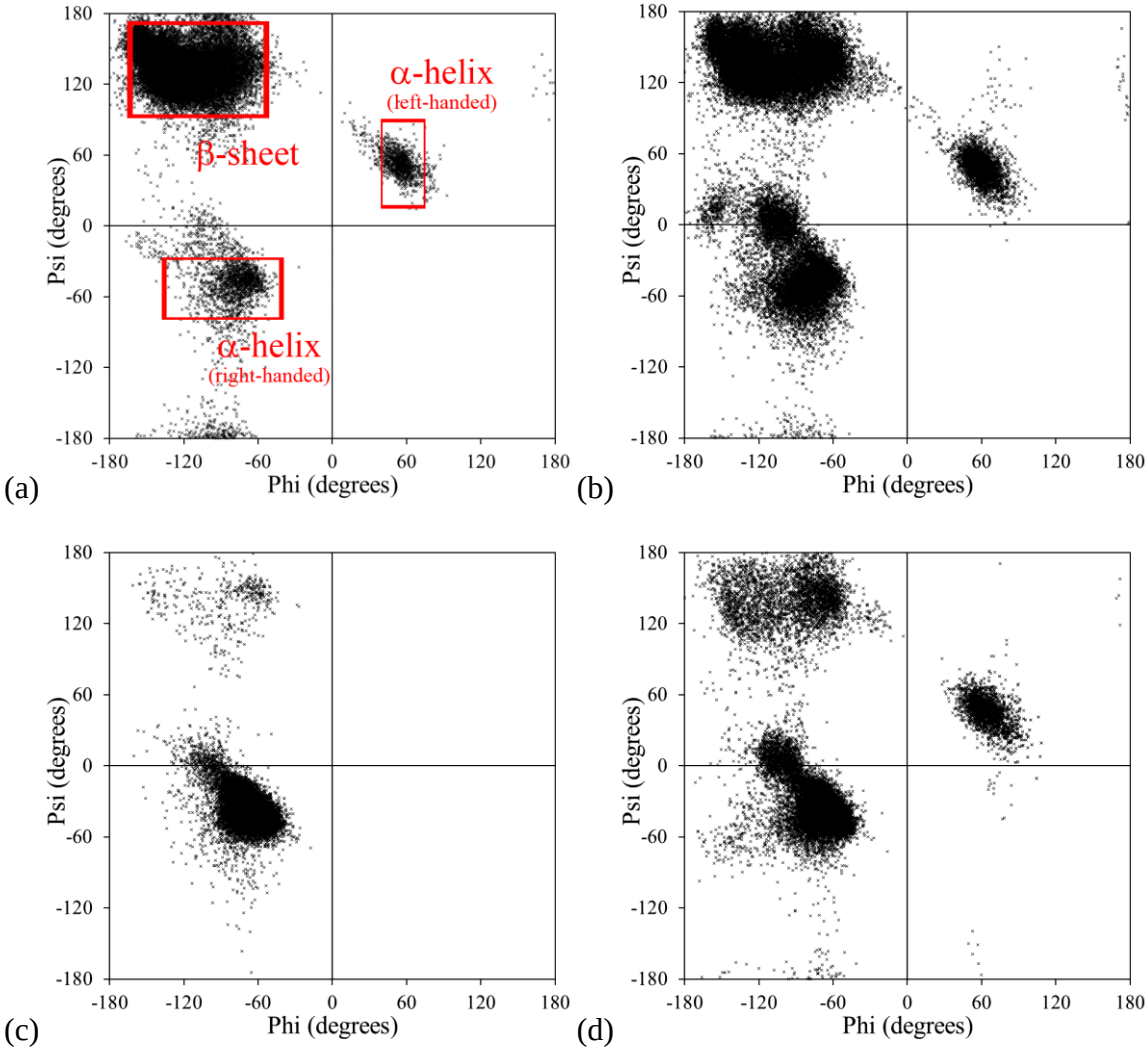

Figure 5.2: Ramachandran plots of the Phi and Psi peptide backbone dihedral angles during the final 6 ns of REMD sampling of (a) the pair of LKβ7 peptides adsorbed to the CH_3-SAM, (b) the pair of LKβ7 peptides adsorbed to the COOH-SAM, (c) the LKα14 peptide adsorbed to the CH_3-SAM, and (d) the LKα14 peptide adsorbed to the COOH-SAM. 3,000 points displayed for each non-terminal amino acid. The labels in (a) indicate the general conformational trends associated with particular Phi and Psi angle values.

As when adsorbed to the CH_3-SAM, the LKα14 peptide maintains a distinct α-helical conformation in solution, and when coupled with a second LKα14 peptide, which

primarily occurred via interactions between the nonpolar leucine amino acid residues (Figure B-8). By following the changes in secondary structure for each amino acid residue though the complete REMD simulation (Fig. 5.3), the simulations showed that both peptide systems retained a particular conformation less strictly when adsorbed to the COOH-SAM, and the conformations adopted near the COOH-SAM conformed to each peptide's intended structural design less frequently.

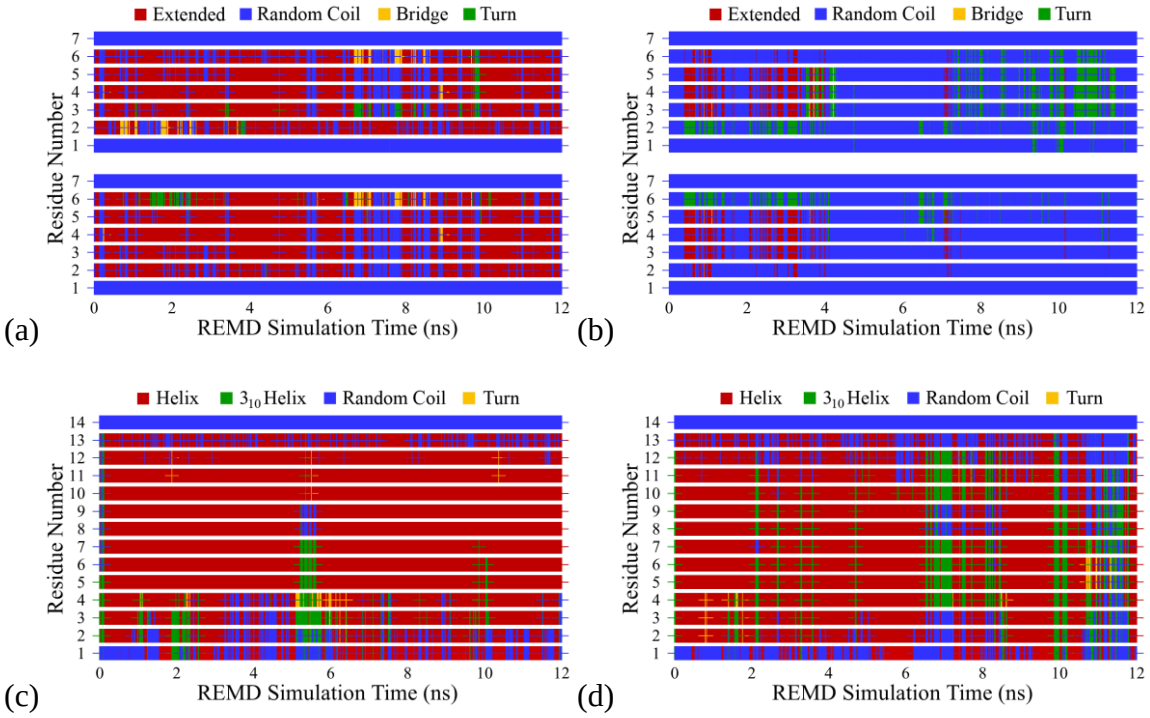

Figure 5.3: Plots of secondary structure for each amino acid residue through the entire REMD simulation for (a) the pair of LKβ7 peptides adsorbed to the CH_3-SAM, (b) the pair of LKβ7 peptides adsorbed to the COOH-SAM, (c) the LKα14 peptide adsorbed to the CH_3-SAM, and (d) the LKα14 peptide adsorbed to the COOH-SAM.

This is particularly true for the LKβ7 pair of peptides, which deviated significantly from an extended β-strand conformation near the COOH-SAM. The behavior of the LKβ7

peptides is similar to that found for the LKβ7 peptides in solution, where the β-strand conformation seen near the CH_3-SAM was almost completely abandoned in favor of a random coil conformation. In distinct contrast to the behavior of LKβ7 peptides, the LKα14 peptide's exhibited a tendency to favor an α-helical conformation with nearly the same consistency when adsorbed to the CH_3-SAM versus moving freely in solution (Figures 5.3 and B-4). Adsorption to the COOH-SAM caused greater disruption of the LKα14 peptide's conformation than adsorption to the CH_3-SAM, but the magnitude of that disruption was much less than the magnitude of the disruption to the LKβ7 peptides' conformation when adsorbed to these different surfaces. It's important to remember that the "sidedness" of both types of these peptides is equivalent, L primarily on one side and K mostly on the other. Therefore, it becomes clear that the structural stability offered by the hydrogen bonding within the helical core of the LKα14 peptide is responsible for the difference in stability between the different peptides. Once separated from each other, the LKβ7 pair of peptides were not able to easily realign in order to maintain a β-strand conformation.

In order to characterize the adsorption of the peptides to the SAM surfaces, measurements were made of the distance between the terminal atoms of each amino acid residue's side-chain and the plane of topmost alkyl carbon atoms of each SAM's alkyl chains. Specifically, the L group's terminus was defined as the geometrical center of the 2 methyl groups at the end of that amino acid's side chain (this approach accommodates rotation of those groups), and the K group's terminus was defined as the nitrogen atom at the end of that amino acid's side chain. The surface separation distance (SSD) of these

groups provides a direct measure of peptide's orientation on the surface. Measurements of the side chain SSDs for the LKβ7 pair of peptides showed that the arrangement of side chains relative to the surface of the CH_3-SAM was most consistent, with both L and K groups staying in narrow ranges of distances (approximately 3 and 5 Å, respectively) from the surface (Fig. 5.4a).

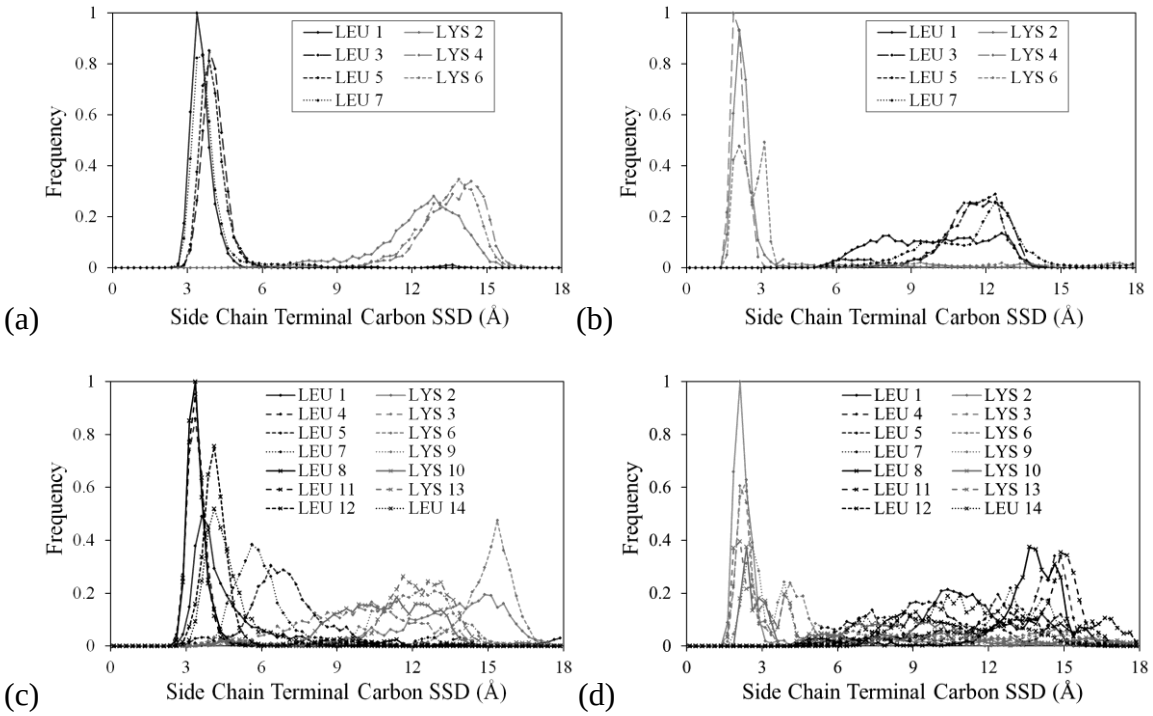

Figure 5.4: Plots of frequency distributions of amino acid side-chain terminal carbon surface separation distances (SSDs, Å) during the last 6 ns of REMD sampling for (a) the pair of LKβ7 peptides adsorbed to the CH_3-SAM, (b) the pair of LKβ7 peptides adsorbed to the COOH-SAM, (c) the LKα14 peptide adsorbed to the CH_3-SAM, and (d) the LKα14 peptide adsorbed to the COOH-SAM. 3,000 measurements for each amino acid, 0.25 Å bin width.

Naturally, in the absence of anchoring to any fixed structure, the side chains most distant from the SAM surface functional groups can be expected to vary in their SSDs much more than side chains participating in surface adsorption. As shown in Fig. 5.4b, the

adsorbing K side chains of the LKβ7 pair of peptides adsorbed to the COOH-SAM showed only a slight difference in SSD consistency from that of the L groups adsorbed to the CH_3-SAM. However, the non-adsorbing L side chain terminal groups vary in SSD by a broader range (approximately 6 Å) than those of the non-adsorbing side chains over the CH_3-SAM, indicating that the adsorbed K side chains are more flexible (permitting more rolling of the peptide backbone in the plane of the surface) than those of the L side chains. Due to the greater length of the LKα14 peptide, and the less linear arrangement of the adsorbing side chains of the helical structure, there is less consistency in the SSDs of adsorbing side chain termini at both SAM surfaces (Figs. 5.4c and 5.4d). The same structural characteristics of the helical peptide also contribute to the increased variability in the SSDs of the non-adsorbing side chain termini.

Another method of evaluating the adsorption characteristics of the peptides was an analysis of the side-chain tilt angles. Here, the tilt angle of a peptide side chain was considered to be the angle between the surface normal and the vector originating at the side chain α-carbon and directed toward the terminal group (as defined for the SSD measurements) of that side chain. The tilt angle measurement populations (Figure B-9), coupled with visualization of MD trajectory frames from the simulations, indicated a tendency of the individual L side chains to adsorb to the CH_3-SAM surface with one of their two terminal methyl groups arranged at closest approach to one of the surface methyl groups (thus, the side chain is tilted, rather than being oriented perpendicular to the surface). This arrangement represents water-excluding point-to-point interaction where the interacting peaks of hydrophobicity (i.e., the water-excluding methyl groups)

serve as points of contact between the peptide and the surface. Similar analyses for the side chains of peptides adsorbed to the COOH-SAM show a tendency toward vertical alignment of the K side chains over the surface. The tilt angles measured for the adsorbing LKα14 side chains are in agreement with experimental findings[152] that show certain leucines tilted most directly toward a hydrophobic surface.

The simulated system consisting of the two LKα14 peptides in solution enabled an analysis of inter-helix structural feature interactions. The Ramachandran plots derived from these simulations (Figures B-3i and B-3j) reflect a more rigid adherence to α-helical character than that seen for the single LKα14 peptide in solution (Figure B-3g,h) or adsorbed to either surface (Figures 5.2c,d and B-3e,f). Populations of distance measurements between the primary interacting groups of the two peptides show ordered L-to-L side chain interactions and disordered K-to-K side chain interactions (Figure B-8), indicating that some measure of conformational stability is provided by the close interpeptide interaction of hydrophobic leucine side chains.

A unique structural characteristic of the pair of LKβ7 peptides is their ability to cooperate in forming parallel or antiparallel β-sheet conformations. The tendency of these peptides to be arranged in such conformations was monitored by measuring the distances between peptide N-termini and C-termini α-carbons. Arrangements of the two peptides with both N-termini in close proximity, as well as with both C-termini in close proximity, was considered to constitute a configuration representative of a parallel β-sheet structure. Arrangements of the two peptides with the N-terminus of each peptide being in close proximity to the C-terminus of the other peptide was considered to

represent a configuration representative of an antiparallel β-sheet structure. In the absence of other factors, an antiparallel conformation is generally favored energetically because this arrangement allows for planar, less strained inter-strand hydrogen bonding between the main-chain carbonyls and amines of the peptides. For the purpose of categorizing these interactions, a distance of 8 Å (sufficiently close for the interacting structures of these peptides to initiate cross-strand β-sheet formation[153, 154]) was used as a threshold. Plots of these measurements (Figures 5.5 and B-6) show antiparallel conformations as being unique to, and predominant in, the adsorption of the pair of LKβ7 peptides to the CH_3-SAM.

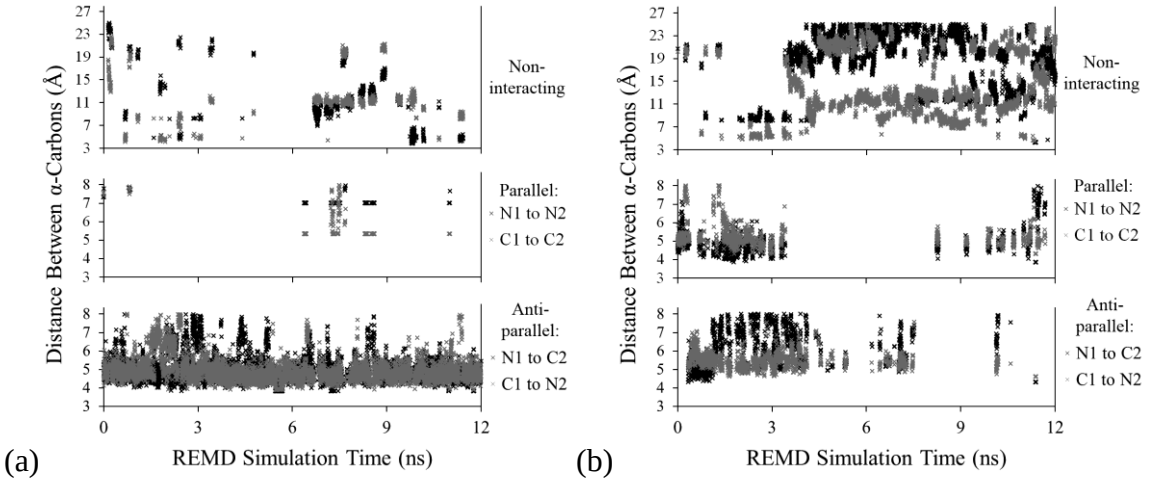

Figure 5.5: Plots of distances between terminal α-carbons (indicative of parallel and antiparallel conformations) during the entire REMD simulation for the pair of LKβ7 peptides (a) adsorbed to the CH_3-SAM, (b) adsorbed to the COOH-SAM.

In the presence of the COOH-SAM, and in solution, these peptides preferred non-interacting conformations to either antiparallel or parallel orientations. The reason for this is believed to be due to entropic effects related to a combination of the small size of

the LKβ7 peptides (i.e., resulting in relatively small number of interchain interactions to stabilize the structure) and the relatively loose, hydrated nature of the interaction of the K side chains with the negatively charged carboxyate groups of the SAM surface . However, in the case of the LKβ7 peptides adsorbed to the CH_3-SAM, the additional stability provided by the relatively strong hydrophobic effects at the interface between the L groups of the peptides and the SAM's hydrophobic surface enabled the energetically preferred antiparallel β-sheet conformation to overcome the entropic driving force to randomize the system.

Water Structure Analyses

Analyses of the solution surrounding the adsorbing peptides offered insights into the roles both water and ions play in the adsorption process. An initial step in these analyses was an examination of the density distributions of each component (water, Na^+ ions, Cl^- ions) in each system, relative to their bulk densities, to see how surface chemistry and the presence of the adsorbed peptides altered the local concentrations of components. Using z-axis density function plots and looking at water solvation layers over each SAM surface, patterns of water density show a clear difference between the CH_3-SAM and the COOH-SAM. The CH_3-SAM had diminished water density at the surface compared with the COOH-SAM as indicated by the first peak in water density occurring at about 3.0 Å versus 1.5 Å for the CH_3 and COOH SAMs, resepectively (Figures 5.6a and 5.6c), making adsorption through water exclusion (the hydrophobic effect) favorable for each peptide's nonpolar L residues.

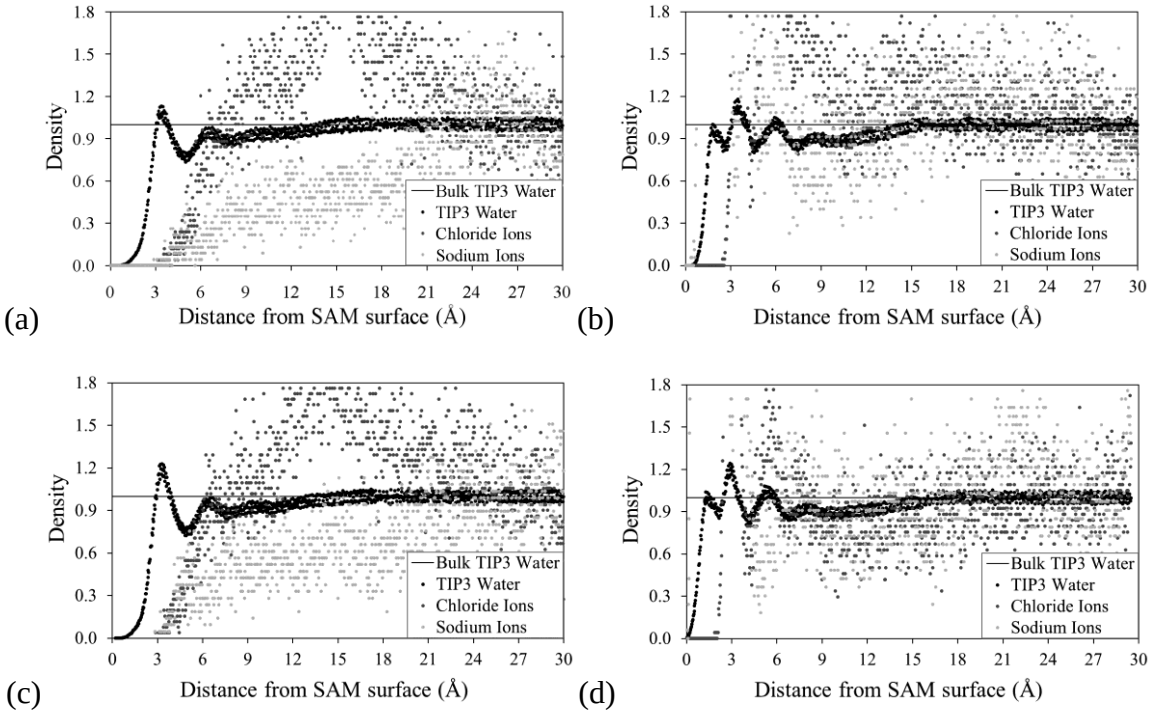

Figure 5.6: Plots of density distributions of TIP3 water, Na^+ ions, and Cl^- ions relative to bulk solution values (density of 1.0) during the last 6 ns of REMD sampling for (a) the pair of LKβ7 peptides adsorbed to the CH_3-SAM, (b) the pair of LKβ7 peptides adsorbed to the COOH-SAM, (c) the LKα14 peptide adsorbed to the CH_3-SAM, and (d) the LKα14 peptide adsorbed to the COOH-SAM. The Na^+ ion distributions in the COOH-SAM plots (b and d) extend beyond the scale of the plot, peaking at relative density values of 2.7 and 2.8 at distances of 1.4 Å and 1.3 Å from the surface, respectively.

In these plots, a large elevation in the density of Cl^- ions is indicative of the position of the positively charged K side chains. Also, the more complex water layering above the COOH-SAM is indicative of the relative positions of the two oxygen atoms in the COOH functional groups of this surface (Figures 5.6b and 5.6d). In these plots, the sharply elevated denstiy of Na^+ ions attracted to the negative charges at the surface can be seen. This ion density is indicative of the strength of the electrostatic interaction available to the positively charged K residue side chains and also emphasizes the fact that adsorption

of the K residues actually reflects an ion-exchange event at the surface between the positive charges of the K residues and the Na^+ ions in solution.

A significant difference in water structure over each of the simulated SAM surfaces was noted from both the density of the water and the water dipole orientations near each of the surfaces. Water near the CH_3-SAM surface maintains greater distance from the surface functional groups and presents with an orientation of the hydrogen-bonding network that is much more parallel to the plane of the surface compared to the COOH-SAM. The population of dipole orientations near the CH_3-SAM surface deviate strongly from bulk behavior, showing a tendency toward an approximately 120° tilt from the surface normal as the water molecules structurally adapt to an inability to form hydrogen bonds with the functional groups of the surface (Figure 5.7a).

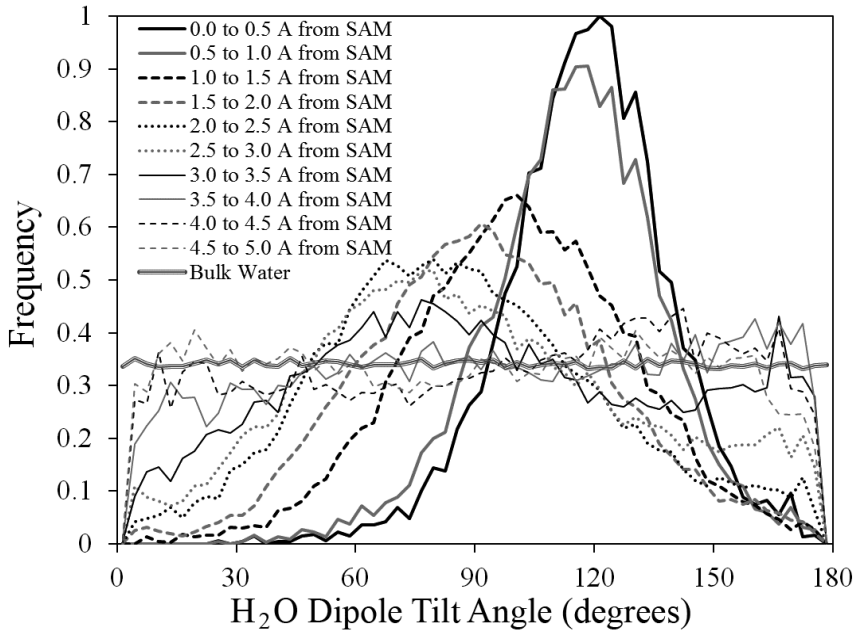

(a)

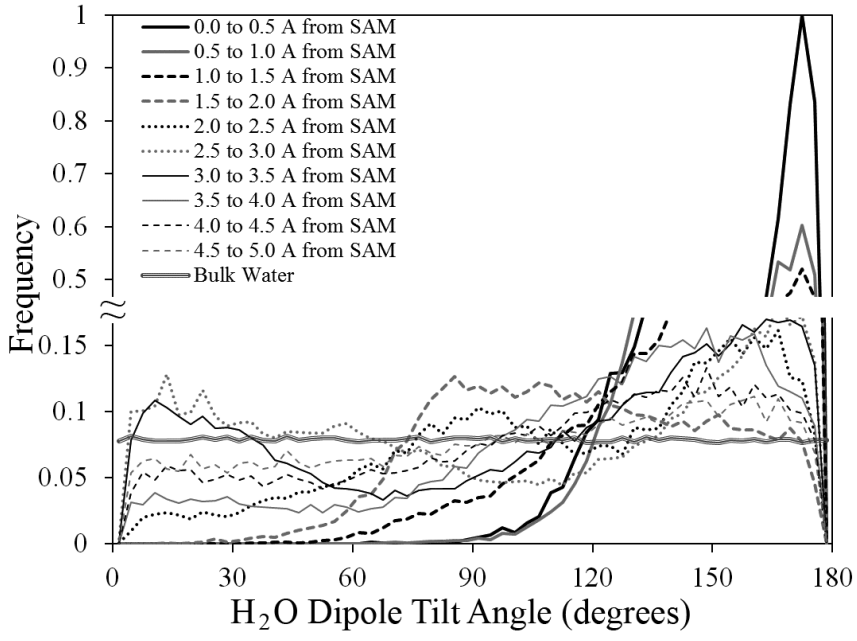

(b)

Figure5.7: Plots of TIP3 water dipole orientations as angles from the (+) z axis (normal to the SAM surface) (a) for the CH_3-SAM, and (b) for the COOH-SAM (with divided frequency scale). Both systems represent approximately 140 mM saline with no peptides present. Frequency is normalized to the number of counts per 3-degree bin and to the sinusoidal distribution of measurements.

The water near the charged COOH-SAM surface interacts closely with the surface functional groups, exhibiting a very strong orientation effect on the water with the water dipoles ordered in a nearly vertical orientation (Figure 5.7b) in response to the negative charges on the surface.

Radial density functions were also calculated for the water near the adsorbed side chain groups (Figure 5.8). These plots, showing radial densities of water near the side chains relative to bulk water density show a dramatic 3 to 4 fold increase in the density of water immediately surrounding the K side chains when these amino acids were not adsorbed to the SAM surface (i.e., over the CH_3-SAM surface or in solution). It should be noted that the longer distance required before achieving bulk water density values can be attributed to the presence of the rest of the peptide, which will thus diminish the number of water molecules within a given distance of the L or K side-chain terminal functional groups compared to bulk water.

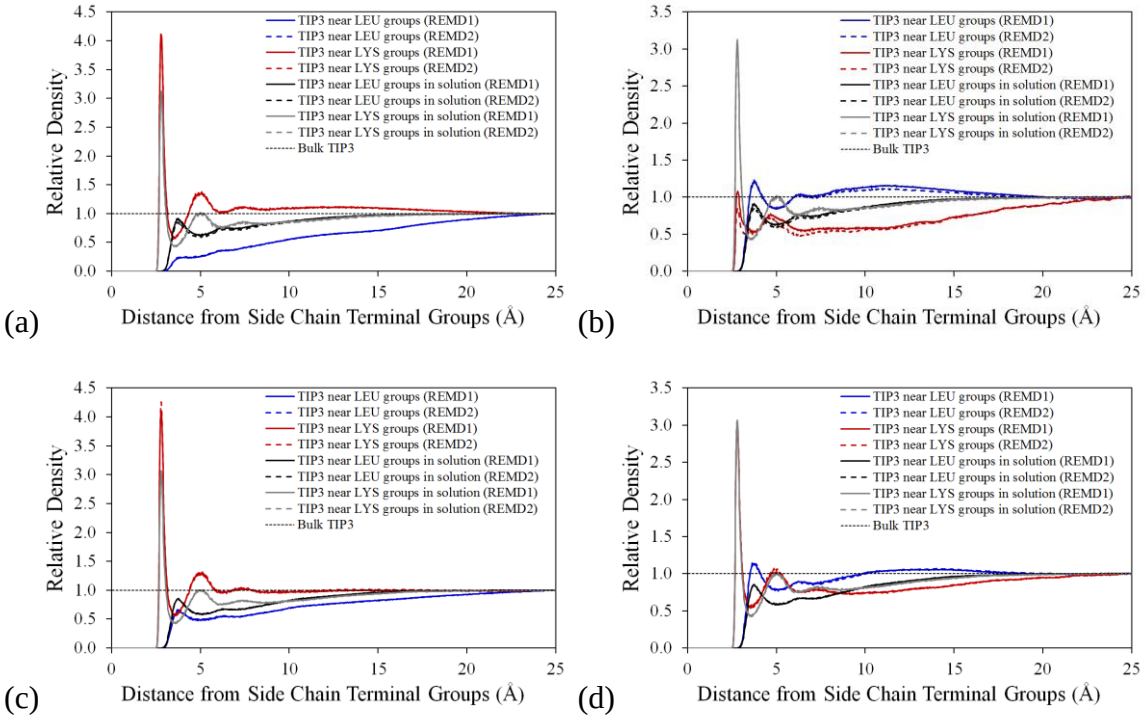

Figure 5.8: Plots of radial density functions of TIP3 water during the last 6 ns of REMD sampling for (a) the pair of LKβ7 peptides adsorbed to the CH_3-SAM, (b) the pair of LKβ7 peptides adsorbed to the COOH-SAM, (c) the LKα14 peptide adsorbed to the CH_3-SAM, and (d) the LKα14 peptide adsorbed to the COOH-SAM. Densities are relative to bulk TIP3 density which is arbitrarily set to unity. The origin of the radial density function for each type of side chain for a particular peptide was a combination of all of the terminal methyl carbons for L side chains or a combination of all of the terminal nitrogen atoms for K side chains. 6,000 REMD low-temperature ensemble structures used for each curve, and each curve consists of 1,000 data points. Grid spacing for RDF calculations was 0.025 Å, and PBCs were observed during RDF calculations.

Additional analyses of water behavior and structure included calculations of water and ion diffusion coefficients and water dipole rotational correlation times (Figures B-11 and B-12). The calculated diffusion coefficient of the TIP3 water model (the original water model from which CHARMM's TIP3 model was derived) has been reported as ranging from 5.2 to 7.0 x 10^{-5} cm^2/sec,[114, 155-157] and our calculated diffusion coefficient

of 5.6 x 10^{-5} cm^2/sec for bulk-like water thus falls within the accepted range. Our calculated values for the diffusion coefficients of Na^+ ions and Cl^- ions in bulk solution, 1.96 x 10^{-5} cm^2/sec and 3.17 x 10^{-5} cm^2/sec, respectively, are similar in value and relative magnitudes to values for ions in pure water at 298 K calculated from experimental results of 1.33 x 10^{-5} cm^2/sec and 2.03 x 10^{-5} cm^2/sec, respectively.[158, 159] The calculated diffusion coefficients of water, Na^+ ions, and Cl^- ions near the CH_3-SAM in the absence of peptides attenuate from bulk solution values within approximately 5 Å from the surface, whereas the diffusion coefficients near the COOH-SAM are reduced more gradually and to a greater extent over a distance of more than 10 Å. Our calculated P2 dipole rotational correlation time for bulk-like water is 0.238 ps, and this value becomes longer as one approaches either surface. Also, as in the case of the diffusion coefficients, the rotational correlation times deviate from bulk solution values much more strongly near the COOH-SAM than they do near the CH_3-SAM, thus reflecting the stronger influence that the charged functional groups have on the behavior of water compared to the influence of hydrophobic groups of a surface. Similar calculations of diffusion coefficients and rotational correlation times were completed for water molecules residing in spherical shells radiating outward from each adsorbed peptide's side chain terminal groups. The calculated diffusion coefficients (Figure B-13) show an attenuation in the rate of diffusuion as the water molecules approach each surface, and this decrease in the rate of diffusion is most pronounced for the case of the peptides adsorbed to the charged COOH-SAM. Similarly, the calculated rotational correlation times (Figure B-15) become longer by approximately 2x near the surface in the case of the peptides adsorbed

to the hydrophobic CH_3-SAM, and by approximately 3x in the case of adsorption to the COOH-SAM.

Conclusions

Our approach used in simulating the interaction of the LKβ7 and LKα14 peptides with functionalized SAM surfaces resulted in secondary structure and orientation data that matches the available experimental studies of matching systems. The MD simulation enhancement of advanced conformational sampling using the REMD technique provided an excellent means of efficiently sampling the molecular systems. As reported for the experimental studies of matching and similar systems, the peptides adsorbed to both surfaces while maintaining their secondary structural characteristics, despite some slight deviations attributable to differences in surface chemistry. The orientations of the residue side chains of both peptides when adsorbed to the SAM surfaces were similar, and it is clear from those orientations that precisely designed surface chemistry would elicit different or prescribed adsorption behavior. There are distinct differences in water and ion density and water dipole orientations over the different surfaces that may play a role in stabilizing the conformations and orientations of the adsorbed peptides. Finally, a very important aspect of this work is the demonstration of the complementary nature of different structural analyses, both simulated and experimental, in providing a more complete picture of a physical phenomenon that govern the interactions between structured peptides with functionalized surfaces, with the CHARMM22 FF providing very reasonable predictive capabilities for peptide adsorption behavior for these structured peptide-surface systems.

CHAPTER SIX

A COMPARISON OF MOLECULAR DYNAMICS FORCE FIELDS FOR THE SIMULATION OF THE ADSORPTION BEHAVIOR OF STRUCTURED PEPTIDES ON FUNCTIONALIZED SURFACES

Introduction

Empirical all-atom MD FFs such as the CHARMM22 FF,[22] the AMBER94 FF,[52] and the OPLS-AA FF[53] have been developed and parameterized for accurate representations of peptide and protein conformations in explicitly represented solutions. However, these development and parameterization efforts have not included consideration of the huge variety of solution-surface interfacial systems where peptides and proteins play very interesting and often critical roles in how physiological environments react to such interfacial systems. The fundamental importance of being able to study these kinds of systems using MD techniques cannot be overstated, so we have begun the process of including peptide and protein simulation in solution-surface interfacial systems within the scope of MD FF and technique development. An initial stage in this endeavor, which encompasses the work presented here, is the comparative evaluation of differences amongst the most widely used and thoroughly validated MD FFs in simulations of peptides and proteins interacting with solid surfaces.

Generally, parameterization and implementation of most modern empirical all-atom FFs is guided by that FF's performance in accurately representing the structural conformations of biomolecules in solution.[52, 131-134] Notably, in the absence of a material surface or other non-solution components. The presence of a material surface in a simulated system requires that the FF in use not only accurately simulates biomolecule-

solvent, biomolecule-ion, and biomolecule-biomolecule interactions, but also requires that it accurately represent biomolecule-surface and solvent-surface interactions as well. Considering these additional performance requirements, it is not yet clear how transferrable existing MD FFs are to the case of peptides or proteins interacting with material surfaces. Given the proven accuracy of modern MD FFs in representing biomolecular interactions, the possibility of acceptable accuracy in representing peptide-surface systems warrants an initial examination, and this type of examination will provide a useful starting point for future MD FF development efforts.

Relative to the level of structural detail provided by MD simulation, current experimental approaches offer a somewhat limited picture of the structural characteristics of peptides adsorbed to material surfaces. However, the details provided by experimental results are sufficient for serving as a general guide to acceptable FF performance. For example, in the case peptide adsorption to a surface, experimental results indicating the overall secondary structure of the adsorbed peptide can serve to support one FF's performance in favor of another if that FF's representation of the peptide matches the experimental result while another FF's representation does not. Additionally, FFs can be evaluated on their performance relative to one another if, for example, one FF is capable of representing a discrete peptide conformation (one that matches an experimental finding or expected result) when another FF is unable to do the same.

In this chapter, the same peptide-SAM surface systems used in Chapter 5 are used in matching simulations that employ the AMBER94 and OPLS-AA FFs where the CHARMM22 FF had been used previously. Here, the methods and results of the

simulations using all 3 FFs are presented in parallel to enable identification of the differences between the different FFs.

Materials and Methods

Model molecular structures for all simulated systems were constructed using the standard CHARMM (version c34b2) suite of simulation tools.[32] Components of each system were constructed using the same FF that would be used for all preparation and production simulations of those systems. The three different FFs used included the CHARMM22 FF,[22] the AMBER94 FF,[52] and the OPLS-AA FF.[53] The specific parameter and topology files that constitute these FFs were the ones included in the CHARMM c34b2 source package. Generally, all peptide-surface model systems were comprised of an orthorhombic layer of mobile water molecules, ions, and peptides bounded above by a fixed bulk water layer and below by a fixed SAM surface with unrestrained functional groups (Figure 6.1).

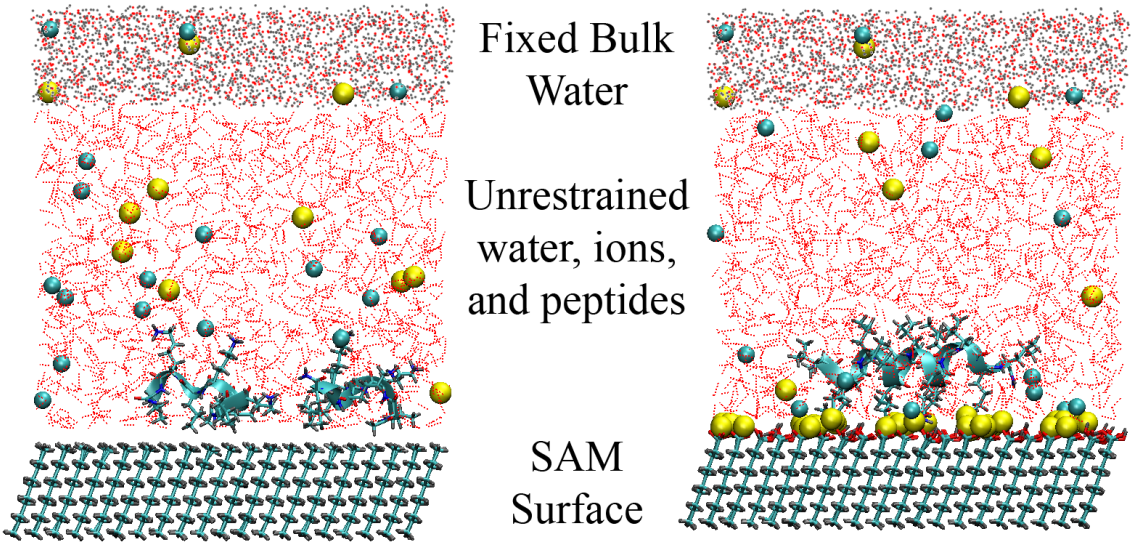

Figure 6.1: Diagrams of two of the simulated systems. In these images, both taken from the production-phase of the REMD simulations, the pair of LKβ7 peptides (left) is shown adsorbed to the CH_3-SAM surface and the single LKα14 peptide (right) is shown adsorbed to the COOH-SAM surface accompanied at the surface by Na^+ (yellow) ions attracted to the negatively-charged surface. Freely diffusing Na^+ and Cl^- (cyan) ions are also present in the solution above each SAM surface. In both images, the unrestrained water is rendered as hydrogen bonds (red dotted lines).

The central layer of mobile water molecules, ions, and peptides is referred to as the mobile core, and for spatial reference purposes, we consider the positive z-axis as the axis directed normal from the functionalized side of the SAM surface. All systems were simulated (setup and production) under 3-D PBCs using the explicit-image model. PME was used for calculation of long-range electrostatics, and parameterization[116] of PME for all simulations included truncation of the real-space summation at 12 Å, a value of 0.34 $Å^{-1}$ for the Ewald method's Gaussian distribution inverse width, and an absolute distance cutoff of 14 Å for generating the interacting pair list. Van der Waals interactions were truncated using a force-based switching function at cutoff distances matching those of the

PME parameterization. All simulations were conducted in the canonical (NVT) ensemble using the VV2 integrator (an implementation of the velocity Verlet algorithm[118]). The Nosé-Hoover method[119] with a thermostat time constant of 0.1 ps was used for temperature control of all replicas. Bond lengths involving heavy atoms and hydrogens (X-H bonds) were held fixed using the SHAKE algorithm,[120] which enabled a 2.0 fs time step to be used for all equilibration and production dynamics.

The mobile core of all simulated systems was constructed beginning with a $45 \times 43 \times 50$ Å^3 volume containing 3,641 TIP3 water molecules. 8 Na^+ and 8 Cl^- ions, sufficient to provide an approximately 140 mM NaCl aqueous solution, were added by replacement of a randomly-selected water molecule for each ion. The mobile core was equilibrated at 298 K and 1.0 atm with the ions held fixed for 100 ps of equilibration, and then all constraints were removed for 1 ns of additional equilibration. The 15 Å thick fixed bulk water layer at the top of the mobile core was comprised of 3 Na^+ and 3 Cl^- ions within TIP3 water. Prior to being held fixed during the production simulations, the fixed water layer, like the mobile core, was equilibrated at 298 K and 1.0 atm. All atoms of this layer were held fixed during the production simulations so that the free water molecules of the mobile core could interface with a bulk water-like surface instead of the periodic image of the hydrophobic bottom of the SAM's alkyl chains. The SAM surfaces were constructed using methods that Latour and coworkers[57-59, 76, 78, 110, 139] and others[64-66, 69, 71, 14064, 65, 140] have used in several previous studies involving SAMs. The hydrophobic methyl-terminated surface and the negatively charged -COOH surface were each represented as 10 Å thick SAMs. 50% of the carboxylic acid groups of the -COOH SAM

were deprotonated (approximating pK_d = 7.4) based on experimental findings.[110] To maintain neutrality of the systems with this SAM, 45 additional Na^+ counter-ions were included in the mobile core for neutralization of the 45 surface charges. For both SAMs, all atoms of the 90 alkyl chains were held fixed in position except for the terminal carbons and functional group atoms (those were left unrestrained). Each of the LK peptide models was constructed in a variety of backbone conformations (for variety in the pool of REMD starting structures), and each was terminated with an acetylated N-terminus and an amidated C-terminus (ACE and CT2, respectively). The LKα14 structure consisted of an α-helical 14-mer LK peptide with a sequence of CH_3-LKKLLKLLKKLLKL-NH_2, and the LKβ7structure consists of a β-strand 7-mer LK peptide (CH_3-LKLKLKL-NH_2). Both peptide designs provide a distinct "sidedness" where one side each folded peptide is dominated by the presence of nonpolar leucine side chains and the other side is dominated by the presence of positively charged lysine side chains. For the LKβ7 simulations, a pair of identical LKβ7 peptides was used in all cases. The peptides were added to their respective systems by replacement of water molecules within a 2.1 Å radius around the outermost atoms of each peptide. Additional Na^+ counter-ions for neutralization of the positively charged K side chains were added by replacing water molecules. Incremental equilibration stages were completed between discrete stages of the model system assembly process.

Overall, three distinct systems (one solo LKα14, one pair of LKα14s, and one pair of LKβ7s) were constructed and simulated as systems of peptides in solution with no SAM surface present (these systems were simulated with cubic geometry), and four distinct

systems were constructed and simulated with the inclusion of a SAM surface. For the four peptide-SAM systems, one solo LKα14 and the pair of LKβ7s were each simulated in the presence of each of the SAMs. Due to the observance of periodic boundary conditions, the sizes of the cubic or orthorhombic mobile cores were selected based on consideration of both the size of the peptides and the radial distance from the peptides within which non-bonded interacting atom lists would be generated. The final positions of the fixed bulk water layer and the SAM surface were adjusted with respect to the mobile core through repeated 500 ps equilibration runs until the boundaries at the top and bottom of the mobile core moved by less than 0.1 Å (during a complete 500 ps simulation) in response to the presence of the inserted SAM and fixed bulk water layers. This procedure ensured that the simulated pressure inside the mobile core was maintained as closely as possible to its equilibrated pressure of 1.0 atm.

The REMD simulations were each coordinated using the MMTSB suite of simulation tools.[33] In order to maximize efficiency of the REMD simulations, the pool of starting configurations for each REMD simulation consisted of 3 different conformations of each peptide system (e.g., random, extended, and helical conformations) evenly distributed through the range of starting temperature replicas. Each REMD simulation was divided amongst 40 replicas spanning a temperature range of 298-520 K with the "extra" replica of each system being assigned an extended (unfolded) starting conformation to the 298 K replica to avoid an imbalance in the distribution of starting conformations. Each REMD simulation was conducted

with 1 ps MD intervals between exchange attempts and multiple equilibration stages prior to initiating the production REMD simulation. It was determined that this simulation configuration resulted in exchange acceptance ratios between 0.16 and 0.25 after approximately 2 ns of REMD simulation time, and the same range of acceptance ratios was maintained through the duration of each simulation. Immediately before each exchange attempt, the coordinates of the atoms of the 298 K replica were saved as a contribution to the overall low temperature (298 K) ensemble of structures. These libraries of ensemble structures were then combined in the form of MD trajectories for analysis.

Since an REMD simulation includes replicas at elevated temperatures, a unique simulation problem for interfacial systems exists where the interaction of interest is between a mobile molecular species in solution and a surface with a fixed position. The possibility of the molecular species (peptides, in this case) drifting away from the surface during the simulation, particularly for high-temperature replicas, must be addressed to maintain the simulated system in an arrangement that continually produces useful data (i.e., sampled states of the peptide interacting with the surface). Additionally, this modification must be done in a way that does not interfere with the interaction of interest. To accomplish this, we used a planar harmonic constraint potential that applied a relatively gentle force sufficient to slow and eventually stop the movement of peptides away from the SAM surface. This force was applied to the center of mass of each peptide to avoid disruption of conformational characteristics, and it was only enabled if the center of mass of the peptide drifted beyond a distance of 10 Å from the topmost

alkyl carbon atoms of each SAM surface. Monitoring of the activation of this potential force during initial parameter testing showed that it was enabled during less than 1% of all dynamics steps.

To provide an additional means of assessing the reproducibility of these complex simulations, each REMD simulation was conducted in duplicate, thus enabling a comparison to be made between matching simulations with different overall trajectories (i.e., different due to selection of different random seeds used in assigning initial atomic velocities). To verify that the selected temperature range was sufficient to cover a sufficient range of conformational sampling, the high-temperature replica structures were examined for deterioration of the low-temperature ensemble's pattern of conformations (i.e., resulting in a randomly structured peptide). For example, the LKα14 peptide, which maintains a helical conformation in solution at 298 K, was seen to adopt an extended or random conformation when simulated at the 520 K temperature level. There are a large variety of approaches to evaluating the state of convergence of an REMD simulation,[141-148] and a consistent metric within all approaches is the convergence of specific system parameters of interest in the simulation. In our simulations, we were primarily concerned with structural features of the peptides and the surrounding solution as they interacted with the surface chemistries presented to them. Based on these structural analyses, all REMD simulations appeared to have achieved convergence of all structural characteristics of interest within 3-5 ns of starting the simulations. Therefore, all simulations were continued through completion of 12 ns in order to generate at least 6 ns of production

data for analysis. During the production phase of each simulation, there was no significant change in the potential energy of any of the systems, so monitoring structural features provided a clearer picture of the progress of the simulations.

Results and Discussion

The first step in a comparison of the CHARMM, AMBER, and OPLS-AA FFs with respect to their ability to accurately model peptide adsorption is to examine the parameters that comprise these FFs to note their differences at this fundamental level. Since the interactions involved in peptide adsorption are predominantly due to intermolecular nonbonded interactions, with bonded interactions playing a secondary role, limiting the comparison of the FF parameters to assigned partial charge (q), Lennard-Jones (LJ) potential well depth (ε), and distance to energy well minimum (r_{min}) values can provide some explanation for differences in behavior between FFs. However, it is important to note that isolated FF parameters cannot, by themselves, explain differences in behavior between FFs. Atomic and molecular interactions prescribed by a particular FF are the result of a complex, concerted effort that can involve a large variety of interaction parameters. The value of examining individual parameters is that it can provide a sense of the magnitude of differences between FFs for a specific type of interaction.

Within the CHARMM22, AMBER94, and OPLS-AA FFs, values of q are independent of atom type, and they calculated and assigned based (most often) on charge fitting using *ab initio* methods. Values for ε and r_{min} are assigned to atom types, so these values will be the same for a particular atom type, regardless of the molecular

environment in which they reside. In Tables 6.1 through 6.5, these FF parameters are listed for each atom in the amino acid residues and SAM alkyl chain terminal groups of interest in this work. In these tables, for clarity, all values are presented rounded to 4 decimal places. The partial charge assignments for the terminal methyl groups of the LEU residue (Table 6.1) differ widely between the different FFs. The most pronounced difference between the FFs here is the partial charge setting for the side chain terminal methyl carbons where the CHARMM22 FF uses a value of -0.2700, the AMBER94 setting is -0.4121, and the OPLS-AA value is -0.1800. In this case, the CHARMM22 FF strikes a balance between the AMBER94 and OPLS-AA values. Additionally, the CHARMM22 ε values for the LEU side chain methyl groups lie between AMBER94 and OPLS-AA ε values, where the AMBER94 ε value for the carbon is relatively large (deeper potential well) and the OPLS-AA ε value is relatively small (shallower potential well).

Table 6.1. FF parameters (q, ε, and r_{min}) for the LEU residue. Potential well depth (ε) values are in kcal/mole, where $\varepsilon_{i,j} = sqrt(\varepsilon_i * \varepsilon_j)$. Distance to potential minimum (rmin) values are in Å units, where $r_{min}(i,j)=(r_{min}/2)_i + (r_{min}/2)_j$.

LEU residue	Topology ID	CHARMM type	AMBER type	OPLS-AA type	*q* (e^- charge)			ε (kcal/mole)			$r_{min}/2$ (Å)		
					CHARMM	AMBER	OPLS-AA	CHARMM	AMBER	OPLS-AA	CHARMM	AMBER	OPLS-AA
bb N-term N	N	NH1	N	N238	-0.4700	-0.4157	-0.5000	-0.2000	-0.1700	-0.1700	1.8500	1.8240	1.8240
bb N-term H	HN	H	H	H241	0.3100	0.2719	0.3000	-0.0460	-0.0157	0.0000	0.2245	0.6000	0.0000
bb alpha-C	CA	CT1	CT	C224	0.0700	-0.0518	0.1400	-0.0200	-0.1094	-0.0660	2.2750	1.9080	1.9643
bb alpha-C H	HA	HB	H1	H140	0.0900	0.0922	0.0600	-0.0220	-0.0157	-0.0300	1.3200	1.3870	1.4031
sidechain C	CB	CT2	CT	C136	-0.1800	-0.1102	-0.1200	-0.0550	-0.1094	-0.0660	2.1750	1.9080	1.9643
sidechain C H	HB1	HA	HC	H140	0.0900	0.0457	0.0600	-0.0220	-0.0157	-0.0300	1.3200	1.4870	1.4031
sidechain C H	HB2	HA	HC	H140	0.0900	0.0457	0.0600	-0.0220	-0.0157	-0.0300	1.3200	1.4870	1.4031
sidechain C	CG	CT1	CT	C137	-0.0900	0.3531	-0.0600	-0.0200	-0.1094	-0.0660	2.2750	1.9080	1.9643
sidechain C H	HG	HA	HC	H140	0.0900	-0.0361	0.0600	-0.0220	-0.0157	-0.0300	1.3200	1.4870	1.4031
term methyl C	CD1	CT3	CT	C135	-0.2700	-0.4121	-0.1800	-0.0800	-0.1094	-0.0660	2.0600	1.9080	1.9643
term methyl H	HD11	HA	HC	H140	0.0900	0.1000	0.0600	-0.0220	-0.0157	-0.0300	1.3200	1.4870	1.4031
term methyl H	HD12	HA	HC	H140	0.0900	0.1000	0.0600	-0.0220	-0.0157	-0.0300	1.3200	1.4870	1.4031
term methyl H	HD13	HA	HC	H140	0.0900	0.1000	0.0600	-0.0220	-0.0157	-0.0300	1.3200	1.4870	1.4031
term methyl C	CD2	CT3	CT	C135	-0.2700	-0.4121	-0.1800	-0.0800	-0.1094	-0.0660	2.0600	1.9080	1.9643
term methyl H	HD21	HA	HC	H140	0.0900	0.1000	0.0600	-0.0220	-0.0157	-0.0300	1.3200	1.4870	1.4031
term methyl H	HD22	HA	HC	H140	0.0900	0.1000	0.0600	-0.0220	-0.0157	-0.0300	1.3200	1.4870	1.4031
term methyl H	HD23	HA	HC	H140	0.0900	0.1000	0.0600	-0.0220	-0.0157	-0.0300	1.3200	1.4870	1.4031
bb C-term C	C	C	C	C235	0.5100	0.5973	0.5000	-0.1100	-0.0860	-0.1050	2.0000	1.9080	2.1046
bb C-term O	O	O	O	C236	-0.5100	-0.5679	-0.5000	-0.1200	-0.2100	-0.2100	1.7000	1.6612	1.6612

All parameters for the LEU residue are shown, including those for backbone (bb) N-terminal and C-terminal atoms, carbons (C) within the residue side chain, hydrogens attached to side chain carbons (C H), carbons of the side chain terminal methyl groups, and hydrogens of the side chain terminal methyl groups.

In the case of the LYS residue (Table 6.2), the ε and r_{min} parameters for the terminal amino hydrogens differ widely between the 3 FFs. For these atoms, the CHARMM22 FF makes use of a relatively deep potential well very close to the terminal H atoms. The AMBER94 FF uses a relatively shallow potential well with a minimum nearly 3 times further from the H atoms. The OPLS-AA FF disregards the ε and r_{min} parameters for H atoms entirely.

Table 6.2. FF parameters (q, ε, and r_{min}) for the LYS residue. Potential well depth (ε) values are in kcal/mole, where $\varepsilon_{i,j} = sqrt(\varepsilon_i * \varepsilon_j)$. Distance to potential minimum (rmin) values are in Å units, where $r_{min}(i,j)=(r_{min}/2)_i + (r_{min}/2)_j$.

LYS residue	Topology ID	CHARMM type	AMBER type	OPLS-AA type	*q* (e^- charge)			ε (kcal/mole)			r_{min}/2 (Å)		
					CHARMM	AMBER	OPLS-AA	CHARMM	AMBER	OPLS-AA	CHARMM	AMBER	OPLS-AA
bb N-term N	N	NH1	N	N238	-0.4700	-0.3479	-0.5000	-0.2000	-0.1700	-0.1700	1.8500	1.8240	1.8240
bb N-term H	HN	H	H	H241	0..31	0.2747	0.3000	-0.0460	-0.0157	0.0000	0.2245	0.6000	0.0000
bb alpha-C	CA	CT1	CT	C224	0.0700	-0.2400	0.1400	-0.0200	-0.1094	-0.0660	2.2750	1.9080	1.9643
bb alpha-C H	HA	HB	H1	H140	0.0900	0.1420	0.0600	-0.0220	-0.0157	-0.0300	1.3200	1.3870	1.4031
chain C	CB	CT2	CT	C136	-0.1800	-0.0094	-0.1200	-0.0550	-0.1094	-0.0660	2.1750	1.9080	1.9643
chain C H	HB1	HA	HC	H140	0.0900	0.0362	0.0600	-0.0220	-0.0157	-0.0300	1.3200	1.4870	1.4031
chain C H	HB2	HA	HC	H140	0.0900	0.0362	0.0600	-0.0220	-0.0157	-0.0300	1.3200	1.4870	1.4031
chain C	CG	CT2	CT	C136	-0.1800	0.0187	-0.1200	-0.0550	-0.1094	-0.0660	2.1750	1.9080	1.9643
chain C H	HG1	HA	HC	H140	0.0900	0.0103	0.0600	-0.0220	-0.0157	-0.0300	1.3200	1.4870	1.4031
chain C H	HG2	HA	HC	H140	0.0900	0.0103	0.0600	-0.0220	-0.0157	-0.0300	1.3200	1.4870	1.4031
chain C	CD	CT2	CT	C136	-0.1800	-0.0479	-0.1200	-0.0550	-0.1094	-0.0660	2.1750	1.9080	1.9643
chain C H	HD1	HA	HC	H140	0.0900	0.0621	0.0600	-0.0220	-0.0157	-0.0300	1.3200	1.4870	1.4031
chain C H	HD2	HA	HC	H140	0.0900	0.0621	0.0600	-0.0220	-0.0157	-0.0300	1.3200	1.4870	1.4031
chain C	CE	CT2	CT	C292	0.2100	-0.0143	0.1900	-0.0550	-0.1094	-0.0660	2.1750	1.9080	1.9643
chain C H	HE1	HA	HP	H140	0.0500	0.1135	0.0600	-0.0220	-0.0157	-0.0300	1.3200	1.1000	1.4031
chain C H	HE2	HA	HP	H140	0.0500	0.1135	0.0600	-0.0220	-0.0157	-0.0300	1.3200	1.1000	1.4031
term amino N	NZ	NH3	N3	N287	-0.3000	-0.3854	-0.3000	-0.2000	-0.1700	-0.1700	1.8500	1.8240	1.8240
term amino H	HZ1	HC	H	H290	0.3300	0.3400	0.3300	-0.0460	-0.0157	0.0000	0.2245	0.6000	0.0000
term amino H	HZ2	HC	H	H290	0.3300	0.3400	0.3300	-0.0460	-0.0157	0.0000	0.2245	0.6000	0.0000
term amino H	HZ3	HC	H	H290	0.3300	0.3400	0.3300	-0.0460	-0.0157	0.0000	0.2245	0.6000	0.0000
bb C-term C	C	C	C	C235	0.5100	0.7341	0.5000	-0.1100	-0.0860	-0.1050	2.0000	1.9080	2.1046
bb C-term O	O	O	O	C236	-0.5100	-0.5894	-0.5000	-0.1200	-0.2100	-0.2100	1.7000	1.6612	1.6612

All parameters for the LYS residue are shown, including those for backbone (bb) N-terminal and C-terminal atoms, carbons (C) within the residue side chain, hydrogens attached to side chain carbons (C H), nitrogen (N) of the side chain terminal amino group, and hydrogens of the side chain terminal amino group.

Parameters for the negatively charged -COO^- SAM surface terminal groups and the neutral, protonated -COOH surface terminal groups are presented in Table 6.3 and Table 6.4, respectively. For both of these terminal groups, the CHARMM22 FF's ε values for both the carboxyl carbon and the attached oxygens are lower in magnitude (indicating a shallower LJ potential well depth) than they are for both the AMBER94 and OPLS-AA

FFs. This relatively weaker LJ interaction places greater emphasis on partial charge assignments in maintaining tight interactions between adsorbed peptides and the surface functional groups. Specifically in the case of the -COO^- SAM surface terminal groups, the difference between the *q* values assigned to the carboxyl C and either of the attached O's is smaller in the CHARMM22 FF than they are in the AMBER94 and OPLS-AA FFs.

Table 6.3. FF parameters (q, ε, and r_{min}) for the deprotonated -COO^- SAM functional group. Potential well depth (ε) values are in kcal/mole, where $\varepsilon_{i,j} = sqrt(\varepsilon_i * \varepsilon_j)$. Distance to potential minimum (rmin) values are in Å units, where $r_{min}(i,j)=(r_{min}/2)_i + (r_{min}/2)_j$.

-$COO^{(-)}$ SAM functional group	Topology ID	CHARMM type	AMBER type	OPLS-AA type	*q* (e^- charge)			ε (kcal/mole)			r_{min}/2 (Å)		
					CHARMM	AMBER	OPLS-AA	CHARMM	AMBER	OPLS-AA	CHARMM	AMBER	OPLS-AA
terminal C	C1	CL	C	C271	0.6200	0.8054	0.7000	-0.0700	-0.0860	-0.1050	2.0000	1.9080	2.1046
carbonyl O	O1	OCL	O2	O272	-0.7600	-0.8188	-0.8000	-0.1200	-0.2100	-0.2100	1.7000	1.6612	1.6612
deprot O	O2	OCL	O2	O272	-0.7600	-0.8188	-0.8000	-0.1200	-0.2100	-0.2100	1.7000	1.6612	1.6612
alkane C	C2	CTL2	CT	C136	-0.2800	-0.1798	-0.1120	-0.0560	-0.1094	-0.0660	2.0100	1.9080	1.9643
alkane H	H2A	HAL2	HC	H140	0.0900	0.0060	0.0060	-0.0280	-0.0157	-0.0300	1.3400	1.4870	1.4031
alkane H	H2B	HAL2	HC	H140	0.0900	0.0060	0.0060	-0.0280	-0.0157	-0.0300	1.3400	1.4870	1.4031
alkane C	C3	CTL2	CT	C136	-0.1800	-0.0120	-0.0120	-0.0560	-0.1094	-0.0660	2.0100	1.9080	1.9643
alkane H	H3A	HAL2	HC	H140	0.0900	0.0060	0.0060	-0.0280	-0.0157	-0.0300	1.3400	1.4870	1.4031
alkane H	H3B	HAL2	HC	H140	0.0900	0.0060	0.0060	-0.0280	-0.0157	-0.0300	1.3400	1.4870	1.4031

This is a partial list of parameters for the -COO^- SAM surface residue, showing only the atoms that comprise the peptide-facing terminal functional group. Atoms shown include the terminal carbonyl carbon (C), the carbonyl oxygen (O), the deprotonated hydroxyl oxygen, and the alkane chain carbons and hydrogens closest to the terminal group.

Table 6.4. FF parameters (q, ε, and r_{min}) for the protonated -COOH SAM functional group. Potential well depth (ε) values are in kcal/mole, where $\varepsilon_{i,j} = sqrt(\varepsilon_i * \varepsilon_j)$. Distance to potential minimum (rmin) values are in Å units, where $r_{min}(i,j)=(r_{min}/2)_i + (r_{min}/2)_j$.

-COOH SAM functional group	Topology ID	CHARMM type	AMBER type	OPLS-AA type	*q* (e^- charge)			ε (kcal/mole)			r_{min}/2 (Å)		
					CHARMM	AMBER	OPLS-AA	CHARMM	AMBER	OPLS-AA	CHARMM	AMBER	OPLS-AA
terminal C	C1	CD	C	C267	0.7500	0.6801	0.5200	-0.0700	-0.0860	-0.1050	2.0000	1.9080	2.1046
carbonyl O	O1	OB	O	O269	-0.5500	-0.5838	-0.4400	-0.1200	-0.2100	-0.2100	1.7000	1.6612	1.6612
hydroxyl O	O2	OH1	OH	O268	-0.6100	-0.6511	-0.5300	-0.1521	-0.2104	-0.1700	1.7700	1.7210	1.6837
hydroxyl H	H2	H	HO	H270	0.4400	0.4641	0.4500	-0.0460	0.0000	0.0000	0.2245	0.6000	0.0000
alkane C	C2	CT2	CT	C136	-0.2100	0.0787	-0.1200	-0.0550	-0.1094	-0.0660	2.1750	1.9080	1.9643
alkane H	H2A	HA	HC	H140	0.0900	0.0060	0.0600	-0.0220	-0.0157	-0.0300	1.3200	1.4870	1.4031
alkane H	H2B	HA	HC	H140	0.0900	0.0060	0.0600	-0.0220	-0.0157	-0.0300	1.3200	1.4870	1.4031
alkane C	C3	CT2	CT	C136	-0.1800	-0.0120	-0.0120	-0.0550	-0.1094	-0.0660	2.1750	1.9080	1.9643
alkane H	H3A	HA	HC	H140	0.0900	0.0060	0.0060	-0.0220	-0.0157	-0.0300	1.3200	1.4870	1.4031
alkane H	H3B	HA	HC	H140	0.0900	0.0060	0.0060	-0.0220	-0.0157	-0.0300	1.3200	1.4870	1.4031

This is a partial list of parameters for the -COOH SAM surface residue, showing only the atoms that comprise the peptide-facing terminal functional group. Atoms shown include the terminal carbonyl carbon (C), the carbonyl oxygen (O), the hydroxyl oxygen and hydrogen (H), and the alkane chain carbons and hydrogens closest to the terminal group.

For the hydrophobic -CH_3 SAM surface terminal groups (Table 6.5), the partial charges of the methyl carbon and hydrogens in the CHARMM22 FF are of much greater magnitude than those of the AMBER94 and OPLS-AA while the ε values are similar, thus causing CHARMM to provide a stronger electrostatic component for the interactions of this SAM surface with atoms in the solution phase compared to AMBER and OPLS.

Table 6.5. FF parameters (q, ε, and r_{min}) for the -CH_3 SAM functional group. Potential well depth (ε) values are in kcal/mole, where $\varepsilon_{i,j} = sqrt(\varepsilon_i * \varepsilon_j)$. Distance to potential minimum (rmin) values are in Å units, where $r_{min}(i,j)=(r_{min}/2)_i + (r_{min}/2)_j$.

-CH3 SAM functional group	Topology ID	CHARMM type	AMBER type	OPLS-AA type	*q* (e^- charge)			ε (kcal/mole)			r_{min}/2 (Å)		
					CHARMM	AMBER	OPLS-AA	CHARMM	AMBER	OPLS-AA	CHARMM	AMBER	OPLS-AA
methyl C	C1	CT3	CT	C135	-0.2700	-0.1825	-0.1800	-0.0800	-0.1094	-0.0660	2.0600	1.9080	1.9643
methyl H	H1A	HA	HC	H140	0.0900	0.0603	0.0600	-0.0220	-0.0157	-0.0300	1.3200	1.4870	1.4031
methyl H	H1B	HA	HC	H140	0.0900	0.0603	0.0600	-0.0220	-0.0157	-0.0300	1.3200	1.4870	1.4031
methyl H	H1C	HA	HC	H140	0.0900	0.0603	0.0600	-0.0220	-0.0157	-0.0300	1.3200	1.4870	1.4031
alkane C	C2	CT2	CT	C136	-0.1800	-0.0104	-0.0120	-0.0550	-0.1094	-0.0660	2.1750	1.9080	1.9643
alkane H	H2A	HA	HC	H140	0.0900	0.0600	0.0060	-0.0220	-0.0157	-0.0300	1.3200	1.4870	1.4031
alkane H	H2B	HA	HC	H140	0.0900	0.0600	0.0060	-0.0220	-0.0157	-0.0300	1.3200	1.4870	1.4031

This is a partial list of parameters for the -CH_3 SAM surface residue, showing only the atoms that comprise the peptide-facing terminal functional group. Atoms shown include the terminal methyl carbon (C), the terminal methyl hydrogens (H), and the alkane chain carbons and hydrogens closest to the terminal group.

The next major component of a comparison of the performance of these FFs is the analysis of peptide structural characteristics sampled from the REMD simulations. Peptide amino acid secondary structure analysis was conducted using the STRIDE[149] utility. Water and ion diffusion calculations were completed using analysis features integral to the CHARMM (version c34b2) suite of simulation tools.[32] REMD simulation performance analysis was completed using analysis tools supplied with the MMTSB[33] package. Visualization software used during all stages of this work included Visual Molecular Dynamics (VMD),[150] and UCSF Chimera.[151]

Contributions to the final, complete low temperature ensemble of structures by the various starting conformations were evenly distributed amongst those starting conformations. In other words, no particular starting conformation contributed

proportionally more than any other starting conformation, indicating that the REMD procedure was functioning as intended for these systems; see Figures B-1 (CHARMM) and C-1 (AMBER, OPLS). Generally, the peptide secondary structure and orientation analyses for each peptide-surface system showed that the simulations represent the experimentally-determined behavior for each of the three FFs.[21, 136-138] In particular, the structural conformations obtained using the CHARMM22 FF were most clearly in agreement with the experimental findings. Additionally, the structural results from the peptide-solution simulations are supported by experimental findings,[55] which have shown that the LKβ7 peptides eventually precipitate out of solution, and that β-sheet conformations are attained at low peptide concentrations where peptide pairs had matching side chain periodicity (as in the case of the two identical LKβ7 peptides). In the absence of peptides with matching periodicity, lone LKb7 peptides have been shown to adopt a helical conformation. Also, the LKα14 peptide has been shown, experimentally, to consistently adopt a helical conformation in solution. The level of structural detail available through the simulations is far greater than that available through the experimental results. For example, the experimental results confirm the overall adsorption orientation of the peptides, as well as the relative affinity of the each amino acid of a given peptide for a given surface. However, the experimental results provide a very general framework of validation for the simulation results that enables conclusions to be drawn about the relative accuracy of each FF's representation of the simulated systems. For all REMD simulations, the duplicate simulations produced

closely matching results (see Appendices B and C for figures from duplicate simulations), indicating consistency of the results obtained for each simulation.

Solution Structures of the LKα14 and LKβ7 Peptides

In solution (no surface present), the LKβ7 pair of peptides did not adopt a particular secondary structure motif with any of the FFs used. There is variation in the structure of these peptides ranging from random coil to slightly helical conformations, with CHARMM favoring random structure, AMBER favoring a higher population of helix and turn conformations, and OPLS favoring a greater population of β-sheet-like conformations. A comparison of the FFs based on the fraction of the REMD 298 K ensemble that adopted a random coil conformation (Figure 6.2) shows distinct differences between the FFs, even where similar conformations are preferred.

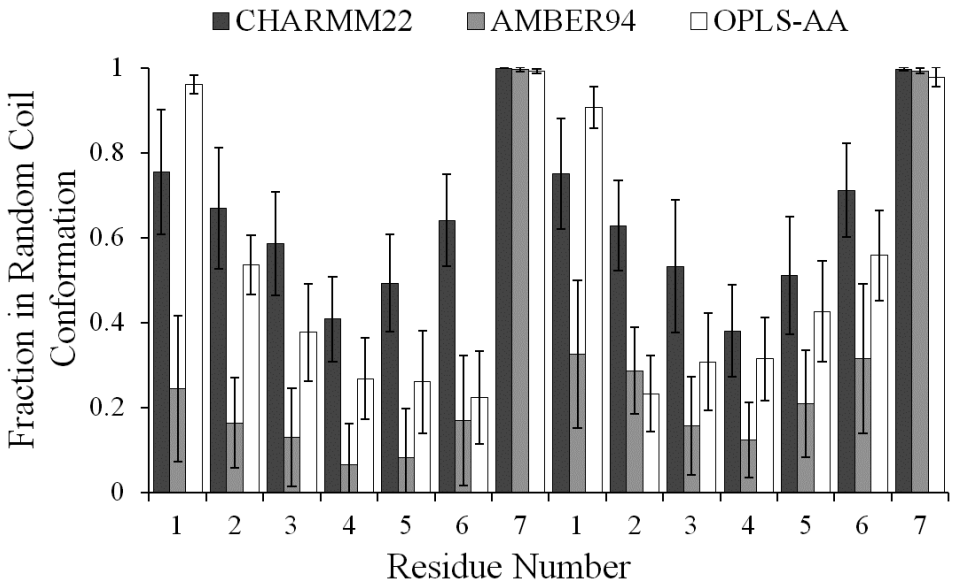

Figure 6.2: Plot comparing the fraction of the REMD 298 K ensemble adopting a random coil conformation for each FF in simulating the pair of LKβ7 peptides in solution. Each column represents 12 independent 1 ns block averages with the error bars representing 95% confidence intervals (n=12) taken from pooled results from the duplicated 6 ns REMD production runs (12 ns total, therefore twelve 1 ns blocks).

Being quite small, it is apparent that these peptides lack the kind of internal structure that the LKα14 has to stabilize its secondary conformational structure. Analyses of secondary structure through the course of the REMD simulation provides some insight into if and how their structural tendencies evolved (Figure 6.3).

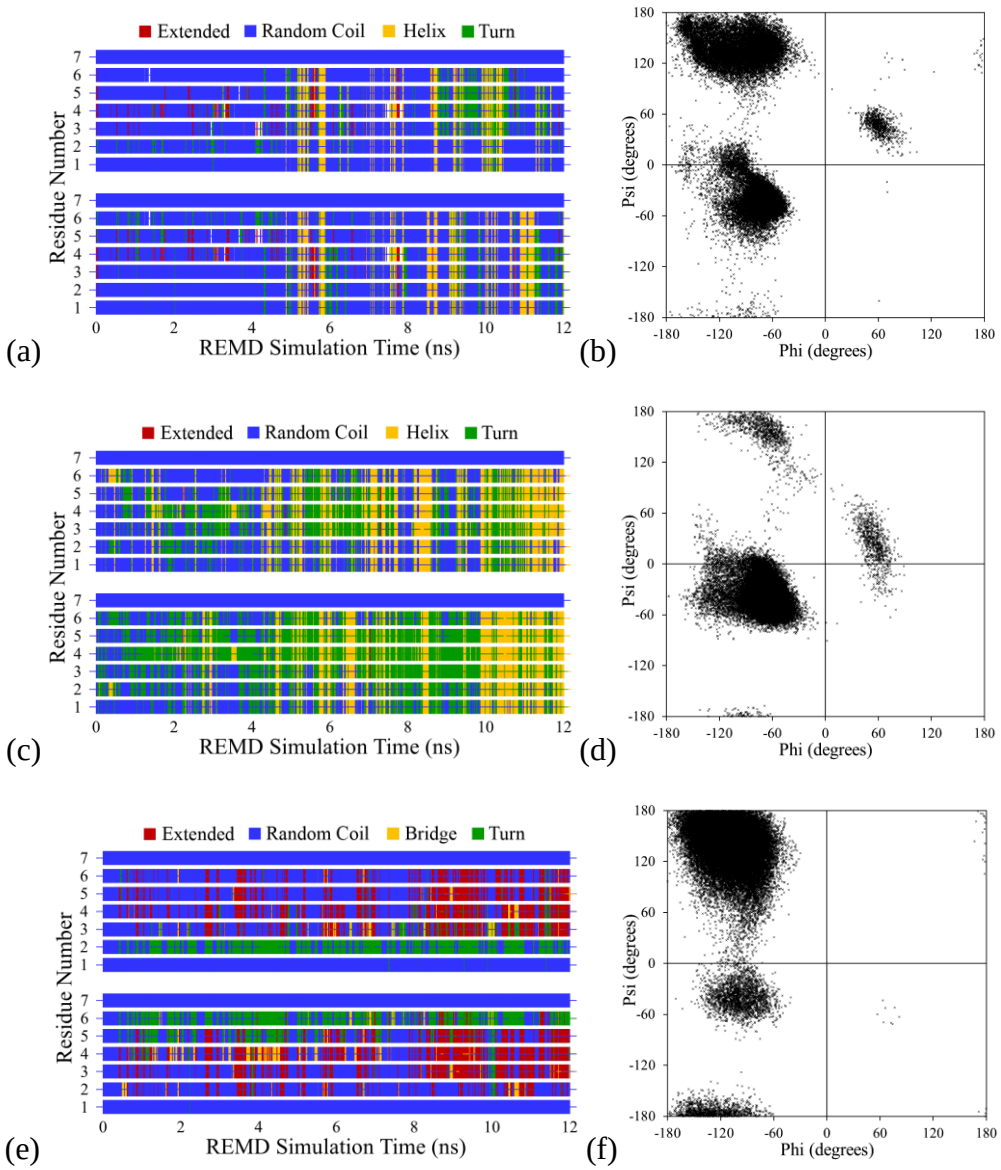

Figure 6.3: Plots of secondary structure for each amino acid residue through the entire REMD simulation (plots a, c, e) and Ramachandran plots of the phi/psi peptide backbone dihedral angles (plots b, d, f) for the pair of LKβ7 peptides in solution using (a,b) the CHARMM22 FF, (c,d) the AMBER94 FF, and (e,f) the OPLS-AA FF. The Ramachandran plots represent structures from the final 6 ns of REMD sampling.

The solution conformation for the LKα14 peptide when using the CHARMM22 and AMBER94 FFs is predominantly α-helical, with the AMBER94 FF permitting some

deviation from helical conformations (Figure 6.4). The OPLS-FF presents the solution conformation of the LKα14 Peptide as being mostly a random coil conformation, with a large number of 3_{10}-helix conformations appearing throughout the simulation. The differences between the FFs in representing the LKα14 peptide with helical structure are summarized in Figure 6.5.

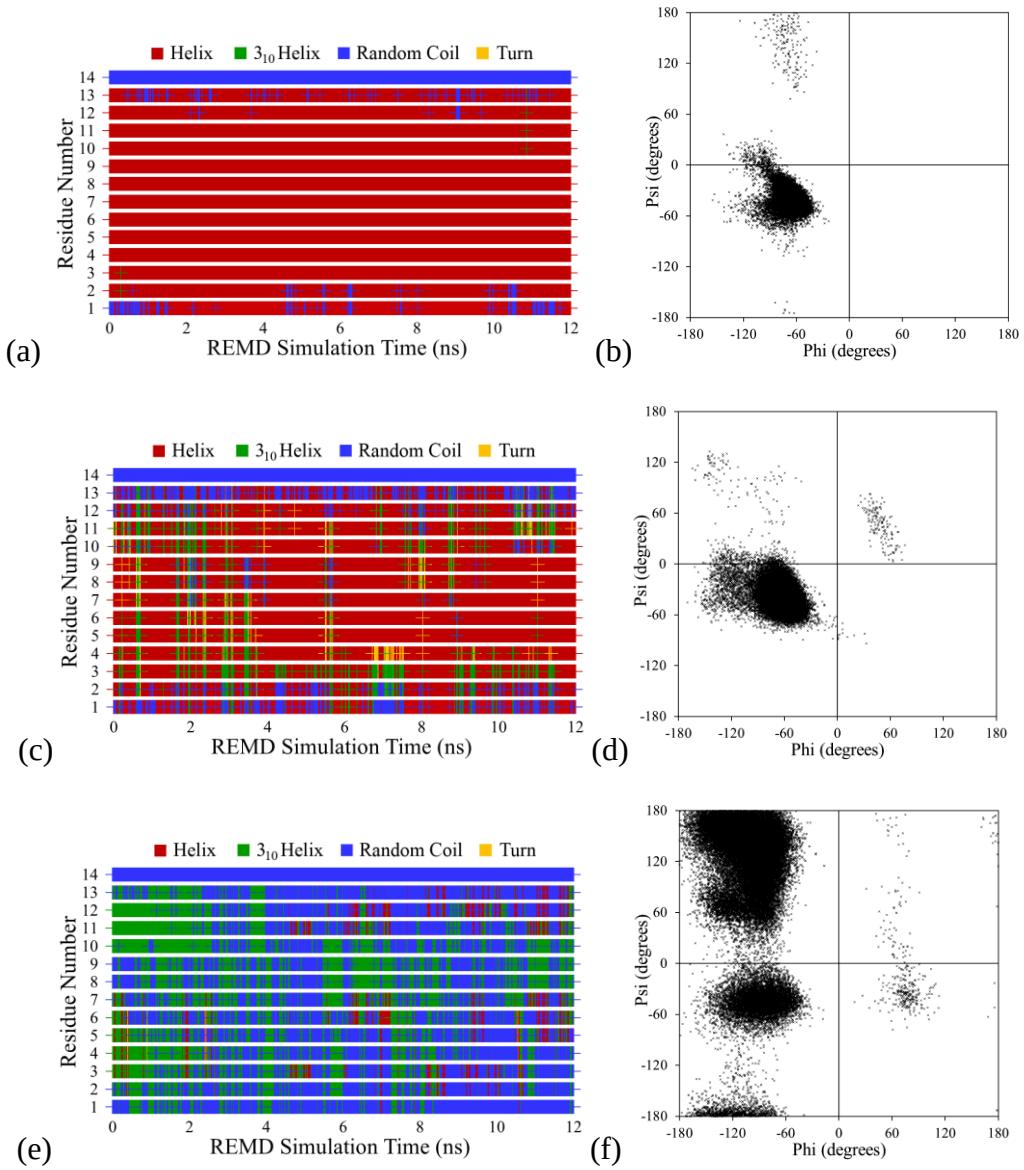

Figure 6.4: Plots of secondary structure for each amino acid residue through the entire REMD simulation (plots a, c, e) and Ramachandran plots of the phi/psi peptide backbone dihedral angles (plots b, d, f) for the LKα14 peptide in solution using (a,b) the CHARMM22 FF, (c,d) the AMBER94 FF, and (e,f) the OPLS-AA FF. The Ramachandran plots represent structures from the final 6 ns of REMD sampling.

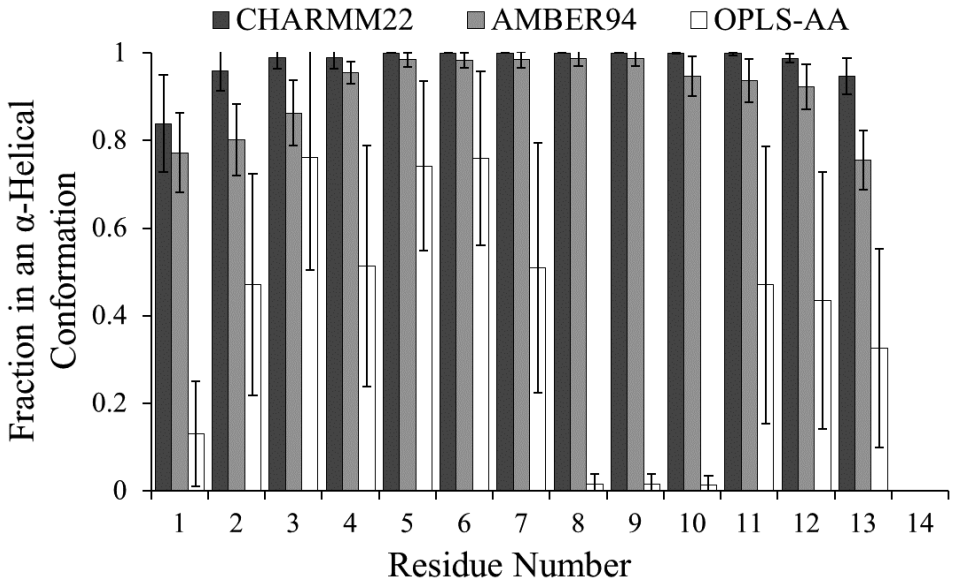

Figure 6.5: Plot comparing the fraction of the REMD 298 K ensemble adopting an α-helical conformation for each FF in simulating the LKα14 peptide in solution. Each column represents 12 independent 1 ns block averages with the error bars representing 95% confidence intervals (n=12) taken from pooled results from the duplicated 6 ns REMD production runs (12 ns total, therefore twelve 1 ns blocks).

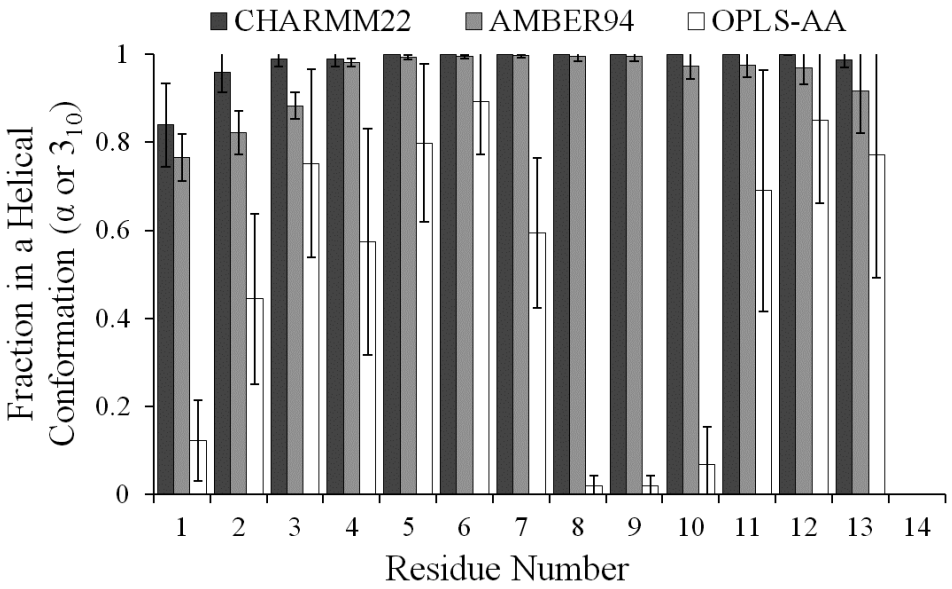

Figure 6.6: Plot comparing the fraction of the REMD 298 K ensemble adopting an α-helical or 3_{10}-helical conformation for each FF in simulating the LKα14 peptide in solution. Each column represents 12 independent 1 ns block averages with the error bars representing 95% confidence intervals (n=12) taken from pooled results from the duplicated 6 ns REMD production runs (12 ns total, therefore twelve 1 ns blocks).

The LKβ7 Pair Adsorbed to the CH_3-SAM

When adsorbed to the CH_3-SAM, the CHARMM22 FF predicts that these peptides deviate from their random coil solution structure and adopting a consistent extended β-strand conformation (Figure 6.7a). The AMBER FF produces a slight shift away from its helical solution conformation toward a more random conformation (Figure 6.7c). The OPLS-AA FF pushes the conformation away from a weakly extended β-strand conformation in solution toward a more random conformation when adsorbed (Figure 6.7e). Ramachandran plots of phi/psi backbone dihedral angles indicate the final conformation populations; that is, the conformations added to the ensemble of structures during the final 6 ns of the REMD simulations. The phi/psi angles produced for the

LKβ7 peptides on the CH_3-SAM surface using the CHARMM22 FF show a distinct β-strand conformation, with minor populations of both right- and left-handed helical conformations (Figure 6.7b). The AMBER94 FF tended strongly toward a helical conformation (Figure 6.7d), possibly due to the relatively deep LJ potential well locking the helical solution structures to the surface without allowing for the unwinding of the small helix. The OPLS-AA FF emphasized a blend of random and β-strand conformations (Figure 6.7f), reflecting the much weaker LJ interactions between the LEU side chain termini and the surface. The overall differences between the FFs in representing the adsorbed pair of LKβ7 peptides as extended β-strands are summarized in Figure 6.8.

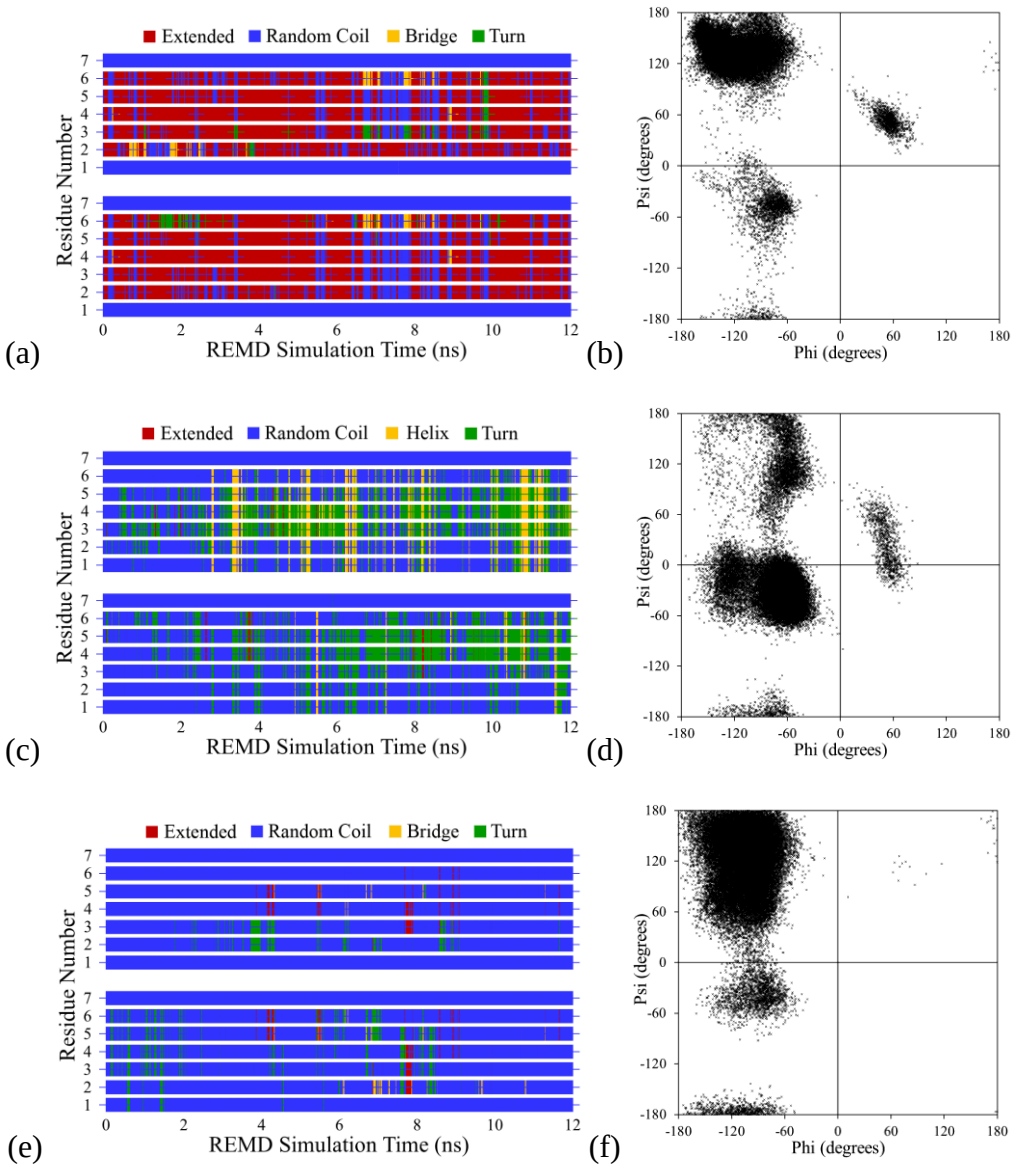

Figure 6.7: Plots of secondary structure for each amino acid residue through the entire REMD simulation (plots a, c, e) and Ramachandran plots of the phi/psi peptide backbone dihedral angles (plots b, d, f) for the LKβ7 pair of peptides adsorbed to the CH_3-SAM using (a,b) the CHARMM22 FF, (c,d) the AMBER94 FF, and (e,f) the OPLS-AA FF. The Ramachandran plots represent structures from the final 6 ns of REMD sampling, 3,000 points displayed for each non-terminal amino acid.

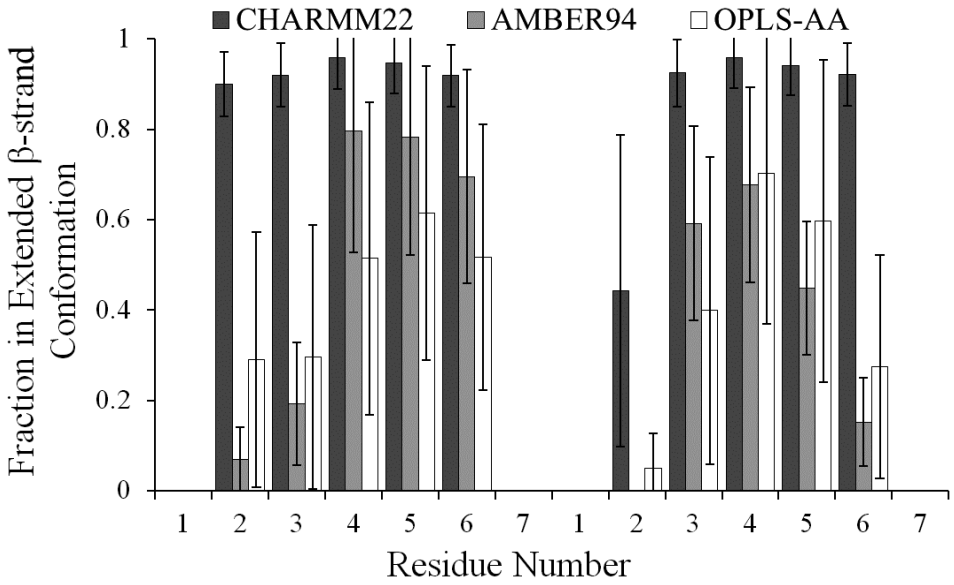

Figure 6.8: Plot comparing the fraction of the REMD 298 K ensemble adopting an extended β-strand conformation for each FF in simulating the pair of LKβ7 peptides adsorbed to the CH_3-SAM. Each column represents 12 independent 1 ns block averages with the error bars representing 95% confidence intervals (n=12) taken from pooled results from the duplicated 6 ns REMD production runs (12 ns total, therefore twelve 1 ns blocks).

Measurements of distances between the terminal backbone carbons of the LKβ7 pair were used to study the formation of β-sheets over the CH_3-SAM (Figure 6.9), but only the CHARMM22 FF showed the development of this type of arrangement with the formation of an antiparallel β-sheet structure (the more energetically favorable β-sheet structure). The difference in FF parameters assigned to the CH_3-SAM terminal group atoms, coupled with the differences in the parameters for the LEU residue terminal groups (Table 6.1) help explain the greater amount of deviation in the LEU side chain terminal methyl groups' distance from the hydrophobic CH_3-SAM, shown in Figures 6.10a, 6.10c, and 6.10e. Additionally, the balance between the CHARMM22 FF's LEU

parameters and the CH_3-SAM's terminal groups may be the key to enabling the LKβ7 peptides to form stable β-sheet structures when adsorbed to this surface.

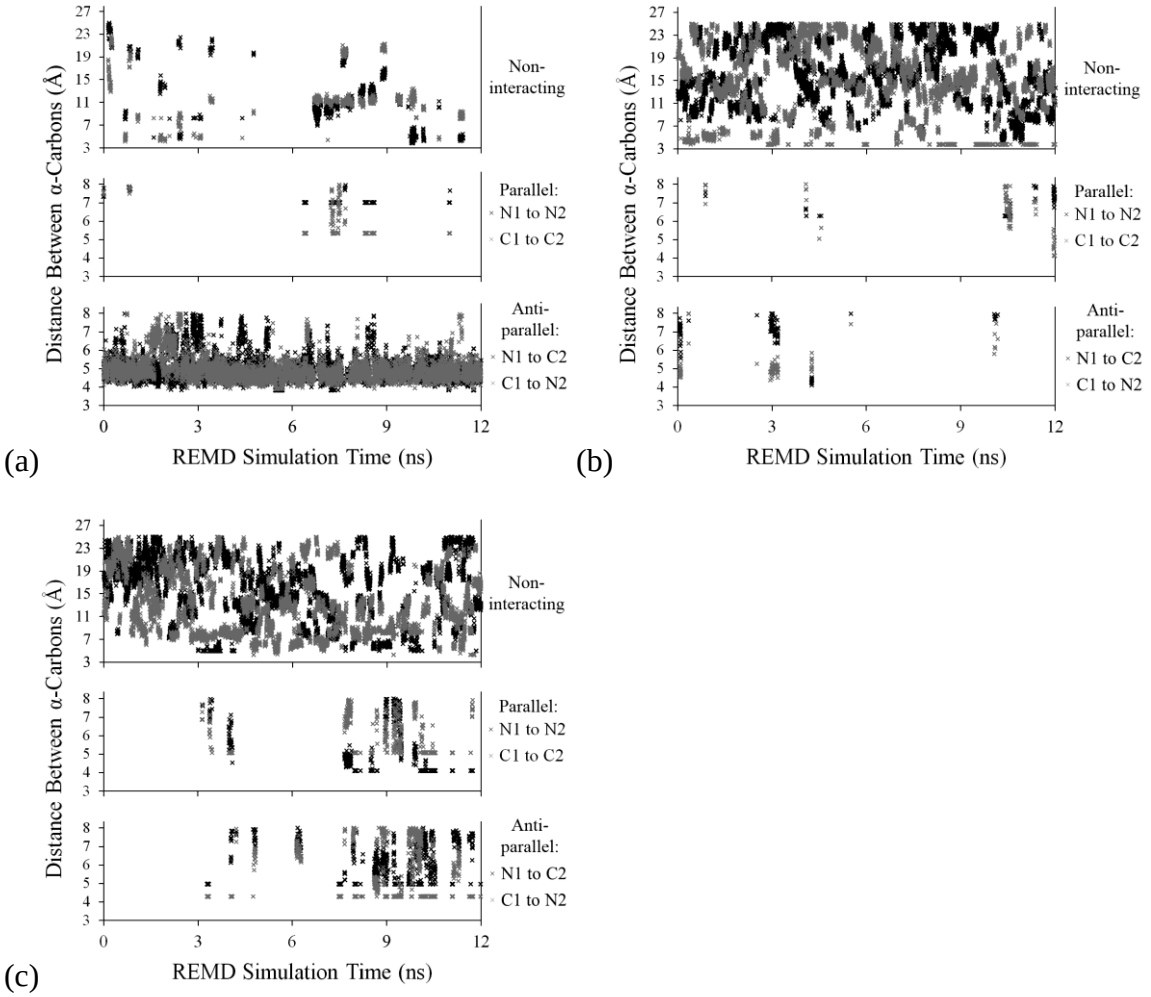

Figure 6.9: Plots of distances between terminal α-carbons (indicative of parallel and antiparallel conformations) for the pair of LKβ7 peptides adsorbed to the CH_3-SAM during the entire REMD simulation for (a) the CHARMM22 FF, (b) the AMBER94 FF, and (c) the OPLS-AA FF.

Evaluating the adsorption characteristics of the peptides to the SAM surfaces involved measurements of the distance between each amino acid residue's side-chain terminus and the plane of topmost alkyl carbon atoms of each SAM's alkyl chains. Specifically, the L group's side-chain terminus was defined as the geometrical center of

the 2 methyl groups at the end of that amino acid's side chain (this approach accommodates rotation of those groups), and the K group's side-chain terminus was defined as the nitrogen atom at the end of that amino acid's side chain. The surface separation distance (SSD) of these groups provides the most direct measure of peptide orientation amenable to adsorption. Measurements of the side chain SSDs for the LKβ7 pair of peptides show that the arrangement of side chains relative to the surface of the CH_3-SAM is consistent with the CHARMM22 and OPLS-AA FFs, with both L and K groups staying in narrow ranges of distances (approximately 3 and 5 Å, respectively) from the surface (Figures 6.10a and 6.10e), while the AMBER94 FF seemed to create a less tightly-bound adsorption arrangement with more variability in side chain SSDs (Figure 6.10c).

Naturally, in the absence of anchoring to any fixed structure, the side chains most distant from the SAM surface functional groups will vary in their SSDs much more than side chains participating in surface adsorption. Additionally, variability in the SSDs of adsorbing side chains can result in amplified variability for the SSDs of the non-adsorbing side chains. Therefore, variability in the SSDs of the adsorbing side chains was the focus of this analysis.

Another method used for evaluating the adsorption characteristics of the peptides was an analysis of the side chain tilt angles. Here, the tilt angle of a peptide side chain was considered to be the angle between the surface normal and the vector originating at the side chain α-carbon and directed toward the terminal group (as defined for the SSD measurements) of that side chain. As with the side chain SSD measurements, the tilt

angle measurement populations for the LKβ7 pair of peptides adsorbed to the CH_3-SAM are well-ordered for the CHARMM22 and OPLS-AA FFs (Figures 6.10b and 6.10f), but much less ordered for the AMBER FF (Figure 6.10d).

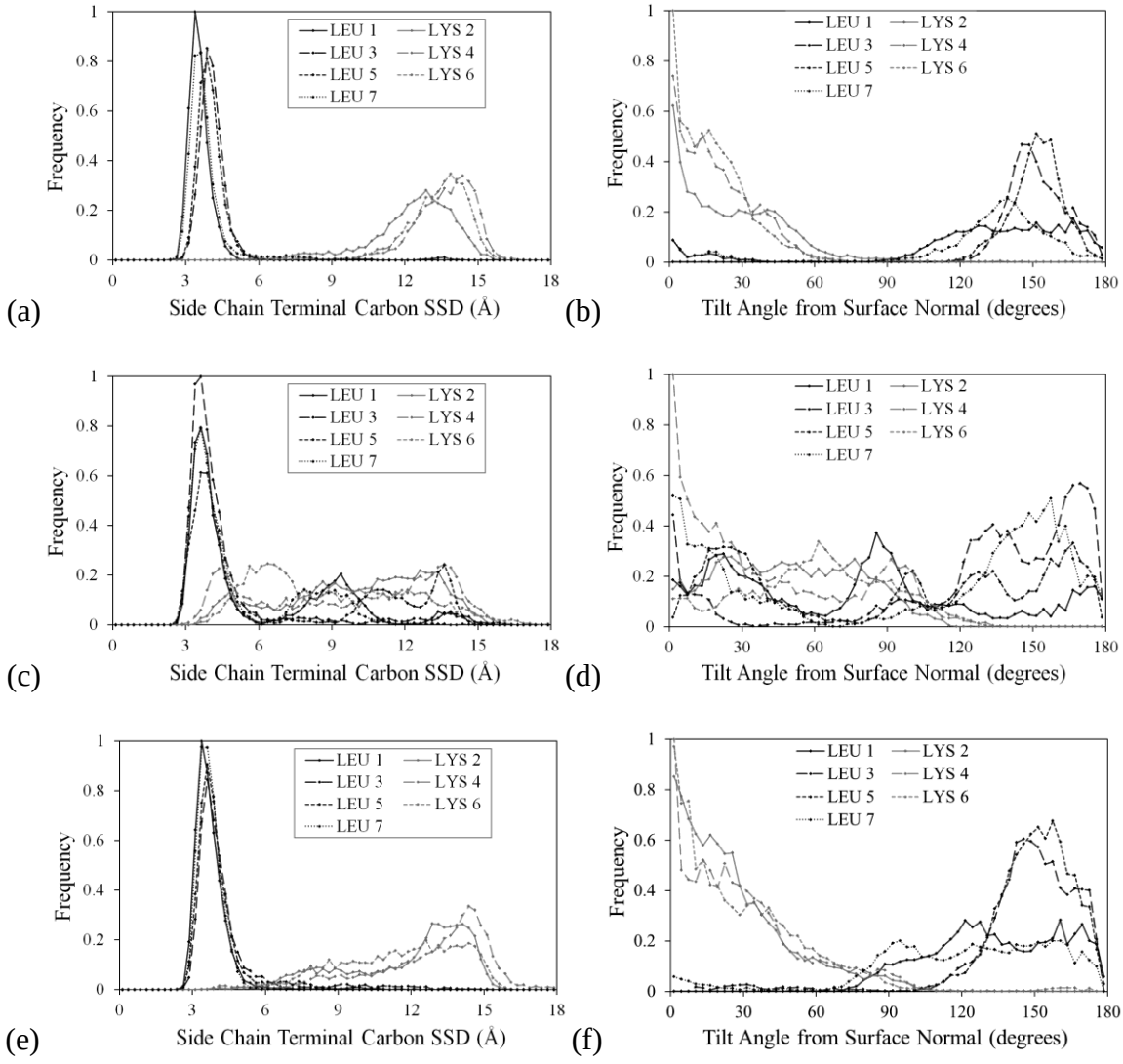

Figure 6.10: Plots of frequency distributions of amino acid side chain terminal carbon surface separation distances (SSD) (plots a, c, e) and amino acid side chain tilt angles (tilt away from the normal vector of the SAM surface) (plots b, d, f) for the pair of LKβ7 peptides adsorbed to the CH_3-SAM during the last 6 ns of REMD sampling using (a,b) the CHARMM22 FF, (c,d) the AMBER94 FF, and (e,f) the OPLS-AA FF. 3,000 SSD measurements for each amino acid, with a 0.25 Å bin width. Tilt angle plots normalized for the number of counts per 3-degree bin and sinusoidal distribution of measurements.

For the CHARMM22 and OPLS-AA simulations, the distribution of L side chain tilt angles, particularly for the two located in the center of the peptide, is consistently in the 140° to 160° range. This observation, coupled with visualization of MD trajectory frames from the simulations, indicates a tendency of the individual L side chains to adsorb to the CH_3-SAM surface with one of their two terminal methyl groups arranged at closest approach to one of the surface methyl groups (thus, the side chain is tilted, rather than being oriented perpendicular to the surface). This arrangement seems to be that of a water-excluding point-to-point interaction where the interacting peaks of hydrophobicity (i.e., the water-excluding methyl groups) serve as points of contact between the peptide and the surface.

The LKβ7 Pair Adsorbed to the COOH-SAM

When adsorbed to the COOH-SAM, the LKβ7 peptides do not adopt a particular secondary structure motif with any of the FFs used (Figure 6.11). In all cases, there is little change from a random coil conformation. Adsorption of hydrophobic groups to a hydrophobic surface through water exclusion tends to be a stronger, less reversible interaction than that between charged groups and a charged surface in the presence of counter-ions. Therefore, it is not surprising that these small peptides are not consistently fixed in any particular conformation. In this peptide-surface system, the electrostatic interactions between the water molecules or sodium ions and the negatively charged surface functional groups is sufficiently strong to overcome or prevent most interactions between the positively charged peptide side chains and the surface. For each FF, the parameters assigned to a TIP3 water molecule include the oxygen's q value of -0.834,

with an ε of -1.52 kcal/mol, and each hydrogen's *q* of 0.417, with an ε of -0.046 kcal/mol (or 0 kcal/mol, in the case of AMBER94). Comparing these parameters to those of the terminal amino group of the LYS residue (Table 6.2), one can see that the amino group's net charge of 0.69 (CHARMM22 and OPLS-AA) or 0.6346 (AMBER94), with a nitrogen atom ε value of -1.7 (AMBER94 and OPLS-AA) or -2.0 kcal/mol (CHARMM22), would have some difficulty overcoming the attraction of a counter ion or a TIP3 water molecule to the surface charges. This explains why these small peptides, which lack the structural stability of the larger LKα14 peptide, failed to interact strongly with the COOH-SAM surface. Analysis of the backbone phi/psi angles shows matching conformations to those found near the CH_3-SAM, but with greater diversity in conformations explored (more diffuse clusters of points on the plots). Additionally, for each FF, there is a larger population of helical conformations amongst the conformations explored. The overall differences between the FFs in representing the adsorbed pair of LKβ7 peptides in random coil conformations are summarized in Figure 6.12.

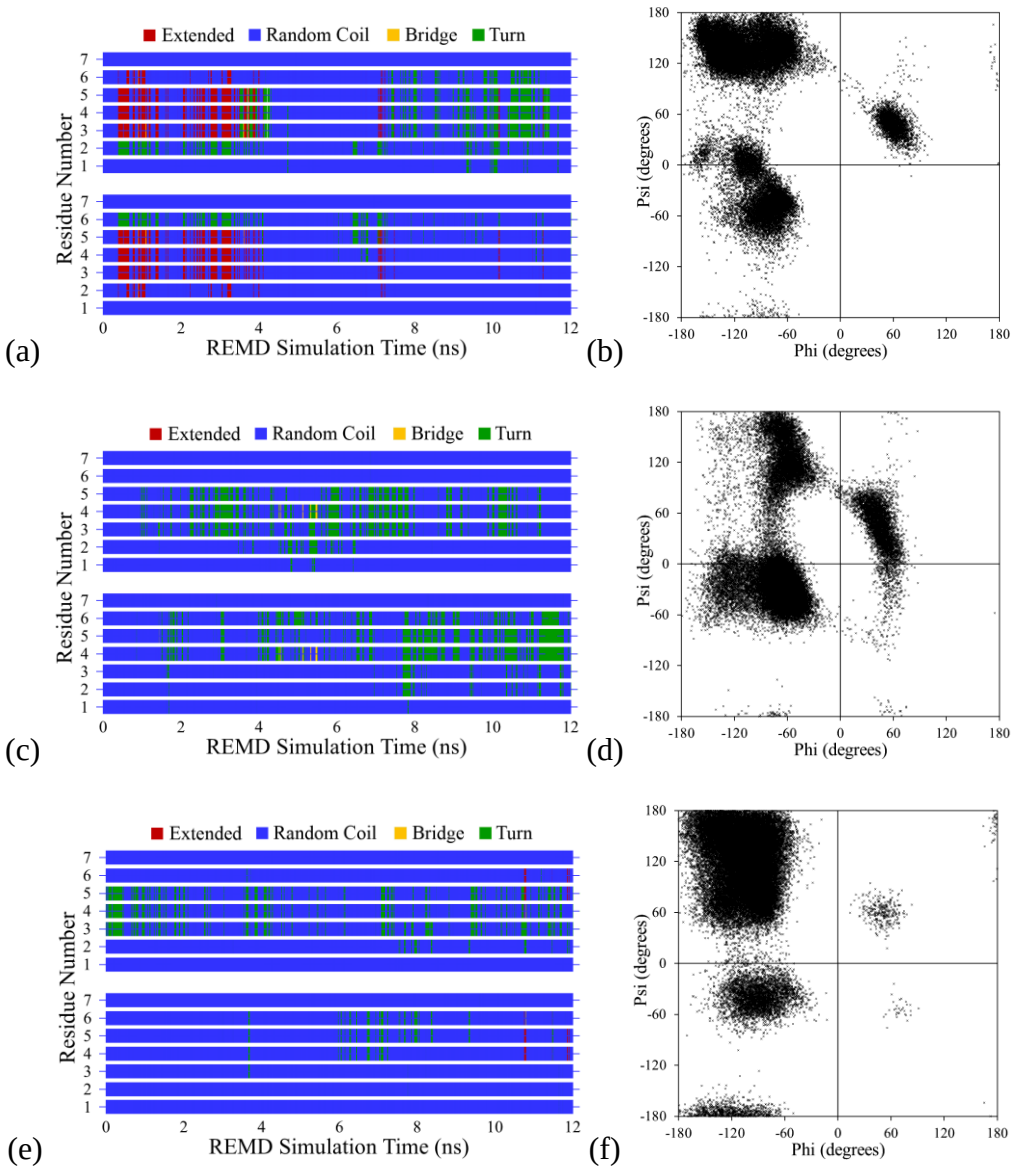

Figure 6.11: Plots of secondary structure for each amino acid residue through the entire REMD simulation (plots a, c, e) and Ramachandran plots of the phi/psi peptide backbone dihedral angles (plots b, d, f) for the pair of LKβ7 peptides adsorbed to the COOH-SAM using (a,b) the CHARMM22 FF, (c,d) the AMBER94 FF, and (e,f) the OPLS-AA FF. The Ramachandran plots represent structures from the final 6 ns of REMD sampling, 3,000 points displayed for each non-terminal amino acid.

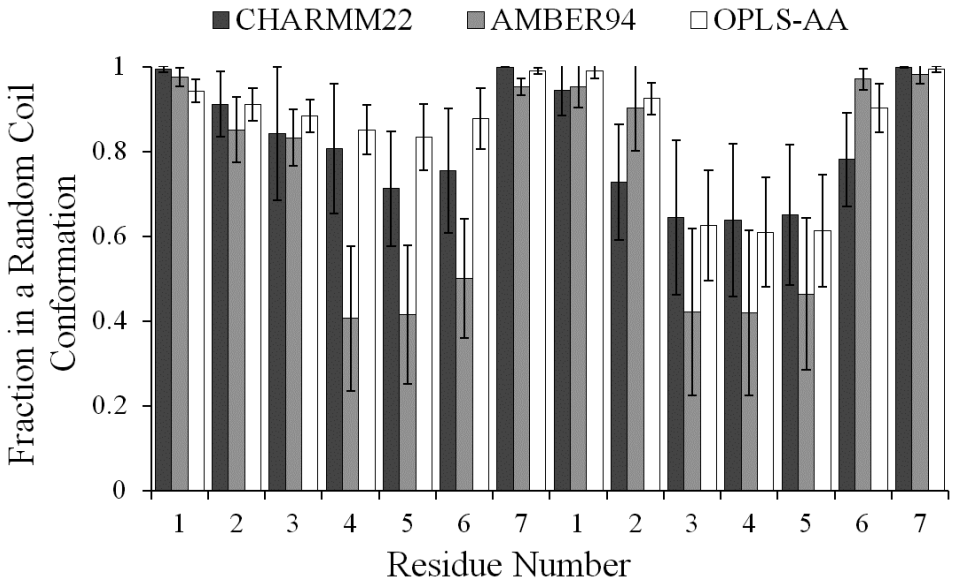

Figure 6.12: Plot comparing the fraction of the REMD 298 K ensemble adopting a random coil conformation for each FF in simulating the pair of LKβ7 peptides adsorbed to the COOH-SAM. Each column represents 12 independent 1 ns block averages with the error bars representing 95% confidence intervals (n=12) taken from pooled results from the duplicated 6 ns REMD production runs (12 ns total, therefore twelve 1 ns blocks).

Measurements of distances between the terminal backbone carbons of the LKβ7 pair over the COOH-SAM (Figure 6.13) indicated that there was virtually no tendency to form an antiparallel or a parallel β-sheet structure.

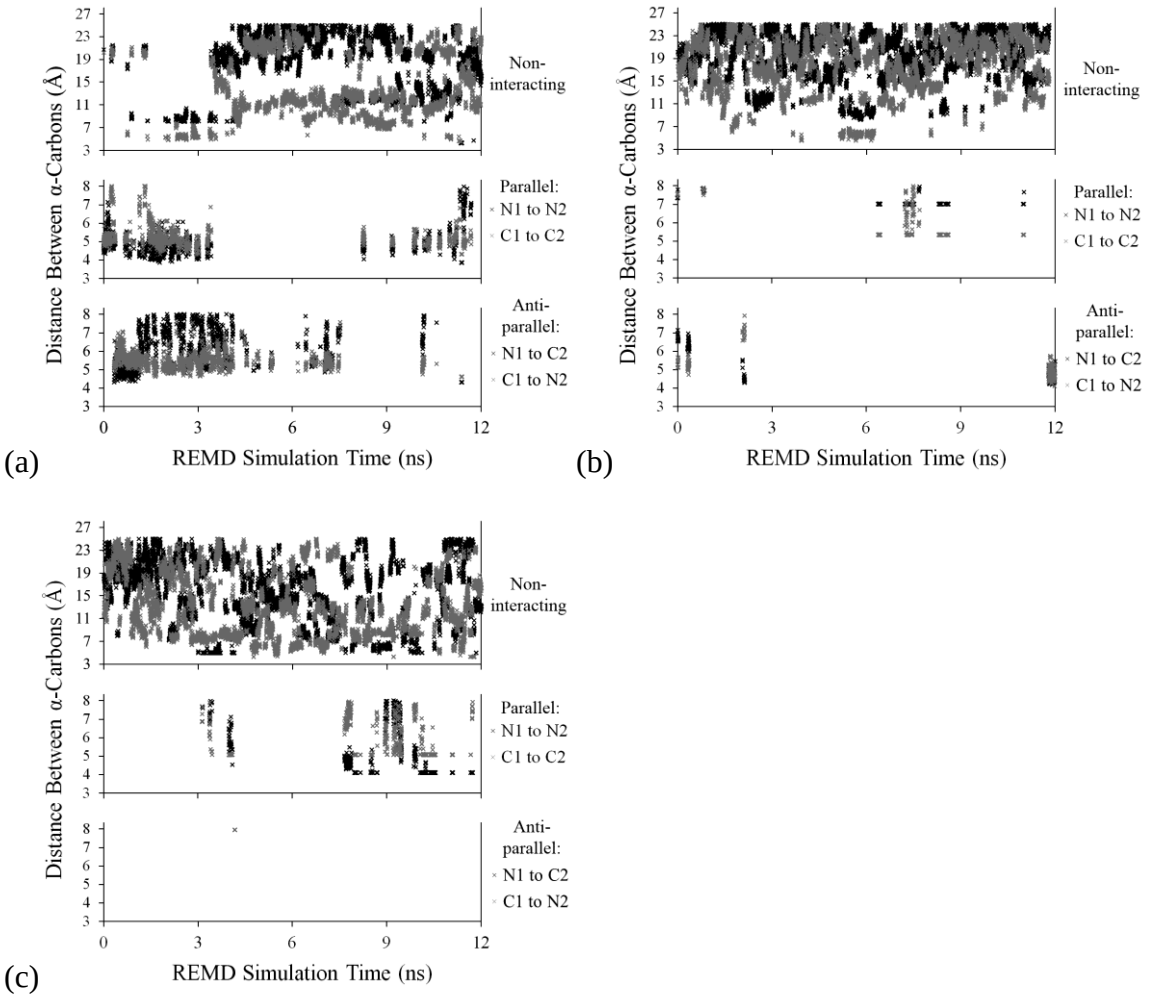

Figure 6.13: Plots of distances between terminal α-carbons (indicative of parallel and antiparallel conformations) for the pair of LKβ7 peptides adsorbed to the COOH-SAM during the entire REMD simulation for (a) the CHARMM22 FF, (b) the AMBER94 FF, and (c) the OPLS-AA FF.

Measurements of the side chain SSDs for the LKβ7 peptides adsorbed to the COOH-SAM were a well-ordered inverse of the same measurements near the CH_3-SAM, but in this case the AMBER FF resulted in data similar to that of the other FFs. The K side chain SSDs fell within a narrow 2-3 Å range centered at approximately 2 Å from the surface (Figures 6.14a,c,e). The L side chain SSDs covered a very broad range of

values, indicating greater movement of the peptide backbones while adsorbed to this surface.

The tilt angle measurement populations for the LKβ7 side chains adsorbed to the COOH-SAM were similar to one another (Figures 6.14b,d,f), as was the case for the other analyses of these systems. The distribution of adsorbing K side chain tilt angles was centered between 150° and 170°, rather than being centered at 180°, indicating that these peptides lie along the surface slightly tilted to one side.

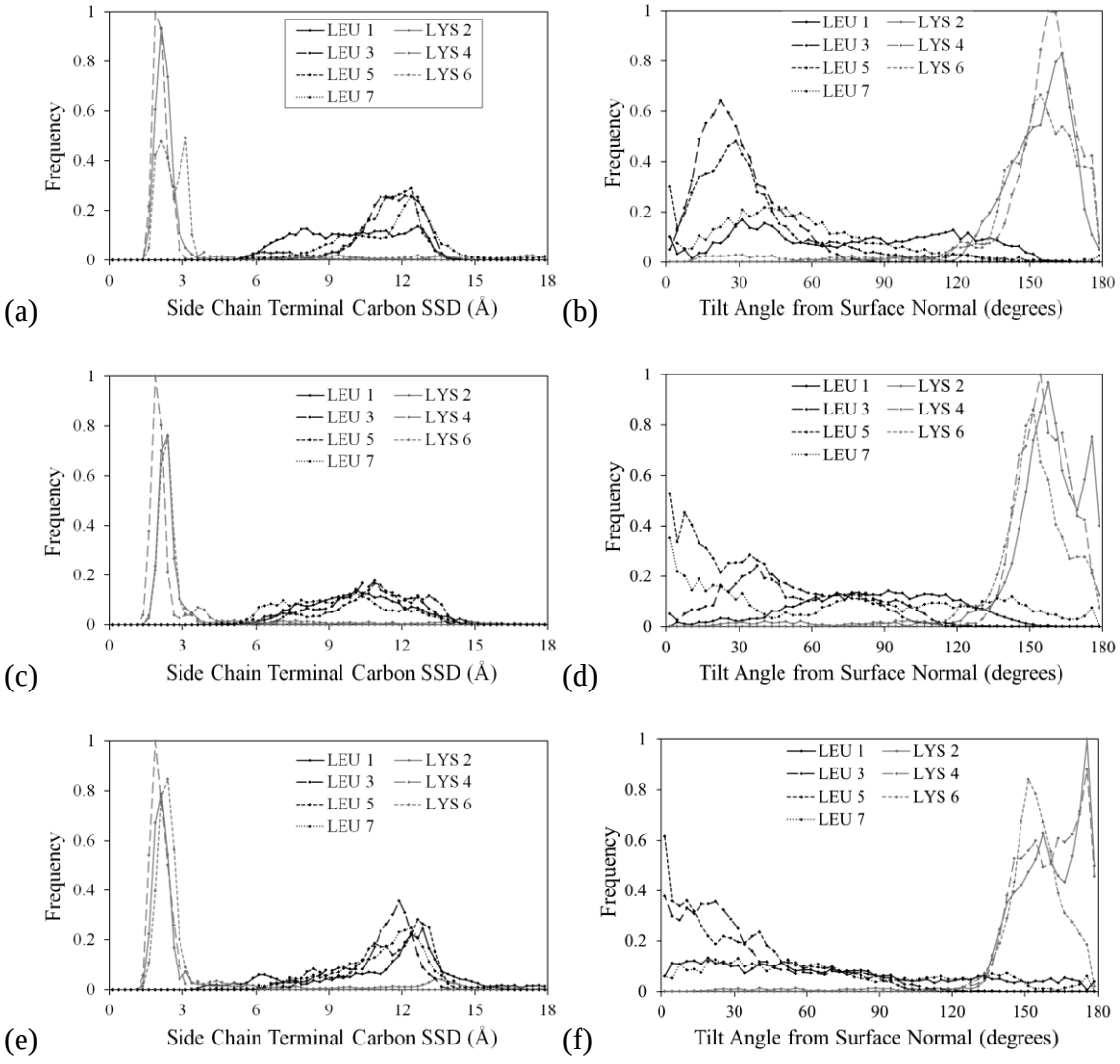

Figure 6.14: Plots of frequency distributions of amino acid side chain terminal carbon surface separation distances (SSDs) (plots a, c, e) and amino acid side chain tilt angles (tilt away from the normal vector of the SAM surface) (plots b, d, f) for the pair of LKβ7 peptides adsorbed to the COOH-SAM during the last 6 ns of REMD sampling using (a,b) the CHARMM22 FF, (c,d) the AMBER94 FF, and (e,f) the OPLS-AA FF. 3,000 SSD measurements for each amino acid, with a 0.25 Å bin width. Tilt angle plots normalized for the number of counts per 3-degree bin and sinusoidal distribution of measurements.

The LKα14 Peptide Adsorbed to the CH_3-SAM

When adsorbed to the CH_3-SAM, the LKα14 peptide maintains a predominantly helical conformation with all three FFs, but the nature of that helical conformation varies amongst the different FFs. The CHARMM22 FF presents a strongly and consistently α-helical conformation throughout the simulation (Figure 6.15a), which matches the solution structure conformations for that FF, and most closely matches experimental findings.[21, 136-138] As in the case of the LKβ7 peptides, it appears that the interplay of the LEU residue and surface methyl group parameters are appropriately balanced in the CHARMM22 FF to permit strong binding of the peptide with minimal disruption of the peptide's internal structure. The AMBER94 FF shows this peptide deviating from an α-helical conformation toward that of a 3_{10}-helix or a random coil (Figure 6.15c) more often than is the case for the solution structure produced using that FF. This behavior might be attributed to the stronger, more rigid interaction between the LEU groups and the surface methyl groups due to the AMBER94 FF's more intense (more negative) ε values. The OPLS-AA FF results in conformations ranging from random coil to 3_{10}-helix and some α-helix (Figure 6.15e), possibly due to this FF's relatively weak ε values. Analysis of the backbone phi/psi angles shows conformations generated using the CHARMM22 and AMBER94 FFs to be distinctly helical (Figures 6.15b and 6.15d), with the AMBER94 population of phi/psi data points being more diffuse. The OPLS-AA phi/psi angles (Figure 6.15f) are similar to those for the LKβ7 peptides, but with many more helical conformations included. The overall differences between the FFs in representing the adsorbed LKα14 peptide in an α-helical conformation are summarized in

Figure 6.16. Differences between the FFs in representing the adsorbed LKα14 peptide in an α-helical or 3_{10}-helical conformation are summarized in Figure 6.17.

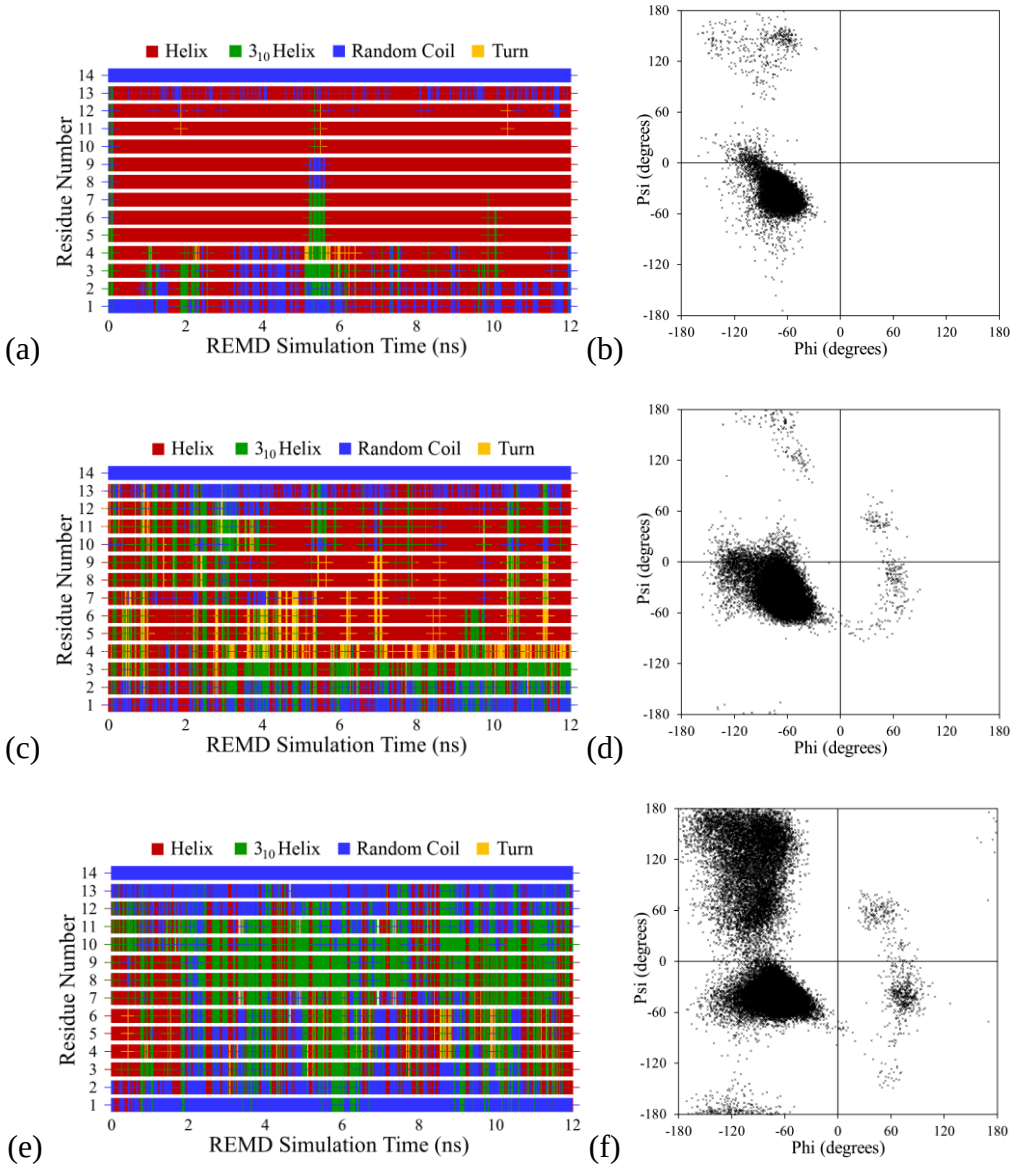

Figure 6.15: Plots of secondary structure for each amino acid residue through the entire REMD simulation (plots a, c, e) and Ramachandran plots of the phi/psi peptide backbone dihedral angles (plots b, d, f) for the LKα14 peptide adsorbed to the CH_3-SAM using (a,b) the CHARMM22 FF, (c,d) the AMBER94 FF, and (e,f) the OPLS-AA FF. The Ramachandran plots represent structures from the final 6 ns of REMD sampling, 3,000 points displayed for each non-terminal amino acid.

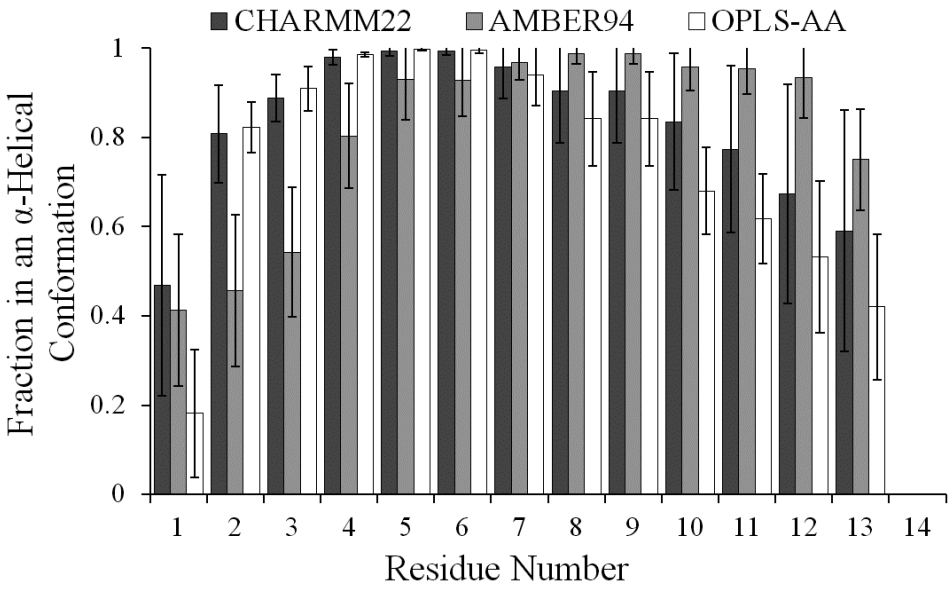

Figure 6.16: Plot comparing the fraction of the REMD 298 K ensemble adopting an α-helical conformation for each FF in simulating the LKα14 peptide adsorbed to the CH_3-SAM. Each column represents 12 independent 1 ns block averages with the error bars representing 95% confidence intervals (n=12) taken from pooled results from the duplicated 6 ns REMD production runs (12 ns total, therefore twelve 1 ns blocks).

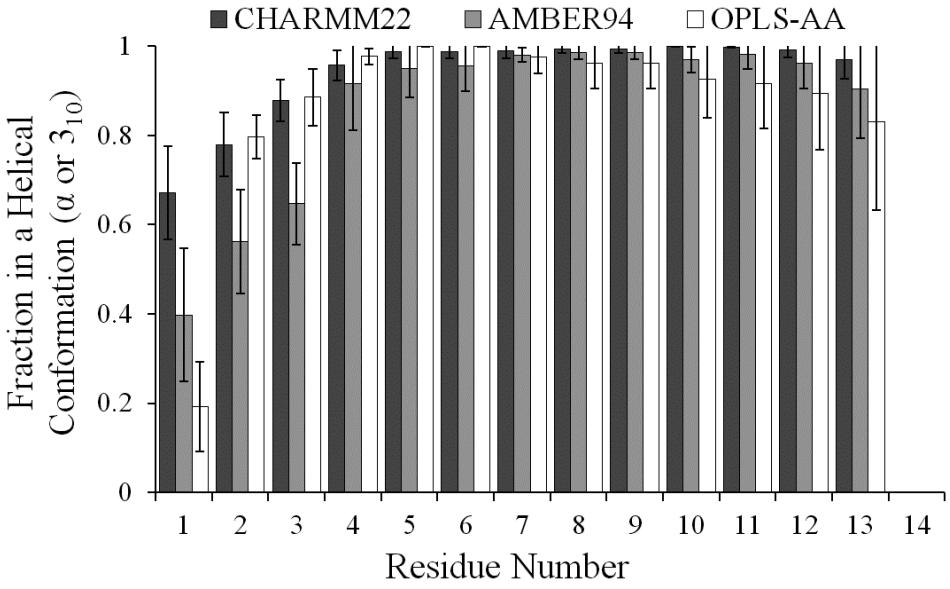

Figure 6.17: Plot comparing the fraction of the REMD 298 K ensemble adopting an α-helical or 3_{10}-helical conformation for each FF in simulating the LKα14 peptide adsorbed to the CH_3-SAM. Each column represents 12 independent 1 ns block averages with the error bars representing 95% confidence intervals (n=12) taken from pooled results from the duplicated 6 ns REMD production runs (12 ns total, therefore twelve 1 ns blocks).

The LKα14 peptide's side chains are not seen arranged in a linear fashion in the way that is possible for the LKβ7 peptides, so it is unavoidable for the side chain SSDs of the LKα14 peptide to be not as well-ordered as they are for the LKβ7 peptides. However, when adsorbed to the CH_3-SAM, the LKα14 peptide's adsorbing side chains are arranged so that their SSDs fall within a 3 Å range, centered at approximately 4 Å from the SAM surface with all three FFs (Figures 6.18a,c,e). This reflects a consistently adsorbed position above the surface, despite the differences in helical conformations amongst the different FFs used.

The tilt angle measurement populations for the LKα14 side chains adsorbed to the CH_3-SAM vary widely with the largest populations of measurements within the 100° to

140° range (Figures 6.18b,d,f). Also for each FF, the non-adsorbing K side chains tend to be directed away from the SAM surface, with tilt angle measurement populations centered near 180°.

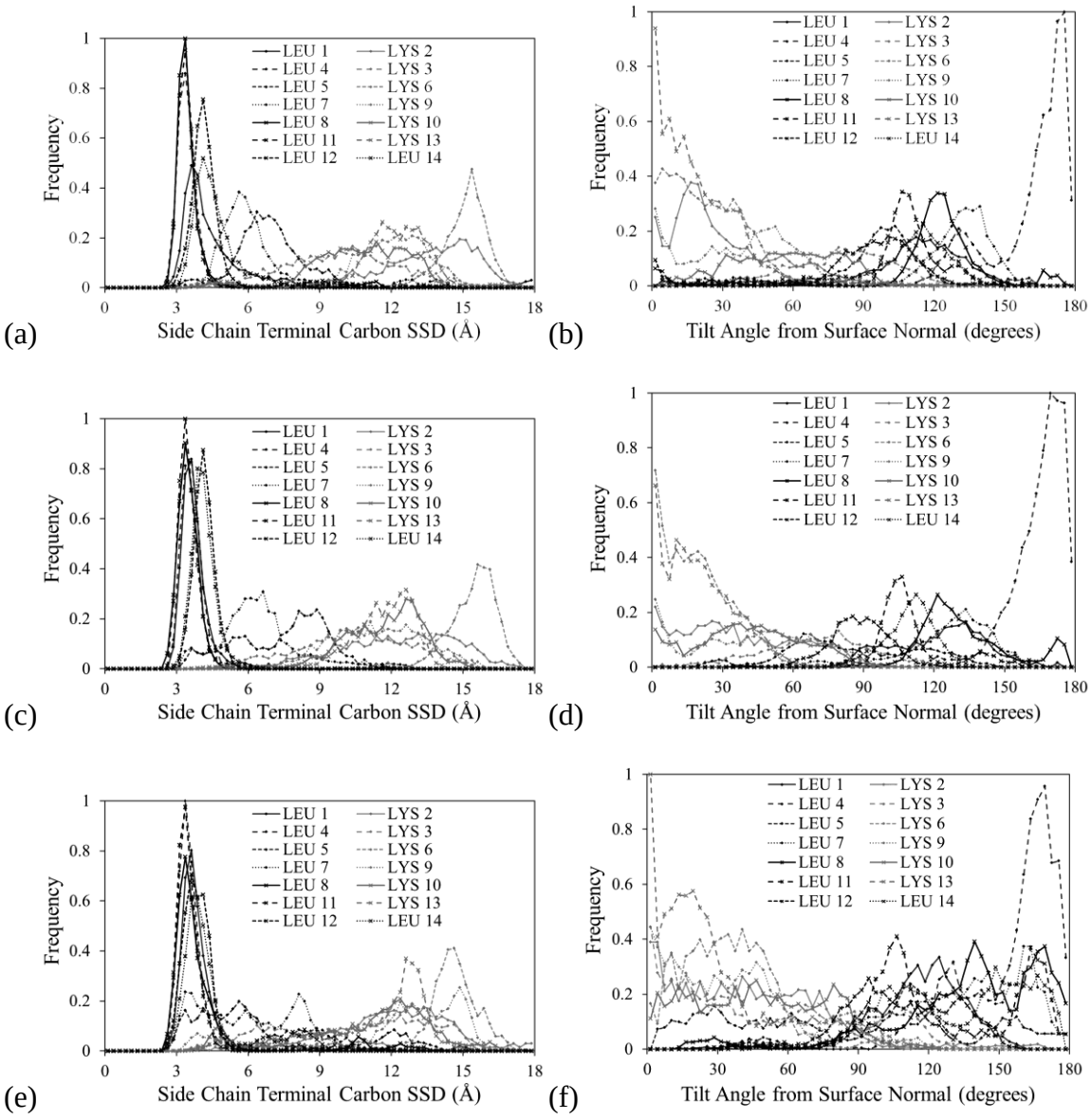

Figure 6.18: Plots of frequency distributions of amino acid side chain terminal carbon surface separation distances (SSDs) (plots a, c, e) and amino acid side chain tilt angles (tilt away from the normal vector of the SAM surface) (plots b, d, f) for the LKα14 peptide adsorbed to the CH_3-SAM during the last 6 ns of REMD sampling using (a,b) the CHARMM22 FF, (c,d) the AMBER94 FF, and (e,f) the OPLS-AA FF. 3,000 SSD measurements for each amino acid, with a 0.25 Å bin width. Tilt angle plots normalized for the number of counts per 3-degree bin and sinusoidal distribution of measurements.

The LKα14 Peptide Adsorbed to the COOH-SAM

As in the case of adsorption to the CH_3-SAM, LKα14 peptides adsorbed to the COOH-SAM maintained a predominantly helical conformation with all three FFs, with some slight variation amongst the different FFs. The CHARMM22 FF presents a strongly and consistently α-helical conformation throughout the simulation (Figure 6.19a), with more deviation from that conformation than was found for adsorption to the CH_3-SAM. The AMBER94 FF shows this peptide deviating from an α-helical conformation toward that of a 3_{10}-helix in many of its conformations (Figure 6.19c). The OPLS-AA FF produced conformations ranging from a random coil to that of a 3_{10}-helix, with almost no α-helical conformations (Figure 6.19e). Electrostatic interactions between the surface functional groups and the positively charged peptide side chains govern peptide conformation in this system, but the LKα14 peptide offers sufficient structural integrity to make displacing counter ions and water from the surface more favorable than was the case for the very small LKβ7 peptides. For this reason, the structural stability of the LKα14 helix helps make a clearer distinction between the FFs than was possible with the LKβ7 peptides. Also more evident with analysis of this peptide-surface system is the failure of the OPLS-AA FF to achieve appropriate modeling of the highly stable LKα14 internal structure. Analysis of the backbone phi/psi angles shows conformations generated using the CHARMM22 FF to be strongly α-helical (Figure 6.19b), but with more deviation from this conformation than was the case in adsorption to the CH_3-SAM. The results from the AMBER94 FF are also strongly helical with a significant amount of deviation from a helical conformation (Figure 6.19d). The OPLS-AA phi/psi angles

(Figure 6.19f), again, were more similar to those for the LKβ7 peptides, but with many more helical conformations included. The overall differences between the FFs in representing the adsorbed LKα14 peptide in an α-helical conformation are summarized in Figure 6.20. Differences between the FFs in representing the adsorbed LKα14 peptide in an α-helical or 3_{10}-helical conformation are summarized in Figure 6.21.

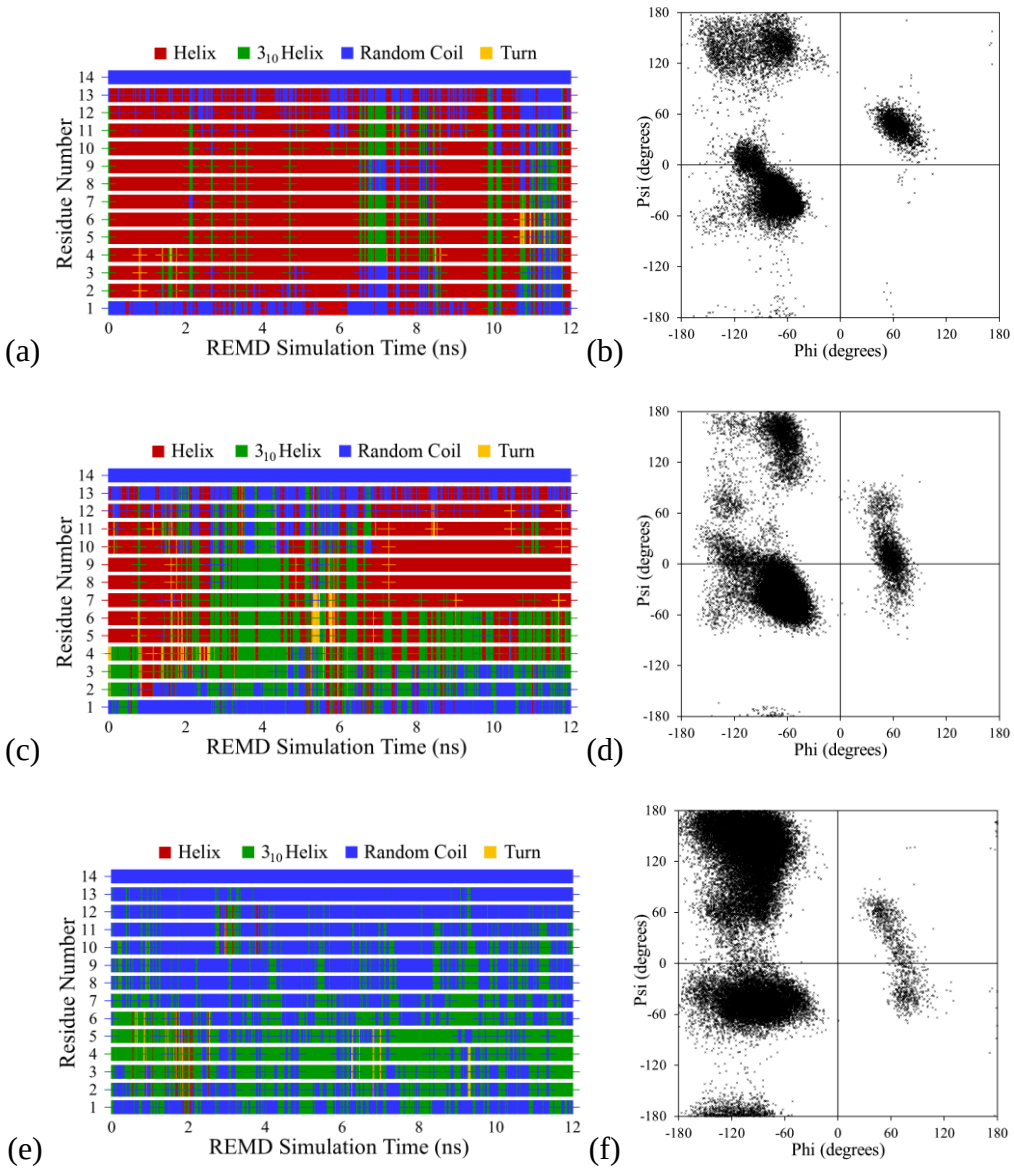

Figure 6.19: Plots of secondary structure for each amino acid residue through the entire REMD simulation (plots a, c, e) and Ramachandran plots of the phi/psi peptide backbone dihedral angles (plots b, d, f) for the LKα14 peptide adsorbed to the COOH-SAM using (a,b) the CHARMM22 FF, (c,d) the AMBER94 FF, and (e,f) the OPLS-AA FF. The Ramachandran plots represent structures from the final 6 ns of REMD sampling, 3,000 points displayed for each non-terminal amino acid.

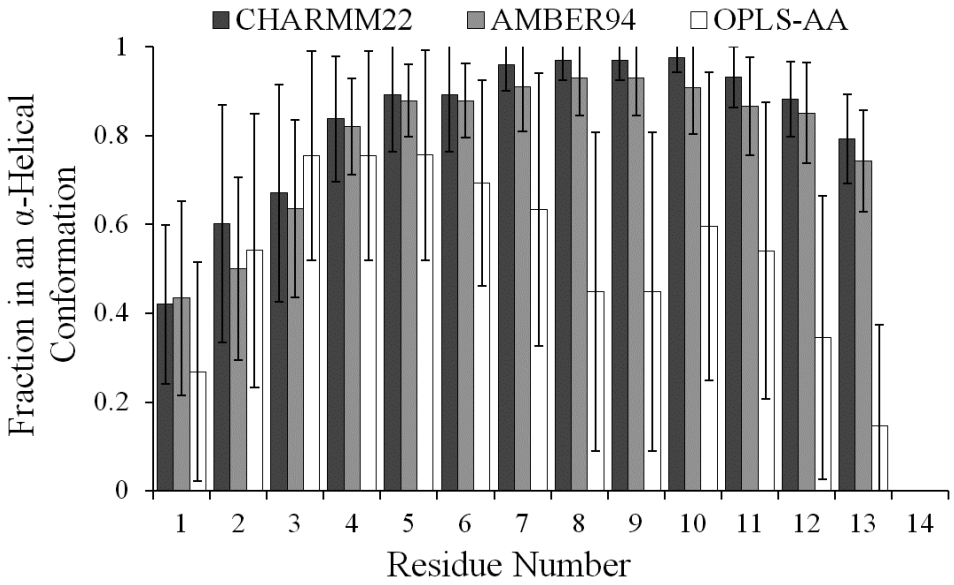

Figure 6.20: Plot comparing the fraction of the REMD 298 K ensemble adopting an α-helical conformation for each FF in simulating the LKα14 peptide adsorbed to the COOH-SAM. Each column represents 12 independent 1 ns block averages with the error bars representing 95% confidence intervals (n=12) taken from pooled results from the duplicated 6 ns REMD production runs (12 ns total, therefore twelve 1 ns blocks).

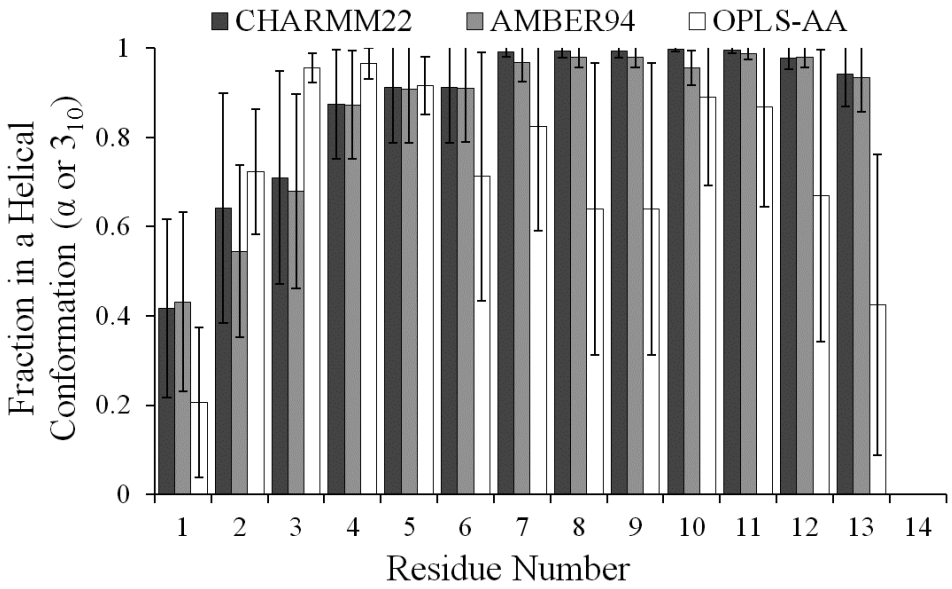

Figure 6.21: Plot comparing the fraction of the REMD 298 K ensemble adopting an α-helical or 3_{10}-helical conformation for each FF in simulating the LKα14 peptide adsorbed to the COOH-SAM. Each column represents 12 independent 1 ns block averages with the error bars representing 95% confidence intervals (n=12) taken from pooled results from the duplicated 6 ns REMD production runs (12 ns total, therefore twelve 1 ns blocks).

Measurements of the side chain SSDs for the LKα14 peptide adsorbed to the COOH-SAM appear to be arranged as inverses to the measurements of the side chains adsorbed to the CH_3-SAM, as expected. The adsorbing side chain SSDs fall within a 3 Å range, centered at approximately 2 Å from the SAM surface with all three FFs (Figures 6.22a,c,e). This arrangement reflects a consistently adsorbed position above the surface, despite the notable differences in helical conformations amongst the different FFs used.

The tilt angle measurement populations for the LKα14 side chains adsorbed to the COOH-SAM vary widely for the CHARMM22 and OPLS-AA FFs (Figures 6.22b,d,f). The tilt angle measurement populations produced using the AMBER94 FF are arranged

similarly, but with one non-adsorbing side chain maintaining its tilt angle so consistently amongst the ensemble of structures that it dominates the frequency plot (Figure 6.19d).

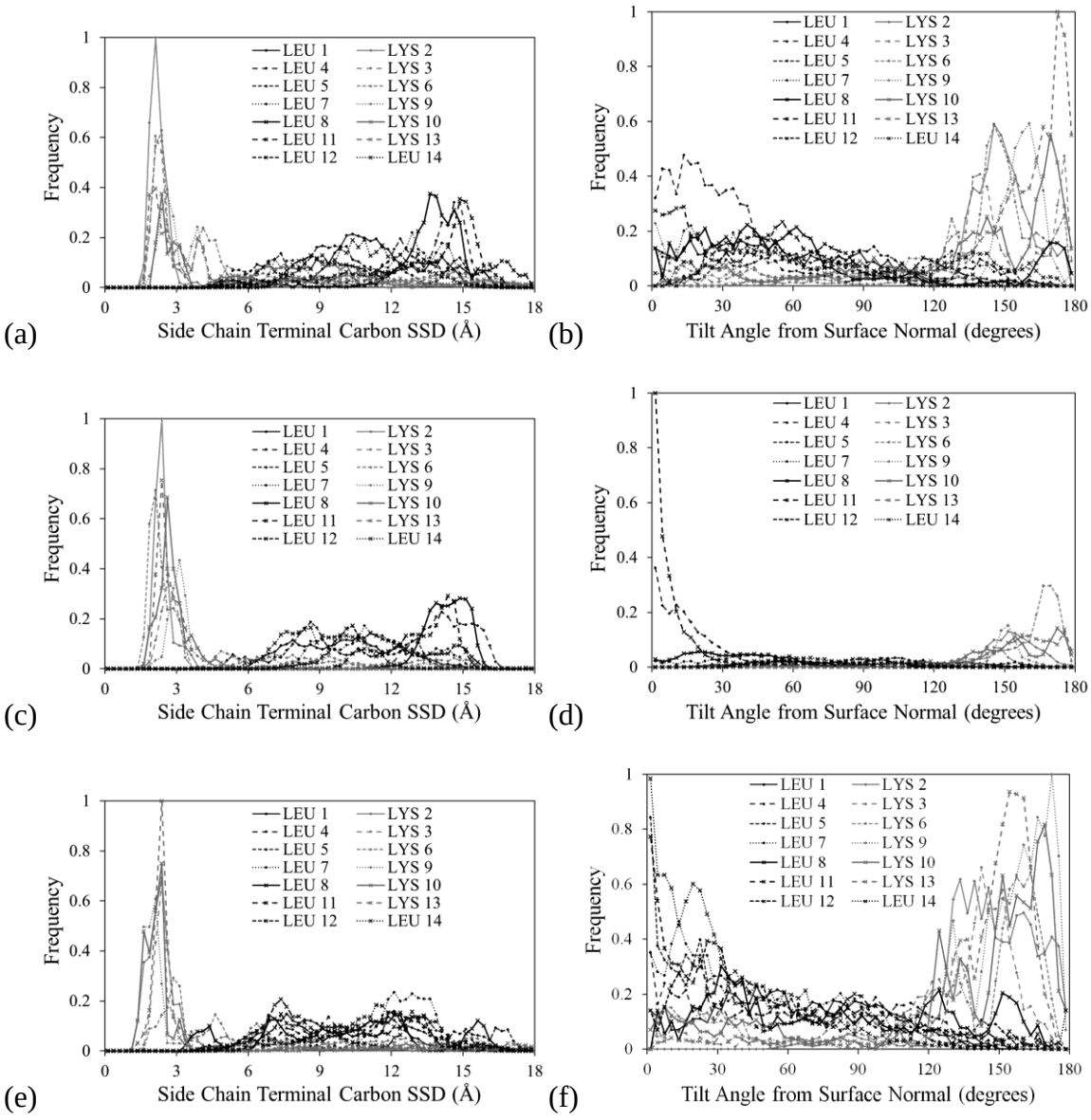

Figure 6.22: Plots of frequency distributions of amino acid side chain terminal carbon surface separation distances (SSDs) (plots a, c, e) and amino acid side chain tilt angles (tilt away from the normal vector of the SAM surface) (plots b, d, f) for the LKα14 peptide adsorbed to the COOH-SAM during the last 6 ns of REMD sampling using (a,b) the CHARMM22 FF, (c,d) the AMBER94 FF, and (e,f) the OPLS-AA FF. 3,000 SSD measurements for each amino acid, with a 0.25 Å bin width. Tilt angle plots normalized for the number of counts per 3-degree bin and sinusoidal distribution of measurements.

A general comparison of FF performance based on adherence to experimentally observed behavior is presented in Table 6.6. From this comparison, it can be seen that the CHARMM22 FF was most successful at replicating experimentally observed behavior. The AMBER94 FF performed almost equally well in simulations involving the LKα14 peptide, but the AMBER94 performance for the LKβ7 systems was inconsistent with particularly poor performance in treating the structure of the LKβ7 peptides when they were adsorbed to either surface. The OPLS-AA FF performance was generally not as good as that of the AMBER94 FF, but the OPLS-AA FF was slightly more successful in guiding the LKβ7 peptides to the surfaces in the correct orientation.

Table 6.6. A qualitative comparison of FF performance, comparing experimentally observed behavior. + Symbols indicate adherence to experimentally observed behavior and – symbols indicate deviation from experimentally observed behavior.

Performance Consideration	Estimation of Performance		
	CHARMM22	AMBER94	OPLS-AA
LKβ7s in solution adopt a helical conformation	+	+ +	-
LKβ7s interact with (adsorb to) the CH_3-SAM surface	+ +	+	+ +
LKβ7s form β-strands when adsorbed to CH_3-SAM	+ +	- -	-
LKβ7s form β-sheet when adsorbed to CH_3-SAM	+ +	- -	-
LKβ7s oriented LEU-down when adsorbed to CH_3-SAM	+ +	+	+ +
LKβ7s interact with (adsorb to) the COOH-SAM surface	+ +	+ +	+ +
LKβ7s form β-strands when adsorbed to COOH-SAM	+	- -	-
LKβ7s form β-sheet when adsorbed to COOH-SAM	- -	- -	- -
LKβ7s oriented LYS-down when adsorbed to COOH-SAM	+ +	+ +	+ +
LKα14 in solution remains α-helical	+ +	+ +	-
LKα14s interact with (adsorb to) the CH_3-SAM surface	+ +	+ +	+ +
LKα14 remains α-helical when adsorbed to CH_3-SAM	+ +	+	+
LKα14 oriented LEU-down when adsorbed to CH_3-SAM	+ +	+ +	+ +
LKα14s interact with (adsorb to) the COOH-SAM surface	+ +	+ +	+ +
LKα14 remains α-helical when adsorbed to COOH-SAM	+	+	-
LKα14 oriented LYS-down when adsorbed to COOH-SAM	+ +	+ +	+ +

Conclusions

Our simulations of the interaction between the structured LK peptides and functionalized SAM surfaces provided a means of evaluating the applicability of the CHARMM22, AMBER94, and OPLS-AA FFs to these unique interfacial systems. Differences, or strengths and weaknesses, amongst these FFs are difficult to identify from a limited number of model system simulations and a limited number of replicates of each simulation, but some significant trends were noted. The CHARMM22 FF most closely matched experimental results for all simulations. The solution conformations (in the

absence of surfaces or fixed atom layers) of the pair LKβ7 peptides and the single LKα14 peptide were both consistent and accurate when using the CHARMM22 FF. The CHARMM22 FF was the only FF with which the pair LKβ7 peptides adopted a β-sheet configuration, which occurred in its adsorbed state but not in solution, and that configuration was known to be the more energetically favorable antiparallel configuration. Additionally, this β-sheet configuration was maintained while the peptides were adsorbed to the CH_3-SAM, which would be expected to provide the needed structural stability in maintaining the peptides in a closely interacting arrangement. The secondary structures and backbone dihedrals of the peptides in the simulations using the CHARMM22 FF more closely adhered to experimental findings. Side chain interactions with the surfaces also matched expected and experimental values more closely when using the CHARMM22 FF.

The results obtained using the AMBER FF approached expected findings and experimental results partially similar to that of the CHARMM22 FF, but in all simulations, the AMBER FF resulted in significantly more variability (i.e., noise) in all measurements made. This situation would likely result in structural information that is less accurate than information obtained using the CHARMM22 FF for the same simulations. The results obtained using the OPLS-AA FF deviated significantly from expected findings and experimental results. In all simulations with the OPLS-AA FF, there was a pronounced tendency for the peptides to adopt a random configuration. Also, enhanced secondary structural ordering induced by relatively strong adsorption to the CH_3-SAM, which was noticeable for the CHARMM22 and AMBER94 FFs, was not

observed when using the OPLS-AA FF. Generally, all three FFs were in close agreement in their handling of peptide structure in solution, but they differed significantly in handling peptide interactions with the surfaces. In particular, these results suggest that peptide-surface interactions tend to modify the overall stabilization of the LKβ7 peptides when those peptides are adsorbed to a surface, thus enabling a β-sheet conformation to form more readily with one FF than it does when another FF is used. Finally, a key component of this work was the demonstration of the complementary nature of different structural analyses, both simulated and experimental, in providing an enhanced examination of physical phenomena. It is not possible to confidently select a particular FF for use in novel simulation approaches, and to identify errors in the predicted behavior, without the validation of results provided by experimental studies.

CHAPTER SEVEN

CONCLUDING REMARKS

Through this research work, an effective approach to simulating peptide adsorption to solid surfaces has been established and demonstrated. In the methods assessment for calculating electrostatic effects, it has been shown that design features unique to systems that include a solid surface can permit the use of the most widely accepted and validated peptide and protein simulation methods. The combination of PBCs in simulation cell imaging and PME summation for calculating long-range electrostatics does not result in the production of detectable nonphysical effects. Normally, accomplishing this for a system with two-dimensional periodicity would require manipulation of many aspects of the three-dimensional mathematical approach used, but that complication has been successfully avoided in this case.

The initial series of peptide-surface structural studies using the CHARMM22 FF made use of the methods established earlier in this work, resulting in highly detailed structural data that matched the more qualitative experimental findings with surpassing detail. These simulations showed distinctions between secondary structure conformations that result from interactions with different surface chemistries. The helical conformation of the LKα14 peptide was maintained more strictly when adsorbed to the hydrophobic SAM surface due to a tighter interaction between the peptide and the surface resulting from mutual water exclusion. The helical conformation of the LKα14 peptide was maintained less strictly when adsorbed to the charged COOH-SAM since the interaction with that surface, involving competition with water and counter-ions for

binding sites, resulted in a much more hydrated, loosely bound association between the peptide and surface.

The pair of LKβ7 peptides, which adopted a predominantly random coil arrangement in solution, maintained a more extended conformation when adsorbed to the hydrophobic surface. This conformation enabled sufficient stabilization for the pair of LKβ7 peptides to adopt an antiparallel β-sheet arrangement when this arrangement lacked sufficient stabilization to form consistently in solution or when adsorbed to the charged COOH-SAM surface. Distance measurements between the surfaces and surface-interacting side chains showed that both types of peptides remained sufficiently close to each surface during the simulations for binding to the surface functional groups to occur. Side chain tilt angle measurements indicated consistency in the orientation of the peptide side chains with respect to each surface. These measurements also suggested a slightly tilted orientation for the L residue side chains, indicating that one of the two methyl groups was oriented at closest approach to surface methyl groups.

Water density analyses showed a sharp increase in water density near the adsorbed K side chains, as well as distinct surface solvation density patterns for each surface. Solvent diffusion coefficient calculations for those systems showed decreases in diffusion rates for water and ions within 5 Å of the hydrophobic surface and within 15 Å of the charged surface, with diffusion rates for both surfaces decreasing to less than half of their bulk solution rates. Rotational correlation time calculations showed an approximate doubling of rotational correlation τ values within approximately 8 Å of each surface (with no peptides adsorbed). With the peptides adsorbed, τ values near the hydrophobic

surface were roughly doubled at the surface with this rotational slowing effect starting at approximately 15 Å from the surface. Near the charged COOH-SAM surface, τ values for water were nearly tripled, with this effect starting at approximately 20 Å from the surface. These analyses and the interplay of these various effects and interactions exemplify the complex nature of the protein adsorption mechanism.

Using experimental findings as a foundation for comparison, the comparison of the CHARMM22, AMBER94, and OPLS-AA FFs revealed relative weaknesses in the AMBER94 and OPLS-AA FFs. The structural data provided by the experimental findings was much more qualitative than what was provided by all of the simulations, so directly comparing the results of each FF's simulation to the experimental results, alone, would be less informative than a direct comparison of structural data from each of the different FF simulations. The structural data resulting from the simulations where the CHARMM22 FF was used matched the experimental results in all comparable ways. Since this was not the case for the results obtained using the AMBER94 and OPLS-AA FFs, it was possible to measure the performance of these FFs against that of the CHARMM22 FF. Although the results obtained using the AMBER94 FF approached expected findings and the experimental results, the AMBER94 FF resulted in significantly more variability (noise) in all measurements made. This situation would likely result in structural information that is less accurate than information obtained using the CHARMM22 FF for the same simulation work. The results obtained using the OPLS-AA FF deviated significantly from expected findings and the experimental results. In all simulations with the OPLS-AA FF, there was a pronounced tendency for the

peptides to adopt a random configuration. Also, enhanced secondary structural ordering induced by relatively strong adsorption to the CH_3-SAM, which was noticeable for the CHARMM22 and AMBER94 FFs, was not observed when using the OPLS-AA FF.

The range of systems studied in this work is limited, so a comprehensive recommendation for the use of the CHARMM22 FF in simulations of peptides or proteins interacting with surfaces cannot be made. However, the nature of the differences between the FFs evaluated here indicates that the CHARMM22 FF is designed and tuned in a way that provides the most accurate and effective FF for this type of work. Additional strides toward a coupled experimental and theoretical approach to strategic material design can be made through emulating the approach used here, but with a much broader range of studied systems. These additional studies will likely result in the identification of tuning opportunities within the CHARMM22 FF for more accurate broad-scope performance. As is the case with most all-atom empirical FFs, many of the parameters within the CHARMM22 FF have been adjusted for optimal performance with simple solvated systems, but there is room for additional tuning adjustments to enable highly accurate simulations of more complex structures and systems. A large variety of coupled experimental and simulation studies will make this possible.

APPENDICES

Appendix A

Additional Figures for Chapter Four: Methods Assessment for the Calculation of Electrostatic Effects

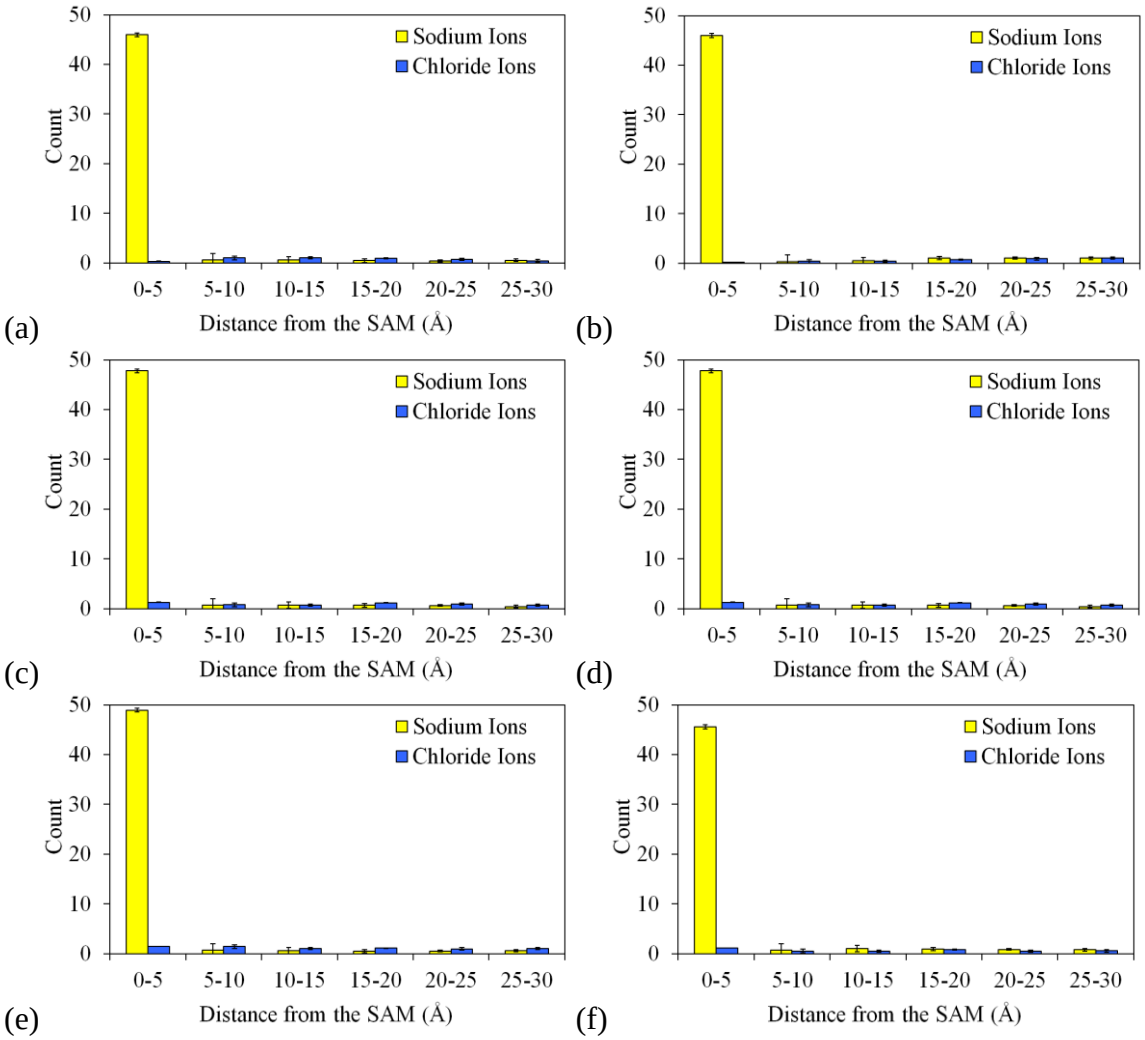

Figure A-1: Plots of Na^+ and Cl^- ion distributions calculated using the isotropic periodic sum (IPS) method with an interacting pair list cutoff at (a) 10 Å, (b) 12 Å, (c) 14 Å, (d) 16 Å, (e) 18 Å, and (f) 20 Å. Each plot represents the final 4.0 ns of production data. This 4.0 ns of data was divided into 400 ps blocks, providing ten independent samples of the average ion population for each bin. These block averages were used to generate a mean and 95% confidence interval for the ion count in each layer of solution above the SAM surface.

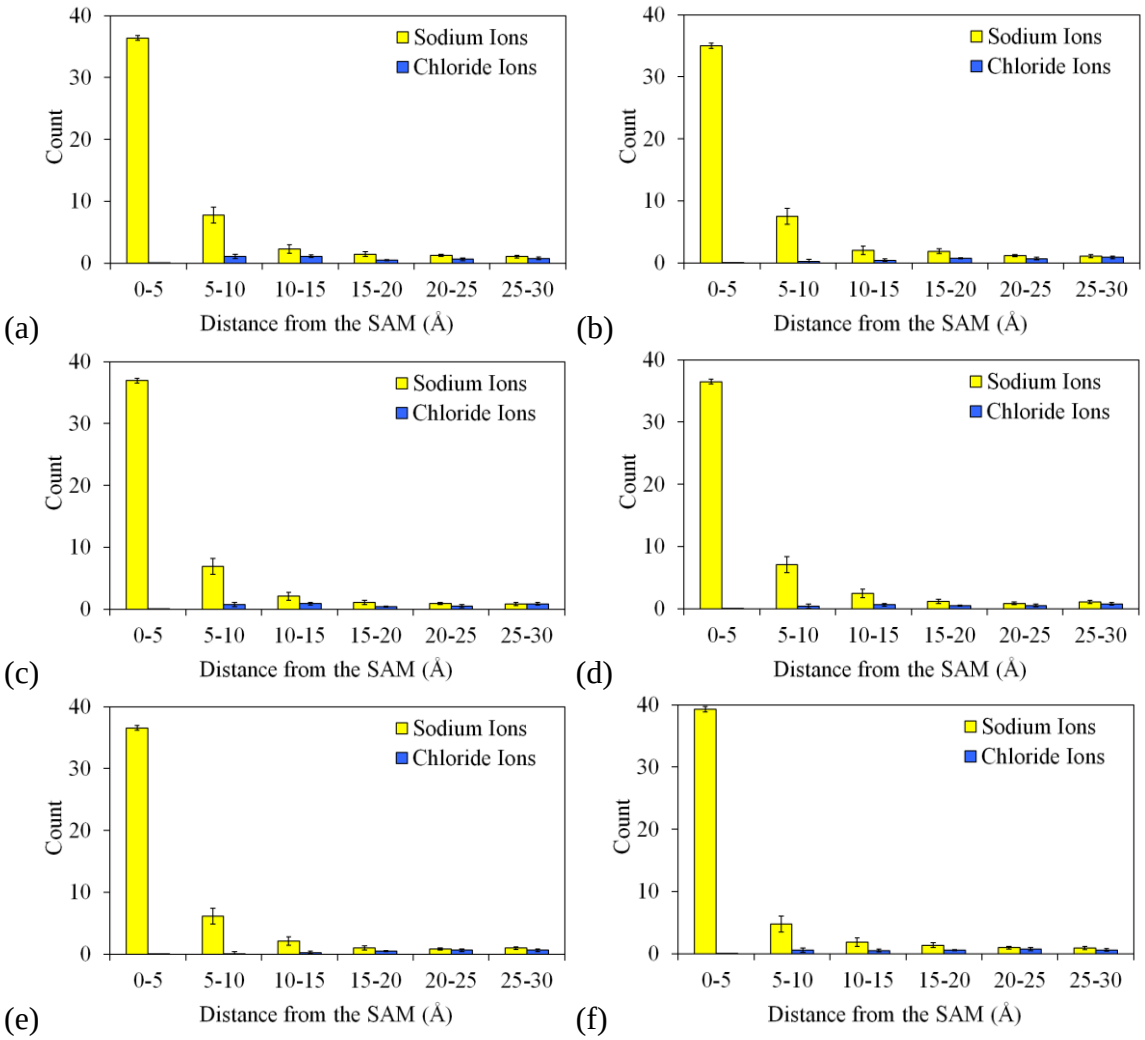

Figure A-2: Plots of Na^+ and Cl^- ion distributions calculated using the anisotropic periodic (APS) sum method with an interacting pair list cutoff at (a) 10 Å, (b) 12 Å, (c) 14 Å, (d) 16 Å, (e) 18 Å, and (f) 20 Å. Each plot represents the final 4.0 ns of production data. This 4.0 ns of data was divided into 400 ps blocks, providing ten independent samples of the average ion population for each bin. These block averages were used to generate a mean and 95% confidence interval for the ion count in each layer of solution above the SAM surface.

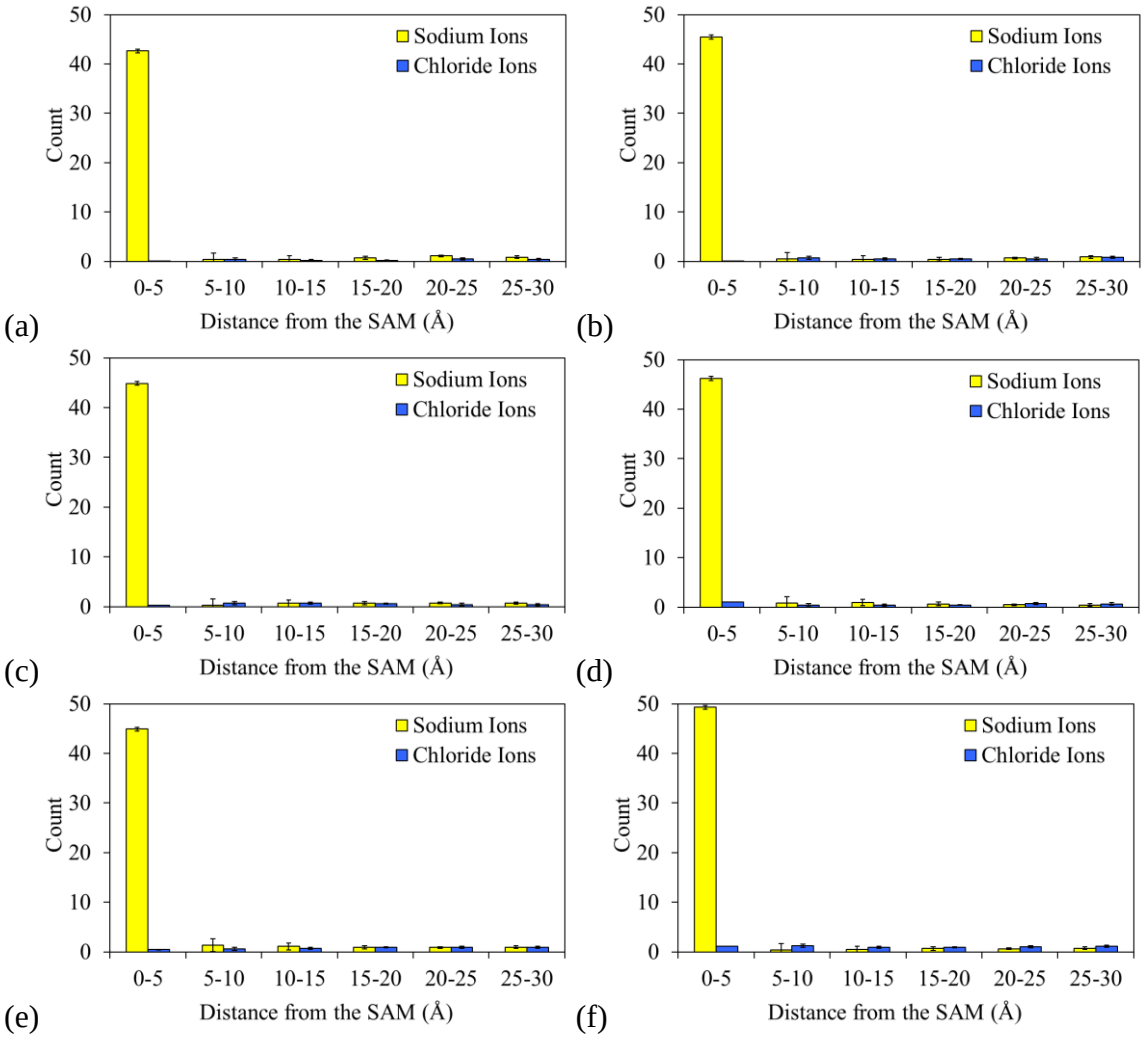

Figure A-3: Plots of Na^+ and Cl^- ion distributions calculated using radial cutoffs of (a) 10 Å, (b) 12 Å, (c) 14 Å, (d) 16 Å, (e) 18 Å, and (f) 20 Å. Each plot represents the final 4.0 ns of production data. This 4.0 ns of data was divided into 400 ps blocks, providing ten independent samples of the average ion population for each bin. These block averages were used to generate a mean and 95% confidence interval for the ion count in each layer of solution above the SAM surface.

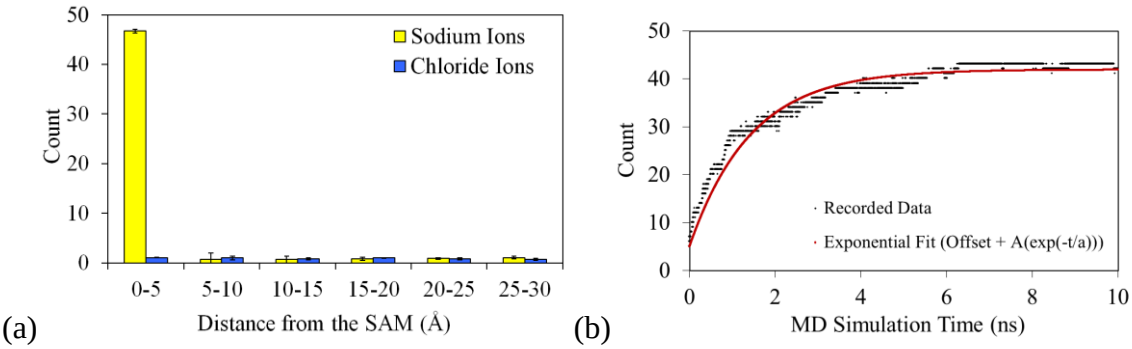

Figure A-4: (a) Plot of Na^+ and Cl^- ion distributions calculated using the PME method. This 4.0 ns of data was divided into 400 ps blocks, providing ten independent samples of the average ion population for each bin. These block averages were used to generate a mean and 95% confidence interval for the ion count in each layer of solution above the SAM surface. (b) Example plot of the exponential fit to the Na^+ ion population within the 5 Å layer closest to the surface. This fit was used as a rough guide in determining the time during the simulation at which the ion population in that layer had stabilized.

Appendix B

Additional Figures for Chapter Five, Molecular Dynamics Simulation of Structured Peptide Adsorption to Functionalized Self-Assembled Monolayer Surfaces

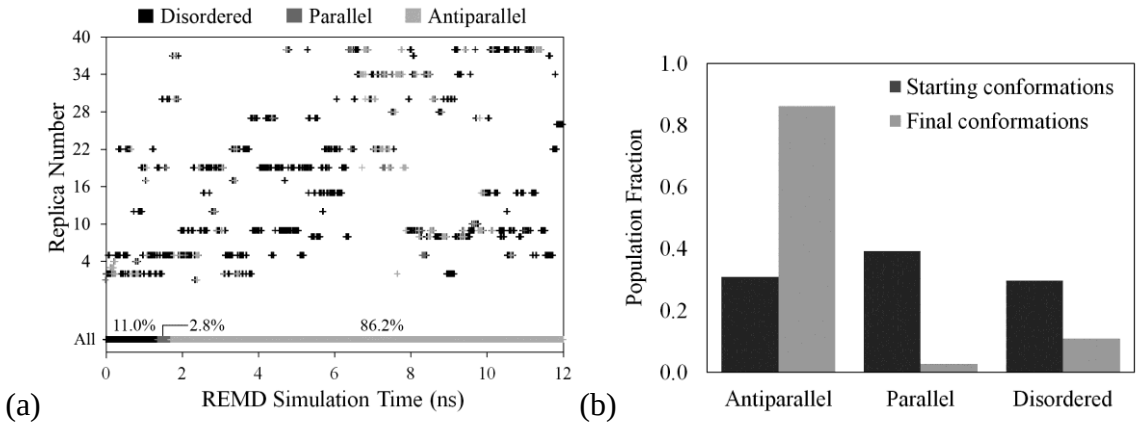

Figure B-1: Plots of replicas that contributed to the 298 K ensemble of structures for the pair of LKβ7 peptides adsorbed to the CH_3-SAM with (a) showing the origins of the final conformations that were contributed to the ensemble, and (b) showing the population fractions of each starting conformation that contributed to the final ensemble and the population fractions of the conformations that constituted the final ensemble.

(a) 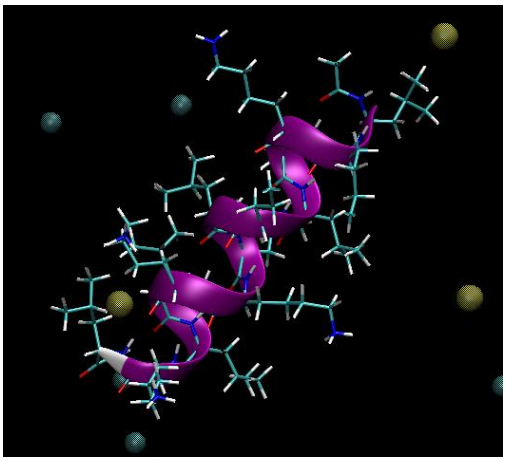 (b) 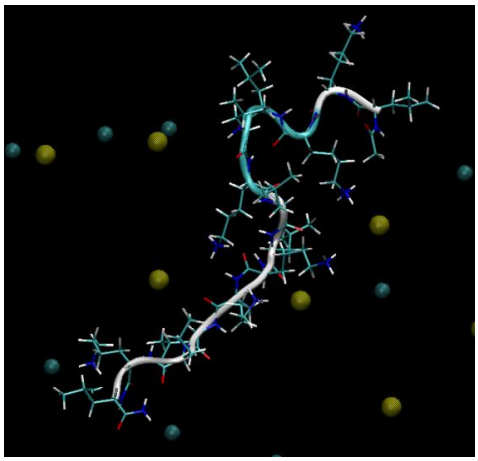

Figure B-2: Images of the LKa14 peptide taken from the production phase of one of the REMD simulations, (a) maintaining a helical conformation at 298 K, and (b) maintaining a randomized conformation at 520 K.

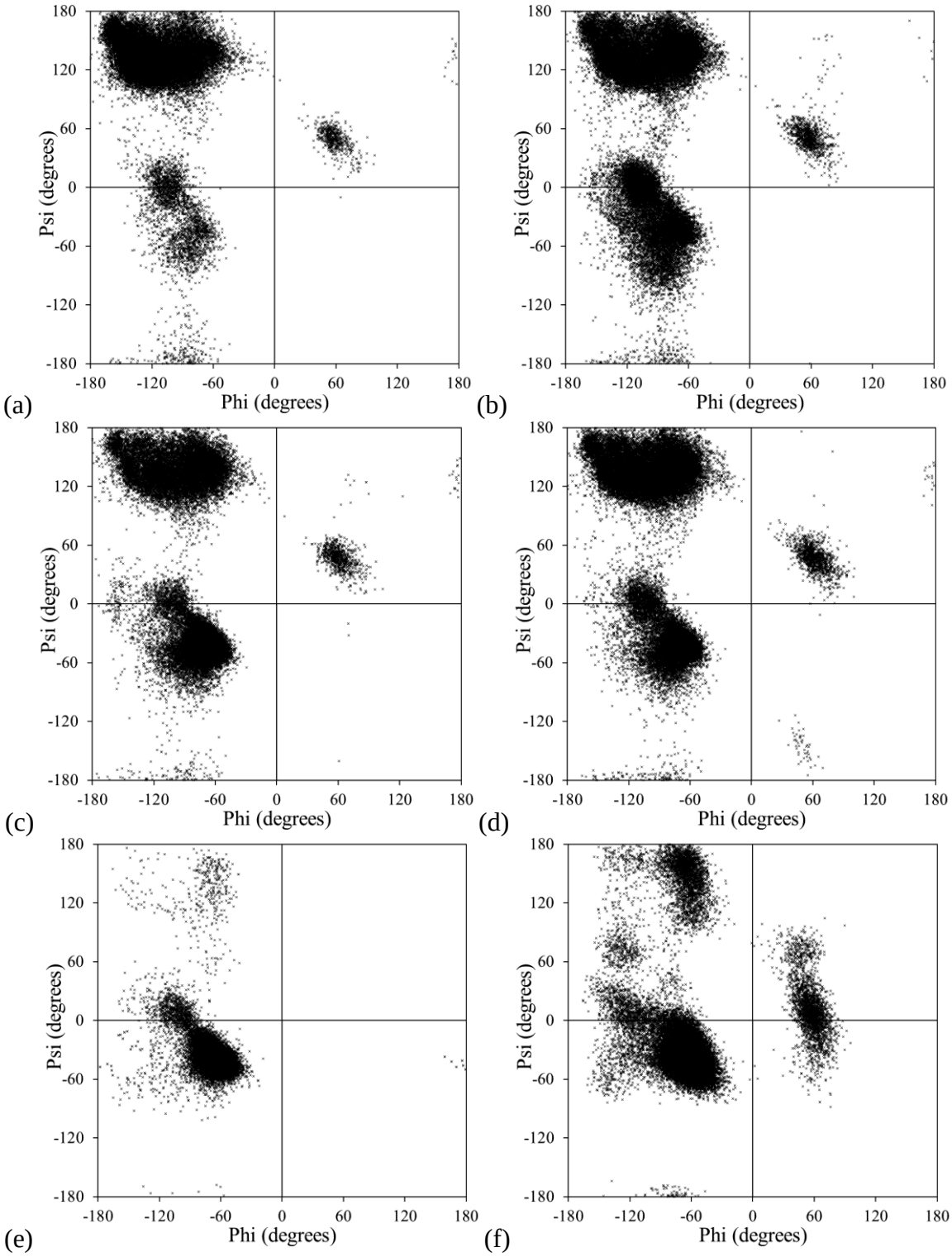
(a)
(b)
(c)
(d)
(e)
(f)
Psi (degrees)
Phi (degrees)
180
120
60
0
-60
-120
-180

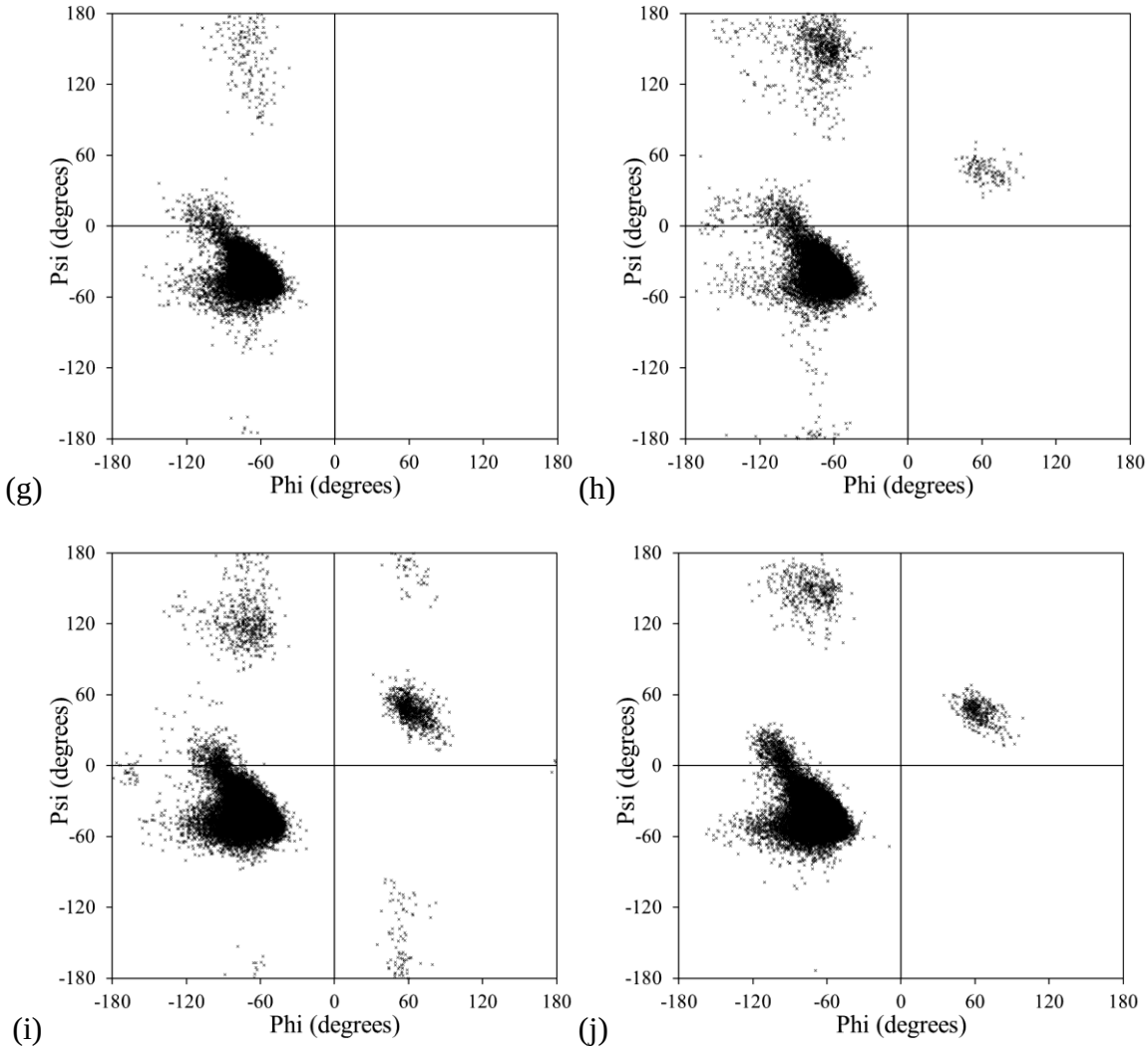

Figure B-3: Additional Ramachandran plots of the Phi and Psi peptide backbone dihedral angles during the final 6 ns of REMD sampling using the CHARMM22 FF of (a) the pair of LKβ7 peptides adsorbed to the CH_3-SAM, (b) the pair of LKβ7 peptides adsorbed to the COOH-SAM, (c,d) the pair of LKβ7 peptides in solution, (e) the LKα14 peptide adsorbed to the CH_3-SAM, (f) the LKα14 peptide adsorbed to the COOH-SAM, (g,h) the LKα14 peptide in solution, and (i,j) a pair of LKα14 peptides in solution. 3,000 points displayed for each non-terminal amino acid. Note that two independent simulations were run for each system. One of each of the adsorbed systems is shown in Figure 5 and both data sets for the simulation in solution are shown here.

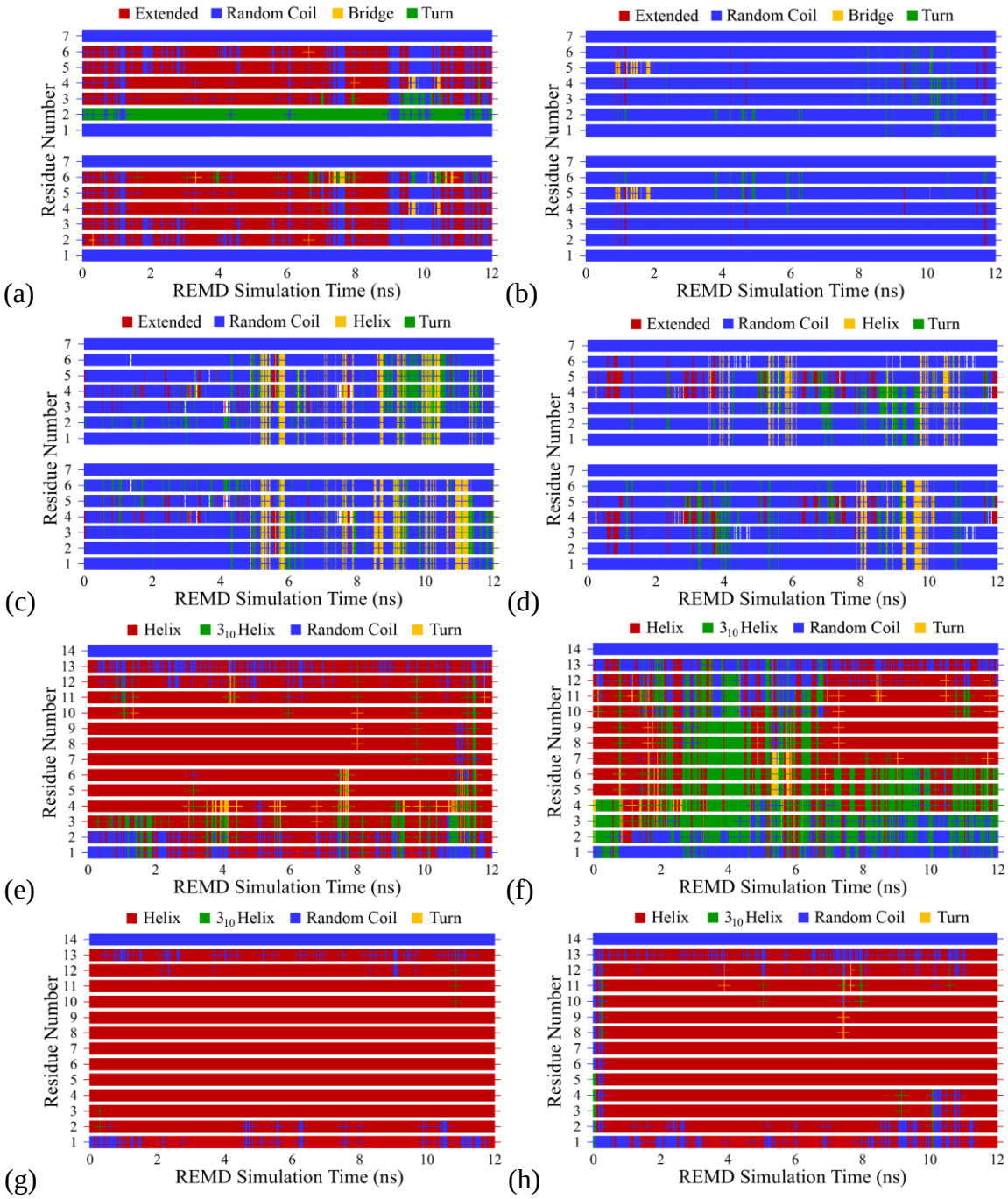
Extended
Random Coil
Bridge
Turn
Residue Number
REMD Simulation Time (ns)
(a)
(b)
Helix
Random Coil
(c)
(d)
3_{10} Helix
(e)
(f)
(g)
(h)

Figure B-4: Additional plots of secondary structure for each amino acid residue through the entire REMD simulation using the CHARMM22 FF for (a) the pair of LKβ7 peptides adsorbed to the CH_3-SAM, (b) the pair of LKβ7 peptides adsorbed to the COOH-SAM, (c,d) the pair of LKβ7 peptides in solution, (e) the LKα14 peptide adsorbed to the CH_3-SAM, (f) the LKα14 peptide adsorbed to the COOH-SAM, and (g,h) the LKα14 peptide in solution.

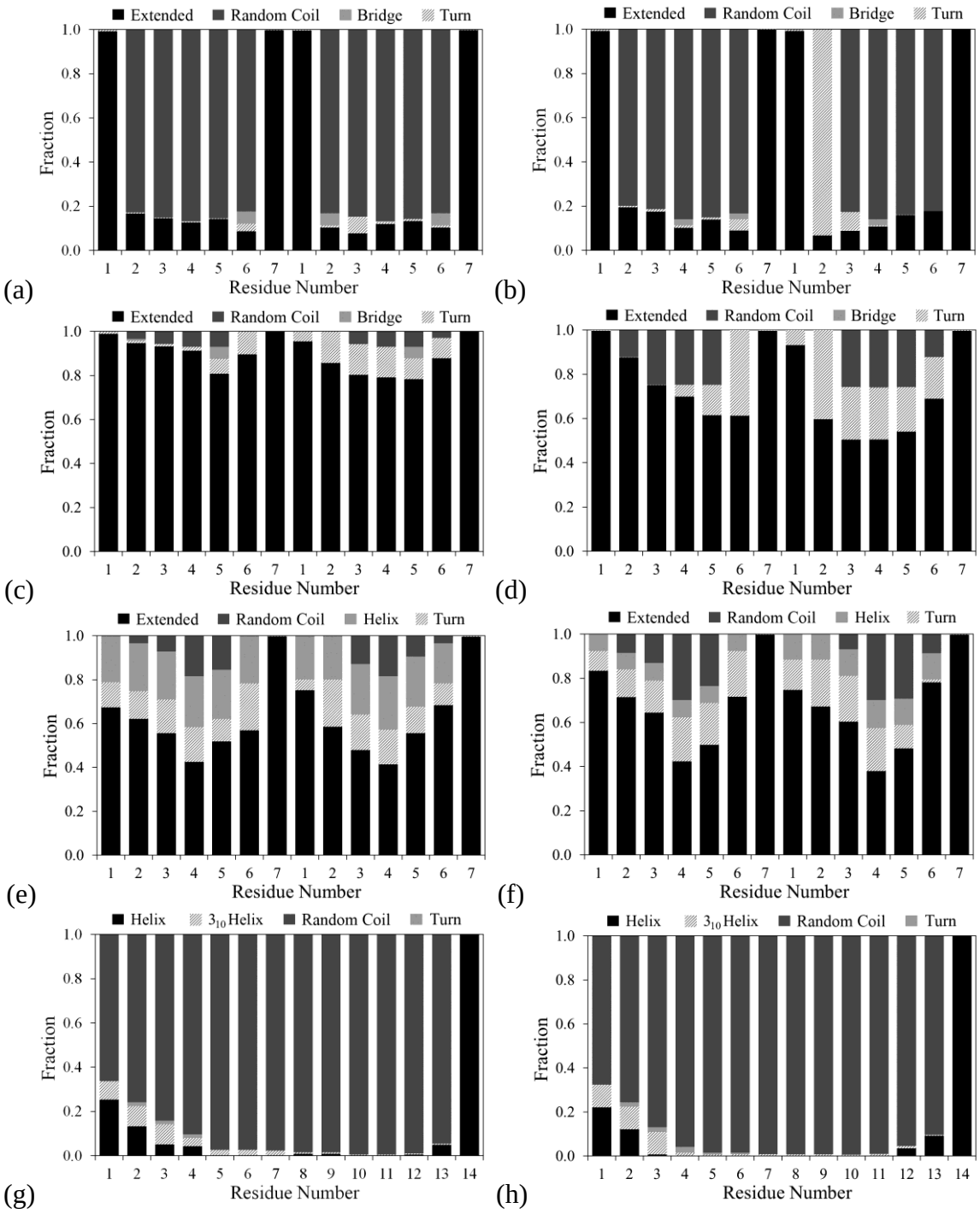
Extended
Random Coil
Bridge
Turn
Helix
3_{10} Helix
Fraction
Residue Number
(a)
(b)
(c)
(d)
(e)
(f)
(g)
(h)

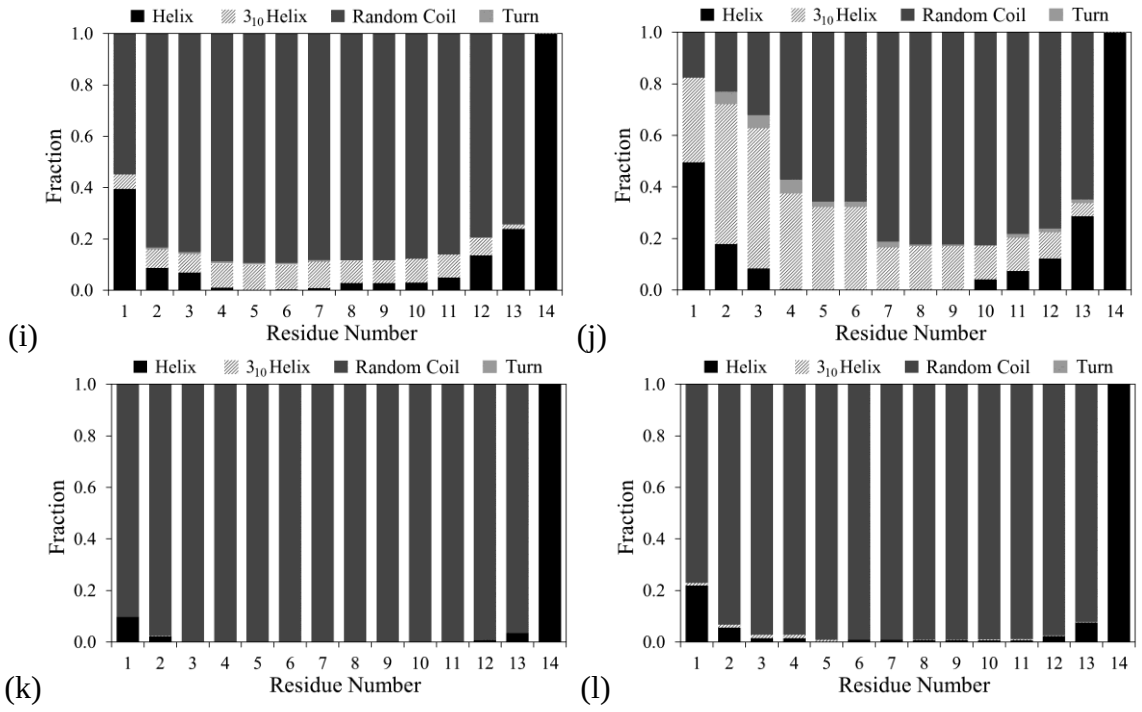

Figure B-5: Plots of fractional secondary structure for each amino acid residue through the entire REMD simulation using the CHARMM22 FF for (a,b) the pair of LKβ7 peptides adsorbed to the CH_3-SAM, (c,d) the pair of LKβ7 peptides adsorbed to the COOH-SAM, (e,f) the pair of LKβ7 peptides in solution, (g,h) the LKα14 peptide adsorbed to the CH_3-SAM, (i,j) the LKα14 peptide adsorbed to the COOH-SAM, and (k,l) the LKα14 peptide in solution.

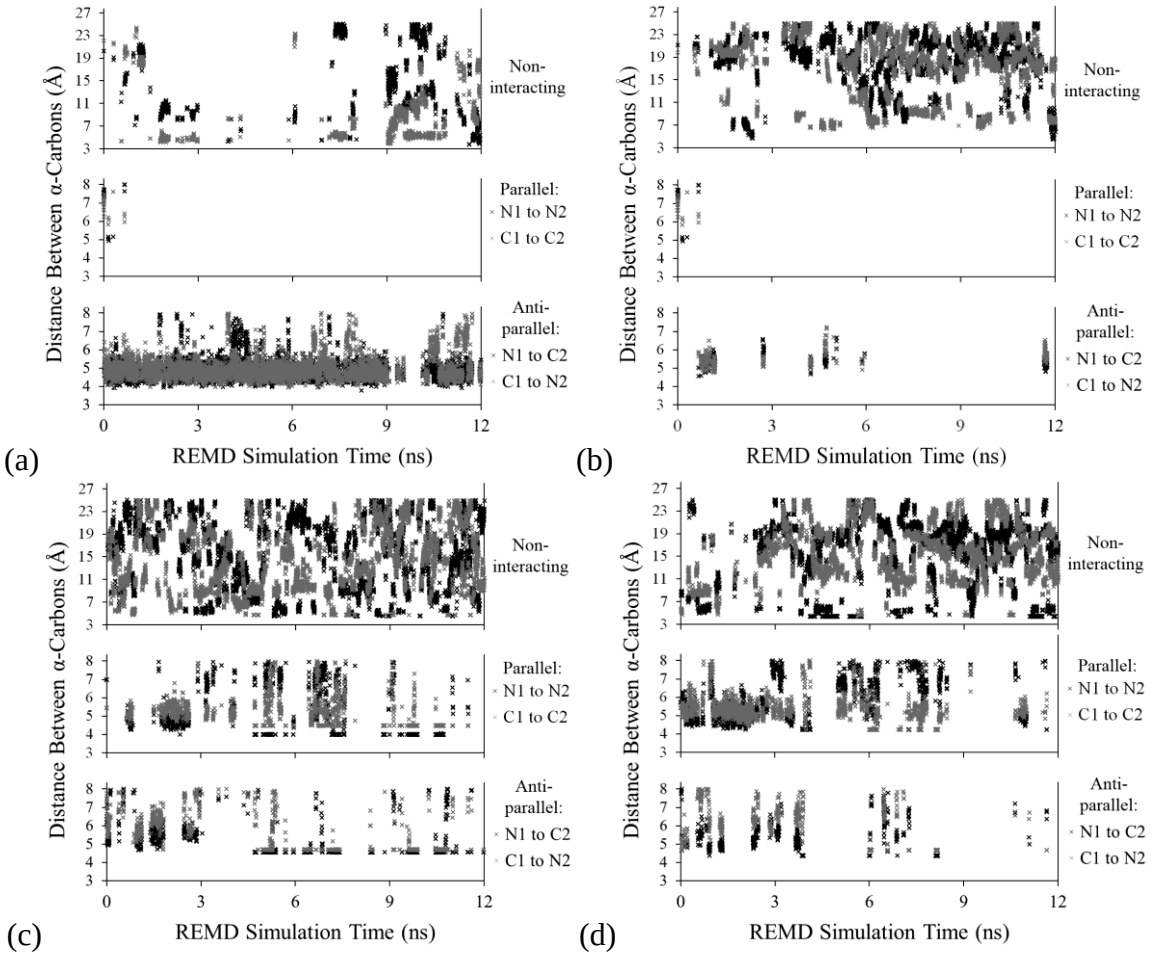

Figure B-6: Additional plots of distances between terminal α-carbons (indicative of parallel and antiparallel conformations) during the entire REMD simulation using the CHARMM22 FF for the pair of LKβ7 peptides (a) adsorbed to the CH_3-SAM, (b) adsorbed to the COOH-SAM, and (c,d) in solution.

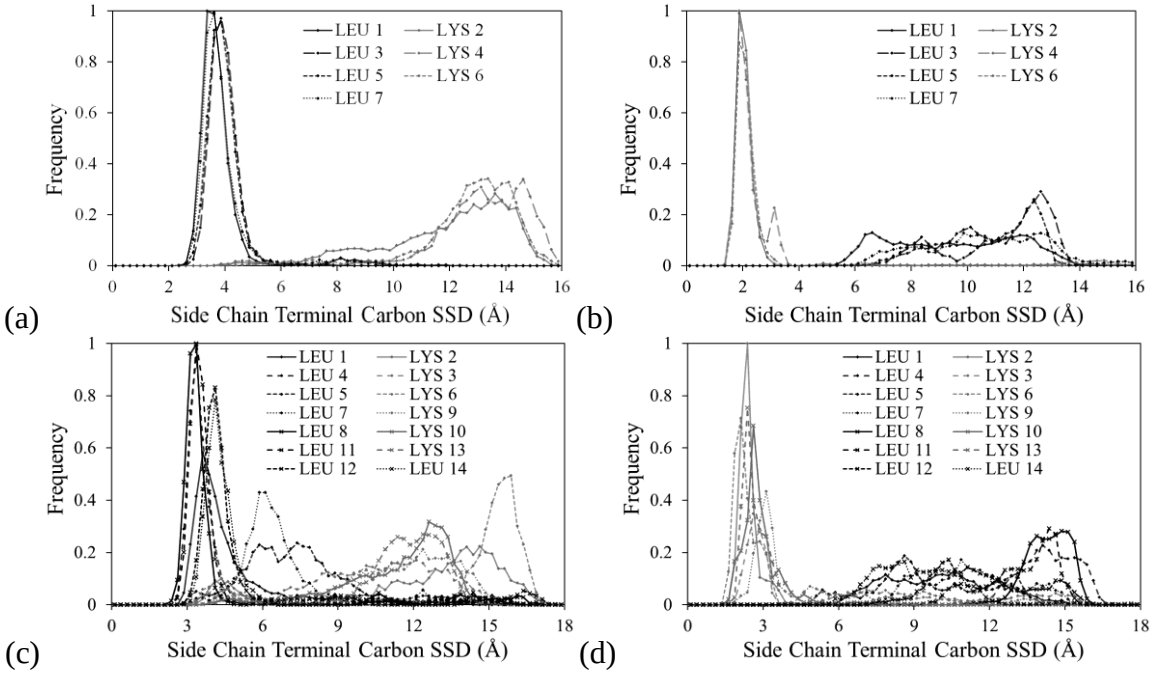

Figure B-7: Additional plots of frequency distributions of amino acid side chain terminal carbon surface separation distances (SSDs, Å) during the last 6 ns of REMD sampling using the CHARMM22 FF for (a) the pair of LKβ7 peptides adsorbed to the CH_3-SAM, (b) the pair of LKβ7 peptides adsorbed to the COOH-SAM, (c) the LKα14 peptide adsorbed to the CH_3-SAM, and (d) the LKα14 peptide adsorbed to the COOH-SAM. 3,000 measurements for each amino acid, 0.25 Å bin width.

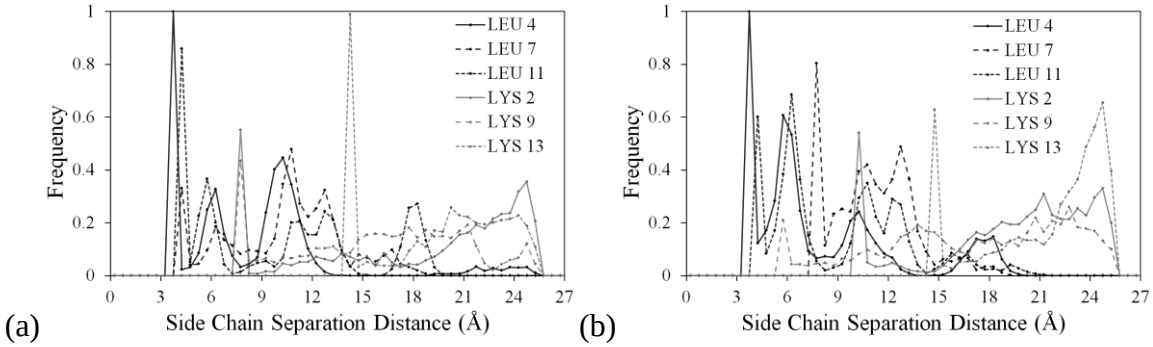

Figure B-8: Plots of interpeptide side chain separation distances for the pair of LKα14 peptides in solution during the last 6 ns of REMD using the CHARMM22 FF, plots represent identical simulations started with different random seeds.

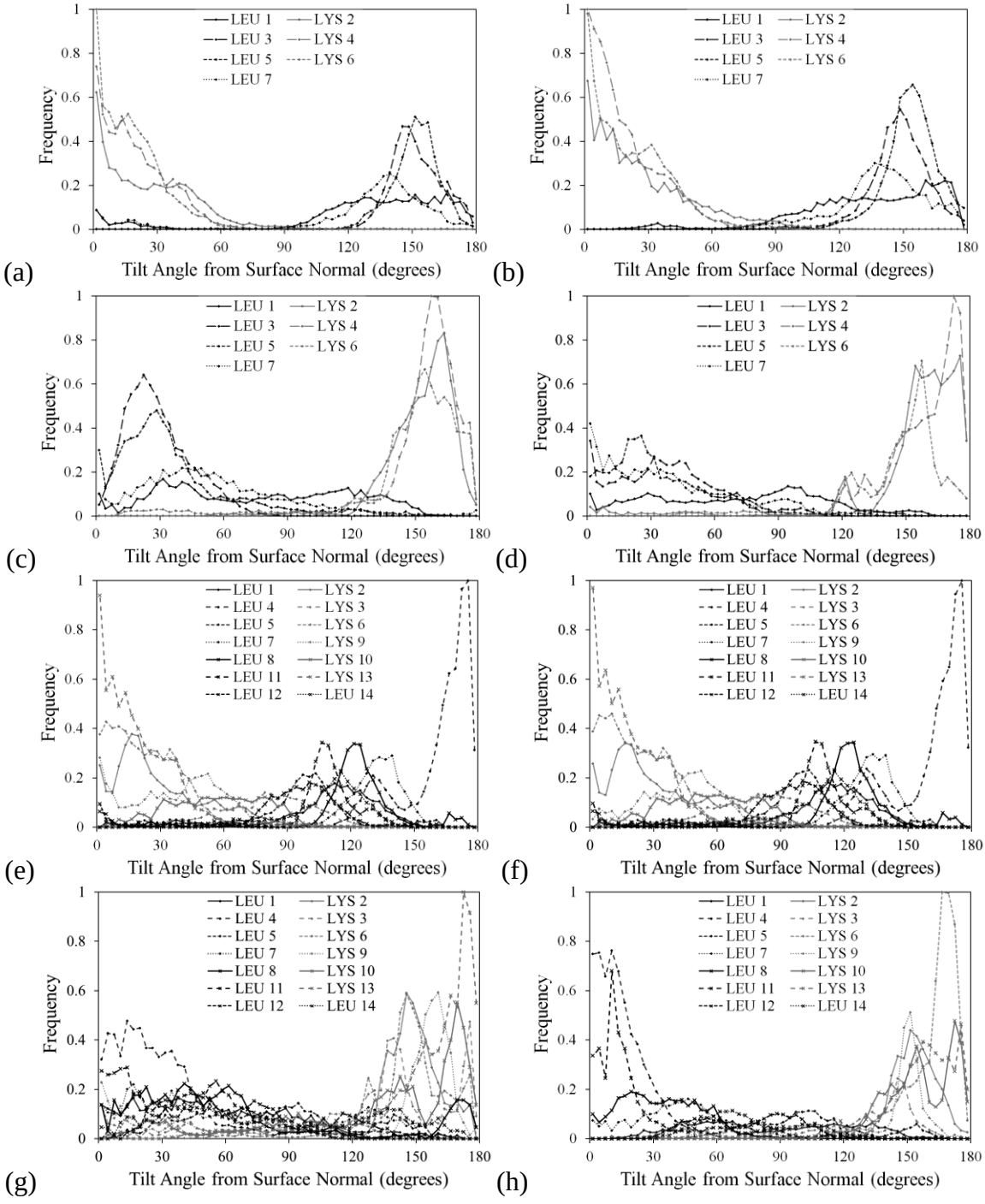
(a)
(b)
(c)
(d)
(e)
(f)
(g)
(h)
Frequency
Tilt Angle from Surface Normal (degrees)
LEU 1
LYS 2
LEU 3
LYS 4
LEU 5
LYS 6
LEU 7
LEU 4
LYS 3
LYS 9
LEU 8
LYS 10
LEU 11
LYS 13
LEU 12
LEU 14

Figure B-9: Pots of frequency distributions of amino acid side chain tilt angles (tilt away from the normal vector of the SAM surface) during the last 6 ns of REMD sampling using the CHARMM22 FF for (a,b) the pair of LKβ7 peptides adsorbed to the CH_3-SAM, (c,d) the pair of LKβ7 peptides adsorbed to the COOH-SAM, (e,f) the LKα14 peptide adsorbed to the CH_3-SAM, and (g,h) adsorbed to the COOH-SAM. Paired plots represent identical simulations started with different random seeds. Plots normalized for the number of counts per 3-degree bin and sinusoidal distribution of measurements.

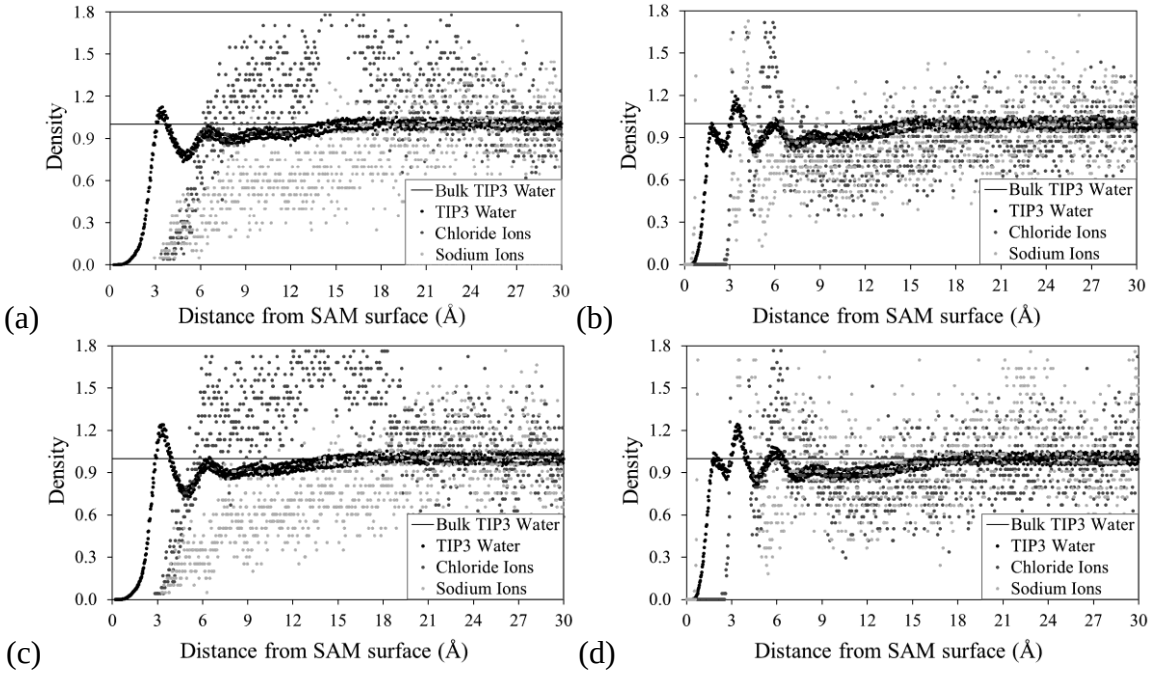

Figure B-10: Additional plots of density distributions of TIP3 water, Na^+ ions, and Cl^- ions relative to bulk solution values (density of 1.0) during the last 6 ns of REMD sampling using the CHARMM22 FF for (a) the pair of LKβ7 peptides adsorbed to the CH_3-SAM, (b) the pair of LKβ7 peptides adsorbed to the COOH-SAM, (c) the LKα14 peptide adsorbed to the CH_3-SAM, and (d) the LKα14 peptide adsorbed to the COOH-SAM. The Na^+ ion distributions in the COOH-SAM plots (b and d) extend beyond the scale of the plot, peaking at relative density values of 2.7 and 2.3 at distances of 1.4 Å and 1.3 Å from the surface, respectively.

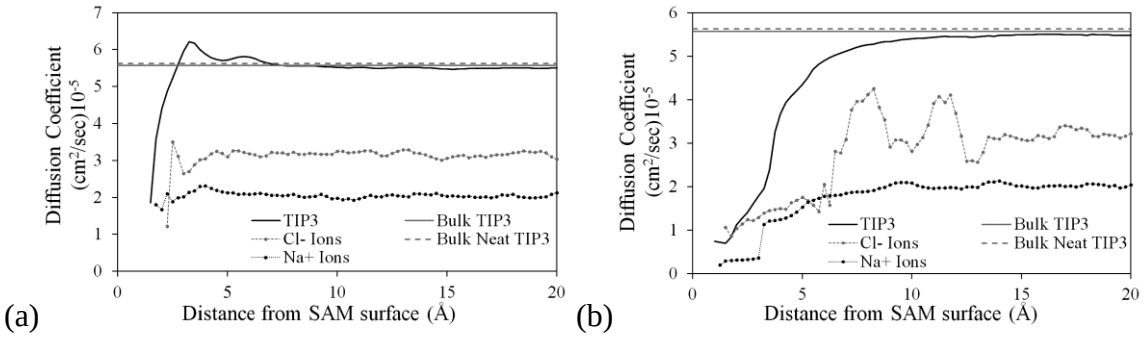

Figure B-11: Plots of calculated diffusion coefficients for TIP3 water using the CHARMM22 FF, Cl- ions, and Na+ ions near the (a) CH_3-SAM, and the (b) COOH-SAM. No peptides present, planar 0.25 Å bins extending along the z-axis from the surface.

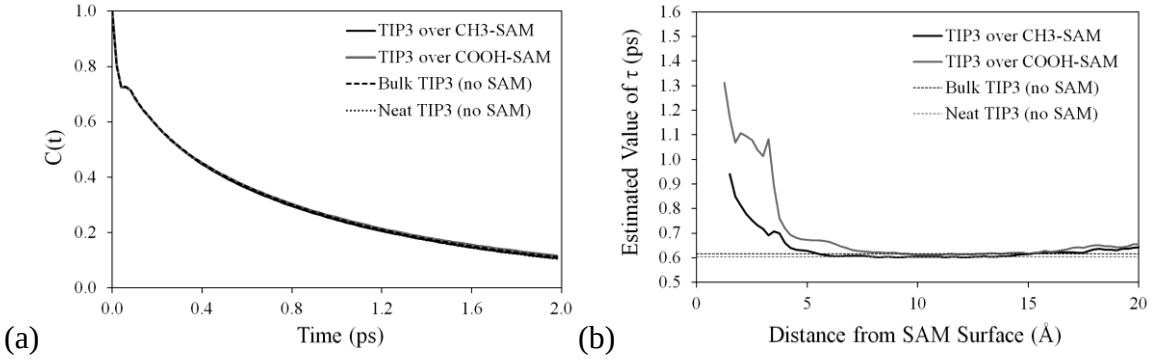

Figure B-12: Plots of (a) calculated rotational correlation functions for TIP3 water above SAM surfaces, and (b) estimated τ values based on the rotational correlation functions. No peptides present. Each curve consists of an individual data point from each planar 0.25 Å bin extending along the z-axis from the surface (along the surface normal).The rotational correlation time is calculated by fitting the exponential decay portion of the corresponding time correlation function (t) to an exponential function of the form C(t) = A exp(-t/τ) where τ is the correlation time. Here, we have calculated the P2 dipole correlation, <P2(u(t)*u(t+tau))>, where u is the unit vector along the water dipole; P2(x)=(3x^2-1)/2. Our average calculated value of τ for bulk TIP3P water is 0.62 ps, and this value is in agreement with values calculated by van der Spoel[157] (0.7 ps) and Marchi[160] (0.76 ps).

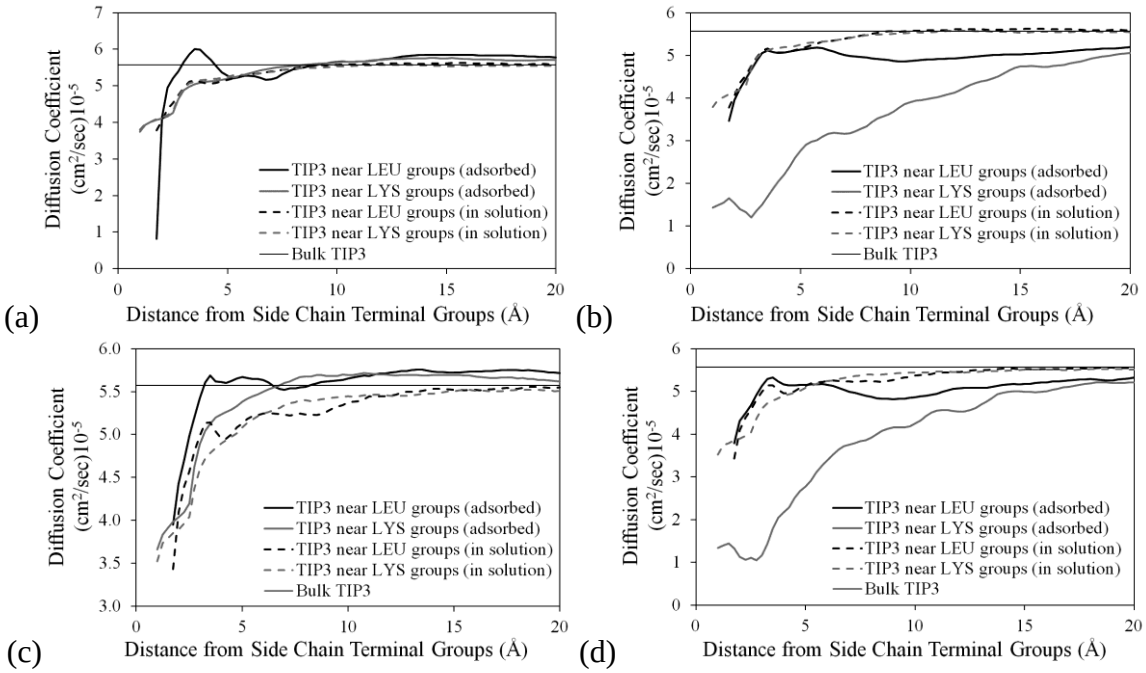

Figure B-13: Plots of calculated diffusion coefficients for TIP3 water surrounding the LEU and LYS groups of (a) the pair of LKβ7 peptides adsorbed to the CH_3-SAM, (b) the pair of LKβ7 peptides adsorbed to the COOH-SAM, (c) the LKα14 peptide adsorbed to the CH_3-SAM, and (d) the LKα14 peptide adsorbed to the COOH-SAM. Spherical 0.25 Å bins (spherical shells) extending from the center of each respective group, using the CHARMM22 FF.

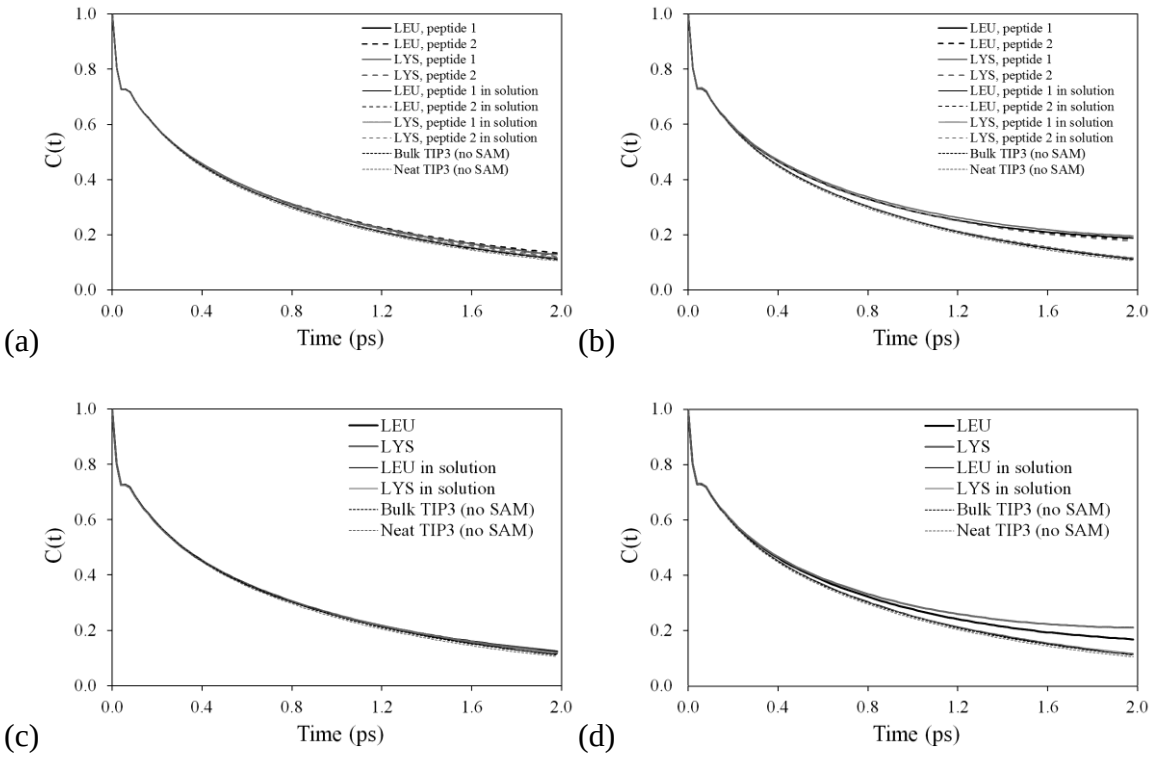

Figure B-14: Plots of calculated rotational correlation functions for TIP3 water surrounding the LEU and LYS groups of (a) the pair of LKβ7 peptides adsorbed to the CH_3-SAM, (b) the pair of LKβ7 peptides adsorbed to the COOH-SAM, (c) the LKα14 peptide adsorbed to the CH_3-SAM, and (d) the LKα14 peptide adsorbed to the COOH-SAM. Each curve consists of 100 data points.

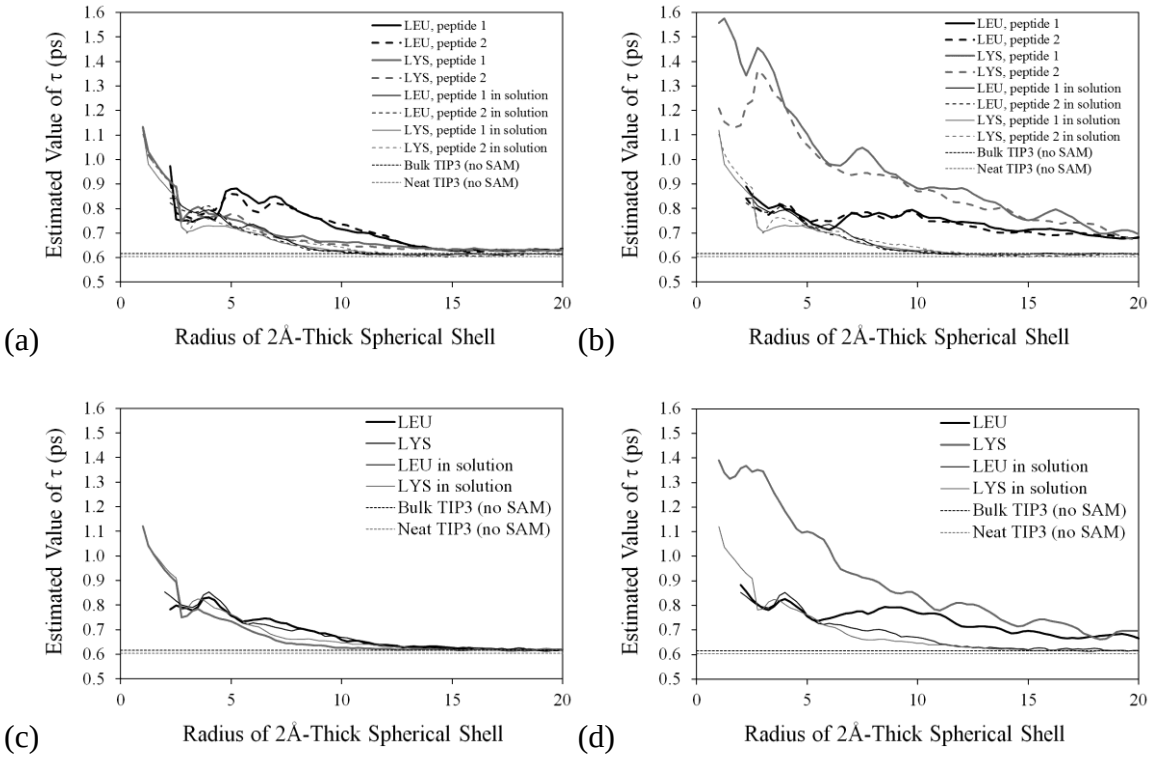

Figure B-15: Plots of estimated τ values based on the rotational correlation functions for TIP3 water surrounding the LEU and LYS groups of (a) the pair of LKβ7 peptides adsorbed to the CH_3-SAM, (b) the pair of LKβ7 peptides adsorbed to the COOH-SAM, (c) the LKα14 peptide adsorbed to the CH_3-SAM, and (d) the LKα14 peptide adsorbed to the COOH-SAM. The origin of the spherical shell for each calculation was a combination of all of the terminal methyl carbons for L side chains or a combination of all of the terminal nitrogen atoms for K side chains. Curves consist of a single data point for each 0.25 Å bin.

Appendix C

Additional Figures for Chapter Six, A Comparison of Molecular Dynamics Force Fields in the Simulation of Peptide Adsorption to Functionalized Self-Assembled Monolayer Surfaces

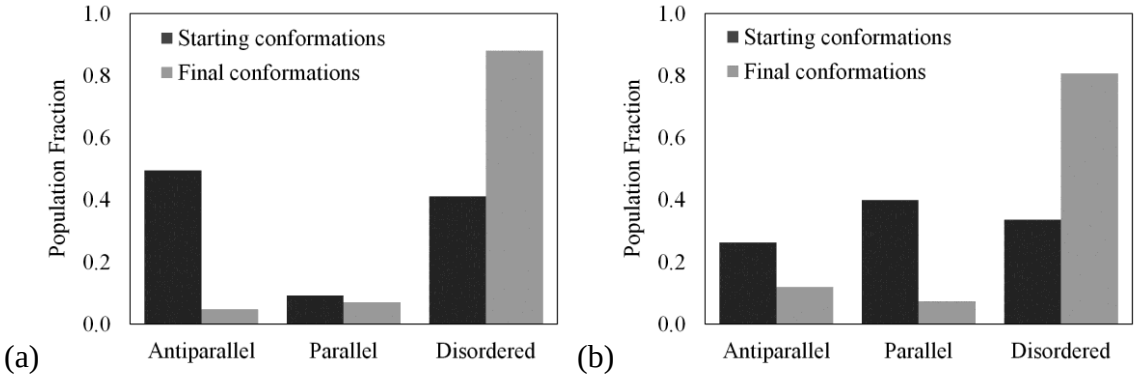

Figure C-1: Plots of replicas that contributed to the 298 K ensemble of structures for the pair of LKβ7 peptides adsorbed to the CH_3-SAM for (a) the AMBER94 FF, and for (b) the OPLS-AA FF. Both plots show the population fractions of each starting conformation that contributed to the final ensemble and the population fractions of the conformations that constituted the final ensemble.

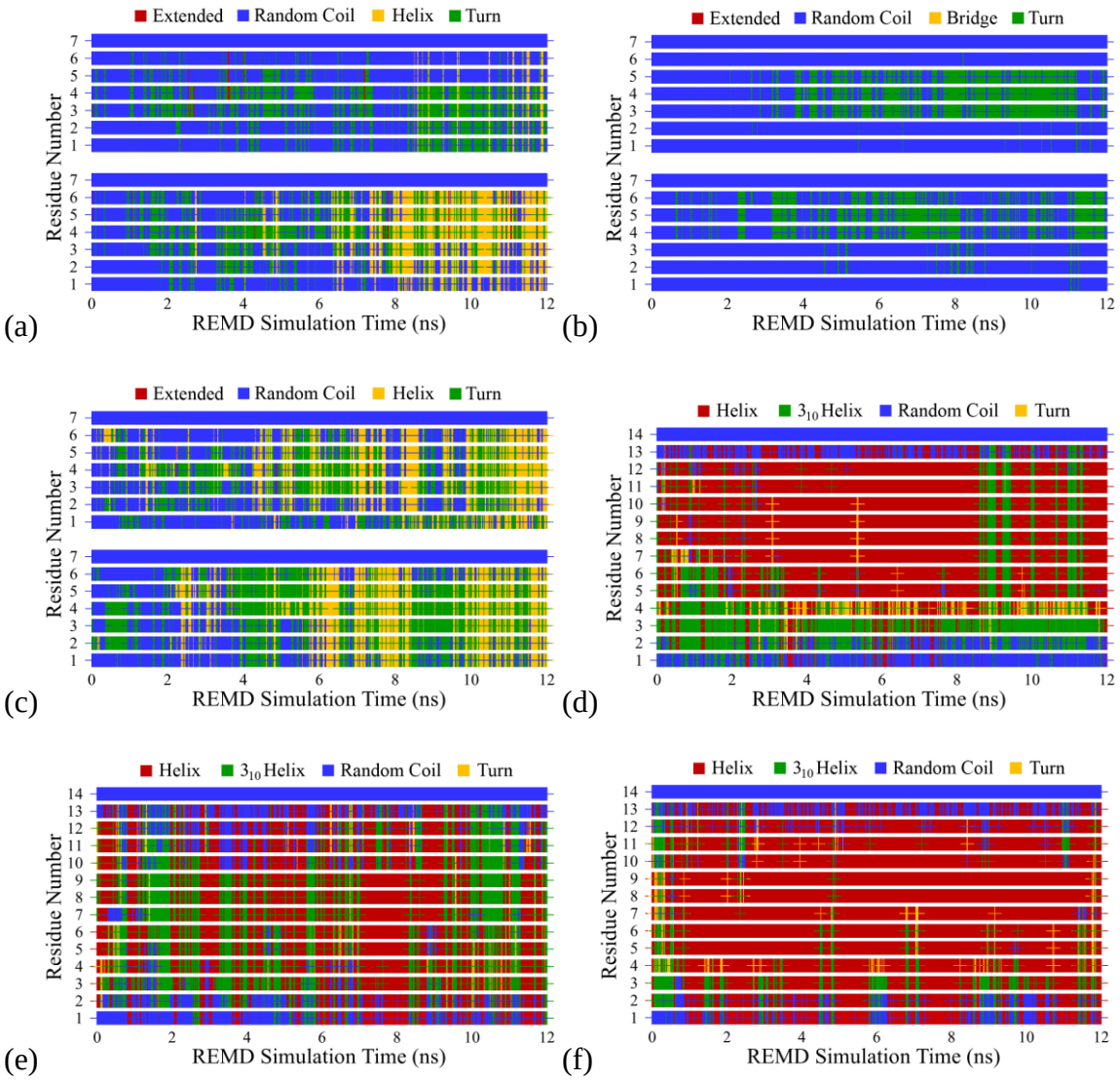

Figure C-2: Additional plots of secondary structure for each amino acid residue through the entire REMD simulation using the AMBER94 FF for (a) the pair of LKβ7 peptides adsorbed to the CH_3-SAM, (b) the pair of LKβ7 peptides adsorbed to the COOH-SAM, (c) the pair of LKβ7 peptides in solution, (d) the LKα14 peptide adsorbed to the CH_3-SAM, (e) the LKα14 peptide adsorbed to the COOH-SAM, and (f) the LKα14 peptide in solution.

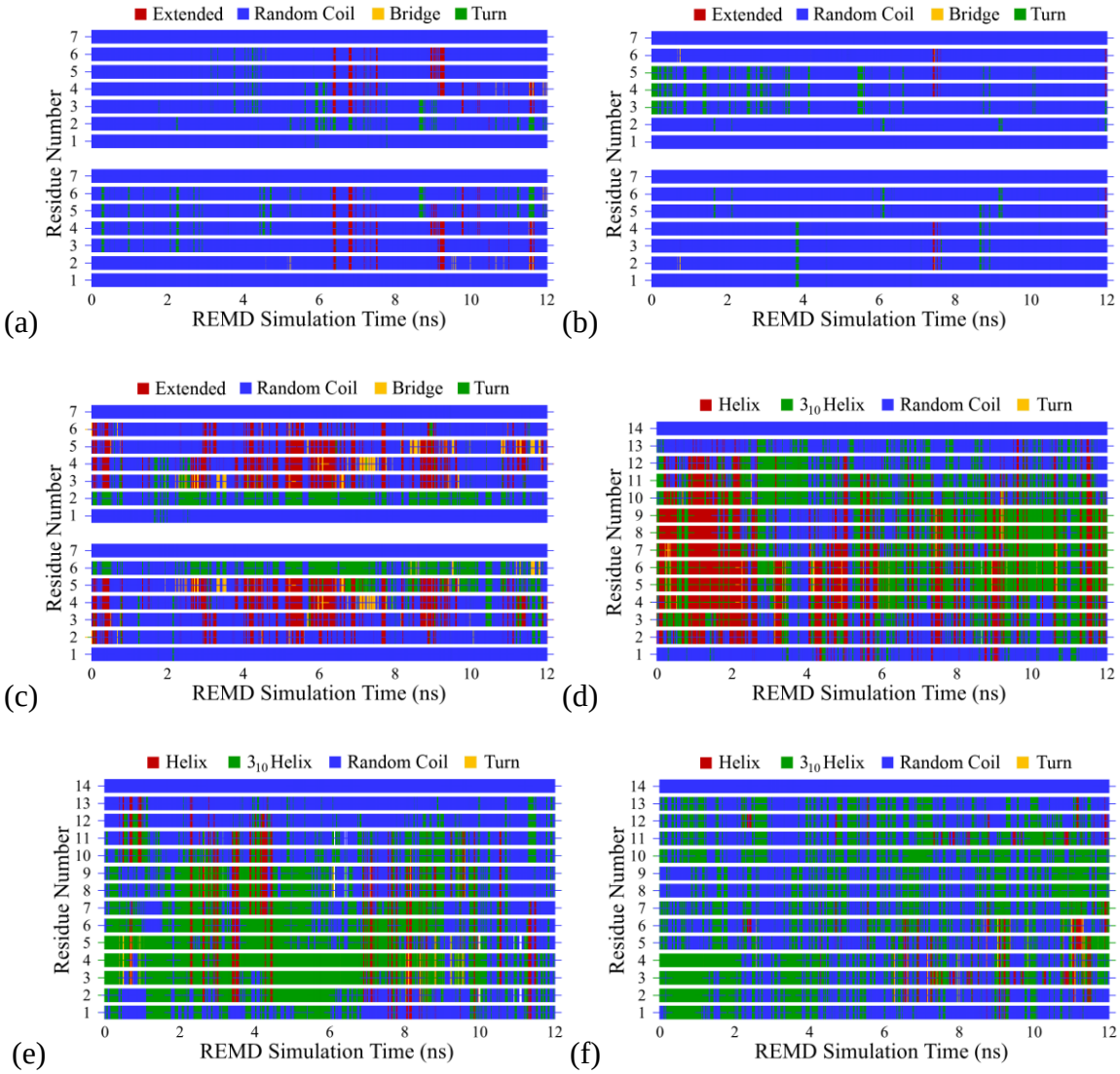

Figure C-3: Additional plots of secondary structure for each amino acid residue through the entire REMD simulation using the OPLS-AA FF for (a) the pair of LKβ7 peptides adsorbed to the CH_3-SAM, (b) the pair of LKβ7 peptides adsorbed to the COOH-SAM, (c) the pair of LKβ7 peptides in solution, (d) the LKα14 peptide adsorbed to the CH_3-SAM, (e) the LKα14 peptide adsorbed to the COOH-SAM, and (f) the LKα14 peptide in solution.

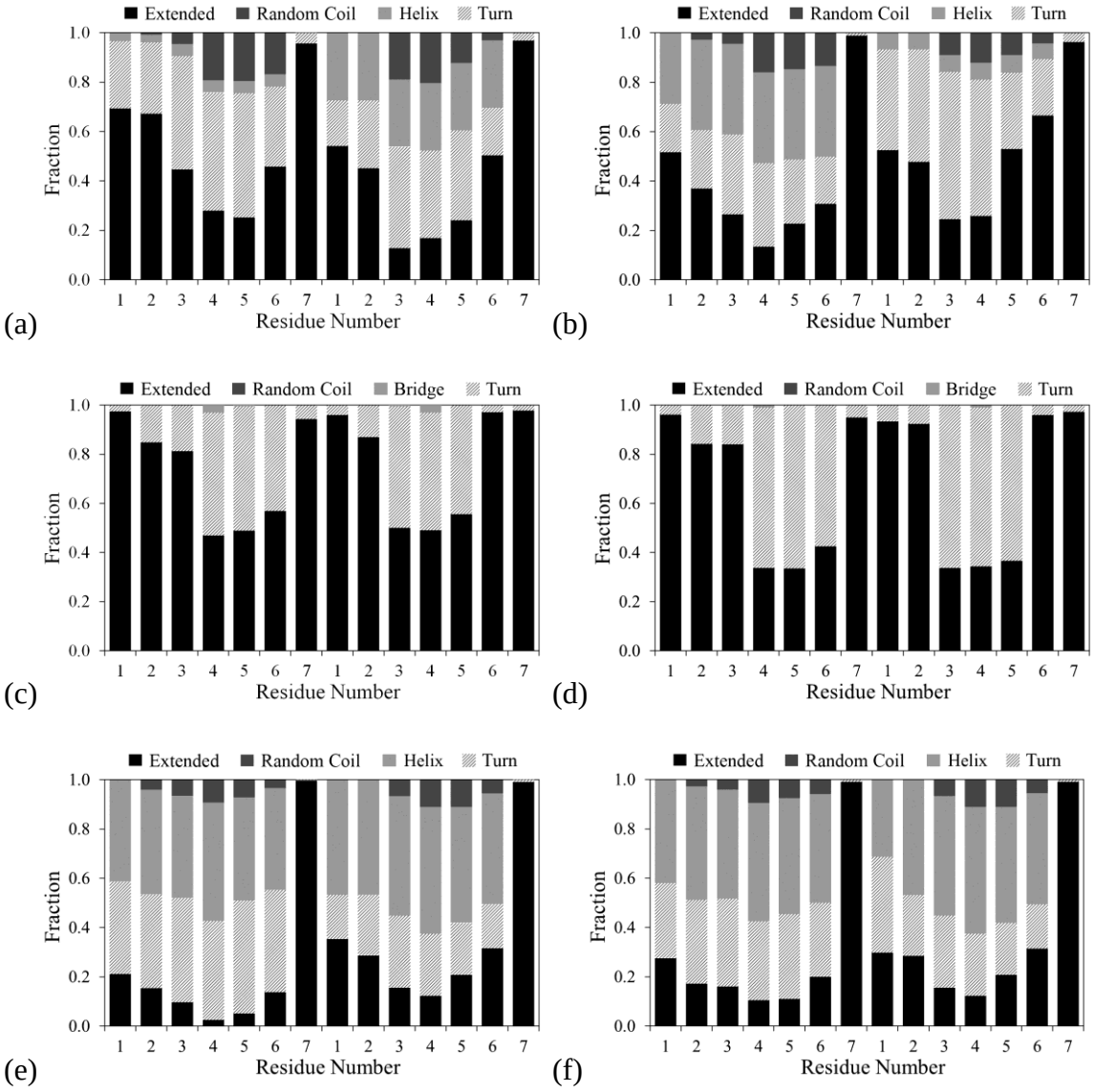
(a)
Extended
Random Coil
Helix
Turn
Fraction
Residue Number
(b)
Extended
Random Coil
Helix
Turn
Fraction
Residue Number
(c)
Extended
Random Coil
Bridge
Turn
Fraction
Residue Number
(d)
Extended
Random Coil
Bridge
Turn
Fraction
Residue Number
(e)
Extended
Random Coil
Helix
Turn
Fraction
Residue Number
(f)
Extended
Random Coil
Helix
Turn
Fraction
Residue Number

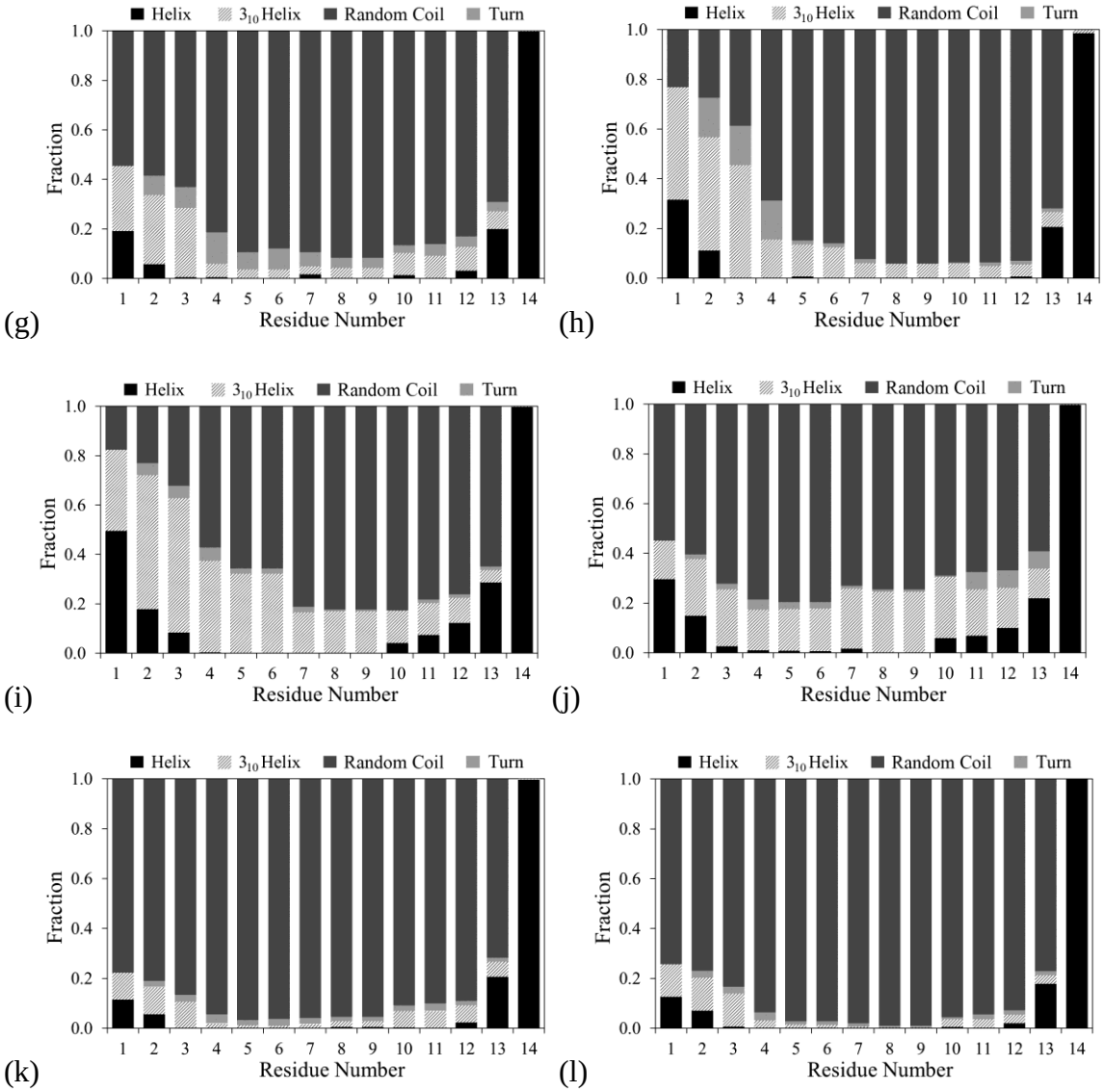

Figure C-4: Plots of fractional secondary structure for each amino acid residue through the entire REMD simulation using the AMBER94 FF for (a,b) the pair of LKβ7 peptides adsorbed to the CH_3-SAM, (c,d) the pair of LKβ7 peptides adsorbed to the COOH-SAM, (e,f) the pair of LKβ7 peptides in solution, (g,h) the LKα14 peptide adsorbed to the CH_3-SAM, (i,j) the LKα14 peptide adsorbed to the COOH-SAM, and (k,l) the LKα14 peptide in solution.

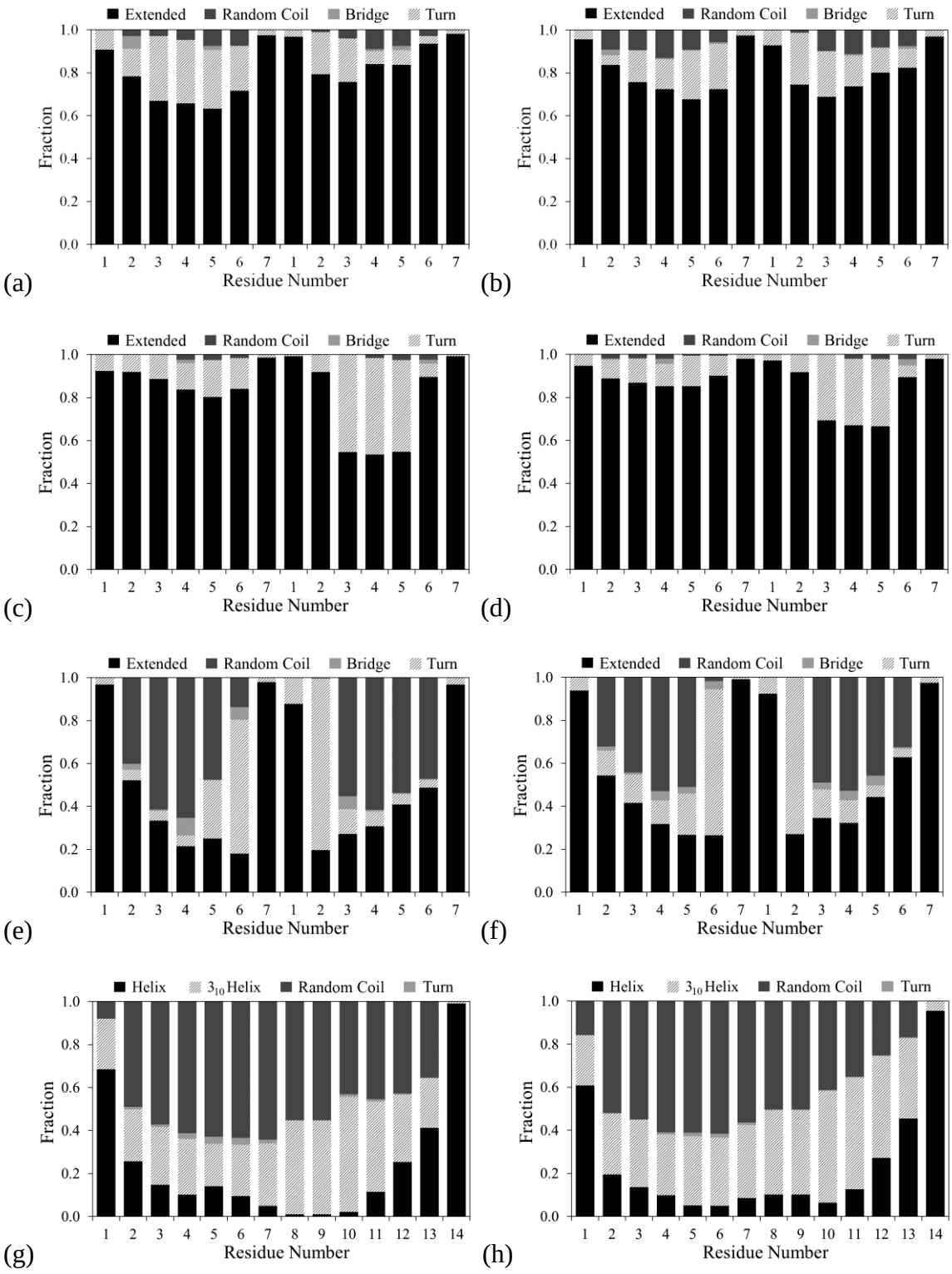
Extended
Random Coil
Bridge
Turn
Fraction
Residue Number
(a)
(b)
(c)
(d)
(e)
(f)
Helix
3_{10} Helix
(g)
(h)

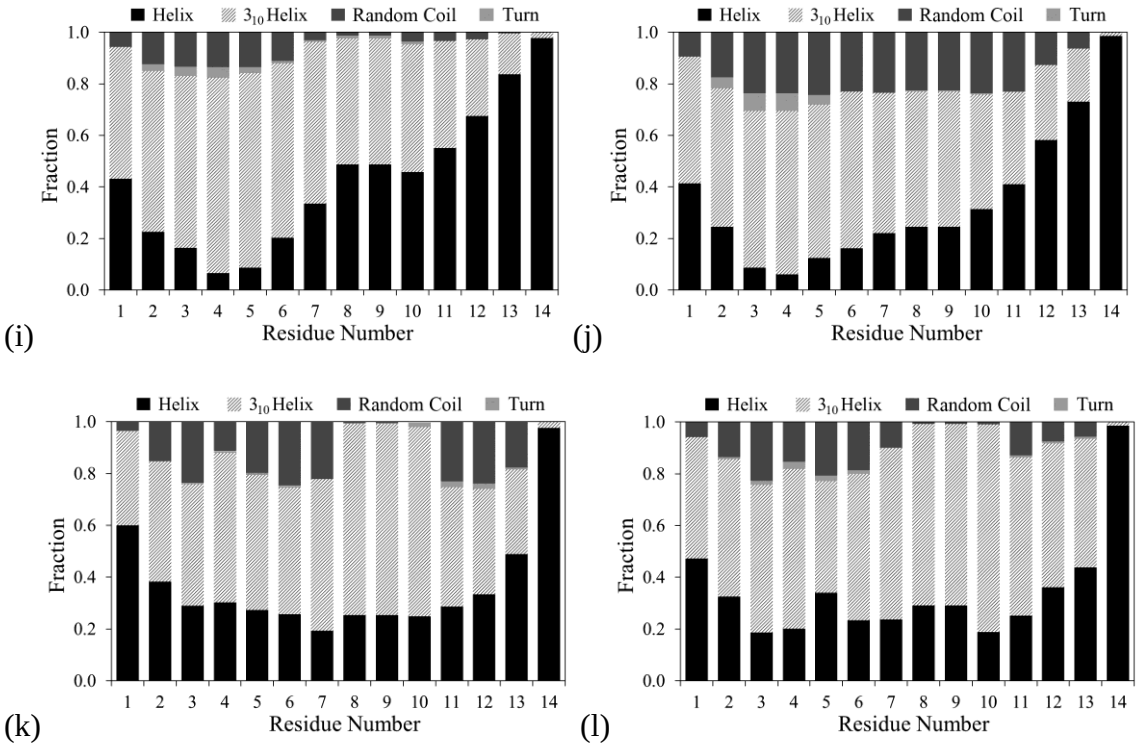

Figure C-5: Plots of fractional secondary structure for each amino acid residue through the entire REMD simulation using the OPLS-AA FF for (a,b) the pair of LKβ7 peptides adsorbed to the CH_3-SAM, (c,d) the pair of LKβ7 peptides adsorbed to the COOH-SAM, (e,f) the pair of LKβ7 peptides in solution, (g,h) the LKα14 peptide adsorbed to the CH_3-SAM, (i,j) the LKα14 peptide adsorbed to the COOH-SAM, and (k,l) the LKα14 peptide in solution.

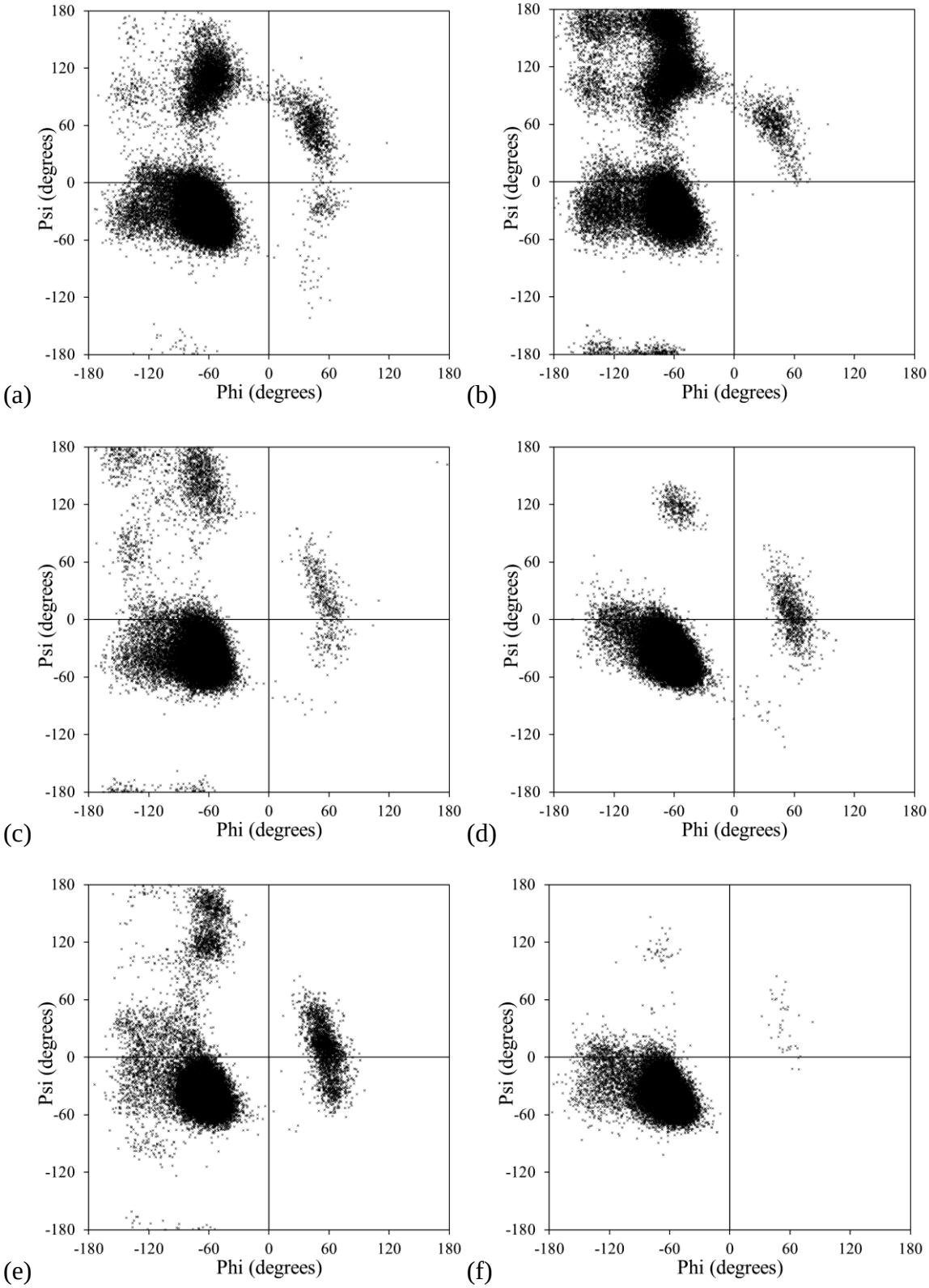
(a)
(b)
(c)
(d)
(e)
(f)
Psi (degrees)
Phi (degrees)
180
120
60
0
-60
-120
-180

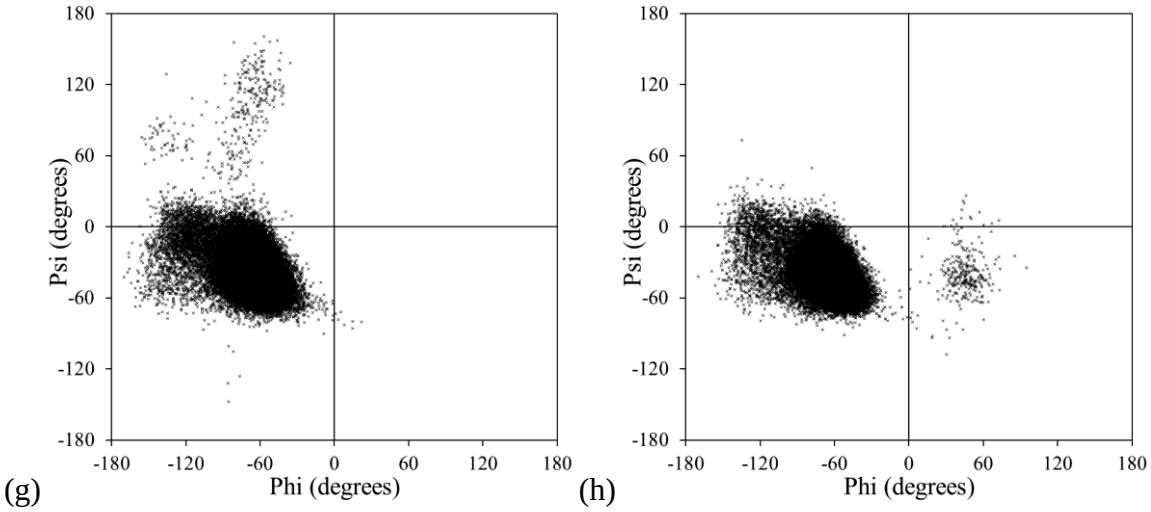

Figure C-6: Additional Ramachandran plots of the Phi and Psi peptide backbone dihedral angles during the final 6 ns of REMD sampling using the AMBER94 FF for (a,b) the pair of LKβ7 peptides adsorbed to the CH_3-SAM, (c,d) the pair of LKβ7 peptides adsorbed to the COOH-SAM, (e,f) the pair of LKβ7 peptides in solution, (g,h) the LKα14 peptide adsorbed to the CH_3-SAM, (i,j) the LKα14 peptide adsorbed to the COOH-SAM, (k,l) the LKα14 peptide in solution, and (m,n) a pair of LKα14 peptides in solution. 3,000 points displayed for each non-terminal amino acid.

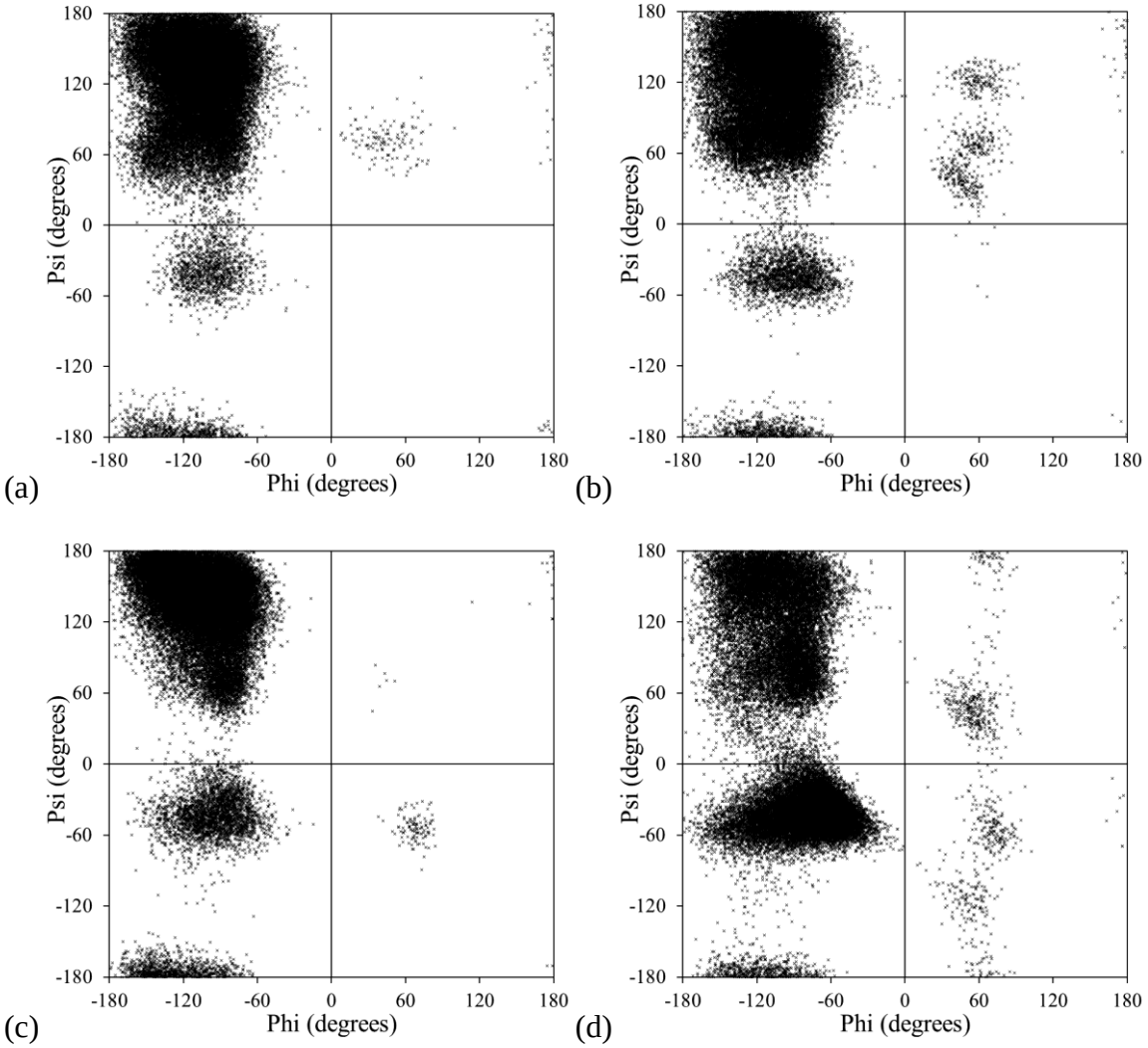
(a)
(b)
(c)
(d)
Psi (degrees)
Phi (degrees)
180
120
60
0
-60
-120
-180

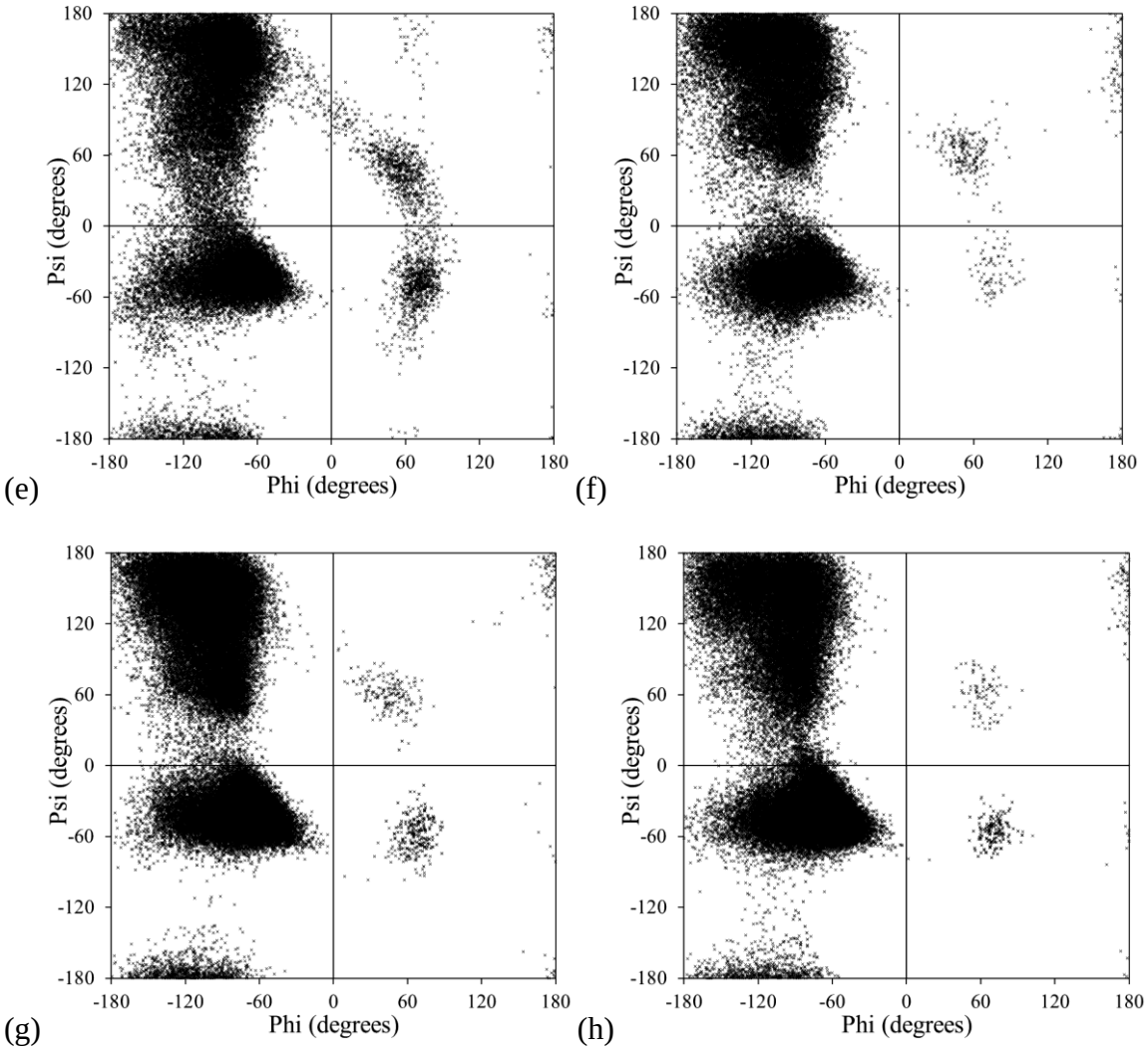

Figure C-7: Additional Ramachandran plots of the Phi and Psi peptide backbone dihedral angles during the final 6 ns of REMD sampling using the OPLS-AA FF for (a) the pair of LKβ7 peptides adsorbed to the CH_3-SAM, (b) the pair of LKβ7 peptides adsorbed to the COOH-SAM, (c) the pair of LKβ7 peptides in solution, (d) the LKα14 peptide adsorbed to the CH_3-SAM, (e) the LKα14 peptide adsorbed to the COOH-SAM, (f) the LKα14 peptide in solution, and (g,h) a pair of LKα14 peptides in solution. 3,000 points displayed for each non-terminal amino acid.

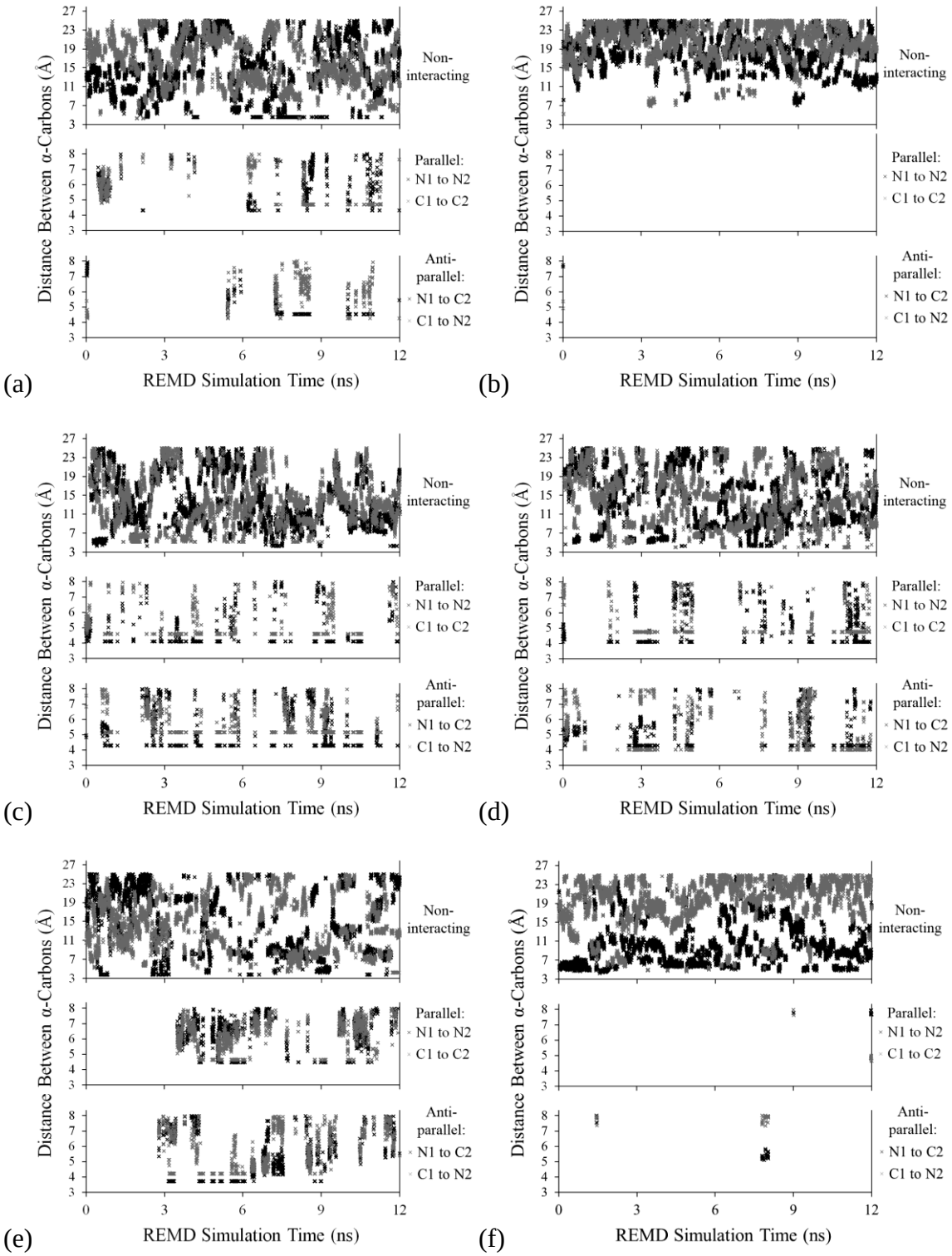
Distance Between α-Carbons (Å)
Non-interacting
Parallel:
N1 to N2
C1 to C2
Anti-parallel:
N1 to C2
C1 to N2
REMD Simulation Time (ns)
(a)
(b)
(c)
(d)
(e)
(f)

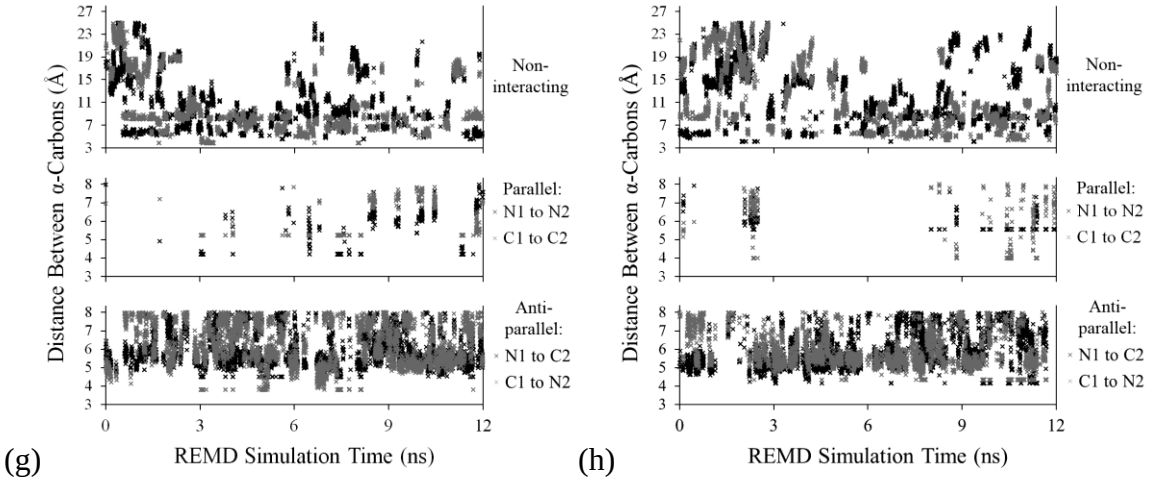

Figure C-8: Additional plots of distances between terminal α-carbons (indicative of parallel and antiparallel conformations) for the pair of LKβ7 peptides during the entire REMD simulation (a) adsorbed to the CH_3-SAM (AMBER94 FF), (b) adsorbed to the COOH-SAM (AMBER94 FF), (c,d) in solution (AMBER94 FF), (e) adsorbed to the CH_3-SAM (OPLS-AA FF), (f) adsorbed to the COOH-SAM (OPLS-AA FF), and (g,h) in solution (OPLS-AA FF).

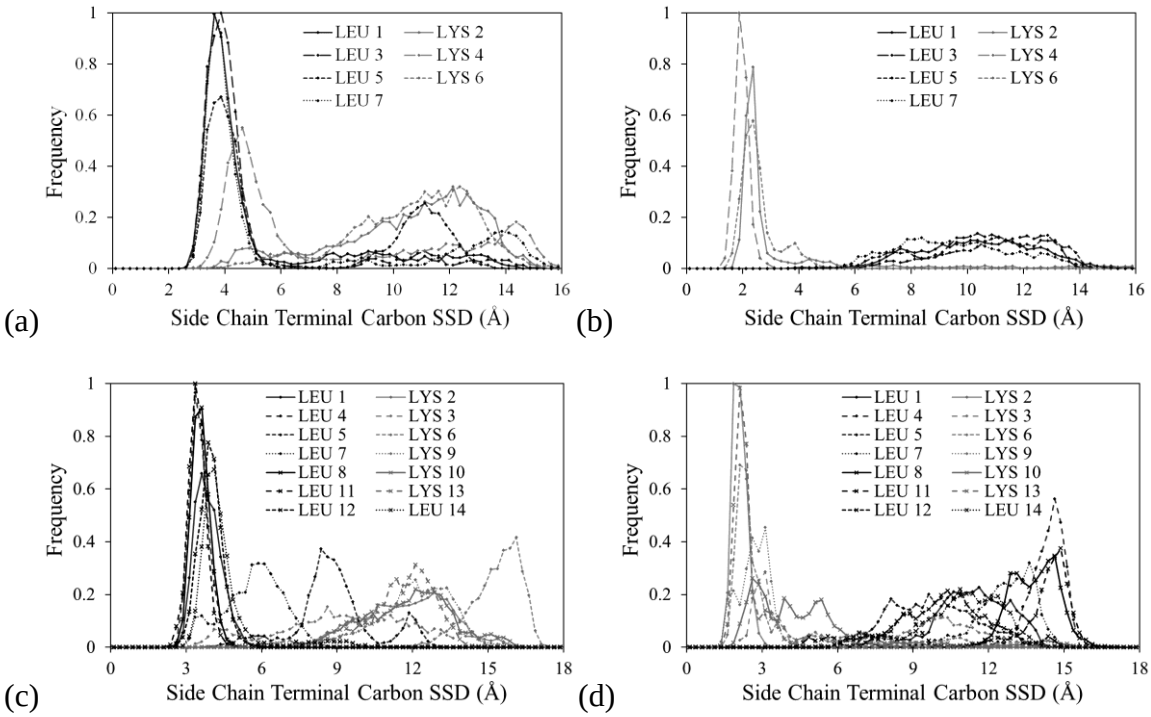

Figure C-9: Additional plots of frequency distributions of amino acid side chain terminal carbon surface separation distances (SSDs, Å) during the last 6 ns of REMD sampling using the AMBER94 FF for (a) the pair of LKβ7 peptides adsorbed to the CH_3-SAM, (b) the pair of LKβ7 peptides adsorbed to the COOH-SAM, (c) the LKα14 peptide adsorbed to the CH_3-SAM, and (d) the LKα14 peptide adsorbed to the COOH-SAM. 3,000 measurements for each amino acid, 0.25 Å bin width.

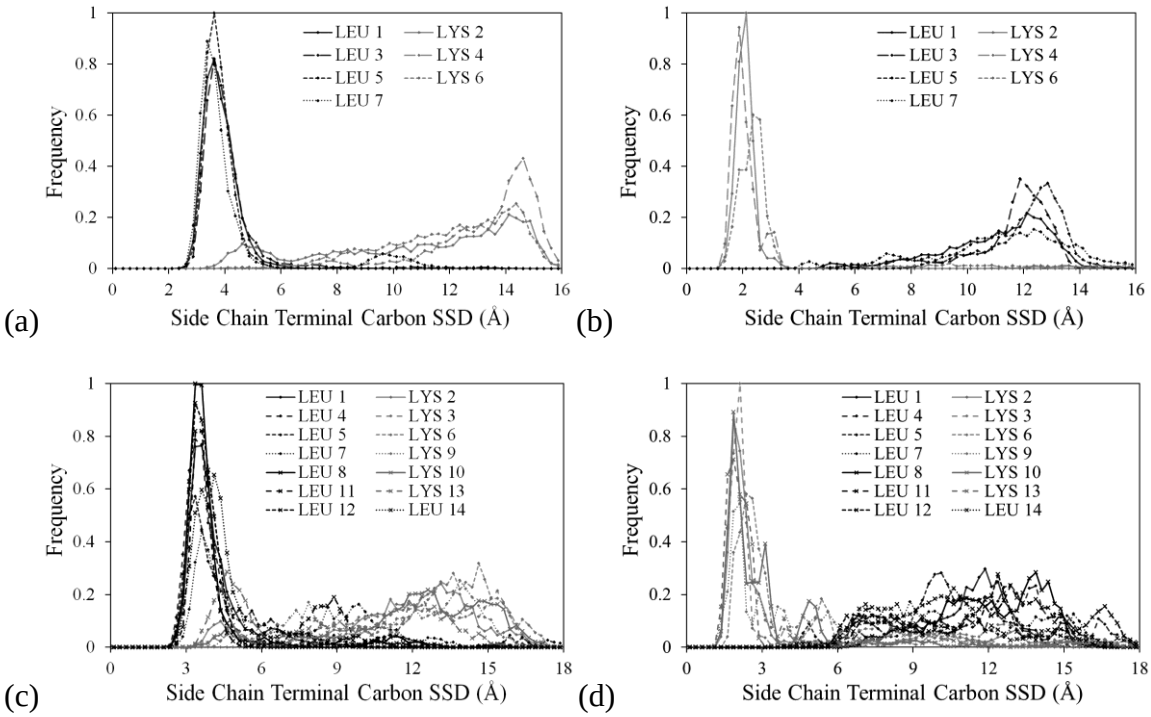

Figure C-10: Additional plots of frequency distributions of amino acid side chain terminal carbon surface separation distances (SSDs, Å) during the last 6 ns of REMD sampling using the OPLS-AA FF for (a) the pair of LKβ7 peptides adsorbed to the CH_3-SAM, (b) the pair of LKβ7 peptides adsorbed to the COOH-SAM, (c) the LKα14 peptide adsorbed to the CH_3-SAM, and (d) the LKα14 peptide adsorbed to the COOH-SAM. 3,000 measurements for each amino acid, 0.25 Å bin width.

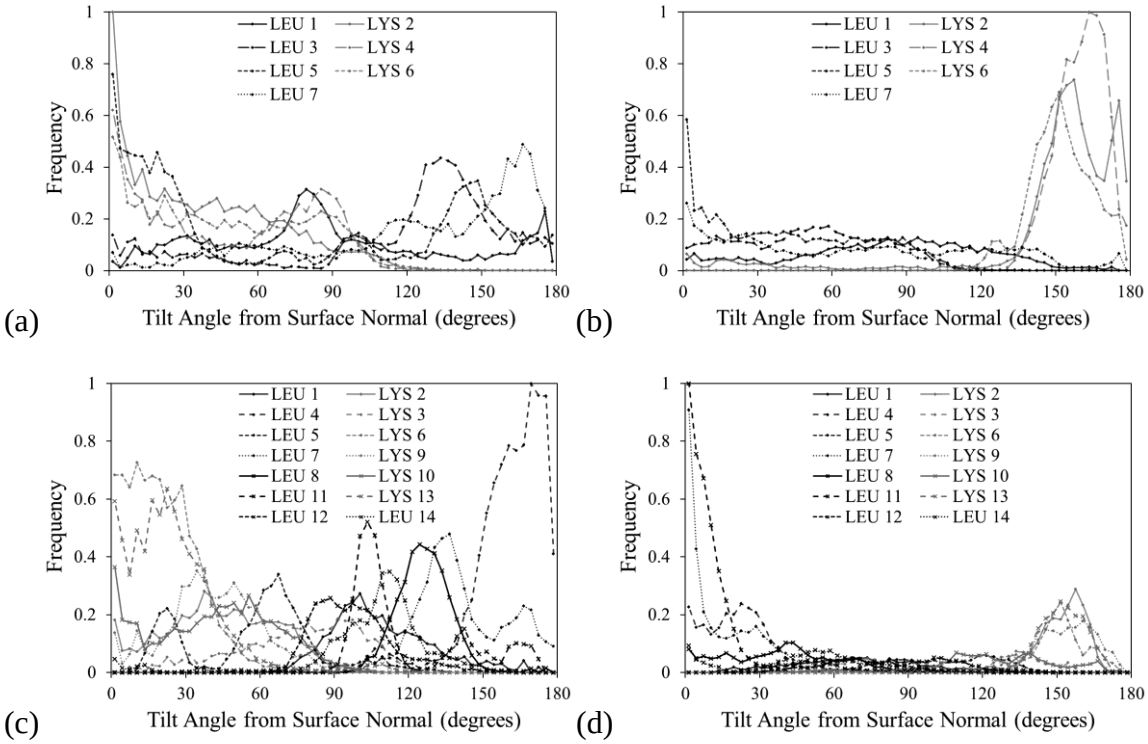

Figure C-11: Additional plots of frequency distributions of amino acid side chain tilt angles (tilt away from the normal vector of the SAM surface) during the last 6 ns of REMD sampling using the AMBER94 FF for (a) the pair of LKβ7 peptides adsorbed to the CH_3-SAM, (b) the pair of LKβ7 peptides adsorbed to the COOH-SAM, (c) the LKα14 peptide adsorbed to the CH_3-SAM, and (d) the LKα14 peptide adsorbed to the COOH-SAM. Plots normalized for the number of counts per 3-degree bin and sinusoidal distribution of measurements.

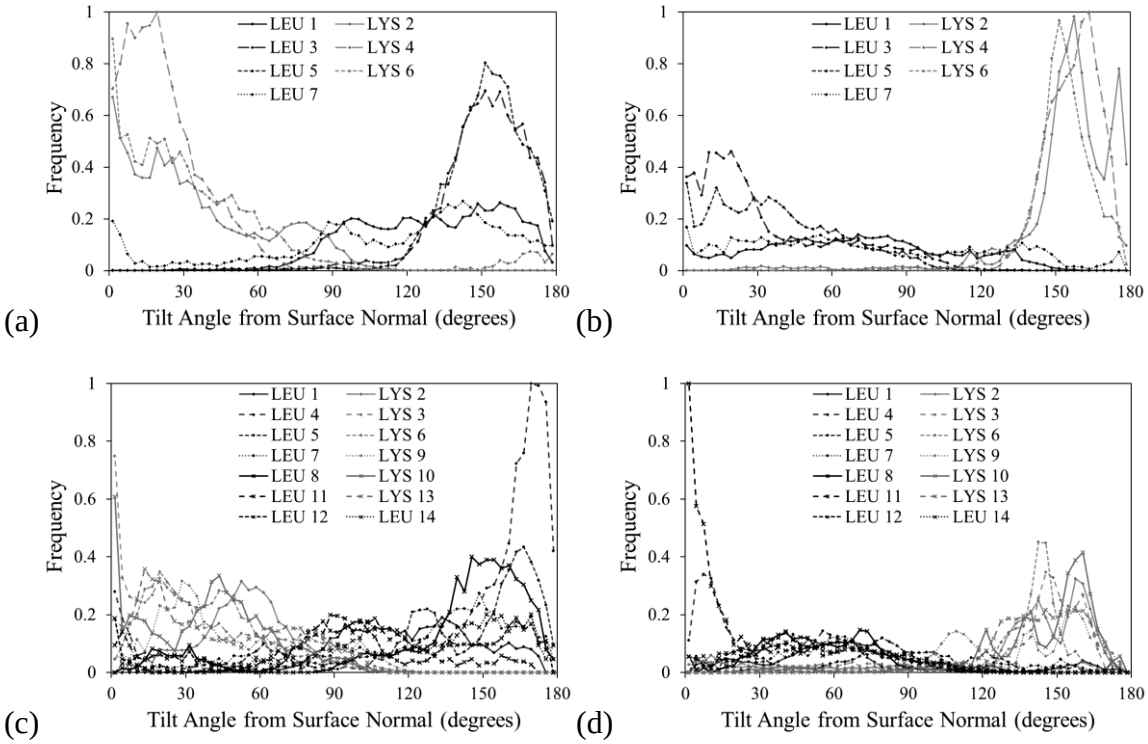

Figure C-12: Additional plots of frequency distributions of amino acid side chain tilt angles (tilt away from the normal vector of the SAM surface) during the last 6 ns of REMD sampling using the OPLS-AA FF for (a) the pair of LKβ7 peptides adsorbed to the CH_3-SAM, (b) the pair of LKβ7 peptides adsorbed to the COOH-SAM, (c) the LKα14 peptide adsorbed to the CH_3-SAM, and (d) the LKα14 peptide adsorbed to the COOH-SAM. Plots normalized for the number of counts per 3-degree bin and sinusoidal distribution of measurements.

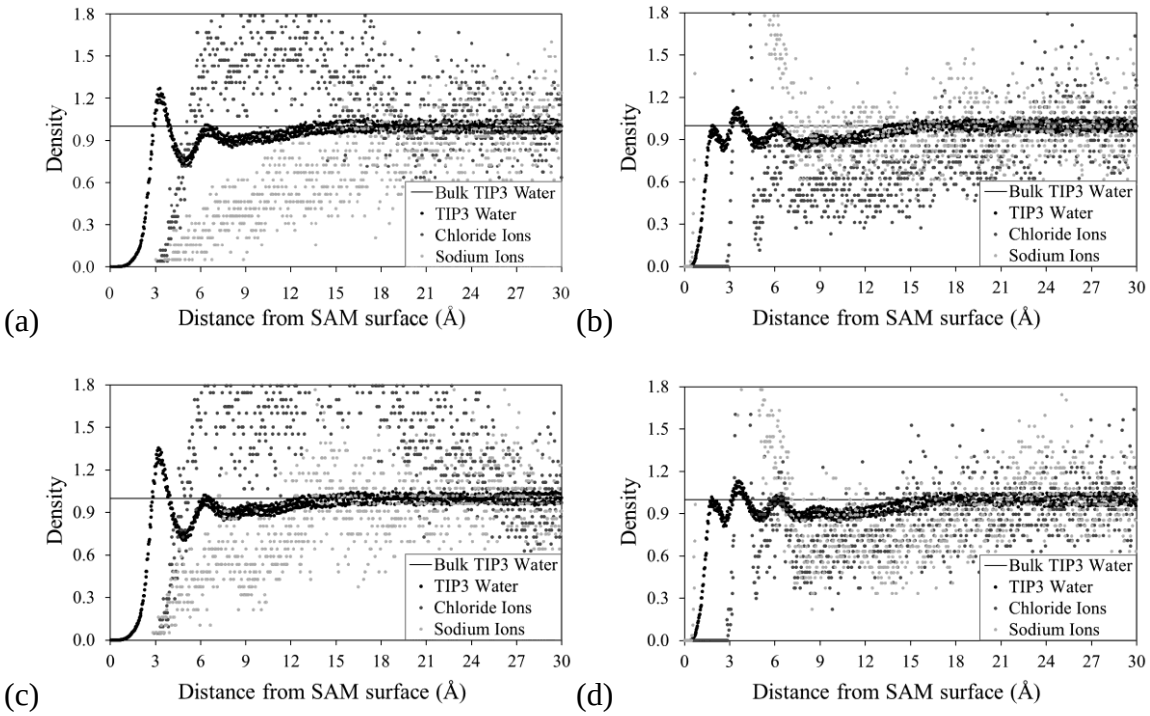

Figure C-13: Additional plots of density distributions of TIP3 water, Na^+ ions, and Cl^- ions relative to bulk solution values (density set to 1.0) during the last 6 ns of REMD sampling using the AMBER94 FF for (a) the pair of LKβ7 peptides adsorbed to the CH_3-SAM, (b) the pair of LKβ7 peptides adsorbed to the COOH-SAM, (c) the LKα14 peptide adsorbed to the CH_3-SAM, and (d) the LKα14 peptide adsorbed to the COOH-SAM. The Na^+ ion distributions in the COOH-SAM plots (b and d) extend beyond the scale of the plot, peaking at relative density values of approximately 140 and 170, respectively, at a distance of 1.5 Å from the surface.

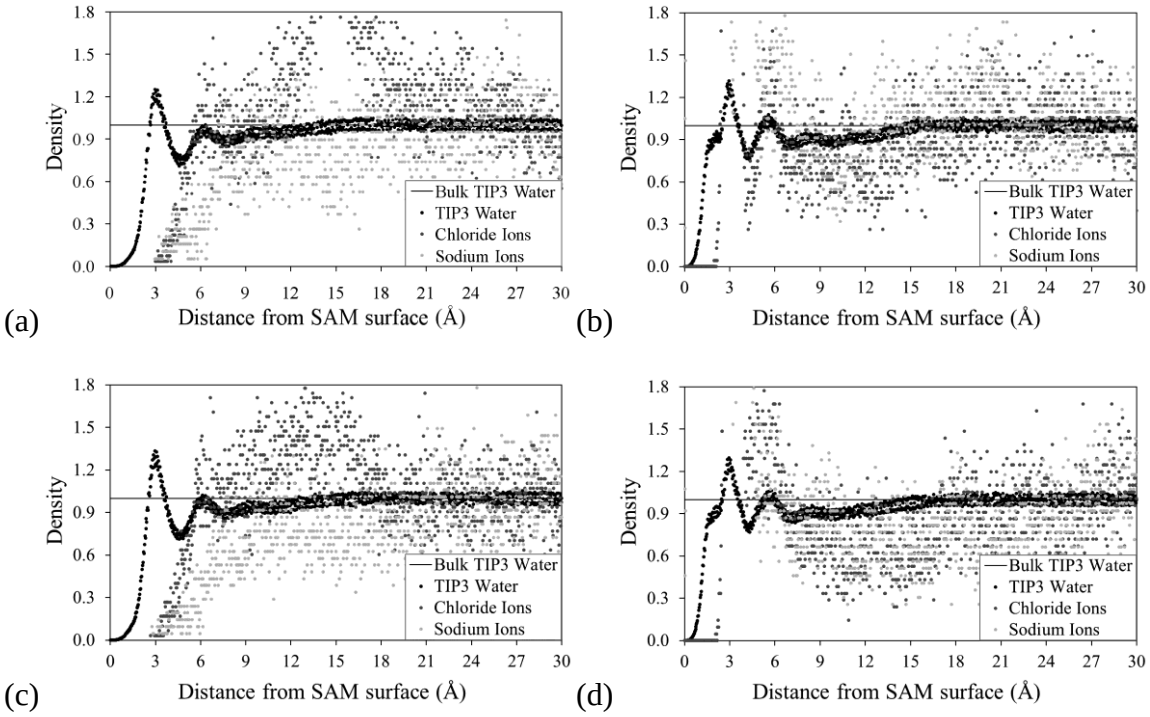

Figure C-14: Additional plots of density distributions of TIP3 water, Na^+ ions, and Cl^- ions relative to bulk solution values (density set to 1.0) during the last 6 ns of REMD sampling using the OPLS-AA FF for (a) the pair of LKβ7 peptides adsorbed to the CH_3-SAM, (b) the pair of LKβ7 peptides adsorbed to the COOH-SAM, (c) the LKα14 peptide adsorbed to the CH_3-SAM, and (d) the LKα14 peptide adsorbed to the COOH-SAM. The Na^+ ion distributions in the COOH-SAM plots (b and d) extend beyond the scale of the plot, peaking at relative density values of approximately 190 and 230, respectively, at a distance of 1.1 Å from the surface.

Appendix D

Simulation Details

This section provides documentation of the technical details associated with conducting the simulations described in this dissertation. Much of this documentation refers to programs, shell scripts, or files that are not explicitly included here, but all of the referenced programs, shell scripts, and files are stored in Clemson University's Palmetto Cluster /bioengr/gcollie directory. File and folder names used are, without exception, sufficiently long to provide some intuitive sense of what data or tasks those files and folders are associated with. Additionally, all input and script files contain comments detailing the purpose for the settings or variables contained therein, so those details will not be presented here. Filename extensions (the 3 or 4 characters following the final period in filenames) are as follows:

*.txt = Plain text file containing notes or input data to be read by programs or scripts.
*.inp = CHARMM dynamics or data analysis input file.
*.out = Simulation or data analysis output files.
*.bash = Shell scripts (PBS job scripts and data analysis scripts).
*.dat or *.data = Data files resulting from some data analysis jobs.
*.crd = Atomic coordinates for a single frame of a simulated system (CHARMM-format coordinates "card" file).
*.psf = CHARMM-format protein structure file (single frame topology file).
*.log = Log files for CHARMM, MMTSB, or STRIDE.
*.cond = MMTSB REMD temperature distribution file.
*.cfg = MMTSB REMD job server or client configuration file.
*.options = MMTSB REMD job client options file (dynamics settings).
*.ninx = MMTSB REMD job acceptance ratios file.
*.pdb = Protein Databank files (CHARMM format.
*.prm = CHARMM parameter library file.
*.rtf = CHARMM topology library file.

Other temporary or test files exist amongst the other files, but they are not useful in recreating any of this work. Most of the parent directories containing project-related files have been made into .tar archive files named with the same name as the original directory, but with the .tar filename extension added.

All of this work, completed on both the Palmetto and the TeraGrid/LONI QueenBee Linux cluster, was completed using the default /bin/bash shell environment (at least version 3.2.25) within a Red Hat Enterprise Linux v4 or v5 operating system. The environment variables were set using the /bioengr/gcollie/bashrc.intel-10.1.ser.mmtsb script. This file (and only this file) was called from the .bashrc file parsed upon system log-in. This file includes environment settings for the Intel version 10.1 C, C++, and Fortran compilers and the Myrinet-enabled MPICH2 communication libraries (used for compiling CHARMM version c34b2).

Environment Setup

For all software setup (compiling & installing) and simulation work, the following lines were added the end of the /home/gcollie/.bashrc file:

```
export MMTSBDIR=/home/gcollie/mmtsb_toolset_mod
export CHARMMEXEC=/home/gcollie/charmm-c34b2-mod-intel-ser-xxl/exec/gnu/charmm
export CHARMMDATA=/home/gcollie/charmm-c34b2-mod-intel-ser-xxl/toppar
export PATH=$MMTSBDIR/perl:$MMTSBDIR/bin:$PATH
export REMOTESHELL=/usr/bin/ssh
```

STRIDE (version dated 29.01.96) was installed with no modifications using the installation and environment setup instructions included with the source package.

MMTSB (package available online during the summer of 2006, no version

number, presumably the first public release) was compiled and prepared as described in the MMTSB documentation with no modifications. CHARMM version c32b2 (used for the Ion Box simulations) and version c34b2 (used for the LK Peptide REMD simulations) were both built using the following source file modifications and procedures.

[CHARMM installation location]/source/fcm/heap.fcm was modified at line #7 and #32 by adding an additional "0" to each of these values:

PARAMETER (HEAPDM=102400000)

PARAMETER (STKSIZ=100000000)

[CHARMM installation location]/install.com was modified to disable auto-vectorization by the Fortran compiler:

At line #893, sed -e 's@GNU-Linux-compiler@mpif77 -vec- -O3 -tpp7 -axW@g'

At line #902, sed -e 's@GNU-Linux-compiler@mpif90 -vec- -O3 -tpp7 -axW@g'

The modified serial build used for MD and REMD simulations was compiled on Palmetto (modules intel/10.1 mkl/10.0 loaded) using this command:

./install.com gnu xxlarge IFORT

The modified parallel build used for MD simulations was compiled on Palmetto (modules intel/10.1 mpich2/1.0.6 mkl/10.0 loaded) using this command:

./install.com gnu xxlarge IFORT M MPICH

Ion Box Simulations and Analysis (presented in Chapter IV)

Model System Construction

All FF parameters and topology files used, including those containing modifications, are located in /bioengr/gcollie/LIBS. All files used to construct the Ion Box systems are located in /bioengr/gcollie/ION.BOX.ARCHIVE/development. The 50% deprotonated carboxylic acid terminated SAM surface was built by merging one SAM composed of -COO^- residues with another SAM composed of -COOH residues. Since these residues do not exist in the CHARMM22 FF, they were added to the top_all27_prot_na.rtf topology file and assigned partial charges based on alkyl carbons and hydrogens and the terminal functional group partial charge assignments were based on the closest structural matches that exist in the FF, glutamic acid (GLU, for -COO^-) and protonated glutamic acid (GLUP, for -COOH). The samgen.COOH.inp and samgen.COO.inp CHARMM input files were used to build these SAMs, and the sam.combine.inp file was used to merge the two SAMs into a single surface ready for inclusion in a simulation.

The fixed water layer at the top of the simulation cell was constructed using the gen.fixlyr.inp CHARMM input file, and this procedure involved replicating and cropping the tip216.crd water box that is included with the CHARMM software package. Sodium and chloride ions were added to this water layer by substituting the calculated number of TIP3 waters with individual SOD or CLA residues to achieve as close to 140 mM NaCl as possible. This water layer was heated to 298 K using the fixlyr.heat.inp CHARMM input file, then the pressure of this layer was adjusted to 1 atm by altering the z-axis height using the fixlyr.cpt.equil.inp CHARMM input file.

The mobile water layer was constructed using the gen.watbox.inp CHARMM input file, and this procedure involved replicating and cropping the built-in tip216.crd water box, then replacing TIP3 waters with SOD and CLA residues. This water layer was heated to 298 K using the watbox.heating.inp CHARMM input file, then the pressure of this layer was adjusted to 1 atm by altering the z-axis height using the watbox.cpt.equil.inp CHARMM input file.

All four segments (SAM surface, ions, fixed water layer, and mobile water layer) were combined and moved into position using the build.inp CHARMM input file. Fine adjustment of the positions of the fixed water layer and the SAM was accomplished using the system.mini.inp CHARMM input file as a test to see if the z-axis height of the mobile water layer moved during equilibration of the complete system. Finally, the complete system was tested with normal MD simulation dynamics procedures using the system.ptest.inp CHARMM input file.

Production Work

The files associated with each distinct method/cutoff are contained in directories named as cut10ad, where "cut" indicates the radial cutoffs method, "10" indicates that settings for a 10 Å radial cutoff were used, and "ad" indicates that this system's ion distribution was adjusted to match that of the analytical distribution prior to starting the first production MD run (this was the case for all of the Ion Box simulations). The IPS, APS, and PME simulations are stored in directories named using the same convention. Within those directories, each 1 ns MD series was begun using the cut10.1ns.equil.s1.inp, where "cut10" indicates the use of a 10 Å radial cutoff, and "s1" indicates that this file is

associated with MD run #1 of the series. The output files resulting from that MD run were named using the same convention. The IPS, APS, and PME simulation input files were also named using the same convention. The starting CRD file for the initial MD run was named system.mini.crd, and the starting protein structure file was named system.mini.psf. Each MD run generated new CRD, PSF, and restart (RST) files to be used for launching the subsequent MD run in the series.

All analysis work done using the output files from these simulations is contained in the "analysis" directory within each method/cutoff parent directory (this is the case for all method/cutoff combinations).

Analysis of Results

The individual 1 ns and 500 ps MD trajectories for each method/cutoff were combined into a single MD trajectory using the merge.all.traj.inp CHARMM input file. In some cases, abnormal termination of an MD run resulted in a trajectory file that was not properly terminated. For those trajectories, the endfix.traj.inp CHARMM input file was used to extract the pre-termination trajectory so it could be merged with the other trajectories prior to analysis.

Once the trajectories were merged, PDB files were generated for each frame of the merged trajectory using the extract.pdbs.inp CHARMM input file. Histogram data was then generated based on the z-axis positions of the SOD and CLA ions using the ionhist.bash script. The resulting data was imported into Microsoft Excel for generation of plots and detailed data analysis. The Excel files that were produced are named

Revised.Ion.Box.Data.Plots.CUT.xlsx, where (in this case) “CUT” indicates that this file contains the ion distribution data for all of the results using radial cutoffs.

Multi-FF LK Peptide REMD Simulations and Analysis (presented in Chapters V and VI)

Model System Construction

All FF parameters and topology files used, including those containing modifications, are located in /bioengr/gcollie/LIBS. All files used to construct the LK peptide models, SAM surfaces, and complete systems are located in /bioengr/gcollie/LK.PEPTIDE.DEVEL. Each different FF used for the production REMD simulations required that the LK peptide models, SAM surface, and complete systems be constructed using the appropriate parameter libraries. To distinguish work done using the different FFs, the directories containing the files used for construction of AMBER94 and OPLS-AA system components are named with .amber or .opls, respectively, at the end of their names. Directories without .amber or .opls in their names contain work involving the CHARMM22 FF. Subdirectories within the /bioengr/gcollie/LK.PEPTIDE.DEVEL directory are named based on the work that is accomplished using the files contained therein. For example, the files used for generating SAM surfaces, peptides, fixed water layers, or water boxes have "gen" followed by "sam," LK peptide names, "fixlyr," or "watrbx" (respectively) in their names (e.g., gen.solo.lka14.xtend.amber). Other details about what work is done with the files contained in these directories should be evident based on their names (e.g., the gen.min.heat.pep.ion.watrbx directory contains files associated with creating, minimizing, and heating the water box with peptides and ions present).

The LK peptides were constructed using unmodified parameters and topology from each respective FF. For neutrality, each peptide was terminated via acetylation with the ACE residue and amination with the CT2 residue.

As was done for the Ion Box simulations, the 50% deprotonated carboxylic acid terminated SAM surface was built by merging one SAM composed of $-COO^-$ residues with another SAM composed of -COOH residues. The hydrophobic methyl terminated SAM surface was built from a single, $-CH_3$-terminated residue that was added to each FF's topology file and assigned partial charges based on alkyl carbons and hydrogens and the terminal functional group partial charge assignments were based on the closest structural match that exists in the FF, alanine (ALA).

The mobile water layer and the fixed water layer at the top of each simulation cell were constructed and prepared using the procedure followed for the Ion Box simulations. Peptides were added to the water boxes in various REMD starting conformations by removing all waters within 2 Å of each peptide atom prior to adding ions to achieve approximately 140 mM saline. Once created, all five segments (SAM surface, ions, peptides, fixed water layer, and mobile water layer) were combined and moved into position using the same fine adjustment of the z-axis positions of the SAM and fixed water layers. The files associated with this stage of system preparation are stored in the /bioengr/gcollie/LK.PEPTIDE.DEVEL subdirectories whose names begin with "build," and there are distinct directories for each system and FF used. Once built, these systems were equilibrated and tested with production dynamics settings using CHARMM input files located in the subdirectories that begin with "eq" (for equilibration). Following

verification that these model systems were ready for production REMD simulation, template MMTSB working directories were created for each system/FF combination using the "mmtsb.s14ch.a.template" naming scheme, where "s14" indicates that this is a single (or solo) LKα14 system, "ch" indicates the inclusion of a -CH_3 terminated SAM, and "a" indicates that this simulation uses the AMBER94 FF. These directories are located in /bioengr/gcollie/LK.PEPTIDE.MMTSB.TEMPLATES.

Within each template directory are the files necessary to launch a production MMTSB REMD job. Here, there is a single .psf file for the simulated system, along with 40 .crd files that make up the population of starting structures. 13 of these will be the coordinates for one starting structure, 13 for another starting structure, and 14 for the third starting structure. Since this distribution was slightly uneven, the starting structure represented by 14 .crd files was assigned to one that does not have the peptide(s) adsorbed to a surface or structured in a predicted conformation. Additionally, the .crd files were numbered so that the REMD temperature distribution would be evenly populated with each of the different starting structures.

Production REMD Simulations

The template directories were copied to the cluster where they were used, and each directory was duplicated and renamed with a final integer (1 or 2) to indicate which of the duplicate REMD jobs was contained in that directory. PBS job scripts to launch the REMD jobs are named job.palmetto.start.mmtsb.bash, where "palmetto" may be substituted for "qb" to indicate which cluster this job was started on. After the initial startup of each REMD job, they were continued whenever stopped or paused using the

job.palmetto.continue.mmtsb.bash script. Within each production REMD directory, a directory called "ensembles" was created to contain the PDB files saved at the end of each dynamics run. Another directory called "workdir" contains the active MD input, output, and other REMD configuration files (see MMTSB documentation for details).

Analysis of Results

Within each production REMD "ensembles" directory, a subdirectory called "analysis" was created to provide a centralized location for all analyses associated with the output PDBs from that REMD job. Here, the first step in the analysis was to use the run.gunzip.pdbs.bash script to unzip the compressed .pdb files saved by MMTSB.

The STRIDE secondary structure analysis of each PDB structure was scripted in run.stride.complete.system.bash. This script created a directory called "stride.output" where the raw STRIDE output was stored. Once STRIDE was run, the output was processed (parsed and organized for import into a spreadsheet) using the run.process.stride.output.complete.system.bash script.

Many of the analysis steps, and all of the CHARMM-based analysis steps, involved operations on an MD trajectory, so a single trajectory (.dcd) file was created from the library of saved and uncompressed PDB structures using the run.build.complete.dcd.bash script. This script uses a list of all the .pdb files to include in the trajectory file, and this list was created using the run.make.pdb.list.bash. Once this trajectory file was created, the order of operations for further analyses was unimportant.

All analyses based on distance measurements between atoms (side chain SSDs, parallel/antiparallel orientations, etc.) were combined in the distances.inp CHARMM

input file, which produces a variety of different output data files with names column headings that reflect the data they contain. Radial distribution function calculations originating at the peptide side chain terminal groups are produced by the rdf.watr.leu.lys.inp CHARMM input file. Side chain angle measurements for the peptides are generated by the side.chain.angles.inp CHARMM input file. Water diffusion properties are calculated using the water.diff.analysis.inp CHARMM input file. Z-axis distribution functions were calculated using the zdf.chloride.inp, zdf.sodium.inp, and zdf.water.inp CHARMM input files for chloride ions, sodium ions and water, respectively. The raw data generated from the various analysis procedures was imported into Microsoft Excel 2010 for statistical analysis and production of plots and tables.

REFERENCES

1. Horbett TA, Brash JL, editors. Proteins at interfaces II: Fundamentals and applications. Oxford University Press; 1995. Based on the March 1994 symposium sponsored by the Division of Colloid and Surface Chemistry at the 207th National Meeting held in San Diego, Calif. Contributions cover the theory and molecular mechanisms of protein adsorption (six papers); competitive adsorption of proteins (ten papers); the conformation and orientation of proteins at interfaces (seven papers); the effects of surface chemistry on protein adsorption (six papers); the role of adsorbed proteins in cell interactions with solid surfaces (four papers); and protein behavior at fluid-fluid interfaces (four papers). Some b&w photographs.

2. Latour RA. Biomaterials: Protein-surface interactions. In: Gary E. Wnek, Gary L. Bowlin, editors. Encyclopedia of biomaterials and biomedical engineering. 2nd Edition ed. Informa Healthcare; 2008.

3. Hunt JA, McLaughlin PJ, Flanagan BF. Techniques to investigate cellular and molecular interactions in the host response to implanted biomaterials. Biomaterials 1997 Nov;18(22):1449-59.

4. Lee JH, Li T, Park K. Solvation interactions for protein adsorption to biomaterial surfaces. In: M. Morra, editor. Water in biomaterials surface science. John Wiley & Sons Inc; 2001. .

5. Kasemo B. Biological surface science. Surf Sci 2002;500:656.

6. Castner DG, Ratner BD. Biomedical surface science: Foundations to frontiers. Surf Sci 2002;500(1-3):28.

7. Roach P, Farrar D, Perry CC. Interpretation of protein adsorption: Surface-induced conformational changes. J Am Chem Soc 2005 Jun 8;127(22):8168-73.

8. Puleo DA, Nanci A. Understanding and controlling the bone-implant interface. Biomaterials 1999 Dec;20(23-24):2311-21.

9. Kasemo B, Gold J. Implant surfaces and interface processes. Adv Dent Res 1999 Jun;13:8-20.

10. Agnihotri A, Siedlecki CA. Time-dependent conformational changes in fibrinogen measured by atomic force microscopy. Langmuir 2004 Sep 28;20(20):8846-52.

11. Andrade JD. Principles of protein adsorption. In: Joseph D. Andrade, editor. Surface and interfacial aspects of biomedical polymers. New York: Plenum Press; 1985.

12. Blitz JP, Gun'ko VM, editors. Surface chemistry in biomedical and environmental science. Springer; 2006.

13. Green RJ, Frazier RA, Shakesheff KM, Davies MC, Roberts CJ, Tendler SJ. Surface plasmon resonance analysis of dynamic biological interactions with biomaterials. Biomaterials 2000 Sep;21(18):1823-35.

14. Nakanishi K, Sakiyama T, Imamura K. On the adsorption of proteins on solid surfaces, a common but very complicated phenomenon. J Biosci Bioeng 2001;91(3):233-44.

15. Sapsford KE, Ligler FS. Real-time analysis of protein adsorption to a variety of thin films. Biosens Bioelectron 2004 Apr 15;19(9):1045-55.

16. Hubbuch J, Linden T, Knieps E, Thommes J, Kula MR. Mechanism and kinetics of protein transport in chromatographic media studied by confocal laser scanning microscopy. part II. impact on chromatographic separations. J Chromatogr A 2003 Dec 22;1021(1-2):105-15.

17. Andrade JD, editor. Surface and iterfacial aspects of biomedical polymers. New York: Plenum Press; 1985. This reference is for the entire book.

18. Hlady VV, Buijs J. Protein adsorption on solid surfaces. Curr Opin Biotechnol 1996 Feb 1;7(1):72-7.

19. Norde W. Driving forces for protein adsorption at solid surfaces. In: Martin Malmsten, editor. Biopolymers at interfaces. New York: Plenum Press; 1998.

20. Ramsden JJ. Puzzles and paradoxes in protein adsorption. Chem Soc Rev 1995;24:73.

21. Breen NF, Weidner T, Li K, Castner DG, Drobny GP. A solid-state deuterium NMR and sum-frequency generation study of the side-chain dynamics of peptides adsorbed onto surfaces. J Am Chem Soc 2009 10/14;131(40):14148-9.

22. MacKerell AD, Jr., Bashford D, Bellott M, Dunbrack RL, Evanseck JD, Field MJ, Fischer S, Gao J, Guo H, Ha S, Joseph-McCarthy D, Kuchnir L, Kuczera K, Lau FTK, Mattos C, Michnick S, Ngo T, Nguyen DT, Prodhom B, Reiher WE, III, Roux B, Schlenkrich M, Smith JC, Stote R, Straub J, Watanabe M, Wiorkiewicz-Kuczera J, Yin D, Karplus M. All-atom empirical potential for molecular modeling and dynamics studies of proteins. J Phys Chem B 1998 04/01;102(18):3586-616.

23. Sutmann G. Classical molecular dynamics. Quantum Simulations of Complex Many-Body Systems: From Theory to Algorithms 2002;10:211-54.

24. Leach AR. Molecular dynamics simulation methods. In: Molecular modelling: Principles and applications. Second Edition ed. Harlow, England: Pearson Education Limited; 2001.

25. Metropolis N, Rosenbluth AW, Rosenbluth MN, Teller AH, Teller E. Equation of state calculations by fast computing machines. J Chem Phys 1953 June 1953;21(6):1087-92.

26. Flake GW. The computational beauty of nature: Computer explorations of fractals, chaos, complex systems, and adaptation. The MIT Press; 2000.

27. Karplus M, McCammon JA. Molecular dynamics simulations of biomolecules. Nat Struct Biol 2002 Sep;9(9):646-52.

28. Latour RA. Molecular simulation of protein-surface interactions: Benefits, problems, solutions, and future directions. Biointerphases 2008;3:FC2.

29. Sugita Y, Okamoto Y. Replica-exchange molecular dynamics method for protein folding. Chem Phys Lett 1999;314:141.

30. Yang L, Shao Q, Gao YQ. Comparison between integrated and parallel tempering methods in enhanced sampling simulations. J Chem Phys 2009 Mar 28;130(12):124111.

31. Pearlman DA, Case DA, Caldwell JW, Ross WS, Cheatham TE, DeBolt S, Ferguson D, Seibel G, Kollman P. AMBER, a package of computer programs for applying molecular mechanics, normal mode analysis, molecular dynamics and free energy calculations to simulate the structural and energetic properties of molecules. Comput Phys Commun 1995;91(1-3):1-41.

32. Brooks BR, Bruccoleri RE, Olafson BD, States DJ, Swaminathan S, Karplus M. CHARMM: A program for macromolecular energy, minimization, and dynamics calculations. J Comp Chem 1983;4(2):187.

33. Feig M, Karanicolas J, Brooks CL. MMTSB tool set: Enhanced sampling and multiscale modeling methods for applications in structural biology. J Mol Graph Model 2004;22(5):377-95.

34. Brooks CL,3rd. Simulations of protein folding and unfolding. Curr Opin Struct Biol 1998 Apr;8(2):222-6.

35. Pande VS, Rokhsar DS. Molecular dynamics simulations of unfolding and refolding of a beta-hairpin fragment of protein G. Proc Natl Acad Sci U S A 1999 Aug 3;96(16):9062-7.

36. Ferrara P, Apostolakis J, Caflisch A. Thermodynamics and kinetics of folding of two model peptides investigated by molecular dynamics simulations. J Phys Chem B 2000;104(20):5000-10.

37. Snow CD, Nguyen H, Pande VS, Gruebele M. Absolute comparison of simulated and experimental protein-folding dynamics. Nature 2002 Nov 7;420(6911):102-6.

38. Lee MR, Duan Y, Kollman PA. State of the art in studying protein folding and protein structure prediction using molecular dynamics methods. J Mol Graph Model 2001;19(1):146-9.

39. Lazaridis T, Karplus M. Thermodynamics of protein folding: A microscopic view. Biophys Chem 2003;100(1-3):367-95.

40. Wu X, Brooks BR. Beta-hairpin folding mechanism of a nine-residue peptide revealed from molecular dynamics simulations in explicit water. Biophys J 2004 Apr;86(4):1946-58.

41. Feig M, Brooks CL,3rd. Recent advances in the development and application of implicit solvent models in biomolecule simulations. Curr Opin Struct Biol 2004 Apr;14(2):217-24.

42. Beck DA, Daggett V. Methods for molecular dynamics simulations of protein folding/unfolding in solution. Methods 2004 Sep;34(1):112-20.

43. Gnanakaran S, Nymeyer H, Portman J, Sanbonmatsu KY, Garcia AE. Peptide folding simulations. Curr Opin Struct Biol 2003 Apr;13(2):168-74.

44. Saiz L, Klein ML. Electrostatic interactions in a neutral model phospholipid bilayer by molecular dynamics simulations. J Chem Phys 2002;116:3052.

45. Zhou F, Schulten K. Molecular dynamics study of a membrane-water interface. J Phys Chem 1995;99(7):2194-207.

46. Tobias DJ, Tu K, Klein ML. Atomic-scale molecular dynamics simulations of lipid membranes. Current Opinion in Colloid & Interface Science 1997;2(1):15-26.

47. Gabdoulline RR, Zheng C, Vanderkooi G. Molecular origin of the internal dipole potential in lipid bilayers: Role of the electrostatic potential of water. Chem Phys Lipids 1996;84(2):139-46.

48. Shepherd CM, Schaus KA, Vogel HJ, Juffer AH. Molecular dynamics study of peptide-bilayer adsorption. Biophys J 2001 Feb;80(2):579-96.

49. MacKerell Jr AD, Feig M, Brooks III CL. Improved treatment of the protein backbone in empirical force fields. J Am Chem Soc 2004;126(3):698-9.

50. Price DJ, Brooks CL,3rd. Modern protein force fields behave comparably in molecular dynamics simulations. J Comput Chem 2002 Aug;23(11):1045-57.

51. Yoda T, Sugita Y, Okamoto Y. Comparisons of force fields for proteins by generalized-ensemble simulations. Chemical Physics Letters 2004;386(4-6):460-7.

52. Cornell WD, Cieplak P, Bayly CI, Gould IR, Merz KM, Ferguson DM, Spellmeyer DC, Fox T, Caldwell JW, Kollman PA. A second generation force field for the simulation of proteins, nucleic acids, and organic molecules. J Am Chem Soc 1995;117(19):5179-97.

53. Jorgensen WL, Maxwell DS, Tirado-Rives J. Development and testing of the OPLS all-atom force field on conformational energetics and properties of organic liquids. J Am Chem Soc 1996;118(45):11225-36.

54. MacKerell AD, Jr., Brooks BR, Brooks III CL, Nilsson L, Roux B, Won Y, Karplus M. CHARMM: The energy function and its parameterization with an overview of the program. In: Encyclopedia of computational chemistry. New York: John Wiley & Sons; 1998.

55. DeGrado WF, Lear JD. Induction of peptide conformation at Apolar/Water interfaces. 1. A study with model peptides of defined hydrophobic periodicity. J Am Chem Soc 1985;107:7684.

56. Xiong H, Buckwalter BL, Shieh HM, Hecht MH. Periodicity of polar and nonpolar amino acids is the major determinant of secondary structure in self-assembling oligomeric peptides. Proc Natl Acad Sci U S A 1995 Jul 3;92(14):6349-53.

57. Basalyga DM, Latour RA,Jr. Theoretical analysis of adsorption thermodynamics for charged peptide residues on SAM surfaces of varying functionality. J Biomed Mater Res A 2003 Jan 1;64(1):120-30.

58. Latour RA, Hench LL. A theoretical analysis of the thermodynamic contributions for the adsorption of individual protein residues on functionalized surfaces. Biomaterials 2002;23:4633.

59. Raut VP, Agashe MA, Stuart SJ, Latour RA. Molecular dynamics simulations of peptide-surface interactions. Langmuir 2005 Feb 15;21(4):1629-39.

60. Ulman A, Eilers JE, Tillman N. Packing and molecular orientation of alkanethiol monolayers on gold surfaces. Langmuir 1989;5:1147.

61. Dubois LH, Nuzzo RG. Synthesis, structure, and properties of model organic surfaces. Annu Rev Phys Chem 1992;43(1):437-63.

62. Poirier GE, Tarlov MJ. The c (4x2) superlattice of n-alkanethiol monolayers self-assembled on au (111). Langmuir 1994;10(9):2853-6.

63. Bain CD, Troughton EB, Tao YT, Evall J, Whitesides GM, Nuzzo RG. Formation of monolayer films by the spontaneous assembly of organic thiols from solution onto gold. J Am Chem Soc 1989;111(1):321-35.

64. Hautman J, Bareman JP, Mar W, Klein ML. Molecular dynamics investigations of self-assembled monolayers. Journal of the Chemical Society, Faraday Transactions 1991;87(13):2031-7.

65. Mar W, Klein ML. Molecular dynamics study of the self-assembled monolayer composed of S (CH2) 14CH3 molecules using an all-atoms model. Langmuir 1994;10(1):188-96.

66. Tobias DJ, Mar W, Blasie JK, Klein ML. Molecular dynamics simulations of a protein on hydrophobic and hydrophilic surfaces. Biophys J 1996;71(6):2933-41.

67. Zhdanov VP, Kasemo B. Monte carlo simulation of denaturation of adsorbed proteins. Proteins 1998 Feb 1;30(2):168-76.

68. Noinville V, Vidal-Madjar C, Sebille B. Modeling of protein adsorption on polymer surfaces. computation of adsorption potential. J Phys Chem 1995;99(5):1516-22.

69. Nordgren CE, Tobias DJ, Klein ML, Blasie JK. Molecular dynamics simulations of a hydrated protein vectorially oriented on polar and nonpolar soft surfaces. Biophys J 2002;83(6):2906-17.

70. Zhou J, Chen S, Jiang S. Orientation of adsorbed antibodies on charged surfaces by computer simulation based on a united-residue model. Langmuir 2003;19(8):3472-8.

71. Zhou J, Zheng J, Jiang S. Molecular simulation studies of the orientation and conformation of cytochrome c adsorbed on self-assembled monolayers. J Phys Chem B 2004;108(45):17418-24.

72. Mantero S, Piuri D, Montevecchi FM, Vesentini S, Ganazzoli F, Raffaini G. Albumin adsorption onto pyrolytic carbon: A molecular mechanics approach. J Biomed Mater Res 2002 Feb;59(2):329-39.

73. Raffaini G, Ganazzoli F. Simulation study of the interaction of some albumin subdomains with a flat graphite surface. Langmuir 2003;19(8):3403-12.

74. Raffaini G, Ganazzoli F. Molecular dynamics simulation of the adsorption of a fibronectin module on a graphite surface†. Langmuir 2004;20(8):3371-8.

75. West JK, Latour R,Jr, Hench LL. Molecular modeling study of adsorption of poly-L-lysine onto silica glass. J Biomed Mater Res 1997 Dec 15;37(4):585-91.

76. Latour RA, Rini CJ. Theoretical analysis of adsorption thermodynamics for hydrophobic peptide residues on SAM surfaces of varying functionality. J Biomed Mater Res 2002 Jun 15;60(4):564-77.

77. Wilson K, Stuart SJ, Garcia A, Latour RA,Jr. A molecular modeling study of the effect of surface chemistry on the adsorption of a fibronectin fragment spanning the 7-10th type III repeats. J Biomed Mater Res A 2004 Jun 15;69(4):686-98.

78. Agashe M, Raut V, Stuart SJ, Latour RA. Molecular simulation to characterize the adsorption behavior of a fibrinogen [gamma]-chain fragment. Langmuir 2005;21(3):1103-17.

79. Oberholzer MR, Wagner NJ, Lenhoff AM. Grand canonical brownian dynamics simulation of colloidal adsorption. J Chem Phys 1997 December 1, 1997;107(21):9157-67.

80. Gray JJ, Bonnecaze RT. Adsorption of colloidal particles by brownian dynamics simulation: Kinetics and surface structures. J Chem Phys 2001 January 15, 2001;114(3):1366-81.

81. Ravichandran S, Talbot J. Mobility of adsorbed proteins: A brownian dynamics study. Biophys J 2000 Jan;78(1):110-20.

82. Juffer AH, Argos P, Vlieg Jd. Adsorption of proteins onto charged surfaces: A monte carlo approach with explicit ions. Journal of Computational Chemistry 1996;17(16):1783-803.

83. Ravichandran S, Madura JD, Talbot J. A brownian dynamics study of the initial stages of hen egg-white lysozyme adsorption at a solid interface. The Journal of Physical Chemistry B 2001 05/01;105(17):3610-3.

84. Bujnowski AM, Pitt WG. Water structure around enkephalin near a PE surface: A molecular dynamics study. J Colloid Interface Sci 1998 /7/1/;203(1):47-58.

85. Liwo A, Lee J, Ripoll DR, Pillardy J, Scheraga HA. Protein structure prediction by global optimization of a potential energy function. Proc Natl Acad Sci U S A 1999 May 11;96(10):5482-5.

86. Liwo A, O&lstrok, dziej S, Pincus MR, Wawak RJ, Rackovsky S, Scheraga HA. A united-residue force field for off-lattice protein-structure simulations. I. functional forms and parameters of long-range side-chain interaction potentials from protein crystal data. Journal of Computational Chemistry 1997;18(7):849-73.

87. Liwo A, Pincus MR, Wawak RJ, Rackovsky S, O&lstrok, dziej S, Scheraga HA. A united-residue force field for off-lattice protein-structure simulations. II. parameterization of short-range interactions and determination of weights of energy terms by Z-score optimization. Journal of Computational Chemistry 1997;18(7):874-87.

88. Dai Y, Evans JS. An energy-based mapping method for identifying the in-plane orientations of polypeptides and other macromolecules at crystalline interfaces. J Chem Phys 2000 March 15, 2000;112(11):5144-57.

89. Jorgensen WL, Chandrasekhar J, Madura JD, Impey RW, Klein ML. Comparison of simple potential functions for simulating liquid water. J Chem Phys 1983;79:926.

90. van der Spoel D, Lindahl E, Hess B, Groenhof G, Mark AE, Berendsen HJ. GROMACS: Fast, flexible, and free. J Comput Chem 2005 Dec;26(16):1701-18.

91. Vernekar VN, Latour RA, Jr. Adsorption thermodynamics of a mid-chain peptide residue on functionalized SAM surfaces using SP. Materials Research Innovations 2005;9(2):53-4.

92. Sun Y, Welsh WJ, Latour RA. Prediction of the orientations of adsorbed protein using an empirical energy function with implicit solvation. Langmuir 2005 Jun 7;21(12):5616-26.

93. Sivaraman B, Fears KP, Latour RA. Investigation of the effects of surface chemistry and solution concentration on the conformation of adsorbed proteins using an improved circular dichroism method. Langmuir 2009;25:3050.

94. Klauda JB, Wu X, Pastor RW, Brooks BR. Long-range lennard-jones and electrostatic interactions in interfaces: Application of the isotropic periodic sum method. J Phys Chem B 2007;111:4393.

95. Loncharich RJ, Brooks BR. The effects of truncating long-range forces on protein dynamics. Proteins 1989;6:32.

96. Schreiber H, Steinhauser O. Cutoff size does strongly influence molecular dynamics results on solvated polypeptides. Biochemistry 1992;6:32.

97. Schreiber H, Steinhauser O. Taming cut-off induced artifacts in molecular dynamics studies of solvated polypeptides: The reaction field method. J Mol Biol 1992;228(3):909.

98. Schreiber H, Steinhauser O. Molecular dynamics studies of solvated polypeptides: Why the cut-off scheme does not work. Chem Phys 1992;168(1):75.

99. Darden TA, York D, Pedersen LG. Particle mesh ewald: An W log(N) method for ewald sums in large systems. J Chem Phys 1993;98(12):10089.

100. Garemyr R, Elofsson A. Study of the electrostatics treatment in molecular dynamics simulations. Proteins 1999;37(3):417.

101. Cheatham TE, III, Miller JL, Fox T, Darden TA, Kollman PA. Molecular dynamics simulations on solvated biomolecular systems: The particle mesh ewald method leads to stable trajectories of DNA, RNA, and proteins. J Am Chem Soc 1995;117:4193.

102. Yeh I, Berkowitz ML. Ewald summation for systems with slab geometry. J Chem Phys 1999;111(7):3155.

103. Kawata M, Mikami M, Nagashima U. Computationally efficient method to calculate the coulomb interactions in three-dimensional systems with two-dimensional periodicity. J Chem Phys 2002;116(8):3430.

104. Arnold A, de Joannis J, Holm C. Electrostatics in periodic slab geometries. I. J Chem Phys 2002;117(6):2496.

105. de Joannis J, Arnold A, Holm C. Electrostatics in periodic slab geometries. II. J Chem Phys 2002;117(6):2503.

106. Brodka A, Grzybowski A. Electrostatic interactions in computer simulations of a three-dimensional system periodic in two directions: Ewald-type summation. J Chem Phys 2002;117(18):8208.

107. Bostick D, Berkowitz ML. The implementation of slab geometry for membrane-channel molecular dynamics simulations. Biophys J 2003 Jul;85(1):97-107.

108. Foloppe N, MacKerell AD, Jr. All-atom empirical force field for nucleic acids: I. parameter optimization based on small molecule and condensed phase macromolecular target data. J Comput Chem 2000;21(2):86.

109. Fogolari F, Brigo A, Molinari H. The poisson-boltzmann equation for biomolecular electrostatics: A tool for structural biology. J Mol Recognit 2002 Nov-Dec;15(6):377-92.

110. Fears KP, Creager SE, Latour RA. Determination of the surface pK of carboxylic- and amine-terminated alkanethiols using surface plasmon resonance spectroscopy. Langmuir 2008;24:37.

111. Israelachvili JN. Intermolecular and surface forces. Second Edition ed. Academic Press; 1992. .

112. Smith JM, Van Ness HC, Abbott M. Introduction to chemical engineering thermodynamics. Sixth Edition ed. McGraw-Hill; 2000. .

113. Ulman A, Tillman N. Self-assembling double layers on gold surfaces: The merging of two chemistries. Langmuir 1989;5(6):1418.

114. Jorgensen WL, Jenson C. Temperature dependence of TIP3P, SPC, and TIP4P water from NPT monte carlo simulations: Seeking temperatures of maximum density. J Comput Chem 1997;19(10):1179.

115. Wang F, Stuart SJ, Latour RA. Calculation of adsorption free energy for solute-surface interactions using biased replica-exchange molecular dynamics. Biointerphases 2008;3(1):9.

116. Feller SE, Pastor RW, Rojnuckarin A, Bogusz S, Brooks BR. Effect of electrostatic force truncation on interfacial and transport properties of water. J Phys Chem 1996;100:17011.

117. Mark P, Nilsson L. Structure and dynamics of liquid water with different long-range interaction truncation and temperature control methods in molecular dynamics simulations. J Comput Chem 2002;23(13):1211.

118. Swope WC, Andersen HC, Berens PH, Wilson KR. A computer simulation method for the calculation of equilibrium constants for the formation of physical clusters of molecules: Application to small water clusters. J Chem Phys 1982;76:637.

119. Evans DJ, Holian BL. The nose-hoover thermostat. J Chem Phys 1985;83:4069.

120. Ryckaert J, Ciccotti G, Berendsen HJC. Numerical integration of the cartesian equations of motion of a system with constraints: Molecular dynamics of *n*-alkane. J Comput Phys 1977;23(3):327.

121. Newman MEJ, Barkema GT. Monte carlo methods in statistical physics. Oxford University Press; 1999.

122. Jonsson B, Wennerstrom H, Halle B. Ion distributions in lamellar liquid crystals. A comparison between results from monte carlo simulations and solutions of the poisson-boltzmann equation. J Phys Chem 1980;84:2179.

123. Joung IS, Cheatham TE, III. Determination of alkali and halide monovalent ion parameters for use in explicitly solvated biomolecular simulations. J Phys Chem B 2008;112:9020.

124. Horbett TA. The role of adsorbed proteins in animal cell adhesion. Colloid Surface B 1994;2:225.

125. Norde W, Haynes CA. Reversibility and the mechanism of protein adsorption. In: Thomas A. Horbett, John L. Brash, editors. Proteins at interfaces II: Fundamentals and applications. Oxford University Press; 1995. Based on the March 1994 symposium sponsored by the Division of Colloid and Surface Chemistry at the 207th National Meeting held in San Diego, Calif. Contributions cover the theory and molecular mechanisms of protein adsorption (six papers); competitive adsorption of proteins (ten papers); the conformation and orientation of proteins at interfaces (seven papers); the effects of surface chemistry on protein adsorption (six papers); the role of adsorbed proteins in cell interactions with solid surfaces (four papers); and protein behavior at fluid-fluid interfaces (four papers). Some b&w photographs.

126. Sun Y, Dominy BN, Latour RA. Comparison of solvation-effect methods for the simulation of peptide interactions with a hydrophobic surface. J Comput Chem 2007 Aug;28(11):1883-92.

127. Pertsin AJ, Grunze M. Computer simulation of water near the surface of oligo (ethylene glycol)-terminated alkanethiol self-assembled monolayers†. Langmuir 2000;16(23):8829-41.

128. Pertsin AJ, Hayashi T, Grunze M. Grand canonical monte carlo simulations of the hydration interaction between oligo (ethylene glycol)-terminated alkanethiol self-assembled monolayers. J Phys Chem B 2002;106(47):12274-81.

129. Sun Y, Latour RA. Comparison of implicit solvent models for the simulation of protein-surface interactions. Journal of Computational Chemistry 2006;27(16):1908-22.

130. Latour Jr RA. Molecular modeling of biomaterial surfaces. Current Opinion in Solid State and Materials Science 1999;4(4):413-7.

131. Hornak V, Abel R, Okur A, Strockbine B, Roitberg A, Simmerling C. Comparison of multiple amber force fields and development of improved protein backbone parameters. Proteins: Structure, Function, and Bioinformatics 2006;65(3):712-25.

132. Mackerell AD,Jr. Empirical force fields for biological macromolecules: Overview and issues. J Comput Chem 2004 Oct;25(13):1584-604.

133. Makarov V, Pettitt BM, Feig M. Solvation and hydration of proteins and nucleic acids: A theoretical view of simulation and experiment. Acc Chem Res 2002 Jun;35(6):376-84.

134. Hobza P, Kabelac M, Sponer J, Mejzlik P, Vondrasek J. Performance of empirical potentials (AMBER, CFF95, CVFF, CHARMM, OPLS, POLTEV), semiempirical quantum chemical methods (AM1, MNDO/M, PM3), and ab initio hartree-fock method for interaction of DNA bases: Comparison with nonempirical beyond hartree-fock results. Journal of Computational Chemistry 1997;18(9):1136-50.

135. Vellore NA, Yancey JA, Collier G, Latour RA, Stuart SJ. Assessment of the transferability of a protein force field for the simulation of peptide-surface interactions. Langmuir 2010;26(10):7396-404.

136. Weidner T, Apte JS, Gamble LJ, Castner DG. Probing the orientation and conformation of Î±-helix and Î²-strand model peptides on self-assembled monolayers using sum frequency generation and NEXAFS spectroscopy. Langmuir 2010 03/02;26(5):3433-40.

137. Apte JS, Collier G, Latour RA, Gamble LJ, Castner DG. XPS and ToF-SIMS investigation of α-helical and β-strand peptide adsorption onto SAMs. Langmuir 2009;26(5):3423-32.

138. Weidner T, Samuel NT, McCrea K, Gamble LJ, Ward RS, Castner DG. Assembly and structure of α-helical peptide films on hydrophobic fluorocarbon surfaces. Biointerphases 2010;5:9.

139. Collier G, Vellore NA, Stuart SJ, Latour RA. Development of molecular simulation methods to accurately represent protein-surface interactions: Method assessment for the calculation of electrostatic effects. Biointerphases 2009;4(4):57-64.

140. Zheng J, Li L, Chen S, Jiang S. Molecular simulation study of water interactions with oligo (ethylene glycol)-terminated alkanethiol self-assembled monolayers. Langmuir 2004 09/01;20(20):8931-8.

141. Simmerling C, Strockbine B, Roitberg AE. All-atom structure prediction and folding simulations of a stable protein. J Am Chem Soc 2002;124(38):11258-9.

142. Kameda T, Takada S. Secondary structure provides a template for the folding of nearby polypeptides. Proceedings of the National Academy of Sciences 2006;103(47):17765.

143. Jas GS, Kuczera K. Equilibrium structure and folding of a helix-forming peptide: Circular dichroism measurements and replica-exchange molecular dynamics simulations. Biophys J 2004;87(6):3786-98.

144. Zhang J, Li W, Wang J, Qin M, Wang W. All-atom replica exchange molecular simulation of protein BBL. Proteins: Structure, Function, and Bioinformatics 2008;72(3):1038-47.

145. Zhang W, Wu C, Duan Y. Convergence of replica exchange molecular dynamics. J Chem Phys 2005;123:154105.

146. Ruscio JZ, Fawzi NL, Head-Gordon T. How hot? systematic convergence of the replica exchange method using multiple reservoirs. Journal of Computational Chemistry 2010;31(3):620-7.

147. Grossfield A, Feller SE, Pitman MC. Convergence of molecular dynamics simulations of membrane proteins. Proteins: Structure, Function, and Bioinformatics 2007;67(1):31-40.

148. Faraldo-Gómez JD, Forrest LR, Baaden M, Bond PJ, Domene C, Patargias G, Cuthbertson J, Sansom MSP. Conformational sampling and dynamics of membrane proteins from 10-nanosecond computer simulations. Proteins: Structure, Function, and Bioinformatics 2004;57(4):783-91.

149. Frishman D, Argos P. Knowledge-based protein secondary structure assignment. Proteins 1995;23:566.

150. Humphrey W, Dalke A, Schulten K. VMD: Visual molecular dynamics. J Mol Graph 1996;14(1):33-8.

151. Pettersen EF, Goddard TD, Huang CC, Couch GS, Greenblatt DM, Meng EC, Ferrin TE. UCSF chimera-a visualization system for exploratory research and analysis. Journal of Computational Chemistry 2004;25(13):1605-12.

152. Weidner T, Breen NF, Li K, Drobny GP, Castner DG. Sum frequency generation and solid-state NMR study of the structure, orientation, and dynamics of polystyrene-adsorbed peptides. Proceedings of the National Academy of Sciences 2010 July 27;107(30):13288-93.

153. Zhu H, Braun W. Sequence specificity, statistical potentials, and three-dimensional structure prediction with self-correcting distance geometry calculations of β-sheet formation in proteins. Protein Science 1999;8(2):326-42.

154. Branden C, Tooze J. Motifs of protein structure. In: Introduction to protein structure. Second Edition ed. New York: Garland Publishing; 1999. Chapter 2 of Branden & Tooze.

155. Price DJ, Brooks CL,3rd. A modified TIP3P water potential for simulation with ewald summation. J Chem Phys 2004 Nov 22;121(20):10096-103.

156. Mark P, Nilsson L. Structure and dynamics of the TIP3P, SPC, and SPC/E water models at 298 K. The Journal of Physical Chemistry A 2001 11/01;105(43):9954-60.

157. van der Spoel D, van Maaren PJ, Berendsen HJC. A systematic study of water models for molecular simulation: Derivation of water models optimized for use with a reaction field. J Chem Phys 1998 June 22, 1998;108(24):10220-30.

158. Robinson RA, Stokes RH, Bates RG. Electrolyte solutions. Second ed. London: Dover Publications; 2002. This classic text, originally published in the 1950s and long since out of print, deals primarily with the measurement and interpretation of conductance, chemical potential, and diffusion in solutions of simple electrolytes. Theoretical interpretations are developed in detail, and extensive tables of thermodynamic and transport properties are featured. Topics include properties of ionizing solvents, limiting mobilities of ions, measurement of chemical potentials and diffusion coefficients, weak electrolytes, "strong" acids, ion association, thermodynamics of mixed electrolytes, and more. Appendices feature more than 90 pages of tabulated properties. Unabridged republication of the Second Revised Edition, 1970.

159. Cussler EL. Diffusion of interacting species. In: Diffusion: Mass transfer in fluid systems. Second ed. Cambridge University Press; 1997.

160. Marchi M, Sterpone F, Ceccarelli M. Water rotational relaxation and diffusion in hydrated lysozyme. J Am Chem Soc 2002;124:6787.